PROBING THE PHOTOCHEMICAL DYNAMICS OF WATER OXIDATION ON n-SrTiO3 THROUGH TIME-RESOLVED OPTICAL SPECTROSCOPY

by

SURYANSH SINGH

B.Tech., Vellore Institute of Technology, 20017

M.S., University of Colorado, 2022

A thesis submitted to the

Faculty of the Graduate School of the

University of Colorado in partial fulfillment

of the requirement for the degree of

Doctor of Philosophy

Materials Science and Engineering

2023

Committee Members:

Associate Professor Tanja Cuk

Assistant Professor Andres Montoya Castillo

Professor Jao van de Lagemaat

Associate Research Professor Sadegh Yazdi

Professor David Jonas

ABSTRACT

Singh, Suryansh (Ph.D., Materials Science and Engineering)

Probing the Photochemical Dynamics of Water Oxidation on n-$SrTiO_3$ through Time-Resolved Optical Spectroscopy

Thesis directed by Associate Professor Tanja Cuk

Photo-electro catalytic water splitting is a sustainable way to produce hydrogen, which is a clean and energy dense fuel. However, high overpotential and poor catalyst life hold back the water splitting process from being used on the scale needed to combat the energy crisis. The bottleneck is the Oxygen evolution reaction [OER], the oxidative half of the overall water splitting process. OER is a complex multi-step process involving 4 distinct electron transfers and several reactive oxygen intermediates (O* intermediates). Theory suggests that the catalytic activity of any material surface is determined by the interaction of the O* intermediates with the surface in any given catalytic environment. Therefore, the key to gaining a better mechanistic understanding of the OER is to isolate and directly observe the O* intermediates on a model surface in different environmental conditions. Analyzing how carrying out OER affects the catalytic surface, in tandem, is also important as it sheds light on problems such as durability of the catalyst.

In this dissertation, I conduct and study photo-electrocatalytic OER holistically on a n-doped Strontium titanate ($SrTiO_3$ or STO) semiconductor. I primarily use time resolved pump probe spectroscopy along with in-situ electrochemistry to isolate the O* intermediates and provide insight into the mechanistic details of OER. Using these techniques in tandem allows for tuning of the reaction conditions and monitoring the subsequent effects on the time evolution

of the intermediates. Moreover, coherent acoustic interferometry is used to study the strain induced in the catalytic surface when carrying out OER. Several imaging techniques, SEM/TEM/EDAX/AFM/XAS, are also used to characterize the changes that the catalytic surface accrues after OER is conducted.

Using time resolved pump probe spectroscopy, I observed that the populations representing the O* intermediates double as a function of pH (pH ranging between 7 to 13) of the solution which links the O* populations to thermodynamic quantities such as the free energy of formation of the first metastable O* intermediate on STO. The O* intermediate (polaron) is stabilized by deformation of the lattice which launches a strain wave that is detected using coherent acoustic interferometry as coherent oscillations in the data. This methodology allows for the detection of spatial extent, magnitude, and generation time of the intermediate induced interfacial strain through the phase and magnitude of the coherent oscillations. OER on any catalytic surface causes restructuring of the surface which is linked to a degradation of catalytic activity. Several imaging techniques were used in tandem with elemental analysis and X-ray spectroscopy to characterize and quantify the changes in the STO surface caused by OER.

Currently I am investigating the conversion of O* intermediates into molecular oxygen and the influence of tuning reaction conditions using a sub nano-second pump, allowing us to access nano-second to millisecond timescales. I have also built an experimental setup capable of performing FSRS (Femto-second stimulated Raman spectroscopy) experiments in reflectance and absorption geometries to study O* intermediates vibrationally on STO surface.

Going forward, FSRS will be used to resonate on the broadband optical transitions of the O* intermediates and differentiate between them using their vibrational signatures. Additionally, the experimental methodology and analysis

techniques developed in this work will be used to explore other OER catalysts, such as TiO_2 and RuO_2 in an effort to generalize the mechanistic understanding of OER to a variety of electrode surfaces.

To my friends and family

ACKNOWLEDGEMENTS

I am grateful to my advisor, Dr. Tanja Cuk, for the constant support, encouragement, constructive feedback, and insightful comments. Her expertise and guidance has been instrumental in shaping my ideas and refining my arguments. I would also like to acknowledge the financial support from the Department of Energy and the Materials Science and Engineering department at the University of Colorado, Boulder.

I would like to extend my heartfelt thanks to my colleagues and peers in the Cuk Research Group for all of their help, support and encouragement. I would also like to thank the members of my committee, Dr. Andres Montoya Castillo, Dr. Jao van de Langemaat, Dr. Sadegh Yazdi, and Dr. David Jonas, for their valuable feedback and suggestions.

I would like to thank my family and friends for their unwavering support and love throughout my academic journey. Their encouragement, understanding, and patience have sustained me during the ups and downs of graduate school. I am grateful to my parents for their unwavering support and sacrifice. Their love and encouragement has been the foundation of my academic pursuits.

Thank you all for your support, encouragement, and guidance. This thesis is a culmination of your contributions, and I am forever grateful.

CONTENTS

TABLES

Table

FIGURES

Figure

CHAPTER I

INTRODUCTION & BACKGROUND

Investment into alternative energy technologies has seen a sharp rise, in recent years, to combat the looming the energy crisis. Splitting water efficiently is at the heart of advancement of several clean, renewable energy technologies such as bio-mimetic photo-catalysis, solar fuels production, and metal air batteries to name a few. Efficient water splitting can also lead to easy access to hydrogen, a highly energy dense and environmentally clean fuel. The notion of splitting water into hydrogen and oxygen, to be used as fuel, has been around since the early 19th century when electrochemical water splitting was discovered. However, exploration of this process didn't gain much traction one account of the process being quite a lot more energetically inefficient than expected and it was impossible to figure out the nature of the inefficiency. Exploration of the water splitting process has seen a resurgence in recent times as technological advancements have allowed one to study the mechanisms of chemical reactions in detail and that knowledge has allowed experimentalists to tune the outcome of many chemical reactions. The overall water splitting process is a pair of two redox reactions, the oxidative half being the Oxygen Evolution Reaction (OER), and the reductive half being the Hydrogen Reduction Reaction (HRR). OER is widely regarded as the bottleneck and is known to be responsible for the inefficiencies associated with the overall water splitting process and thus needs to be studied in detail.

Catalytic reactions are generally described by a set of reaction steps involving meta-stable intermediate chemical species that reorganize reactants into products[1]. Yet, catalytic activity of any catalyst is still primarily judged by the cumulative product evolution, with a primary example being the steady state current in

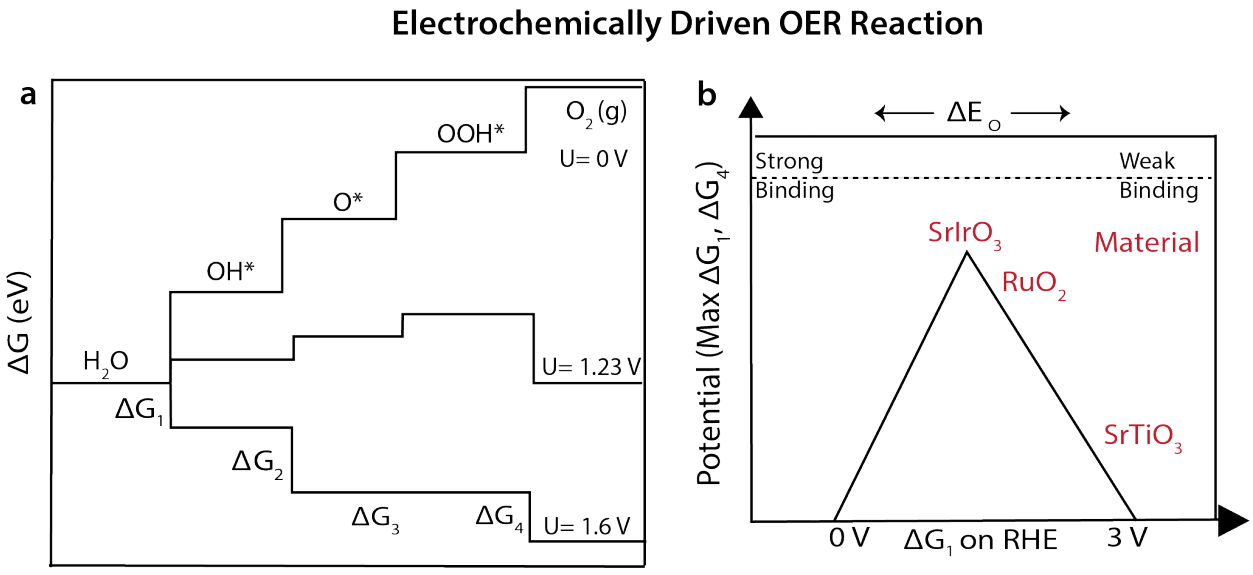

Figure 1.1: (a) Free Energies of individual OER reaction steps as a function of potential applied on the electrode in a purely potential driven mechanism. (b) The free energy of the first electron and proton transfer step (ΔG_1) as a descriptor of total OER activity in a volcano plot

electrochemical environments[2]. For OER, the proposed mechanism, depicted using reactions 1 – 4, for the single site case is a set of four steps that involve electron and proton transfers[3]. In the simplest proposed mechanisms, these steps occur as a sequence of four, single electron and proton transfer steps[4-5]. The M-OH* intermediate, resulting from the first electron and proton transfer from water, is expected to initiate the formation of the first chemical bond of O_2 (O-O)[3], with corresponding ΔG_1(OH*) and ΔG_3(O-O). In theoretical studies of OER, this first OER intermediate is often used to differentiate the activity of different catalytic systems[6], inclusive of metals and metal-oxides and has only recently been detected experimentally. Figure 1.1A shows the free energies for all four steps, while the theoretical thermodynamic potential need for OER is 1.23 V per electron transfer, in practice a significantly higher applied potential is needed to conduct OER. The higher applied potential is necessitated because the potential required for each of the steps does not equal 1.23 V exactly, for some steps it can be higher or lower than 1.23 V, so the minimum applied potential is determined by the step with the highest required potential/free energy. The step that requires the highest applied potential is the rate

limiting step. Transition metal oxides, such as strontium iridate ($SrIrO_3$), iridium oxide (IrO_2), ruthenium oxide (RuO_2), and similar semiconductors, are known to be the most efficient materials for catalyzing OER[7-9]. This is shown as a volcano plot in fig. 1.1B. where the commonly used OER catalysts are shown relative to each other with respect to the free energy of the rate limiting step ($\Delta G_1(OH^*)$)[10]. Moreover, industrial scalability of OER using the efficient catalysts is also held back by high raw material and manufacturing costs.

$$M - OH_2 + h^+ \longrightarrow M - OH^* + H^+ \qquad \Delta G_1 \qquad (1)$$

$$M - OH^* + h^+ \longrightarrow M - O^* + H^+ \qquad \Delta G_2 \qquad (2)$$

$$M - O^* + H_2O + h^+ \longrightarrow M - O - OH^* + H^+ \qquad \Delta G_3 \qquad (3)$$

$$M - O - OH^* + H_2O + h^+ \longrightarrow O_2 + M - OH_2 + H^+ \qquad \Delta G_4 \qquad (4)$$

Figure 1.2 shows a multi-site catalytic cycle evolving oxygen from a series of electron and proton transfer steps that suggests the formation of meta-stable intermediate populations. OER is a reaction that is extremely environment specific and involves multiple steps that subsequently involve multiple meta-stable intermediates (O* intermediates) [6,11-12]. The reaction can occur using a multi-site or a single site mechanism. The rate limiting step itself and the evolution of intermediates themselves can vary with reaction conditions, including pH & ionic strength of the solution, nature of the spectator ions etc. for a given catalytic surface while having a similar product yield. While multiple theoretical mechanistic models have been proposed for OER[6,11-12], direct experimental exploration of the OER mechanism is lacking. This extreme sensitivity of OER upon the environment implies that designing experiments to systematically study its mechanism is very challenging on account of the many variables that directly influence the catalytic process. However, it also implies that aspects of the reaction can be tuned according to predefined goals if one can understand the complexity and intricacies of a given

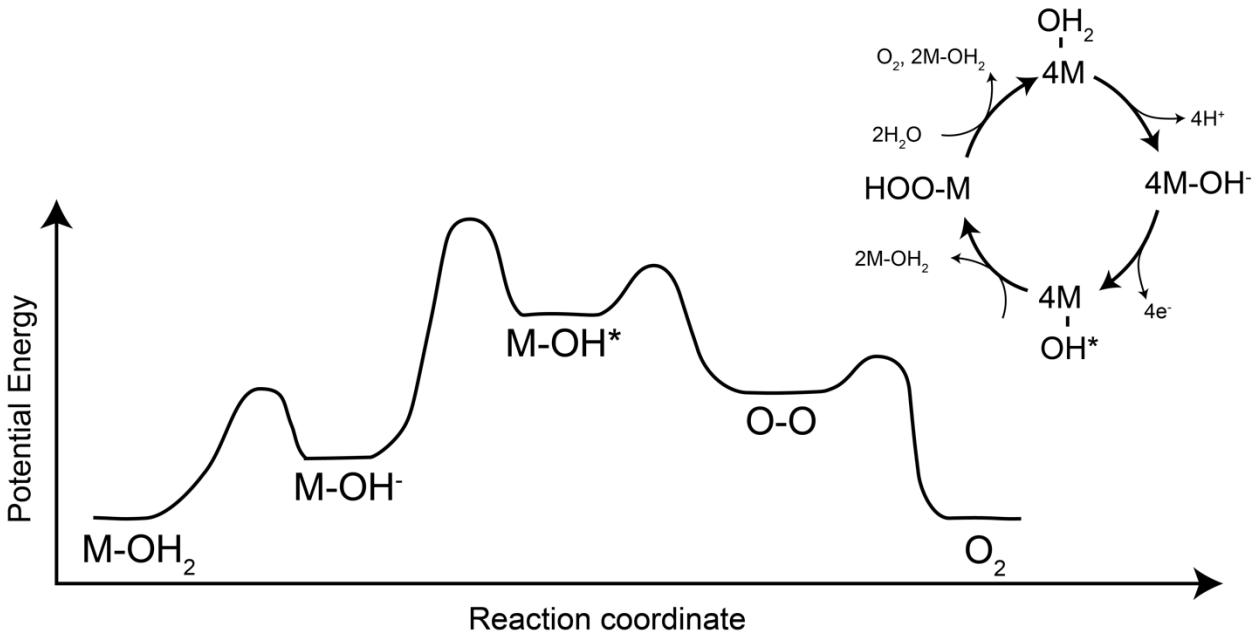

Figure 1.2: Potential Energy Surface (PES) of an OER catalytic cycle. The cycle depicted is a multi-site mechanism for which the 4 individual electron and proton transfer steps all occur at the surface, creating 4 M – OH* prior to O – O bond formation.

catalytic system. Thus, a complete mechanistic understanding of OER on a highly selective model surface involving the various steps and characteristic intermediates along with their dependencies on the catalytic environment is required to tailor the catalytic process for specific goals[13].

Different methodologies have been applied previously to try and isolate and detect reaction intermediates as a function of time and to relate the experimental and theoretical axes causally, especially in regard to homogeneous catalysis[4], where reactions have been halted at points within the catalytic cycle by potential, light, or changing reactant flows. A major step beyond this would be to directly time-resolve the reaction steps, obtain their rates of forward and back transfer, and follow meta-stable populations. Such experiments would provide both kinetic and thermodynamic quantities by which to tailor the material and its environment for desired functionality, such as the selectivity and speed of product evolution[14].

In order to be able to time-resolve a catalytic cycle for its reaction steps, there are at a minimum three critical considerations. One is that the cycle should be triggered at a distinct time-point and that the trigger should initiate a fully spontaneous (e.g., downhill) reaction. The spontaneous reaction means that the catalysis proceeds through sequential steps, such that each meta-stable intermediate occurs with a separate potential energy minimum (fig. 1.2) that describes its bonding environment, and one occurs after another. In this regard, a time-axis exists that tracks the spatial coordinate of the potential energy surface (PES). The distinct time-point is necessary such that the "birth" of each intermediate is captured and separated from intermediates occurring before and after. Ideally, an ultrafast trigger of the reaction is utilized, since charge-trapping at material interfaces can occur in less than a picosecond.

Second, the spectroscopic probe of the bonding environment should be sufficiently time-resolved, multi-modal, and surface-sensitive. Sufficient time resolution allows one to collect time-traces that resolve sequential kinetics. Multiple modalities are required in order to obtain information on both vibrational normal modes and the electronic states of the intermediates. A vibrational spectroscopy targets the shape of the PES bounding the intermediate, while an optical spectroscopy targets its minimum. While vibrational spectroscopy readily defines the intermediates molecularly, the optical spectroscopy encompasses a broader set of intermediates—independent of a particular geometry—whose populations lead to kinetic events. This dichotomy is important since not one distinct geometry will necessarily lead to bond formation events[15-16]. Finally, it is important that the probe is surface sensitive, and this is achieved in the most facile fashion using optical reflectance techniques—a simple reflectance of a UV-VIS probe and the utilization of an evanescent wave in the mid-infrared regime. There are certainly many non-linear

optical probes now available to get more surface sensitive, of which second harmonic and sum frequency generation are the most well-known. However, these have not been utilized yet to investigate an on-going chemical reaction in time.

Third, it is important to apply appropriate phenomenological analyses to the spectral and kinetic data. The purpose of these analyses is two-fold: 1) Resolve the intermediate's "bare" spectral signatures from a complex, condensed-phase environment and from other species present at the interface, and 2) Connect the observed spectra and kinetics of the reaction intermediates to the reaction conditions controlled by the experimentalist. These analyses include principal component analysis[17] of the optical (visible) probe and Fano Resonances[18] of the vibrational probe, among others. Their utility is best manifest upon seeing first the spectral and kinetic data that needs to be de-constructed from its environment, which for electrochemistry is the solid-liquid interface.

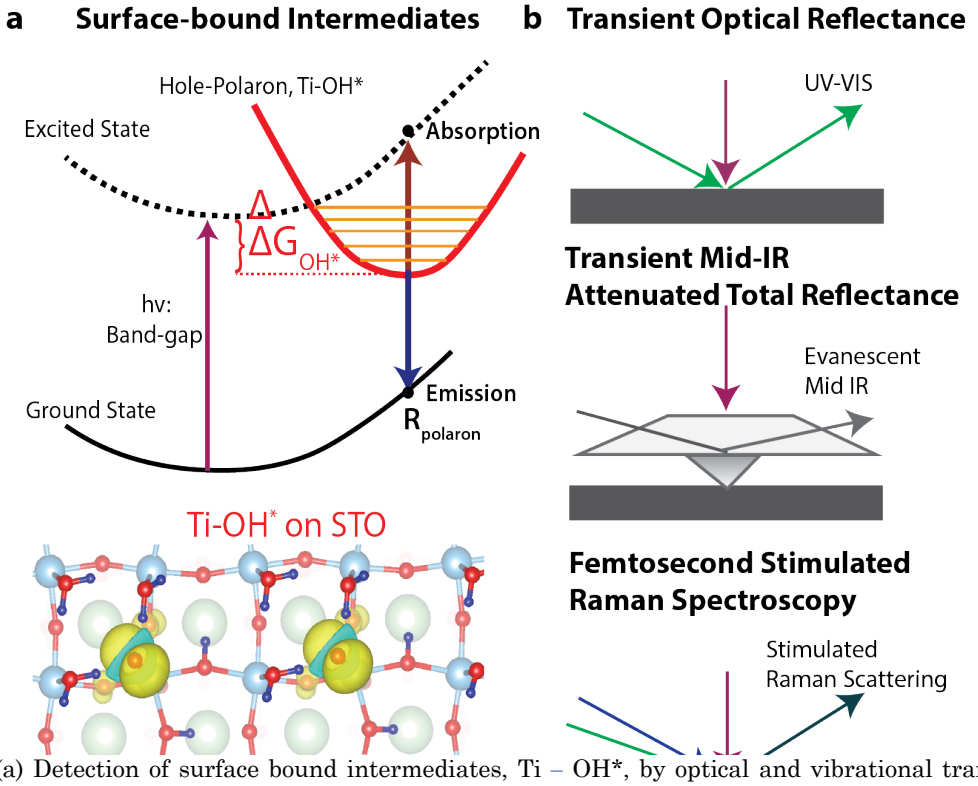

Figure 1.3: (a) Detection of surface bound intermediates, Ti – OH*, by optical and vibrational transitions. (b) Techniques include optical reflectance, attenuated total internal reflection - IR (ATR), and Femtosecond stimulated Raman spectroscopy (FSRS).

Exploration of OER through theoretical methods has provided some key insights that are instrumental to the studies that I will discuss in the later chapters of this dissertation. Analysis of the electrochemical water-splitting process using density functional theory (DFT) calculations on rutile oxide surfaces (TiO_2 RuO_2 and IrO_2) strongly suggest that the binding energies of the different intermediates follow linear scaling relationships[10,19]. Additionally, these linear scaling relationships have been experimentally confirmed for several OER catalysts. The linear scaling relationships imply that the binding energies of the subsequent intermediates of the catalytic OER process depend linearly on the binding energy of the first intermediate (M – OH*). The relationships thus allow for various OER catalysts to be characterized based on the thermodynamic quantities related to the first intermediate.

Previous studies from the Cuk Group have identified some pertinent information about the OER intermediates on n-doped strontium titanate, $SrTiO_3$ (nSTO or STO), using time resolved spectroscopy. Firstly, the electronic energy levels of the reactive intermediates were found to lie within the bandgap of STO through optical spectroscopy using a 400 nm narrowband probe[20]. Since the electronic energy levels of reactive intermediates lie within the bandgap of STO they are also referred to as "midgap states" from a semiconductor physics perspective. Through the same series of time-resolved experiments the formation and decay timescales of the mid-gap states were also reported.

Since optical spectroscopy probes electronic energy levels, it lacks the energetic resolution to differentiate intermediates if they have similar electronic energy levels. To identify reactive intermediates definitively, in addition to differentiating the geometrically diverse forms of a given intermediate, one needs a spectroscopic probe with a greater energetic resolution. In the vibrational regime using an infrared probe (IR), a reactive intermediate was observed through a well-

defined sub-surface vibration of lattice oxygen atoms that are in close proximity to the surface[21-22]. This sub-surface vibration was assigned as the vibrational signature associated with the terminal oxyl (Ti – O*) radical by accompanied DFT calculations. The associated DFT calculations also predict another intermediate known as the bridge radical (Ti – O* – Ti), however this radical is not expected to be IR active due to the lack of a dipole moment and was thus has not experimentally observed so far. Going to a probe even lower in energy, THz probes, one can study changes in the local environment of the reactive intermediates by exploring the oscillatory THz signal reported previously. The THz probes could potentially shed light on the effect of carrying out OER on a molecular scale.

Chapter 2: The experimental setup used to investigate photo-electro catalytic OER is described. The pertinent details of the semiconductor-aqueous interface and its behavior upon photoexcitation are explained from a electrochemical perspective. In addition, this chapter provides an introduction to time-resolved pump-probe spectroscopy and electrochemical techniques that will be utilized in subsequent chapters and can serve as a reference for the reader. Finally, the Singular Value Decomposition methodology, which will be employed in Chapter 3, is also discussed in detail in this chapter.

Chapter 3: Discusses the measurement of theoretical descriptors of photo-electro catalytic OER through the use of time resolved broadband pump probe spectroscopy on ultrafast timescales. I also discuss some observations when the temporal range of the spectroscopic technique is extended to microsecond timescales.

Chapter 4: Discusses the use of coherent acoustic interferometry to identify the effect OER has on the surface of the catalyst while OER is occurring, induced interfacial strain due to polaron formation distorting the surface locally.

Chapter 5: A discussion about the aftermath of conducting OER on the catalytic surface through imaging techniques. This chapter quantifies the amount of degradation/changes that the catalytic surface goes through after being used to catalyze OER.

Chapter 6: This chapter showcases the use of Femto-second stimulated Raman spectroscopy (FSRS) to differentiate the possible intermediates formed during OER. This chapter also discusses the foreseeable avenues that can be explored going forward to extend the work showcased in this thesis along with exploring some of the questions borne out of the work that still remain unanswered.

CHAPTER II

EXPERIMENTAL SETUP & METHODOLOGY

The goal of this chapter is to establish the experimental setup and highlight the important aspects such as the catalytic surface, initial state of the system, pertinent variables, and spectroscopic techniques used to conduct and study OER.

To systematically study the catalytic mechanism of OER one would require a model system to conduct spectroscopic experiments that allow for resolving the catalytic cycle spectrally and temporally. In addition, the spectroscopic experiments themselves will need to be designed meticulously such that they reaffirm the existing literature and expand upon that knowledge at the same time. One of the model systems for time-resolving catalysis at solid-liquid interfaces is the n-type semiconductor/aqueous interface for OER from water. While there are several materials that can serve as the catalyst in this model system, we have chosen the Niobium-doped semiconductor strontium titanate (referred to as nSTO or STO throughout this document) as the catalytic surface for the studies in this dissertation for a couple of reasons First, it is an extremely selective catalyst towards OER and doesn't facilitate many side reactions. While there are other catalysts that have a higher efficiency, such as IrO_2 and RuO_2[7-9], they can also support other processes and side reactions. High selectivity towards OER is thus imperative as it makes isolating effects caused by OER simpler during experiments. Second, it has a titania (TiO_2) terminated surface which benefits us because TiO_2 is one of the most thoroughly researched materials in the context of OER and the associated literature provides a solid foundation for mechanistic exploration. Third, STO has a higher quantum efficiency of charge separation (Q.E. > 75%) upon bandgap photoexcitation. Lastly, STO is commercially available as a single crystal of various sizes and doping densities

from multiple manufacturers. Lastly, STO is a d0 compound, such that: 1) the ground state has little background excitations, since the O 2p bonding orbitals are filled and the 3d anti-bonding orbitals are empty, and 2) electron-transfers out of the bonds come from the O 2p bonding orbitals, rather than 3d orbitals which exhibit complex electron-electron repulsions. Therefore, the model system is likely the simplest of the transition metal oxides on which to time-resolve the OER reaction. However, the methodologies presented here on the STO/aqueous interface should be applied to other materials in order to be able to truly design solar-to-fuel systems around the reaction steps of catalysis. The transient spectroscopic techniques and analyses will be most translatable to transition metal oxides and for oxidative reactions in which the electron transfers out occur from the valence band. The doping density for STO used primarily in the vast majority of experiments in this work is 0.1% Nb wt.%. Some experiments in this work use STO of other doping densities like 0.5% Nb wt.% and 0.7% Nb wt.% and the clarification is made when necessary.

Time Resolved Pump Probe Spectroscopy

In time-resolved pump-probe experiments, the system is first exposed to a pump pulse which triggers the reaction that one wants to probe. In the semiconductor-aqueous interfacial system the pump photoexcites the semiconductor resulting in generation of charge carriers, also referred to as photo-induced charge carriers, which can then interact with other species in the system and trigger reactions. A probe pulse is then incident on the sample after a time delay relative to the pump pulse, controlled by the experimentalist, and interacts with the interface where the reaction has been triggered. The probe pulse is then collected by a spectrometer and its spectrum is referred to as “probe shot”. The system essentially repeats this sequence multiple times for each value of the time delay. In each experiment there will be many different values of time delays that will be acquired.

The maximum time delay in the set of time delays spans the temporal extent of the pump probe experiment.

During the course of a time resolved pump probe experiment, many probe shots are taken and averaged. There are two distinct types of probe shots and they're referred to as "pump off" shots and "pump on" shots. The "Pump off" shots are probe shots when the sample hasn't been exposed to the pump pulse and thus effectively represents the equilibrium state of the system. The "Pump on" shots are probe shots that were preceded by a pump pulse separated by some time delay and represents the triggered state of the system. "Pump on" shots are expected to be different than "Pump off" shots because the refractive index of the system changes upon exposure to the pump, this could be due to the pump inducing a change in the distribution of charge carriers or by triggering a process that results in the same. To gain information about the system or the triggered process by the pump pulse one effectively looks at the difference between the "Pump on" and "Pump off" probe shots. In a given experiment, many probe shots are collected and averaged for each time delay. The number of shots averaged are also sometimes referred to as "number of averages" and it is usually between 2000 and 5000 shots. A schematic depicting the above is shown in figure 2.1A.

In a time resolved pump-probe experiment, the time delay b/w the pump and probe can be treated as an experimental condition to be varied during the experiment. The collection of time delay points forms the "delay" axis. It is important to note that the same range on the delay axis can be probed using a different number of delay points depending on other experimental constraints. There is a finite amount of time spent during acquisition of data corresponding to every time delay point, determined by the number of shots/delay that the camera is set to acquire, and is referred to as "active time". Every "active time" period is followed by "down time" during which the

setup, performs some immediate processing of the freshly acquired data, resets, updates the time delay and readies for another round of acquisition. Acquisition of all delay points that span the delay axis counts as 1 repeat. Multiple repeats can be acquired per experiment if allowed by the scan speed and the sample space/row. The total acquisition time is the sum of all the "active time" and "down time" throughout the experiment. The sample is exposed to the pump beam throughout the duration of

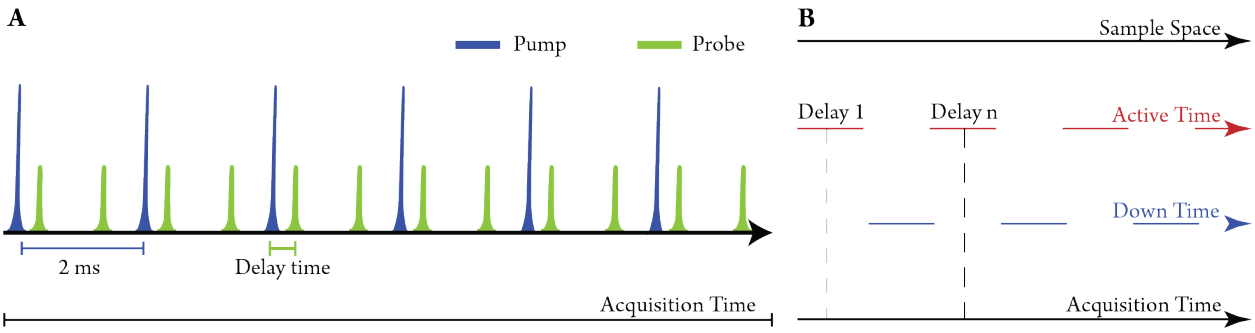

Figure 2.1: Time resolved pump probe spectroscopy overview. (A) Cartoon showing sequential on and off shots of the pump and probe pulses. Delay time is the time between pump and probe pulses in the on shot, and acquisition time is the total time passed over all shots taken. (B) Illustration depicting the progression of a time resolved experiment with time delay as an experimental condition vs the acquisition time axis. (A) shows the events taking place in detail during the active time for a given delay in (B).

the experiment. A representation of the above is shown in figure 2.1B.

The information extracted about the system through such an experiment is largely dependent on three primary factors, first, the energetic resolution provided by the employed spectroscopic probe, Second, the extent of the time delay that can be introduced between the pump and probe pulses. And third, the temporal resolution of the experiment which is largely determined by the pulse duration of the pump pulse. Note, that the pulse duration of the probe does not limit the temporal resolution because we detect the probe in a spectrally dispersed fashion. For example, a broadband white light continuum (WLC) as a probe will inform us of the electronic states of geometrically diverse intermediates as an average along with their time evolution but will fail to resolve them structurally. To differentiate the intermediates

(with similar electronic energy levels) structurally one would use vibrational spectroscopy like time-resolved IR or Raman spectroscopy, with a suitable probe, and identify distinct vibrational signatures of the O* intermediates. Different regimes of time-resolved spectroscopy are set apart by their energetic resolution and inform us about different aspects of the system. For the experiments on the ultrafast timescale mentioned in this work we use an 800 nm (fundamental) output, with a pulse duration of 200 fs at 1 kHz repetition rate, that is split into the pump and the probe lines. Figure 2.2 shows a basic version of the layout of the optical setup used for time resolved pump probe experiments. A detailed optical diagram can be found in the Appendix.

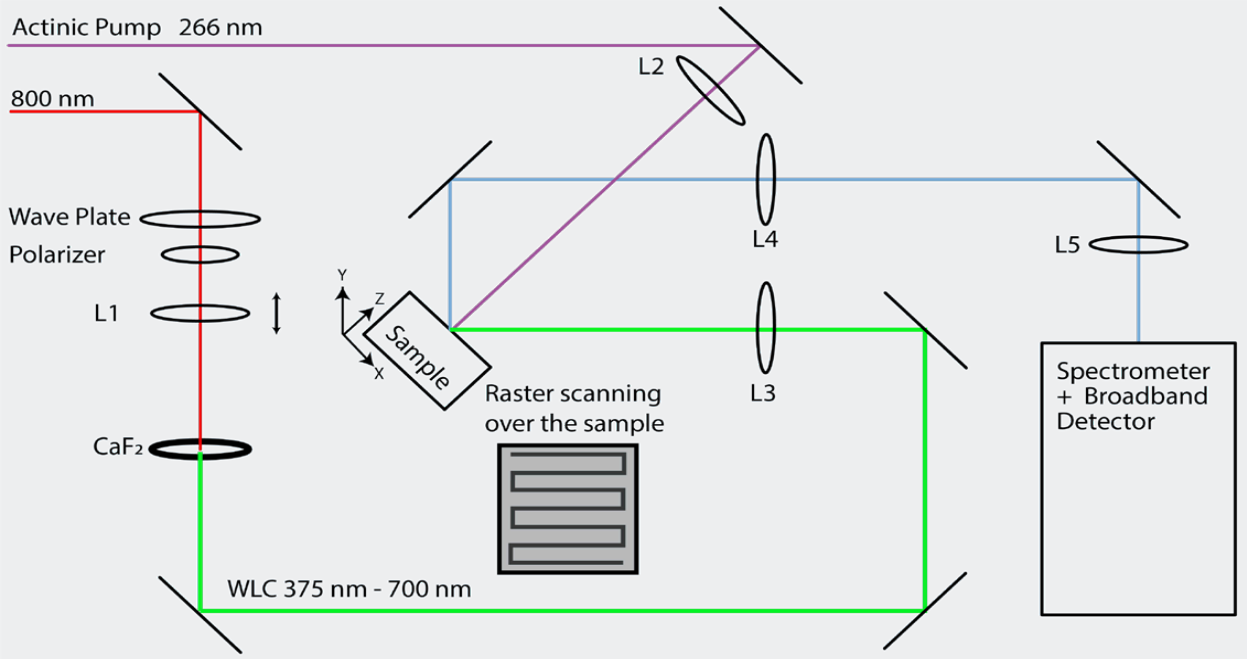

Figure 2.2: Transient reflectance optical setup overview. The pump (266 nm) that excites the catalysis and the visible broadband probe (WLC), and the spectrometer/broadband array detector. The generation of the WLC probe is also shown. The reflectance geometry is shown along with the sample's raster style movement.

Pump (266 nm): Third Harmonic Generation (THG)

The pump pulse of 266 nm is generated by taking one arm of the split fundamental (800 nm) through a chopper to modulate the repetition rate to 500 Hz

followed by two sequential sum frequency generation (SFG) processes. The required optics are from a commercially bought kit from Eksma Optics called Femtokit Basic FK-800-200-M. The first SFG process results in doubling of the fundamental which outputs 400 nm pulses and the second SFG process "adds" the 400 nm output (from first SFG) with the leftover 800 nm to output 266 nm pulses with a pulse duration of 400 fs. The fundamental and the output of the first SFG process need to be corrected for polarization mismatch (utilizing a waveplate) and temporal walk-off (utilizing a birefringent material) before going through the second SFG process. After the second SFG process, there are three collinear beams on the table which are the leftover fundamental (800nm), output from first SFG (400nm), and the desired pump (266nm). The three beams go through a pair of harmonic separators (special mirrors with coatings that are designed to reflect a narrow wavelength range) designed for 266 nm light, or through a Pellin-Broca Prism to isolate the desired pump beam from the other two beams which are caught by a beam dump to limit scatter. Figure 2.3 depicts the THG process diagrammatically. The pump line has an electronically controlled stage that can be programmed to move small distances, incurring path

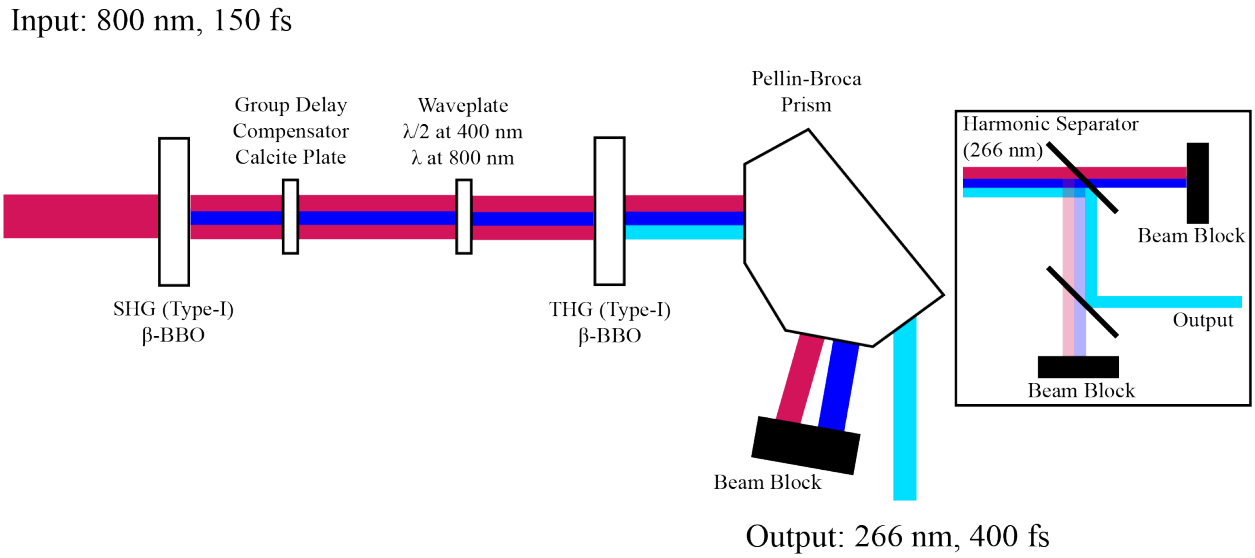

Figure 2.3: A schematic showing the third harmonic generation utilized to generate and isolation of 266 nm light on the optical table.

length differences between the pump and the probe lines resulting in a time delay (up to 4 ns) between the pulses when arriving at the sample. The maximum time delay in such a setup is limited by the maximum path length difference that can be introduced which in turn is limited by the design of the electronic delay stage. Note, the placement of the electronic delay stage is limited by the design of the setup and in principle can be placed on either the pump or the probe lines. Experiments employing the ultrafast pump beam, generated with the aforementioned method, are hereby referred to as "Ultrafast timescale transient reflectance (TR) experiments".

Longer time delays, on the microsecond timescale, between the pump and probe can be achieved by using a separate pump source. In contrast these expriments are called "Microsecond timescale transient reflectance (TR) experiments". Our optical setup uses a second laser source, Picolo 1 from InnoLas, for pump probe experiments where longer time delays need to be accessed. In such a configuration, where the pump and probe beams are obtained from separate sources, it is imperative to synchronize the two sources to be able to use them for a pump probe experiment. Synchronization between the sources means that one source is triggered to fire a pulse with respect to the other source. The firing of the second pulse is digitally controlled using Digital Delay Generator (DDG).

Probe: White Light Continuum (WLC) Generation

The UV-VIS spectroscopic probe is generated on the other arm of the split fundamental (800 nm) known as the probe line; the generation process is shown in figure 2.2. On the probe line the fundamental (800 nm) is focused into a constantly moving Calcium fluoride (CaF_2) crystal, a highly non-linear material with a large third order electronic susceptibility, to generate a broadband white light continuum (WLC) also referred to as supercontinuum, though self-phase modulation, spanning a wavelength range that encompasses the entire visible spectrum (375 nm – 700 nm).

Self-phase modulation (SPM) is a non-linear optical effect that is primarily responsible for supercontinuum generation[23]. When an ultrafast pulse of light, of sufficient intensity, travels through a nonlinear medium it can make the refractive index dependent on the intensity of the incident light. This variable refractive index imposes a phase shift in the pulse causing the frequency spectrum to broaden, with the fundamental frequency at the center, into a supercontinuum. Note that the broadening of the frequency spectrum is also sometimes referred to as the temporal aspect of SPM. The extent of broadening is dependent primarily on three factors, the material used, intensity of incident light, and the thickness of the material used. Out of these three factors, the intensity is the most important one. Supercontinuum generation occurs after a certain intensity threshold when the third order effects become significant. However, if the intensity is too high then higher order effects also start becoming significant and can lead to multi-filament generation which is a highly noisy supercontinuum unusable for any spectroscopy. This implies that the intensity needs to be controlled carefully to achieve a high quality and low noise supercontinuum. The intensity can be varied by either modulating the power of the incident beam or by changing the focal length of the lens used to focus the incident beam onto the material. A Supercontinuum in principle can be generated using any material as the medium, even air, however, the threshold intensity for supercontinuum generation generally scales with the third order electronic susceptibility of the medium. Similar supercontinuum, encompassing the entire visible spectrum, have been generated using Yttrium aluminum garnet (YAG) as the medium. The thickness of the medium is important to a certain extent because a thicker medium can impose more phase change upon the light but can introduce multifilament generation if the medium is too thick.

We use a CaF_2 crystal as the nonlinear medium for supercontinuum generation. The crystal is mounted on a stage to allow the crystal to be moved circularly in a plane perpendicular to the optical axis of the incident beam of light. CaF_2 accrues defects, in the form of F-centers, quickly when used for supercontinuum generation when static which causes it to do multi-filament generation rendering it unusable. Constant motion prevents the same area of the crystal from being continuously exposed and thus prolongs the usable lifetime of the CaF_2 crystal.

Electrochemistry techniques

The photo-electro catalytic experiments are performed in the electrolytic cell, shown in figure 2.4A, in tandem in-situ electrochemistry where the exposed surface of the catalyst (n-STO) serves as the anode, on the other hand a platinum wire housed inside the cell serves as the cathode. An Ag/AgCl (SSC) reference electrode is also present to complete the electrochemical system. It is important to note that the SSC reference electrode scales in a Nernstian fashion (59 mV/pH). All three electrodes are connected to a potentiostat (CHI 650E from CHI instruments) which allows us to control the electrochemical configuration of the system. The electrolytic cell is designed such that the catalyst can be exposed to the ultrafast pump pulse for photoexcitation of the catalyst along with the probe pulse. The potentiostat is also capable of performing several purely electrochemical experiments, Cyclic Voltammetry (CVs), Open Circuit potential-time (OCPT) measurements, Impedance-potential measurements, and Amperometry being used frequently, which help with characterizing the catalyst surface electrochemically and in understanding the equilibrium state of the system.

Cyclic Voltammetry

Cyclic Voltammetry (CV) is a powerful electroanalytical technique used to study the redox behavior of electroactive species within a system, present in the

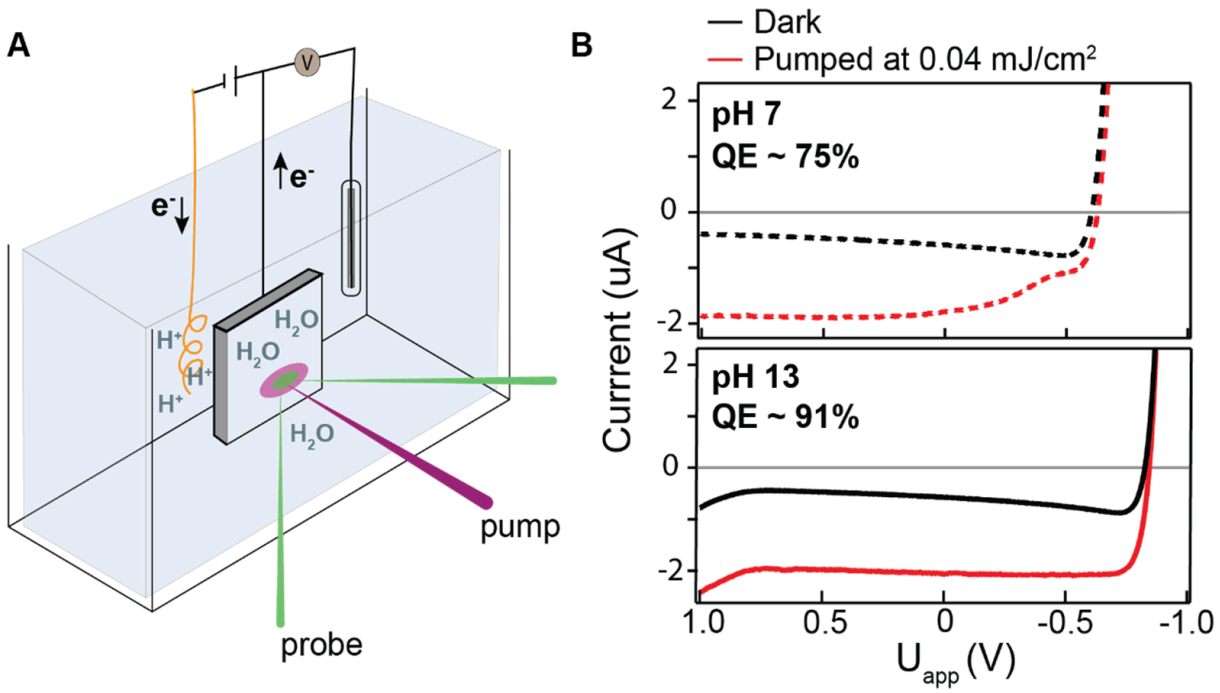

Figure 2.4: A) Cartoon of the electrochemical cell and the pump probe beam configuration; B) Cyclic voltammogram of nSTO for 2 pH conditions, only the anodic sweep is shown.

solution or molecular species adsorbed on the surface of the electrode. In cyclic voltammetry, the potential is scanned back and forth between two potential limits over a defined number of cycles or sweeps and the resulting current response is measured and recorded. CV experiments are incredibly helpful for us in four primary ways, First, using a CV allows one to confirm that there are no foreign electroactive species present in the system, additionally running a CV for multiple sweeps can "clear" the system of trace amounts of foreign electroactive species by forcing them to react. Second, since we must prepare the semiconductor so it can be electrically contacted, the voltammogram from a CV can serve as a check for the quality of the electrical contact with the back of the semiconductor through its shape and the intensity of the current for a given voltage. This helps confirm that the system is behaving like a diode by the flat shape of the voltammogram. If the shape of the voltammogram is not flat but is significantly tilted, this indicates "ohmic" behavior suggesting that the sample preparation might have been faulty. Third, for the

semiconductor-aqueous interfacial systems like STO-aqueous interface, one can perform a CV with or without photoexcitation of the semiconductor electrode resulting in "Light on CV" and "Dark CV" respectively. Examples of CVs are shown in figure 2.4B. The difference between the currents for a particular sweep and a particular voltage, within the ideal diode regime like 0 V, is the photocurrent of the system. Comparing the photocurrent with the incident fluence of the pump beam results in the quantum efficiency of charge separation for the system. Lastly, we can analyze the dark CVs to find the applied potential where the photocurrent becomes zero, this value of applied potential is an important quantity of the system known as open circuit voltage (V_{OC}). Applying V_{OC} to the system puts the system in a forward bias to the point of extinguishing the current, this state of the system is equivalent to the system being in open circuit, see STO/Aqueous interface section for a thorough explanation of electrochemical configurations, configuration during photoexcitation. Figure 2.5 shows the trend of V_{OC} vs solution pH and reports a slope of 43.1 mV/pH.

Quantum Efficiency of charge separation (Q.E.) is defined as the ratio of the number of photo-induced charges to photons adsorbed. For a given fluence (F in mJ/cm^2), we calculate the number of photons incident on the sample per second (P), considering the chopped rep. rate of the laser (R = 500 Hz), excitation spot area (A), and pump photon energy (E = 4.66 eV). A loss factor (L = 0.8) needs to be accounted as the measurement of pump power occurs right before the sample cell, but the Quartz window of the sample cell isn't perfectly transparent and reflects some 266 nm light, in addition the aqueous solution column also absorbs some 266 nm light, therefore it's estimated that ~ 80% of the incident light makes it to the STO surface.

$$P = \frac{F * R * A * L}{E} \qquad (5)$$

The number of free charges is calculated by taking the difference of the current Light on CV (I_L) and Dark CV (I_D) at 0V and dividing by the electronic charge (e):

$$N = \frac{I_L - I_D}{e} \quad (6)$$

The Q.E. as a percentage is thus:

$$Q.E. = \frac{N}{P} * 100 \quad (7)$$

Typically, the Q.E. is measured to be ~70% or higher for a fluence of 0.04 mJ/cm² on 0.1% Nb STO.

Open Circuit potential - Time Measurements

Open-circuit potential - time (OCPT) measurement is a useful technique for studying the electrochemical properties of photoactive materials, which are materials that can absorb light and generate electrical charge carriers. OCPT measurements involve the measurement of the potential difference between a photoactive material and a reference electrode, with no external current flowing between the electrodes. The OCPT reflects the tendency of the photoactive material to generate electrical

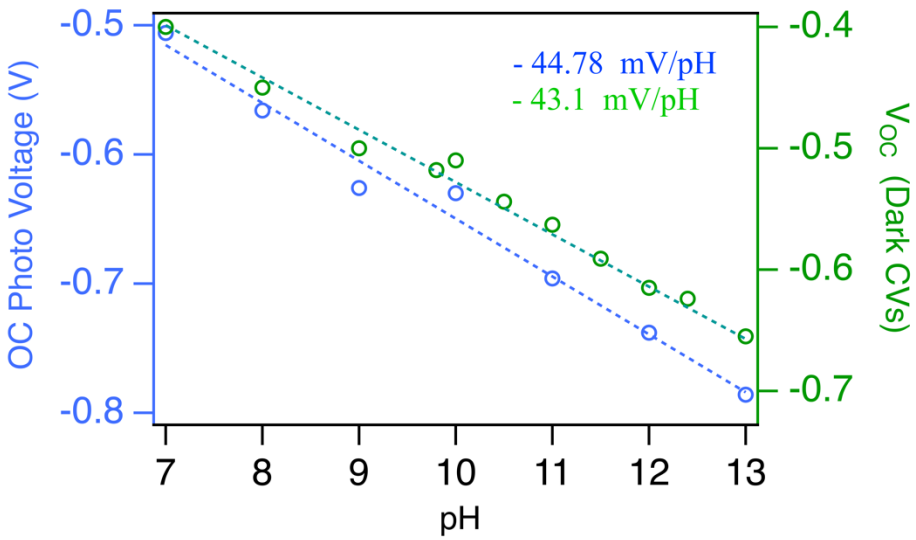

Figure 2.5: Graph showing the trends of OCPV and VOC vs pH. The slope is also reported on the graph.

charge carriers in the presence of light and can be affected by factors such as the bandgap energy of the material, the intensity and wavelength of the incident light, and the presence of surface defects and impurities.

We use OCPT measurements, to measure the difference in open circuit potential of the semiconductor in dark conditions (not exposed to pump light) vs light on conditions (exposed to pump light) when the semiconductor is in contact with a solution of a particular pH. The measured difference is the open circuit photo-voltage (OCPV) which reflects the change in the flat band potential (U_{FB}) of the semiconductor when it has been equilibrated with the solution of a certain pH value. We measure the OCPV of our system while varying the solution pH. Figure 2.5 shows the trend of OCPV vs solution pH and reports a slope of 44.78 mV/pH. The presence of a trend throughout the explored pH range (pH 7 – pH 13) is extremely important as it solidifies the notion that modulating the solution pH is directly affecting the adsorption onto the electrode surface and affecting the resulting equilibration of the system in the dark. For instance, if we notice OCPV varying with solution pH only until a certain pH and plateaued after that, it will imply that varying solution pH past that point is redundant as the electrode surface isn't being affected at all.

Impedance Potential Measurements (IMPE)

Impedance-potential measurements are an incredibly useful technique that is used to study the electrochemical behavior of materials in different environments. These measurements are particularly useful for investigating the properties of solid-liquid interfaces and the performance of electrochemical devices such as batteries, fuel cells, and sensors. We use them to study the semiconductor-aqueous (nSTO-water) interface created in our experiments.

One of the most commonly used tools for interpreting impedance-potential data is the Mott-Schottky analysis, which provides valuable information on the electronic

properties of the material under study. This analysis is based on the principles of electrochemical impedance spectroscopy (EIS), which measures the response of a material to an applied AC voltage. A good overview of Mott-Schottky analysis for semiconductor-aqueous interface is given by R. De Gryse et al, ref 24.

Mott-Schottky plots are a type of EIS analysis that plots the capacitance of a material as a function of the applied potential. These plots can provide information about the doping concentration, charge carrier density, and flat-band potential of a material, as well as the presence of surface states and other defects. Equation 9 depicts how the capacitance of the diode system relates to other properties of the system. The x-intercept of the above equation when fit to the data represents the flat band potential, U_{FB}, of the system. The Flat band potential of the diode system is applied potential necessary to forward bias the diode system to the point where the built in electric field is completely extinguished resulting in flattening of the bands of the diode system. An example Mott-Schottky plots is shown in fig. 2.7d.

We primarily use the Mott-Schottky analysis to confirm the doping density of the commercially bought STO samples that we use in OER experiments. The Mott-Schottky analysis together with the Cyclic voltammetry serves as a two-step check for our semiconductor samples and the fidelity of the electrochemical contact.

Amperometry

Amperometry is a simple electrochemical measurement where the potentiostat applies a constant potential to the working electrode, with respect to a known reference like SSC, and current is read out and reported as an amperometric i-t curve. We use this technique, in-situ, along with every pump-probe experiment conducted in CC configuration. Since we're studying a photocatalytic system the amperometric i-t curve reports on the photocurrent generated within the system during the pump-probe experiment as a function of acquisition time.

We are primarily interested in the magnitude and stability of the photo-current during the pump probe experiments. A change in the magnitude of the photocurrent on a given sample can occur primarily due to difference in Q.E. of charge separation or due to fluctuations in the power of the incident pump beam. Examples of amperometric i-t curves can be seen in (Fig 3.3A).

STO/Aqueous Interface

The semiconductor catalyst nSTO during these experiments is in direct contact with an aqueous environment and forms a Schottky barrier at the semiconductor-aqueous interface. The Schottky barrier is a type of electrical junction that is formed when a semiconductor comes in direct contact with another material, typically a metal, that can serve as a reservoir for charge carriers (i.e., the fermi level of the material doesn't change significantly when accepting or donating charge carriers on account of an excess of charge). The Schottky barrier is formed naturally at the interface due to equilibration of the chemical potential of electrons with the chemical species in the aqueous solution causing the bands of the semiconductor, conduction band (CB) and valence band (VB) to bend resulting in an electric field at the interface. For aqueous interfaces for which ions in the electrolyte or adsorbed on the surface cannot be reduced or oxidized (spectator ions such as Na^+ or SO_4^{2-} in the STO-aqueous

interfacial system), the relevant reaction that levels the chemical potential across the interface is the O_2/H_2O oxidation-reduction reaction. The free ions in the solution adsorbed onto the surface form a dipole which is known as the Helmholtz layer. The resulting electric field in the semiconductor can then be utilized upon photoexcitation to separate photo-excited electron-hole pairs, such that the valence band (VB) holes accumulate at the interface and evolve O_2 from water. The electric field or the Schottky diode, shown in figure 2.6, can itself be biased in the forward or backward regime by applying a potential, relative to the reference electrode, to the back of the working electrode. The electrochemical configuration where a bias or potential is applied to the back of the working electrode is known as "Closed Circuit"

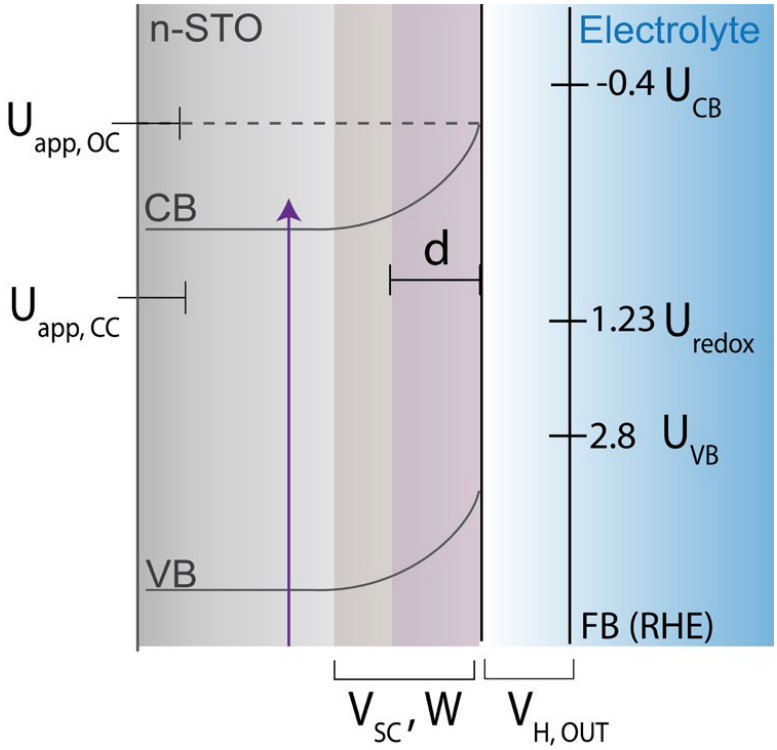

Figure 2.6: n-STO/electrolyte interface with potentials (U) and potential differences (V) designated. $U_{app,OC}$, $U_{app,CC}$ refers to the steady state potential at the back of the electrode under open, closed circuit conditions during photo-excitation. V_{SC}, W, and d refer to the full voltage drop across the diode in the semi-conductor (including any absorbed interfacial dipoles), its depletion width, and the adsorption depth of the above band-gap light excitation. $V_{H, OUT}$ refers to the voltage drop across the Helmholtz layer of free ions. The potentials of the conduction, U_{CB}, and valence, U_{VB} bands are shown for flatband (FB) conditions on the RHE scale which are not the same as that at the interface, due to the relevance of the Helmholtz layer.

configuration (CC). In CC configuration the curvature of the bands is preserved to a large extent which allows the photocarriers generated upon photoexcitation to be separated, electrons follow the bands down, this is the current that is measured using amperometry during the experiment, holes on the other hand travel to the surface and interact with suitable surface sites. It is also possible to not apply any potential to the back of the working electrode, effectively breaking the circuit, and the resulting electrochemical configuration is known as "Open Circuit" configuration. Since in OC configuration, the back of the electrode has no potential applied to it, upon photoexcitation no current is read, the bands flatten and most of the photocarriers recombine resulting in a large reduction in the number of the holes that make it to

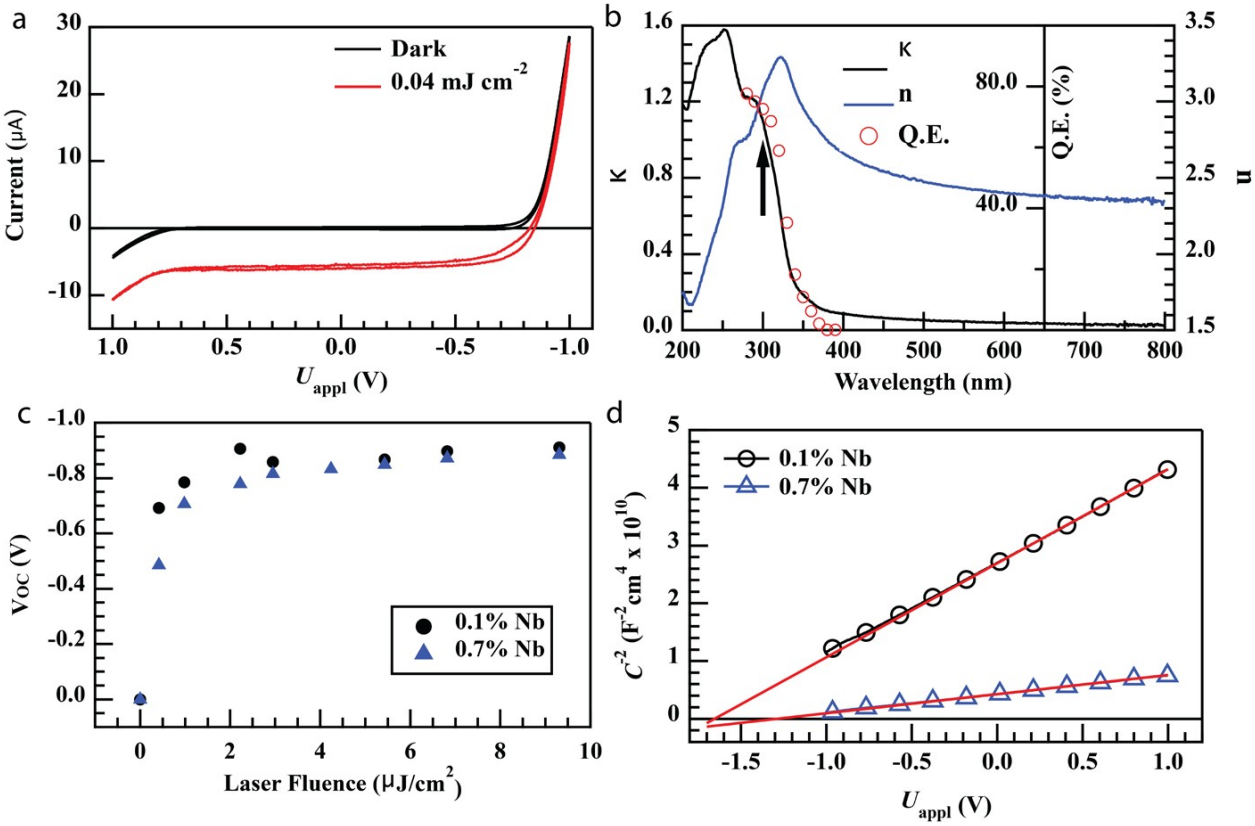

Figure 2.7: Steady state response of nSTO/aqueous diode using Ag/AgCl (SCE) at pH 13 and 0.04 mJ/cm² of 266 nm light excitation. (A) Current-voltage in the dark and under light excitation. (B) n, k values of nSTO, Q.E. compared with k that guides adsorption depth of light excitation. (C) Photovoltage at open circuit (V_{OC}) for 0.1% Nb and 0.7% Nb STO samples as a function of laser fluence. (D) Mott-Schottky plots for 0.1% and 0.7% Nb STO.

the surface as compared to CC configuration for the same fluence. Figure 2.6 depicts the Schottky diode and the level alignment at the aqueous interface.

Understanding the resulting electric field in the semiconductor is at the heart of understanding the Schottky Barrier and how it facilitates processes happening at or around the interface. The resulting electric field and the Schottky barrier under an applied bias is detailed using the standard solid-state diode equations. Figure 2.7a shows the results of steady-state current measurements from cyclic voltammetry on STO as the photoanode. It can be clearly seen that in dark conditions there is a difference of ~1.6 V between the cathodic and anodic current. For a wide bandgap, n-doped semiconductor (STO specifically) where the conduction band (CB) is at -0.4 V vs. RHE and the valence band (VB) is at 2.8 V vs. RHE, the electrons and holes straddle the O_2/H_2O potential at 1.23 V vs. RHE. Given that the Fermi level is close to the CB of an n-doped semiconductor, the reduction reaction is facile and takes little applied potential cathodic of equilibrium. For the oxidative reaction, on the other hand, one would expect about 1.6 V is needed from the onset of the reductive reaction to initiate the OER from empty (hole) states in the VB.

The current versus voltage curve, from cyclic voltammetry, under photoexcitation exhibits an ideal diode like behavior. For cathodic voltages more negative than −0.85 V vs. SCE the n-type semiconductor is in a forward bias regime where the surface electric field that separates the electron–hole pairs (depletion layer) decreases in width until there is no longer any photo-current. Under anodic voltages, the semiconductor is largely in a reverse-bias regime where the width of the depletion layer is maximized, and the anodic current is largely potential-independent. Both the shape of this curve and the quantum efficiency of the photocurrent (>75%)[25], defined as the ratio of the photocurrent to the absorbed light flux, are similar to that obtained with a continuous xenon lamp source. The high

quantum efficiency is achieved by ensuring that the excitation absorption depth is smaller than or equal to the width of the depletion layer. The excitation absorption depth is approximated by d = λ/4πk, where λ is the excitation wavelength (266 nm) and k is the imaginary part of the refractive index. As shown in Figure 2.7b, where the quantum efficiency is plotted together with the index of refraction as a function of wavelength, the quantum efficiency closely follows k. Using the Schottky approximation for the n-type semiconductor/liquid interface, the depletion width (Figure 2.6) is given by the n-p junction equations according to:

$$W = \sqrt{\frac{2\epsilon\epsilon_0}{e_0 N d}\left|V_{SC} - \frac{k_B T}{e_0}\right|} \qquad (8)$$

where N_d, ϵ, ϵ_0, e_0, k_B, and T represent the doping density, the dielectric constant of the semiconductor, the vacuum permittivity, the electronic charge, the Boltzmann constant, and the absolute temperature, respectively. V_{SC} is the potential difference across the diode in the semiconductor (Figure 2.6) when the chemical potential of the electrons and the redox reaction equilibrate in open circuit. The potential differences are reported as back to front faces of the semiconductor with respect to the electrolyte. $-V_{SC}$ needs to be applied to "flatten" the bands such that there is a negligible voltage drop in the semiconductor. It can be measured by open circuit potential measurements (OCPT). The open circuit photo-voltage that results (V_{OC}) is that needed to eliminate the built-in electric field by shuttling electrons to the back of the sample and holes to the front; Figure 2.7c shows the photo-voltage for several light fluences for which V_{OC} is the measured open circuit potential (U_{OC}) with light on with respect to its value with light off. The value saturates at -0.85 V already at fairly low fluences and close to the onset of the photo-current in Figure 2.7a. For the Schottky equation under bias, V_{SC} is replaced by $V + V_{SC}$, where V is the potential drop applied across the semiconductor. When light shines on the sample in open circuit $V=V_{OC}$,

such that the voltage drop across the semiconductor is zero and the depletion width is negligible.

Given the nominal doping density of STO (Nb 0.1% wt) and the measured Schottky barrier from the photo-voltage, or 0.85 V, eq. (8) gives W = 25 nm. One can then compare the depletion width to the excitation absorption depth, which for 266 nm excitation is $d = \lambda/4\pi k$ = 17 nm. As shown in Figure 2.7b, the Schottky barrier has a high QE for charge-separation when d is significantly less than W. Further, the QE decreases according to k as d becomes larger than W for longer excitation wavelengths.

In order to relate the built-in (V_{SC}) and applied (V) voltages to relevant circuit potentials denoted by U (U_{app} of the working electrode, U_{REDOX} of the H_2O/O_2 reaction, and U_{FB} of the semiconductor Fermi level), one needs to consider a non-ideal diode in which a Helmholtz screening layer exists, which adds V_H to V_{SC} in the Kirkoff's equations for the circuit. We get to this below. However, in both instances V_{OC} measures the built-in voltage of the Schottky barrier.

Table 1 shows the relevant diode parameters for photo-induced charge separation at the STO/aqueous interface used most routinely: the STO bandgap, the usual excitation wavelength, the excitation absorption depth, depletion width, and the built-in voltage (V_{SC}). The charge/cm^2 needed to equilibrate the chemical potential across the interface is given by N_dW. This charge density is much higher than the fluence at which the photo-voltage (Figure 2.7c) saturates (2 μJ/cm^2 = 2 x 10^{12} cm^{-2}); this is anticipated since electrons travel to the back of the electrode during photoexcitation (a width of 0.5 mm), which means a much smaller capacitance than that of the depletion layer (25 nm) is utilized to level the potential across the bulk of the sample. The capacitances are treated as parallel plate capacitors, both for the built-in voltage across the depletion layer and for the photo-voltage drop across the

full thickness of the semiconductor; more complex forms can be treated which consider diffusion lengths in addition to the sample depth[26]. The fluence used to excite the STO/aqueous interface to evolve O_2 from water is nearer to that of the depletion layer, 0.04 mJ/cm^2, or 4 x 10^{13} holes/cm^{-2} at 75% QE. In most of the work, we utilize the 0.1% Nb-doped SrTiO3 samples described in this table. However, highly doped samples (0.7% wt. Nb) are utilized to ascertain the role of dopants and doping density. They have similar diode characteristics, albeit a smaller depletion width (9 nm) and somewhat lower quantum efficiency (~65%).

Table 1	nSTO (0.1% Nb)
Band Gap	3.15 eV
Pump Excitation	4.66 eV (266 nm)
Absorption depth (d)	17 nm (266 nm)
Depletion Width (W)	25 nm
Built-in Voltage (V_{SC})	0.85 V
Positive charge in W	2 x 10^{13} cm^{-2} (N_dW)
Flatband potential of semiconductor (U_{FB})	-0.5 V vs. RHE -1.5 V vs. SCE (pH 13)
Valence Band (U_{VB})	2.8 V vs. RHE
Conduction Band (U_{CB})	-0.4 V vs. RHE
Doping Density (N_d)	8 x 10^{18} cm^{-3}
Excitation Fluence	0.04 mJ/cm^2
Hole Fluence (75% Q.E.)	4 x 10^{14} cm^{-2} (2% of S_0)
Excitation area	5 x 10^{-4} cm^2
Turnover rate	1 O_2/site-sec

Next, the full interfacial energetics of the semiconductor-electrolyte interface are considered, which includes modeling of the potential distribution across both the

depletion layer (V_{SC}) and the Helmholtz layer (V_H)[24,27]. The Helmholtz layer comes from free ions, adsorbed ions or molecules, new surface bonds with solution species, and oriented dipoles in the electrolyte that accumulate at the interface (Figure 2.8a). Here, we consider the two most prominent origins of this layer at the n-type semiconductor-aqueous interface and for the particular case of transition metal oxides18. The inner Helmholtz layer will derive from increasing the pH of the solution from the point of zero charge. While point of zero charge is difficult to measure, under neutral conditions, as described below, STO is partially hydroxylated (a mixture of hydroxylated ($M-OH^-$) and water adsorbed ($M-OH_2$) metal sites) and will deprotonate with higher pH. The effect on the potential distribution at the interface derives from lowering the vacuum level on the solution side, making it harder to pull another electron out. The effect on the equilibration of the electrode and electrolyte chemical potentials is to add a Helmholtz potential drop to the bare Schottky diode, leading to a new potential drop between the back of the electrode and the interface,

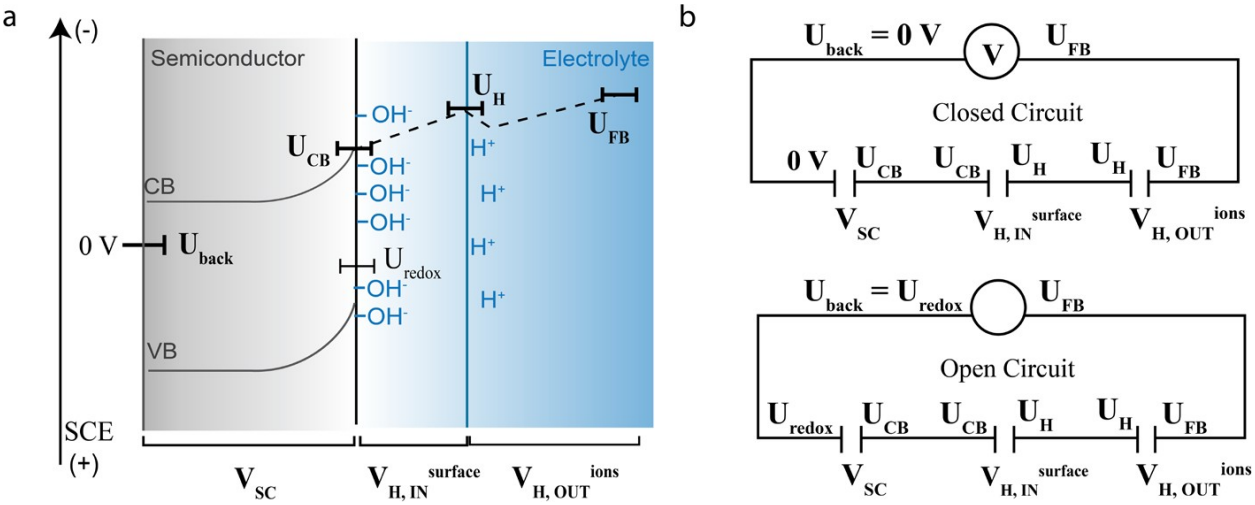

Figure 2.8: Inner and Outer Helmholtz Layers. (A) Diagram of interface, including the potential at the back of the electrode, U_{back}, potential at the edge of the bare semiconductor, U_{CB}, the potential at the end of the inner Helmholtz layer, U_H, and the flatband potential (U_{FB}). In the diagram, U_{back} is at 0 V vs. SCE for the closed circuit condition, which is ~0.4 V above U_{redox} at pH 13 such that without light excitation, water oxidation is not possible. It becomes U_{redox} for the open circuit condition. (B) Equivalent circuits for open and closed circuit with 0 V vs. SCE, where V_{SC}, $V_{H,IN}$, and $V_{H,OUT}$ denote voltage drops across the bare semiconductor, the inner Helmholtz layer, and the outer Helmholtz layer. $V_{H,IN}$ is due to the interfacial dipole and increases with +59 mV/pH from the point of zero charge. From the circuit diagrams and a measurement of V_{OC} that defines V_{SC} + $V_{H,IN}$, an estimate of $V_{H,OUT}$ is 0.88V.

V_{SC} + $V_{H,IN}^{surface}$. De-protonation increases the vacuum level at the surface of the semiconductor through the interfacial dipole ($M-OH^-$). On the other hand, the Nernstian potential for OER also increases cathodically with pH. While the former occurs as a coverage, and the latter as a proton transfer within the OER reaction mechanism, they both scale cathodically with 59 mV/pH since in either case the change in free energy arises from the increase in entropy for transferring protons to the bulk electrolyte volume. Therefore, the over-potential for OER is thought to be maintained with pH.

The other origin of the Helmholtz layer are the free ions in the electrolyte needed to transport charge effectively (e.g. SO_4^{2-}-, H^+, OH^-, PO_4^{2-}). These will accumulate at the interface to screen the charge in the electrode, which will be positive for the n-type semiconductor interface and anodic potentials. The physical picture with the free ions accumulating to screen through the dielectric (water) is an apt one to motivate such a parallel plate capacitor. The capacitor model for the interface is given in Figure 2.8b and includes the capacitance of the "bare" semiconductor (C_{SC}) and the Helmholtz layer (C_H) in series. In the deGryse derivation of the potential drop across the interface, only the free ions are considered as screening the depletion width, which is the element $C_{H,\,OUT}$ in the circuit diagrams; we return to $C_{H,\,IN}$ below. It leads directly to the Mott-Schottky equation19, for which the total capacitance ($1/C^2$) is related to the Fermi level of the semiconductor when no V_{SC} exists (U_{FB}), the doping density (N_d), and the Helmholtz capacitance (C_H):

$$\frac{1}{C^2} = \frac{1}{C_H^2}\left[1 + \frac{2C_H^2}{q\varepsilon N_d}\left(U - U_{FB} - \frac{kT}{q}\right)\right] \qquad (9)$$

U is the potential applied to the back of the semiconductor. An example Mott-Schottky plot for the n-STO/aqueous interface is shown in figure 2.7d and the values obtained from the fitted equation are shown in Table 1. These capacitance measurements are obtained from measuring the current while sweeping the voltage

and are traditionally done using alternating current (results should be frequency independent within the linear region of the Mott-Schottky plot). The doping density is derived from the slope of $1/C^2$, while the flatband potential (U_{FB}) is from the intercept given a known Helmholtz capacitance, C_H. Commonly a C_H of 20 μF/cm^2 is utilized for transition metal oxide semiconductors16. With this, U_{FB} = -1.5 vs. SCE is obtained at pH 13, or -0.5 vs. RHE, which is close to the value of the CB of STO (-0.4 vs. RHE) with literature values obtained by both calculation and experiment across a number of semiconductors using a common methodology[18]. Further, the difference of 0.1 V is likely due to differences in doping density, since the flatband voltage describes the potential of the last filled electron rather than the CB edge. With this CB edge, and the band-gap of STO, the VB edge will then be located at 2.8 V vs. RHE (Table 1). The value for the potential drop across the semiconductor is better obtained from the photo-voltage measurements at open circuit (Figure 2.7c, Table 1) which includes the inner Helmholtz layer.

One can also include an "inner" Helmholtz layer due to adsorbed species, which for transition metal oxides would arise from de-protonation[28]. A hydroxylated layer can also be understood as a parallel plate capacitor: a layer of interfacial dipoles (e.g. $M-OH^-$) all pointing in the same direction across the planar interface. As described above, the N_dW charge in the depletion layer is approximately ~10^{13} cm^{-2} whereas the surface site density of STO is ~10^{15} cm^{-2}. Therefore, the charge associated with the interfacial dipolar hydroxylation could over-screen the charge in the semiconductor at higher pH which is then compensated by H+ leading to the non-monotonic potential change in Fig. 2.8a[29]; importantly, the extent of over-screening depends on the amount and distribution of negative charge within $Ti-OH^-$ coverage of a surface. In the circuit diagrams, the free H^+ are grouped with the free counter-ions (SO_4^{2-}-, OH^-, PO_4^{2-}) in the outer Helmholtz layer. For open circuit conditions at

equilibrium, only the positive charge in the depletion layer is compensated by the inner and outer Helmholtz layers. Under closed circuit conditions and light excitation, the positive charge necessarily includes hole-trapped species would, which can be higher than the charge in the semiconductor, in the range of 10^{13}-10^{14} cm^{-2} (Table 1)[25].

Next, the interfacial energetics are modelled for two conditions utilized frequently in the experiments: open circuit, for which the back of the electrode is allowed to equilibrate with the solution chemical potential and closed circuit, for which it is held at 0 V vs. SCE[30]. The chemical potential of the solution is U_{redox}, the oxidation/reduction potential of H_2O/O_2. The diode in the semiconductor will be divided into the "bare" semiconductor without deprotonation (V_{SC}), the inner Helmholtz layer $V_{H,IN}^{surface}$ due to hydroxylation, and the outer Helmholtz layer $V_{H,OUT}^{ions}$ due to free ions. In this modelling, the closed and open circuit conditions are modelled in the dark; this is the starting surface from which the photo-driven one is created. Further, for 0 V vs. SCE, water oxidation in the dark is not possible. The case for moderate hydroxylation is considered, such that the outer Helmholtz layer is not dominated by H^+ accumulation. U_H denotes the potential at the end of the inner, Helmholtz layer.

The equivalent circuits for the two conditions are modelled by parallel plate capacitors in series (Figure 2.8b). Applying Kirchoff's law to the closed circuit conditions gives:

$$0\ V - U_{FB} = V_{SC} + V_{H,IN}^{surface} + V_{H,OUT}^{ions} \qquad (10)$$

Here, the potential change over the entire circuit is equal to $0\ V - U_{FB}$. This is what the potentiostat needs to apply to the working electrode to place it at a potential of 0 V vs. SCE; prior to the application of the potential, the back of the working electrode is presumed to be in ohmic contact with the counter electrode at the

semiconductor Fermi level. U_{FB} increases cathodically with 59 mV/pH due to the interfacial dipole, which increases the potential drop across the interface. Such an increase is in accord with both proton transfers to the electrolyte and obtaining U_{FB} from the Mott-Schottky equation that only treats the capacitance of free ions. Put another way, U_{FB} includes how the interfacial dipole and $C_{H,IN}$ modulates the potential drop across the depletion layer. On the other side of the equation, the potential drop across the bare semiconductor, V_{SC}, remains constant and independent of pH since the back of the electrode is held constant at 0 V vs. SCE. On the other hand, de-protonating the surface by pH increases the potential after the inner Helmholtz plane (U_H). Thus, $V_{H,IN}^{surface}$ increases with 59 mV/pH to compensate for the cathodic increase in U_{FB}, while $V_{H,OUT}^{ions}$ remains constant. Consequently, the voltage drop across the full Schottky diode ($V_{SC} + V_{H,IN}^{surface}$) increases with pH.

In open-circuit conditions, the floating potential at the back of the electrode equilibrates to U_{redox}. The voltage applied across the interface is that needed to equilibrate the chemical potential of the electrolyte to that of the semiconductor: $U_{redox} - U_{FB}$. Applying Kirchoff's law (Fig. 2.8b) gives:

$$U_{redox} - U_{FB} = V_{SC} + V_{H,IN}^{surface} + V_{H,OUT}^{ions} \qquad (11)$$

Note that in the absence of the Helmholtz layer, $U_{redox} - U_{FB}$ is simply equal to the built in voltage. As opposed to the closed circuit conditions, both U_{redox} and U_{FB} change equivalently with pH to keep the voltage applied across the interface constant with pH. On the other side of the equation, $V_{H,OUT}^{ions}$ is constant (since U_H changes equivalently as U_{FB}) while as the surface deprotonation increases, $V_{H,IN}^{surface}$ increases with 59 mV/pH. This is equivalent to the closed-circuit condition. However, now, because the potential at the back of the electrode is not held constant and allowed to equilibrate with U_{redox}, V_{SC} decreases with 59 mV/pH such that voltage across the full Schottky diode ($V_{SC} + V_{H,IN}^{surface}$) is constant with pH. This is the voltage drop measured

by the photo-voltage measurements at open circuit: $-V_{OC} = V_{SC} + V_{H,IN}^{surface} = 0.85$ V. Since these two add to give V_{OC}, these photo-voltage measurements are also pH independent. With U_{FB} = -0.5 v. RHE, and U_{REDOX} = 1.23 v. RHE, one can then utilize V_{OC} to obtain $V_{H,OUT}^{ions}$ = 0.88 V. This is quite a large voltage drop across free ions of the electrolyte not uncommon for n-type semiconductors, which means that the semiconductor bands at the electrolyte interface are quite a bit lower than when they are at the flatband potential (*i.e.,* not in contact with the electrolyte) as cartooned in Fig. 2.8a and denoted in Fig. 2.6. Such a Helmholtz voltage is nonetheless still compatible with a linear Mott-Schottky equation that explicitly incorporates V_H and $C_{H,\,OUT}$ as developed by De Gryse with NiO in mind[24]. It is also relevant to state that this potential drop, $V_{H,OUT}^{ions}$ is constant both in the closed and open circuit conditions with changes in pH such that the surface can be utilized to modulate equilibria of reactions without simultaneously changing the potential across the outer Helmholtz layer. Finally, to separate VSC from $V_{H,IN}^{surface}$, one would need to know the potential of zero charge fairly accurately, for which $V_{H,IN}^{surface} = 0$, which is not attempted here.

We have not the Helmholtz voltage drop for the closed-circuit case, either in the dark or for light excitation. Since the Helmholtz drop is fairly large, it means that any change in potential at the back of the electrode will be distributed to an extent over the semiconductor depletion layer and the free-ion Helmholtz layer19. Another complicating factor is photo-induced charge separation which leaves an accumulation of holes in the electrode and at the interface prior to transferring out during water oxidation. This can also change the balance of potential drops in the circuit, as has been reported in the past for the STO/aqueous interface[25]. Therefore, for the most part, in closed circuit, the 0 V vs. SCE condition is maintained at the back of the electrode and a common fluence is utilized to initiate water oxidation. This allows for the dark equilibrium to be characterized by the Helmholtz model well, and for a

common, though much less quantified change, to this model occurring under photo-driven conditions.

Scanning Methodology: Continuous vs Static

Conducting photo-electrocatalytic OER is known to restructure the catalytic surface and the pump probe technique averages over many pulses, it is important to find a methodology by which the initial state of the surface prior to excitation is recovered for each pulse. Without this, there isn't a distinct time-point at which the catalytic reaction is triggered, and kinetic steps associated with re-structuring would affect the kinetics derived from the elementary reaction steps16. Restructuring can be caused by many reasons, e.g., possible side reactions with their unique kinetic signatures being one and can result in the loss of catalytic activity. We clearly observe this change in our system upon conducting OER, most significantly in CC

Figure 2.9: Optical images of: A) 7 um/s and 28 um/s scans. The 7 um/s scans are the faint tan lines at the top. The 28 um/s scans are not visible in an optical microscope. Their location was determined by nearby slower scans and the 100 s spots, an example of which is the faint tan spot in an otherwise

configuration. Figure 2.9 shows an image taken through a microscope of the sample and it clearly shows a change in the appearance of the sample surface. Upon exposing a particular fixed spot on the sample with the pump in CC configuration, we note a significant permanent change in the reflectivity of STO on the minute timescale and a significant change in photocurrent after 10 minutes. The significant change in reflectivity due to the surface restructuring is an additional contribution that clouds the interpretation and negatively impacts the integrity of the pump probe signal. To avoid the contribution of the surface restructuring on the pump probe signal we employ raster scanning of the sample which is enabled by mounting the sample cell on a 3-axis stage controlled by programmable actuators and controllers.

The scanning methodology makes sure that a fresh area of the sample is probed for every data point and the photocurrent is stable. OC configuration, however, does not cause significant restructuring of the catalytic surface but we conduct pump probe experiments in OC configuration using the scanning methodology to maintain consistency. Quantification of changes incurred by STO surface during the photo-electro catalytic OER using SEM/TEM imaging is presented in detail in chapter 5. Figure 5.3 shows the degradation of the catalyst surface for different scanning methodologies using SEM images.

In continuous scanning methodology the ratio of total acquisition time to total active time is found to be fairly consistent throughout the experiment for a particular scan speed. Thus, the ratio of active time to down time for any delay point within the experiment doesn't change significantly. This implies that a particular point on the delay axis is associated with a particular range of time points on the acquisition axis. We can go one step further and link the delay axis to the acquisition axis by assigning a representative time point for every time delay, middle of the corresponding active time period, thus making the delay and acquisition axes comparable to one another.

The scanning methodology can be implemented in 3 primary ways, namely, continuous scanning, static scanning, and continuous step scanning. The following subsections are going to illicit the details of each methodology along with pointing out the differences. Note, continuous scanning and static scanning methods were developed when the pump beam line wasn't being gated in any way exposing the sample to the pump during the active and down time of the experiment.

Continuous Scanning

Continuous scanning implies that the sample is raster scanned at a constant speed. Continuous scanning creates dark rows on the sample due to the raster scanning. In continuous scanning method each pump shot arrives on a nominally "clean" sample surface and so sequential time delay points can be treated irrespective of the preceding ones. Scan speed of 7 um/s is predominantly used for most experiments in this dissertation, however, as seen in Chapter 5, there is still some constant amount of restructuring/degradation associated with 7 um/s scan speed. Moving to faster scan speeds reduces the constant amount of this degradation but the scan speed of 7 um/s is chosen to provide a good balance between data quality and judicial use of limited sample space.

Static-Scanning

In static scan, acquisition and delay times are acquired over multiple spots on the sample that are separated by a fixed distance. Each spot is exposed to the 266 nm pump for a fixed amount of time (e.g., 100 seconds/spot). This implies that the first shot arrives on a clean spot, but the subsequent shots arrive on the same spot which is now degraded.

Continuous Step Scanning

Continuous step scanning can be thought of as a cross between the continuous scanning method and the static scanning method. This method was allowed by the addition of a shutter on the pump line that gates the pump along with the discovery

that no significant degradation to the sample surface occurs within the first 20 seconds of exposure. In this method, a given spot is exposed to the pump beam for the duration of time that the camera needs to acquire the necessary number of averages (maximum 5 seconds). After the last shot acquired the shutter is triggered which blocks the pump and stops the exposure of the sample. After the necessary down time the sample is moved to another spot (35 um apart) and then the next time delay is acquired in a similar fashion. This method allows even more efficient use of sample space than the continuous scanning method without compromising the quality of the data. All the data going up to the microsecond timescales was taken with the continuous step scanning method. The continuous step scanning methodology produces a degradation pattern similar to that of continuous scanning methodology.

Principal Component Analysis: Singular Value Decomposition (SVD)

Singular Value Decomposition (SVD) is a widely used mathematical technique for decomposing a matrix into three component matrices, which can help in analyzing high-dimensional data. The technique is applicable to matrices of any size, including those with missing or incomplete data.

At a high level, SVD breaks down a matrix into three component matrices: a diagonal matrix of singular values, and two unitary matrices which contain the left and right singular vectors. The singular values provide a measure of the importance of each dimension of the data, while the left and right singular vectors provide a basis for the row and column spaces of the original matrix, respectively.

Mathematically speaking (SVD)[17] is a factorization of any matrix into the $U*S*V^T$ form where U and V are unitary, or orthogonal when M is real, and S is a diagonal matrix. SVD of a dispersed transient reflectance (TR) spectrum can be interpreted as a sum of one-dimensional (1D) spectra multiplied by their associated 1D kinetic traces, with each component weighted by a singular value. Mathematically

stated, the dispersed TR spectra with frequency along the columns and time delay along the rows, $M^{(pH)}$ is decomposed as:

$$M^{(pH)} = U^{(pH)} \cdot S^{(pH)} \cdot \left(V^{(pH)}\right)^{T} \qquad (12)$$

The dimensionality of the data matrix (M) determines which unitary matrix (U or V) contains the 1D spectral and kinetic components. M can be structured as wavelengths x time delays (Lambda x T) or in its transposed form (T x Lambda). The unitary matrix U will contain the one-dimensional components corresponding to the first dimension of M, i.e., U will have spectral components if first dimension of M is wavelengths (lambda).

SVD is distinguishable from any other rank one decomposition (shown in the second equality above) by requiring that the square matrices $U^{(pH)}$ and $V^{(pH)}$ form an orthonormal spectral and kinetic basis and that the components are ordered by decreasing singular value. Because the singular values are component weights, only components that have large singular values contribute significantly to the dispersed TR spectrum. For all optical spectra shown in this work, only the first two singular values are significant, indicating that our data sets are predominantly composed of two spectral and kinetic components. Hence, we limit further analysis and discussion to only two SVD components. An example of the SVD analysis can be seen in figures 3.8 and 3.15.

When analyzing multiple datasets while varying reaction conditions, it can be helpful to think of datasets shown in this work to have wavelengths and time delays as intrinsic axes, whereas the reaction condition, such as solution pH or solution ionic strength or fluence of excitation light, as the extrinsic axis.

Rotation Analysis

In general, the spectral components obtained from SVD of the dispersed TR spectra do not yet correspond to spectra of any given species. Ideally, if an entire

dataset can be described by different kinetics of the same species as a function of the reaction condition (e.g., pH), the two dominant spectral SVD components from one reaction condition can be transformed from another one using a rotational transformation matrix, when appropriate reflections are taken into consideration. In this scenario, the rotation matrix can be obtained by employing a pseudoinverse, as shown in eq. 13:

$$R = \left(U_{1,2}^{(pH\ 13)}\right)^{T} U_{1,2}^{(pH\ 7)} \cong \begin{bmatrix} \cos\theta_{ij} & -\sin\theta_{ij} \\ \sin\theta_{ij} & \cos\theta_{ij} \end{bmatrix} \qquad (13)$$

Here, θ_{ij} represents the angle of rotation between the pair of spectral bases in the two-dimensional subspace. In practice, minor deviations in R from being a pure rotational matrix can be attributed to noise and systematic errors between the dispersed TA spectra. An example of rotation analysis is shown in figure 3.9 of chapter 3.

Spectrally Constrained SVD

The orthonormal pairs of spectral and kinetic component vectors obtained from SVD span a two-dimensional subspace on which the physically relevant spectral and kinetic basis vectors lie on. Thus, the pairs of species spectra and kinetics are linear combinations of the raw SVD component vectors. Choosing a specific set of linear combinations is known as constrained SVD. In principle, one can only constrain the components of one of the intrinsic axes of the data set (spectra or kinetics) to a known basis in order to analyze the changes in the constrained components of the other intrinsic axis (kinetics or spectra) with respect to the extrinsic axis (i.e., solution pH or ionic strength). Mathematically, the spectral basis $U^{(t)}$ and its corresponding constrained weighted kinetic vectors $V^{(t)}$ can be obtained from the n^{th} reaction condition using eq. 14:

$$M^{(n)} = U^{(n)} \cdot S^{(n)} \cdot \left(V^{(n)}\right)^{T}$$
$$= U^{(n)} \cdot X^{(n)} \cdot \left(X^{(n)}\right)^{-1} \cdot S^{(n)} \cdot \left(V^{(n)}\right)^{T} = U^{(t)} \cdot \left(V^{(t)}\right)^{T} \qquad (14a)$$

Where,

$$U^{(t)} = U^{(n)} \cdot X^{(n)};\ V^{(t)} = \left(X^{(n)}\right)^{-1} \cdot S^{(n)} \cdot \left(V^{(n)}\right)^{T}$$

And,

$$X^{(n)} = \begin{bmatrix} a(n) & \alpha(n).b(n) \\ \beta(n).a(n) & b(n) \end{bmatrix}$$

$$a(n)^2 + a(n)^2\beta(n)^2 = b(n)^2 + b(n)^2\alpha(n)^2 \qquad (14b)$$

Where a(n) and b(n) are normalization factors such that the column vector norms are 1.

For the pH dependent data shown in figure 3.1 and 3.2 in chapter 3, we need to quantify the changes in the dispersed TA spectra as a function of pH, the most relevant reaction condition. We will be using this data set as an example for the constrained SVD analysis. Qualitatively, the spectra are comprised of two contributions that respond differently to the change in pH: absorption (overall positive change in absorption) and emission (overall negative change in absorption). Therefore, we attribute an absorption-only and an emission-only spectral component as the targeted spectral basis of constrained SVD. However, we do not have independent constraints to determine this physically relevant spectral basis. Consequently, we use eq. 14 parametrically to determine these basis spectra. Initially, we chose a range of $\alpha(n)$ and $\beta(n)$, while making sure to keep the column vectors of Xn normalized using eq. 14(b). This assures the physically relevant spectra maintain the same amplitude while allowing the spectral shape to change with the parametrization. Figure 2.10A and 2.10B exhibit the normalized set of absorption-only and emission-only spectra for pH 13 and pH 7, for a range of values of $\alpha(n)$ and $\beta(n)$. The similarity of the absorption-only and emission-only spectra for nearby $\alpha(n)$ and $\beta(n)$ gives confidence that the constrained SVD spectra can be associated with species' populations and their optical transitions using the parametrization. Subsequently, one can determine that the absorption-only and emission-only spectra

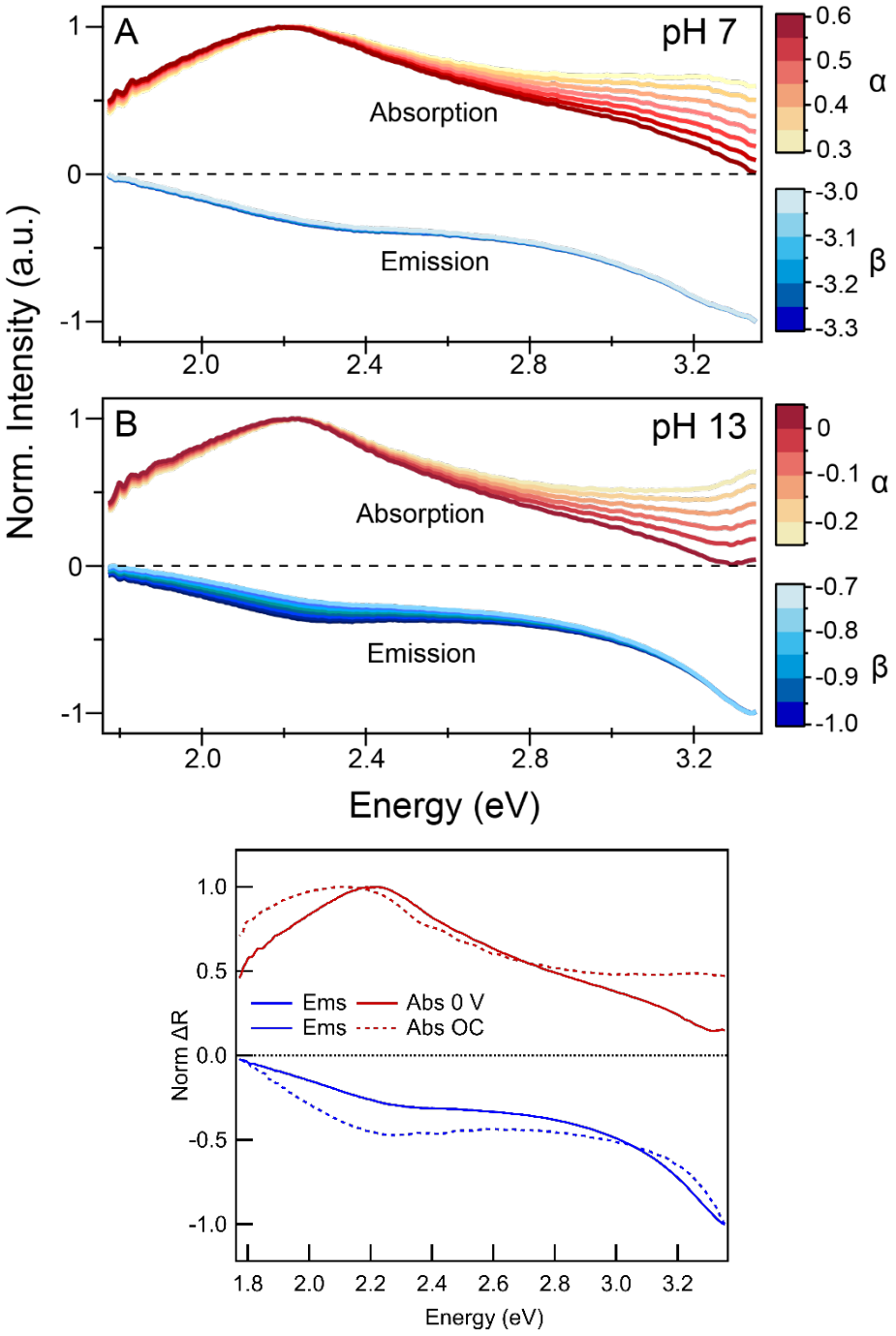

Figure 2.40: (A) and (B) Constrained SVD spectra covering the range of α and ß that, when used in eq. 7, result in purely absorptive and emissive spectral components. (C) Averaged absorptive and emissive components over the range of α and ß respectively.

vary minimally from one pH to another, which identifies, along with the rotation analysis, that they can be used as a set of spectral basis vectors to represent the entire pH dependent set. Subsequently, the spectral basis vectors thus obtained are

normalized to obtain $U^{(t)}$ as shown in Figure 3.5D in chapter 3. Thereafter, $X^{(n)}$ is obtained using the pseudoinverse $\left(U^{(n)}\right)^{T} \cdot U^{(t)}$. Since the basis spectra cannot be derived exactly using a linear combination of $U^{(t)}$ for any given n, the entries of $X^{(n)}$ are such that $a(n)^2 + a(n)^2\beta(n)^2 \leq 1$; $b(n)^2\alpha(n)^2 + b(n)^2 \leq 1$. In fact, the diagonal entries of $\left(X^{(n)}\right)^{T} \cdot X^{(n)}$ provide a measure of consistency of the determined basis spectra. In this work, we always obtain these diagonal entries > 0.98, indicating our basis spectra are reliable. Finally, the same constrained SVD method can be applied to 0 V and OC conditions, which significantly modulates the ratio of the absorption-only versus emission-only components in the raw spectra, and yet fairly similar spectral shapes are derived as can be seen in Figure 2.10 (C).

Constraining the spectra allows us to extract the constrained weighted kinetics which for the data set shown in figure 3.10B of chapter 3 were then fit with the following exponentials:

Emission: $\left(V^{(t)}\right)^{T} = A_1^n e^{-\frac{t}{T_1^n}} + A_2^n e^{-\frac{t}{T_2^n}} + A_3^n$; where A_1^n, $A_2^n < 0$

Absorption: $\left(V^{(t)}\right)^{T} = A_1^n e^{-\frac{t}{T_1^n}} + A_2^n e^{-\frac{t}{T_2^n}} + A_3^n e^{-\frac{t}{T_3^n}} + A_3^n$;

where $A_1^n < 0$ and A_2^n, $A_3^n > 0$

The detailed analysis of the data used in this example is present in chapter 3 under the “Modulating the Ti-OH* reaction equilibria by pH” section.

CHAPTER III

FREE ENERGY DIFFERENCE TO CREATE THE M-OH* INTERMEDIATE OF THE OXYGEN EVOLUTION REACTION BY TIME-RESOLVED SPECTROSCOPY

Original Publication

This work has been previously published as Vinogradov, I., Singh, S., Lyle, H. et al. Free energy difference to create the M-OH* intermediate of the oxygen evolution reaction by time-resolved optical spectroscopy. Nat. Mater. 21, 88–94 (2022).

Introduction

OER is a multi-step catalytic process where each step is described by a set of meta-stable intermediate chemical forms. Given several underlying and separate reaction steps, multiple mechanistic models could explain the same outcome[6,11-,12]. Thus, there exists a need for experiments to access the individual reaction steps[11,12]. To do so through the free energy differences (ΔG) between intermediates would directly underpin the theory[3] and would provide thermodynamic quantities by which to tailor the material and its environment for desired functionality[13]. One of the most important and studied reactions in this context is the electrochemically driven oxygen evolution reaction (OER) on transition-metal oxide surfaces[4,5]. The $M-OH^*$ intermediate, created upon the first electron and proton transfer from water, is expected to initiate the formation of the first chemical bond of O_2 (O–O), with corresponding free energy differences $\Delta G_1(OH^*)$ and $\Delta G_3(O–O)$[3,19]. With scaling relationships[10], $\Delta G_1(OH^*)$ becomes a predictive theoretical descriptor of OER activity: when $\Delta G_1(OH^*)$ is large, forming $M-OH^*$ is rate limiting, and when it is small, forming the O–O bond is rate limiting. However, to date, these thermodynamic and

calculated limitations on O_2 evolution have been compared against experiment using the electrochemical current, which is inherently kinetic.

A series of time-resolved studies of photo-electrochemically driven OERs have isolated the spectral and kinetic signatures of the hole-trapping $M-OH^*$ intermediate, including titanium oxyls ($Ti-O^{\circ-}$ terminal and $Ti-O^{\circ+}-Ti$ in-plane)[21,22], the cobalt oxo ($Co=O$)[31] and the iron oxo ($Fe=O$)[32]. The $M-OH^*$ notation is generic for all these intermediates, with H^+ either bound to the oxygen site or having transferred to a nearby one[20,33]. While vibrational spectroscopies determine these detailed bonding geometries[34,35], optical spectroscopy[21,36] revealed easily trackable electronic levels created in the middle of the semiconducting bandgap that target the total population of $M-OH^*$. Using these mid-gap levels, ultrafast optical studies of $SrTiO_3$ (STO) followed the picosecond formation of the first intermediate population from delocalized valence band (VB) holes[21] and its subsequent, microsecond decay towards the next reaction step[37].

While such time-resolved studies structurally identified transient surface intermediates and provided insight into their role in the catalytic cycle, comparatively little experimental information exists on their energetics. In this chapter I will present a set of time-resolved spectroscopic experiments and analysis methodology designed to be capable of isolating the reaction steps and capturing their thermodynamic properties[38,39]. In photo-electrochemistry, light excites the reaction instantaneously from a surface prepared by the dark equilibrium with the electrolyte. Therefore, the first proton and electron transfer can be well separated in time, with the proton transfer occurring in the dark and the electron transfer occurring only upon photoexcitation of VB holes:

$$Ti-H_2O + OH^-(aq) \leftrightarrow Ti-OH^- + H_2O\,(aq) \quad (15)$$

$$Ti-OH^- + h^+ \rightarrow Ti-OH^* \quad (16)$$

In reaction (2), h^+ represents a hole. Using the self-ionization of H_2O into OH^- and H^+, reaction (1) can be written with a product H^+, instead. Both reactions equivalently describe the acidity of a water-absorbed Ti site. If one adds an electron at the chemical potential of the delocalized hole to each side of reaction (2), the hole-trapping reaction is equivalent to an electron transfer out of the electrode, such that the two reactions net to $Ti-OH_2 \rightarrow Ti-OH^* + H^+ + e^-$ where e^- represents an electron. Note, STO surface can support several different sites that can be suitable for hole trapping however for the sake of simplicity we will be representing them with the notation used in reaction 15 and 16. To clarify further clarify, we are looking at one type of the several possible sites (denoted by $Ti-OH_2$) such that the equilibrium constant for the reaction represents the pKa of the site.

The first reaction is thus an explicit equilibrium defined by the free energy difference for surface hydroxylation, ΔG_{OH-}, or equivalently, the pKa of $Ti-OH_2$. The second reaction forms a meta-stable species, where $\Delta G_{OH^*}(U_{VB})$ is the free energy difference between a hole at the VB edge potential (U_{VB}) and a trapped hole, $Ti-OH^*$. U_{VB} is utilized since the photo-excited holes are presumed to thermalize to the VB edge before transfer given the inefficiency of hot-hole transfer from bulk semiconductor crystals[40,41]. By being separable, the surface hydroxylation prior to light excitation can shift the reaction equilibria, which allows our work to identify $\Delta G_1(OH^*)$ by time-resolved optical spectra. In particular, the sigmoidal pH dependence of the picosecond $Ti-OH^*$ population generates a Langmuir isotherm of a meta-stable intermediate on the photo-driven surface. For surfaces in which the hydroxylation can be modulated in an accessible pH range, the work closes a vital missing gap between the observation of the kinetics and structure of catalytic intermediates and experimental determination of the energetics of elementary steps. The results show how reaction kinetics, inherent in experimental investigations, can

begin to be analyzed with respect to measured, rather than largely theoretical, free energy differences.

Transient optical spectra of the electrochemical interface

Figures 3.1 and 3.2 show the primary pH-dependent optical spectra from which we draw our conclusions. The transient data are taken under steady-state conditions of photo-electrochemical O_2 evolution using pulsed (150 fs, 500 Hz) bandgap (266 nm, 4.66 eV) excitation of n-doped STO (n-STO; 0.1%, 0.5% and 0.7% Nb STO). Here, the surface is probed by a broad-band optical pulse (375–700 nm, 1.7–3.3 eV). The

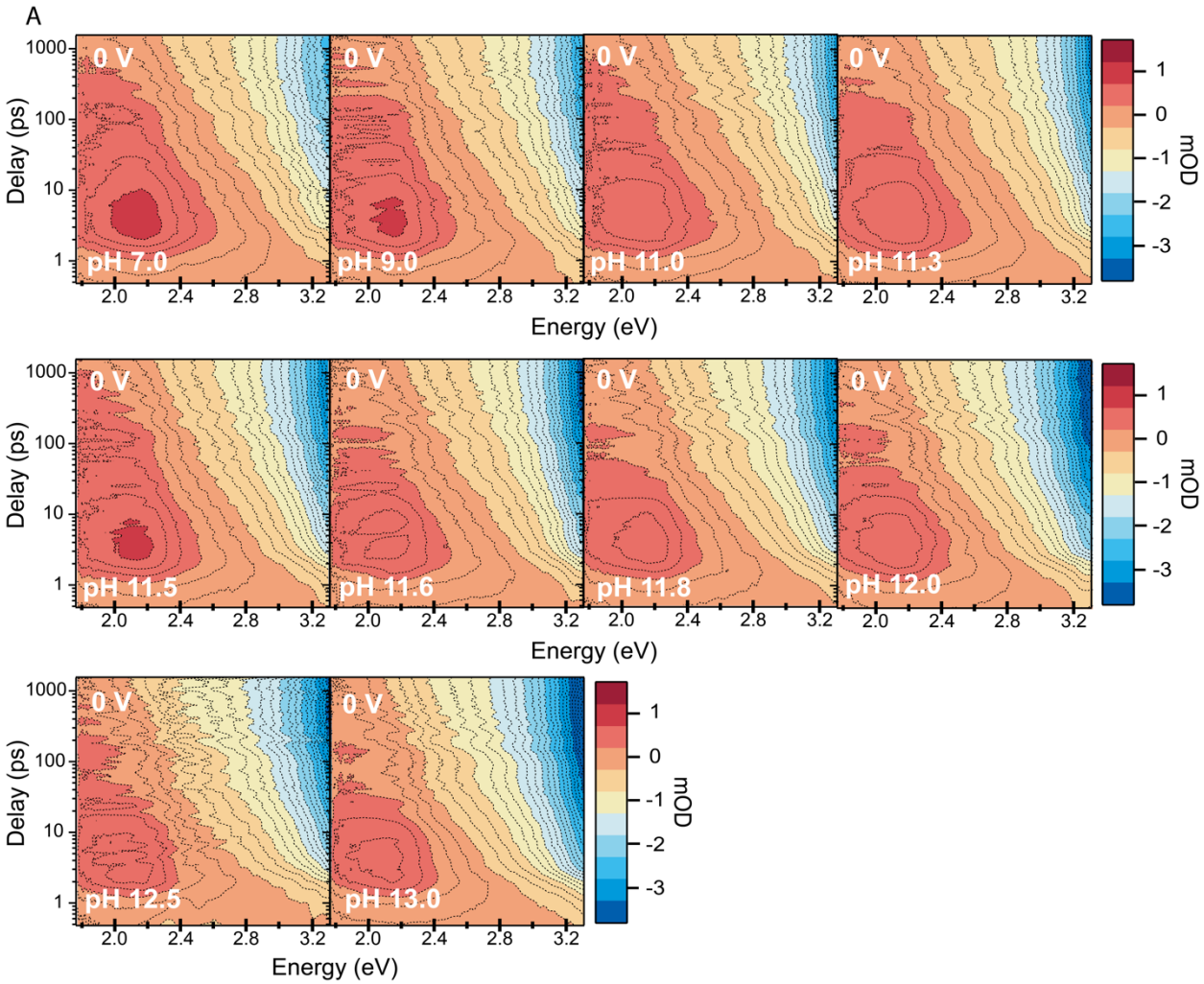

Figure 3.5: pH dependence of transient optical spectra for phosphate buffered solutions at 0V in closed circuit conditions showing absorption (red) and emission (blue).

spectroscopic setup as well as the pump and probe generation are described in detail in chapter 2.

While there is a high quantum efficiency of charge separation (~75%), side reactions do affect the sample surface. Therefore, to obtain the high-quality kinetic data, we employ a continuous scanning method also described in detail in chapter 2. Assessment as well as quantification of the changes to the surface during OER is the primary focus of chapter 5 of this dissertation.

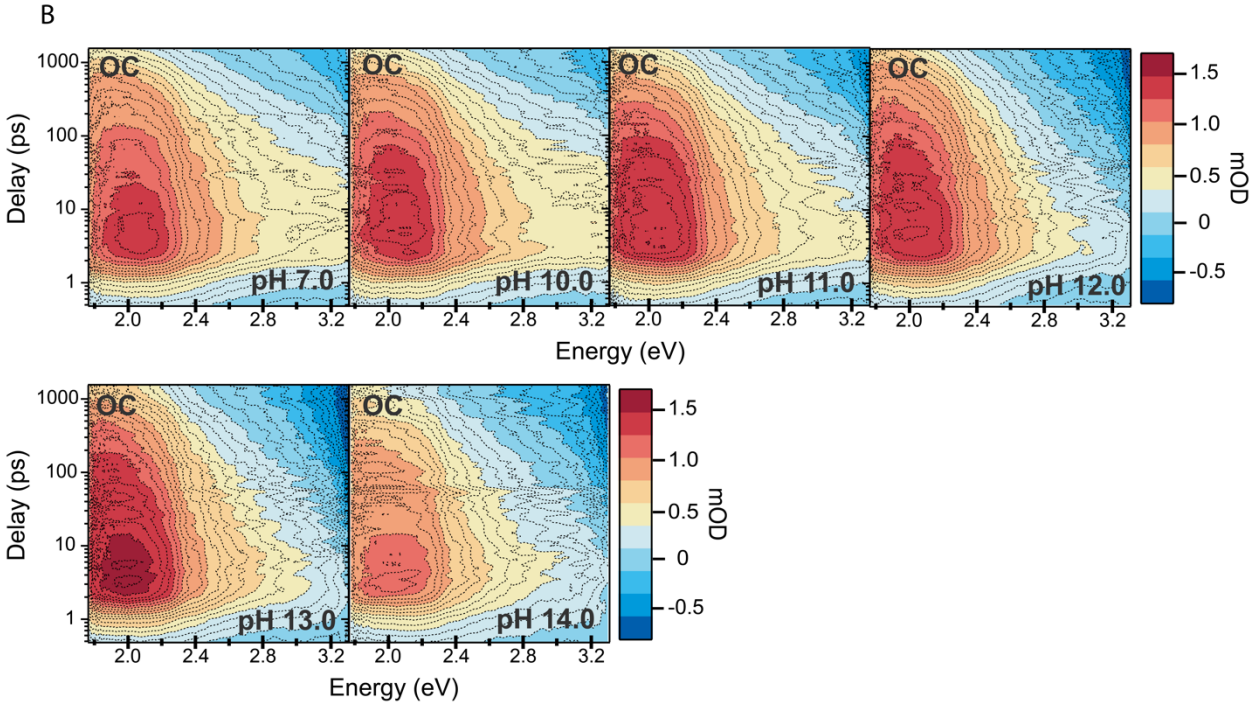

Figure 3.2: pH-dependence of transient optical spectra for unbuffered solutions in open circuit conditions showing absorption (red) and emission (blue). Note that the mOD scale is different in this figure as compared to figure 1.

At a photo-excitation density, or fluence, of 0.04 mJ cm^{-2}, one maintains a constant steady-state current to within 0.5% in a single measurement (Fig. 3.3), which corresponds to a turnover frequency of ~1 O_2 per site per second of the illuminated area. The cartoon (Fig. 3.5A) shows the level alignment of the valence and conduction bands of STO with the Nernstian potential of water oxidation on the reversible hydrogen electrode (RHE) scale. The primary data are taken with a constant 0 V versus saturated calomel electrode (SCE) applied to the back of the

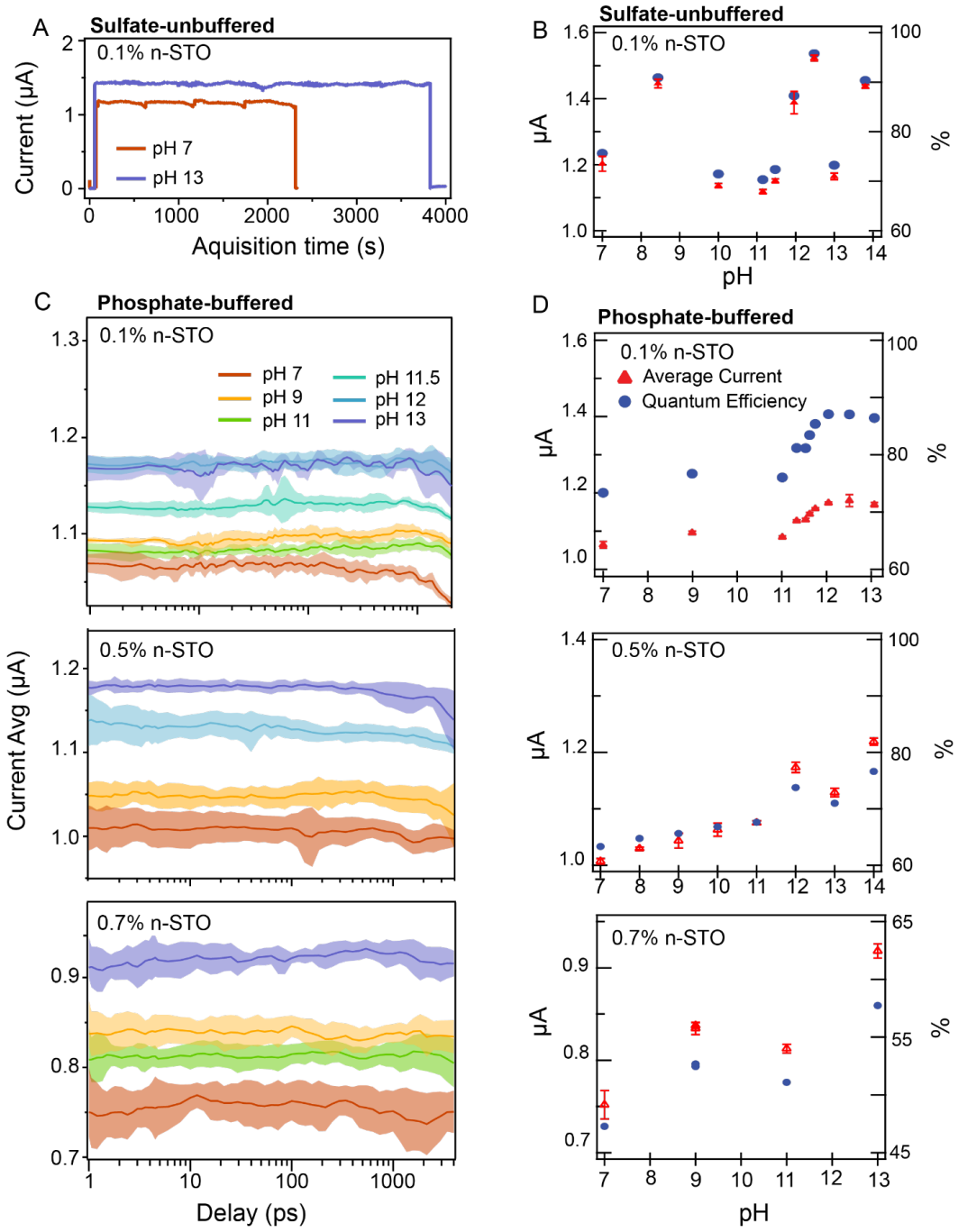

Figure 3.3: (A) Raw current; (B) average current and its standard deviation vs pump-probe delay; (C) average current/Q.E. vs pH in phosphate-buffered and sulfate-unbuffered conditions, (D) average current/Q.E. vs sodium ion concentration in two unbuffered pH conditions in Na_2SO_4. The phosphate buffered data is shown for all three STO samples: 0.1%, 0.5%, and 0.7% Nb doping.

electrode. A constant 0 V versus SCE is chosen to maintain the same potential drop across the part of the electric double layer that involves free ions in the electrolyte (phosphate, sulfate, OH^-, H^+), such that reaction (15) can be considered fairly

independently of salt concentration (Fig. 2.8). With this electrochemical configuration, the Schottky barrier will necessarily increase with pH due to the interfacial $Ti-OH^-$ dipole[27] (Fig. 2.8). Data taken at open circuit, shown in Figure 3.2, aid in the assignment of spectral components and in the interpretation of the pH dependence. Finally, as shown in figure 3.4, 0.1% Nb and 0.7% Nb STO were characterized for hydroxylation at near neutral conditions by ambient pressure X-ray photoelectron spectroscopy.

Upon excitation, a delocalized hole in the valence band can relax to create $Ti-OH^*$. When a hole traps to an oxygen site, $Ti-O$ the distances distort and mid-gap levels form, as described in detail for TiO_2 (refs. [20,33]) and for STO (refs. [21,42,43]). These mid-gap levels are relatable to $\Delta G_1(OH^*)$ by the $\Delta G_{OH^*}(U_{VB})$ of reaction (16):

$$\Delta G_1(OH^*) = VB\ (RHE) + \Delta G_{OH^*}(U_{VB})(eV) \quad (17)$$

The redox level (RHE) corresponding to $\Delta G_1(OH^*)$ for STO is shown schematically in Fig. 3.5A (purple dotted line). The pH dependence of reaction (15) is that of the RHE scale (−59 mV per pH unit), which results from a cathodically increasing VB edge due to the interfacial dipole[27]. With equation (17), $\Delta G_1(OH^*)$ for different materials can also be placed within the bandgap of STO (purple block, Fig. 3.5A), rising within the gap and lower on the RHE scale for stronger oxygen binding within $M-OH^*$ (volcano plot, Fig. 3.5B).

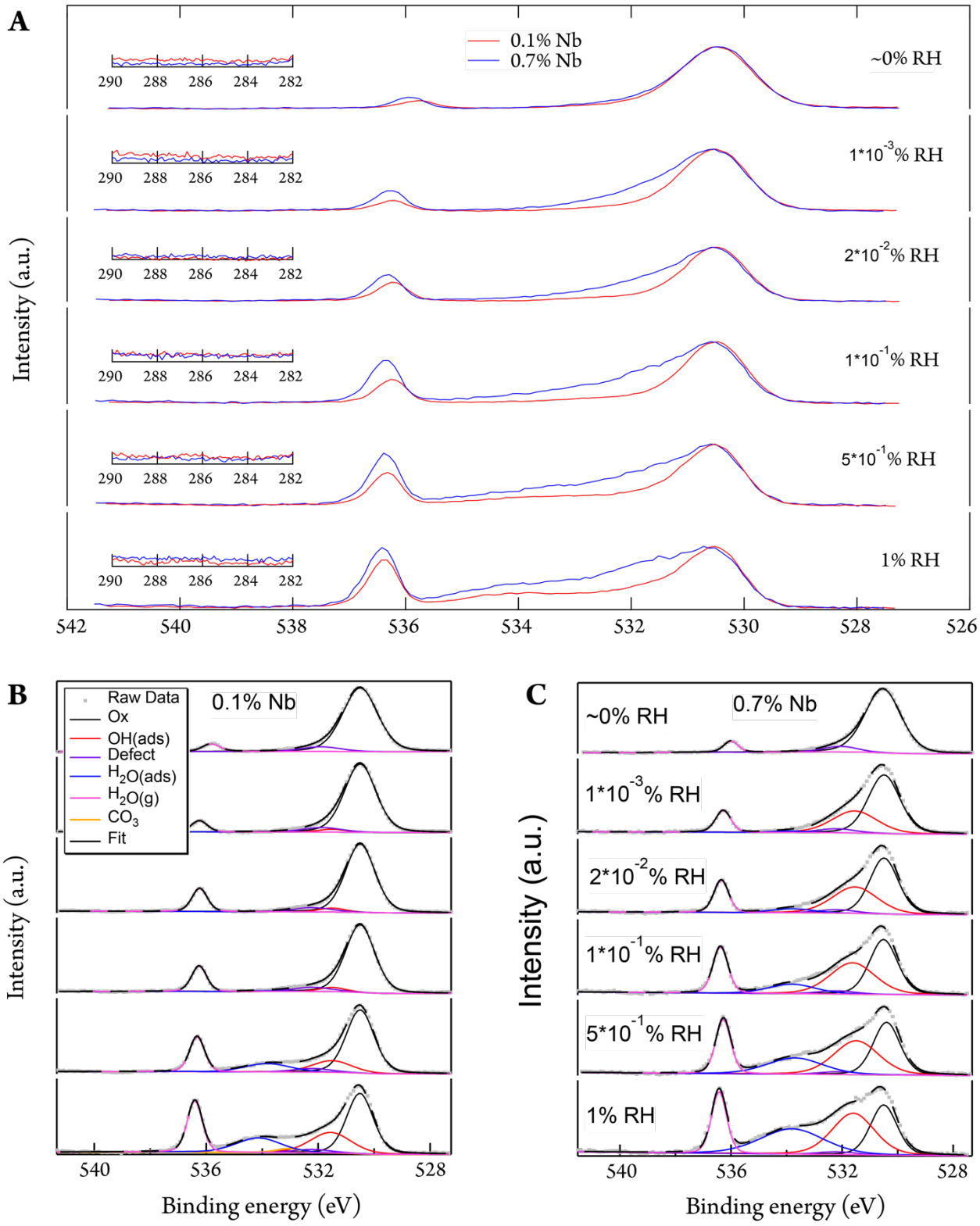

Figure 3.4: AP-XPS Data for 0.1% and 0.7% Nb doped STO compared for select relative humidity (RH%) (A). The insets show that the carbon contamination on these AP-XPS runs was negligible. Fits of the 0.1% Nb-STO (B) and 0.7% Nb-STO AP-XPS data by peaks representing lattice oxygen (Ox, black), hydroxyl groups (OH, red), adsorbed water groups (H_2O (ads), blue), and water vapor (H_2O(g), purple).

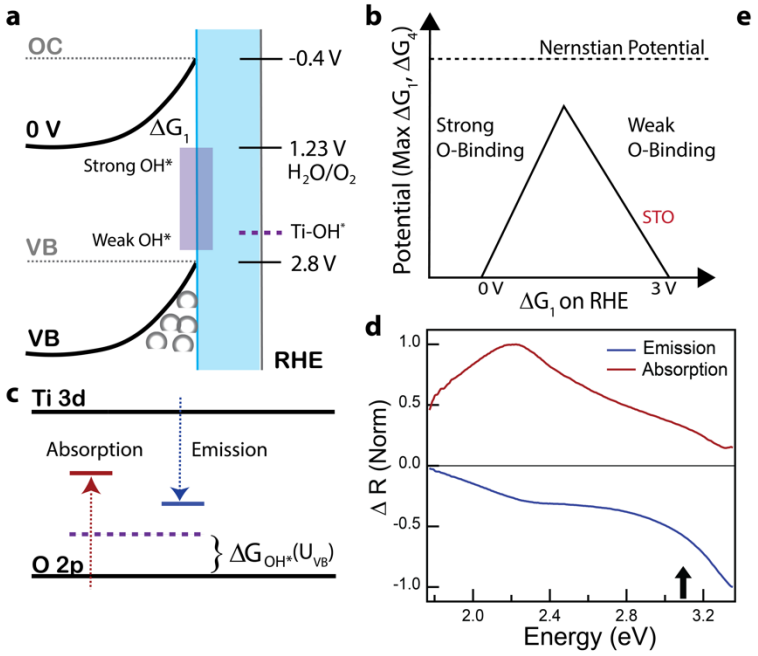

Figure 3.5: Photo-electrochemical configuration and optical spectra. a) Cartoon of energy level alignments at closed (0 V vs. SCE) and at open circuit (OC) on the RHE scale (pH 0). b) Volcano plot of OER theoretical analysis, depicting strong and weak oxygen-binding branches c) Cartoon of the optical transitions induced by Ti-OH* intermediates, leading to emission (blue arrow) and absorption (red arrow). The dashed purple level corresponds to the redox level for creating Ti-OH*, also depicted in a). The optical transitions are vertical ones, which involve states in the CB and VB respectively that are at the reaction coordinate of the distorted Ti-O bonds in Ti-OH*; the difference in the blue and red lines reflects that these are unique for the CB and VB. d) Emission and absorption derived by a constrained, singular value decomposition of the optical spectra in e) Transient optical spectra of the absorption (red) and emission (blue) in the visible regime for select pH at closed circuit.

Emissive optical transitions in the visible regime (blue arrow, Fig. 3.5C, blue emission, Fig. 3.5D) result from conduction band (CB) electrons transitioning to the newly created $Ti-OH^*$ at the distorted reaction coordinate (blue line, Fig. 3.5C). Photoluminescence of STO samples routinely assigns the spontaneous emission peak between 2.4 eV and 2.8 eV to localized holes[42,44,45]. The recent transient optical spectroscopy during OER characterized the stimulated emissive optical dipole transitions[21] by a 1.3 ps kinetic growth, which also occurred in the vibrational spectroscopy identifying the titanium oxyl ($Ti-O^-$)[22]. Here, the broad-band probe records this emission in time for lightly doped Nb 0.1% STO as a function of pH (Fig. 3.1). From these optical spectra, acoustic phonon oscillations have been subtracted out (Figure 4.2A). The acoustic phonon oscillations are the primary focus of the next

chapter and are discussed in detail therein. The emission (blue) appears clearly during in situ OER and increases with higher pH (Fig. 3.1). However, the emission seems independent of salt concentration as can be seen in fig. 3.6. It is important to note that in all TR experiments, Na^+ is the only counter cation present in the solution. Na_2SO_4 was used to control the Na^+ concentration at two unbuffered conditions, pH 7 and pH 13. In open circuit conditions for which electrons can more easily recombine with $Ti-OH^*$, the emission is much less pronounced but has the same trend with pH (Fig. 3.2) and salt concentration (Fig. 3.6). Moreover, the emission appears dominantly as a ~2 ps kinetic growth after the initial excitation, as expected for an exoergic $\Delta G_{OH^*}(U_{VB})$, with the timescale assigned previously[21].

Alongside this emissive transition, an absorptive transition (red arrow, Fig. 5C, red absorption, Fig. 5D) also exists. We find the absorption to be less sensitive to the $Ti-OH^*$ population: the absorption appears most prominently at open circuit condition, exhibits decay kinetics and is not substantially modulated by surface conditions (pH). An absorptive transition in the visible regime could arise from VB electrons promoted to an excited potential energy surface (red line, Fig. 5C) for which the $Ti-O$ distortion is maintained and a VB hole is left behind, as proposed for titania[20] and other transition-metal oxides[46,47]. A red-shifted absorption to the emission has been attributed to the intermediate population in iron oxide[36] but to the VB hole population in a variety of oxides[25,48,49]. Since the proposed absorptive transition is modulated by the VB density of states for hole occupation, a function of both trapped and VB holes, one might expect the kinetics to exhibit a complex interplay of the two populations. By contrast, the CB electron density of states responsible for the emissive transition is independent of the trapped hole population.

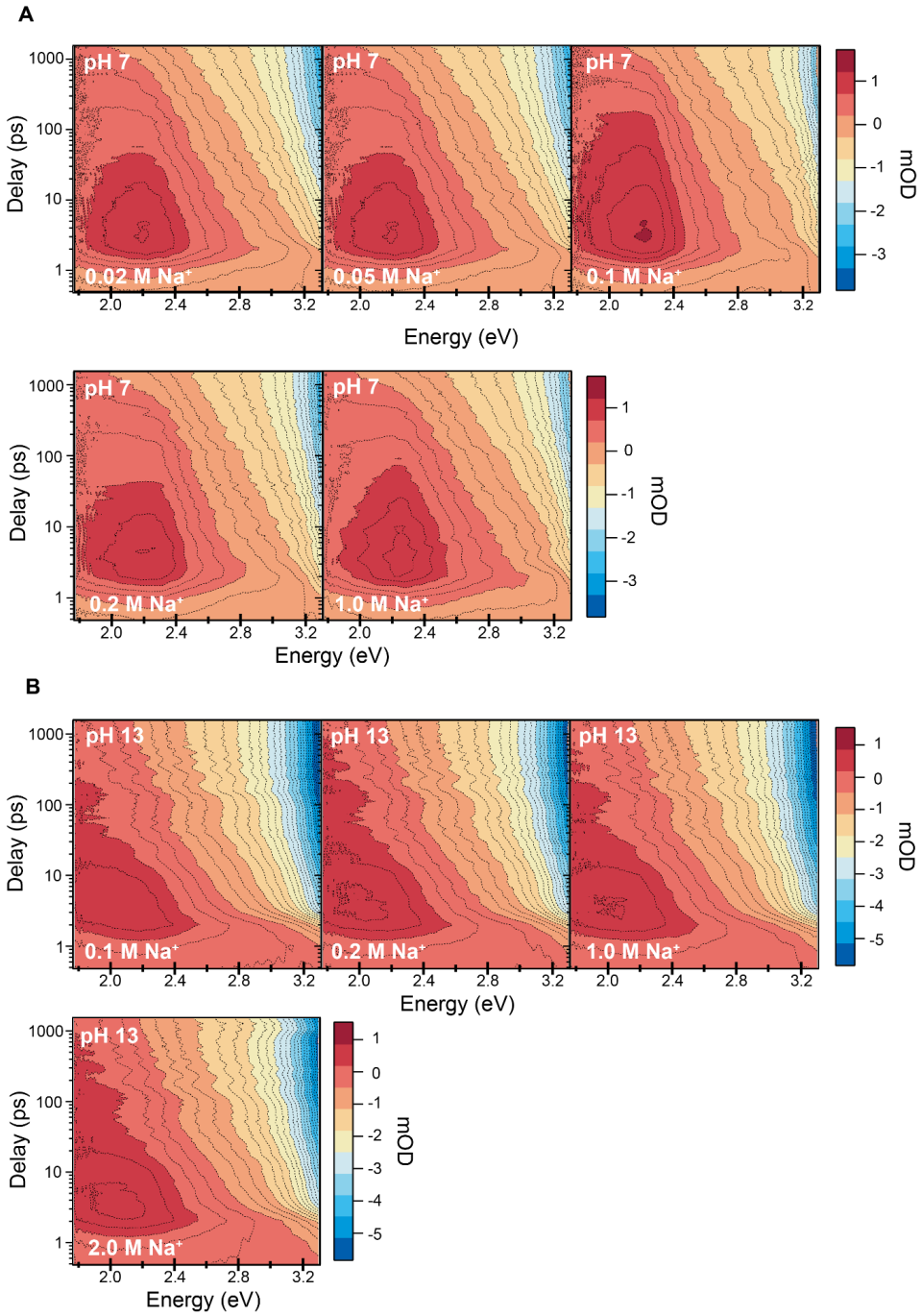

Figure 3.6: Transient optical spectra of varying Na^+ concentration in (A) pH 7 conditions and (B) pH 13 conditions. Both pH conditions were unbuffered in closed-circuit (0 V). Note the change in mOD scale between pH 7 and 13.

A physical interpretation of the TR signal can be seen in the energy level diagram in Figure 3.7, where panel A shows that upon excitation, valence band (VB) electrons (blue) are excited by the pump to the conduction band (CB), forming free

electrons in the CB and holes in the VB. Polarons created by hole-trapping form mid-gap levels (red bars) between the bands. The solid red bars depict the ground electronic state of the polaron, and the dashed red bars, an electronically excited state of the polaron that also occurs in the middle of the band gap. Electron polarons due to Nb dopants are also present (purple bars). Transition arrows represent optical electron transitions, which can be between localized mid-gap states, band and mid-gap states, and interband. Electrons can also transition to the excited hole-polaron state (dashed red bar), which maintains the polaron nuclear configuration. Green arrows represent observable transitions in the UV-VIS range of our WL probe (approximately 1.8 to 3.25 eV). Black arrows represent transitions of approximately < 1 eV not observable with a visible probe.

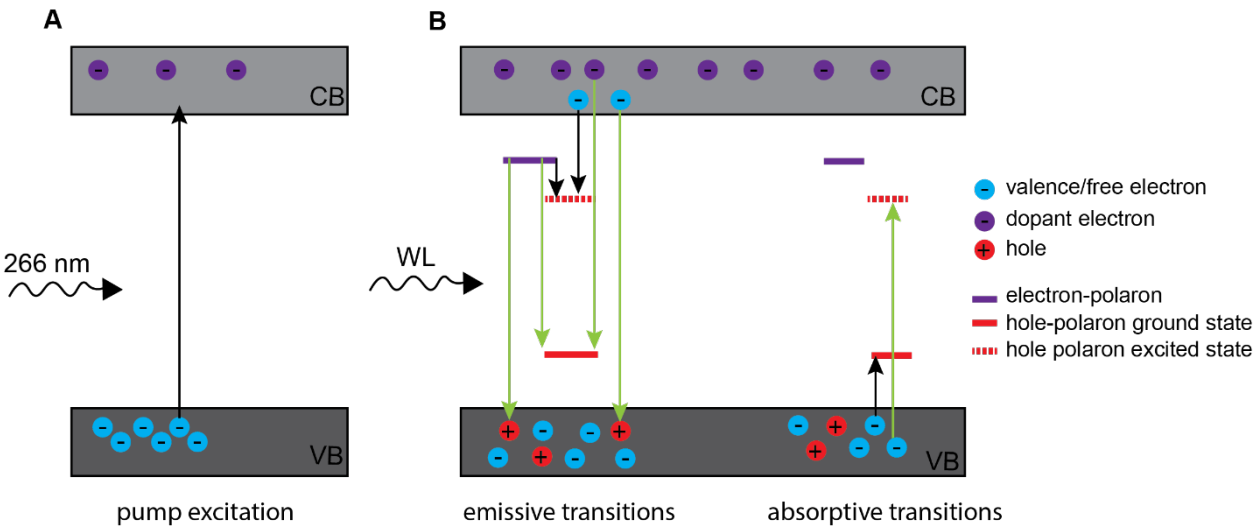

Figure 3.7: Energy level diagram of optical transitions for our STO system.

Using Fermi's golden rule, the optical transition between two continuums in a one-dimensional spectroscopy will be a convolution of density of states (DOS) of the initial and final states. While true for the both the ground and excited states of the hole-polaron, transitions to the ground state should more directly count the hole-polaron population since transition probability is also directly proportional to either

the CB (emission) or VB (absorption) density of states. In the case of CB electrons emitted to the ground hole-polaron state, the occupation of the CB states is independent of the formation of the midgap states. On the other hand, the occupation of VB states changes directly as a result of VB holes forming hole-polarons.

Principal component analysis of the optical spectra

The spectra shown in Fig. 3.5D are the result of a principal component analysis constrained[50,51] to have a pure emissive component and an absorptive one. We first show how two predominant spectral components exist in common for the full dataset. Singular value decomposition[17] (SVD) directly yields two dominant components for each reaction condition, the two components (spectral and kinetic) in their raw form along with the singular values are shown in fig. 3.8. If these are common to the dataset, one should be able to reconstruct one reaction condition's optical spectra from a linear combination of the principal components of another, or

$$M^{(\mathrm{pH}\ 13)} \approx \left(U_{1,2}^{(\mathrm{pH}\ 7)} \cdot R^{-1}\right) \cdot S_{1,2}^{(\mathrm{pH}\ 13)} \left(V_{1,2}^{(\mathrm{pH}\ 13)}\right)^{T} \qquad (18)$$

$M^{(\mathrm{pH}\ 13)}$ is a matrix of the spectral-kinetic data at pH 13. The columns of $U_{1,2}^{\mathrm{pH}}$ and $V_{1,2}^{\mathrm{pH}}$ are orthonormal and represent the SVD spectra and kinetics, respectively; T denotes transpose. $S_{1,2}^{(\mathrm{pH}\ 13)}$is a diagonal matrix that defines the singular values of the two components. The linear combination matrix is $R = (V_{1,2}^{(\mathrm{pH}\ 13)})^{T} U_{1,2}^{(\mathrm{pH}\ 7)}$. If a common two-component basis exists, R will be a rotation matrix (accounting for reflections).

We show the similarity between the pH 13 dataset reconstructed from its own two SVD components in Fig. 3.9A and the pH 7 SVD components in Fig. 3.9A. The rotation matrix can be calculated for any pair of reaction conditions within a dataset with small error bars. This rotation analysis shows a sigmoidal pH dependence already encoded in the 0.1% Nb STO data by a common basis set without constraints (Fig. 3.9C) and quantifies little dependence of the spectral components on

the salt concentration (Fig. 3.9D). It also shows little pH dependence for highly doped (0.5%, 0.7% Nb) STO (Fig. 3.9C).

SVD is discussed in full detail in a dedicated section in chapter 2.

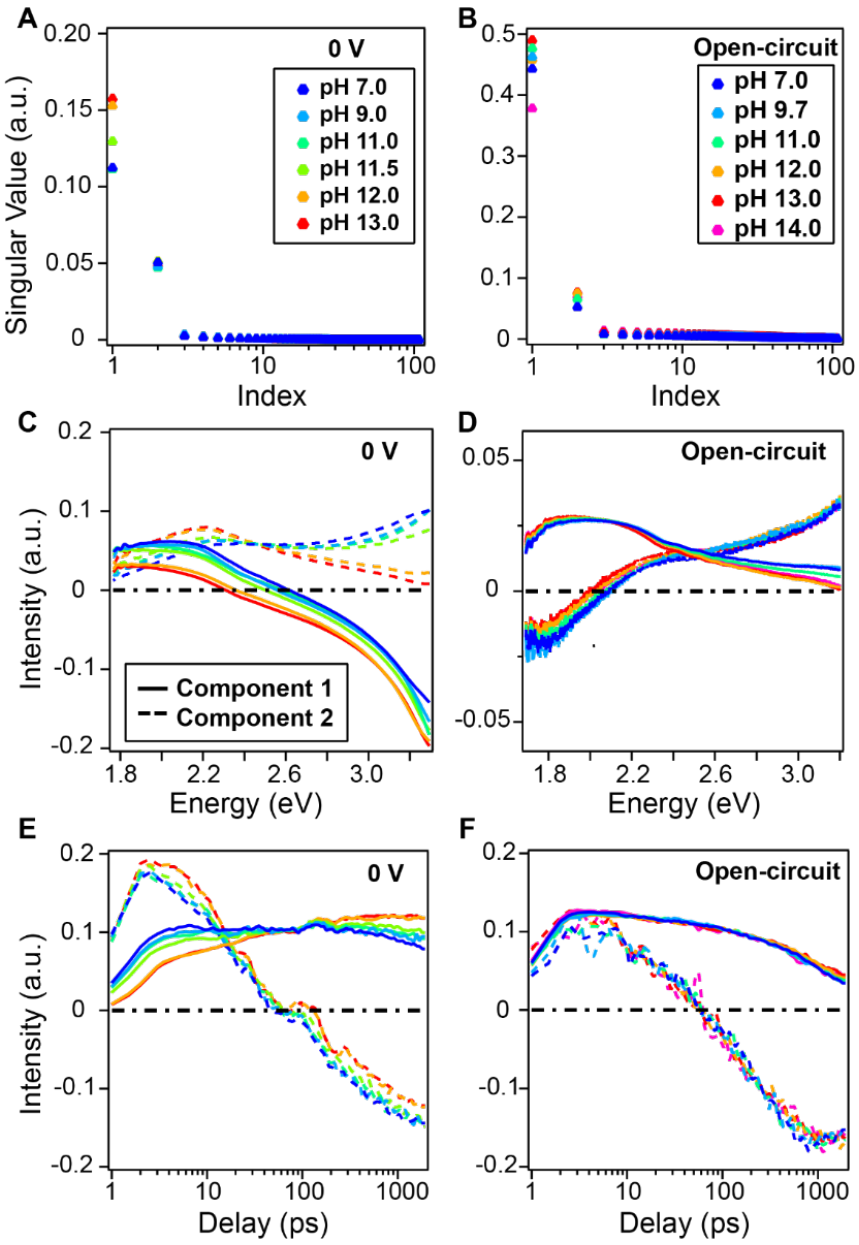

Figure 3.8: Unconstrained SVD of TR data in closed-circuit (phosphate-buffered) and open-circuit (sulfate-unbuffered) condition; (A) and (B) show the singular values of data sets with varying pH; (C) and (D) show the spectra of the significant (first two) components; (E) and (F) show the associated kinetic traces of the two components. All data shown was phonon removed prior to SVD analysis.

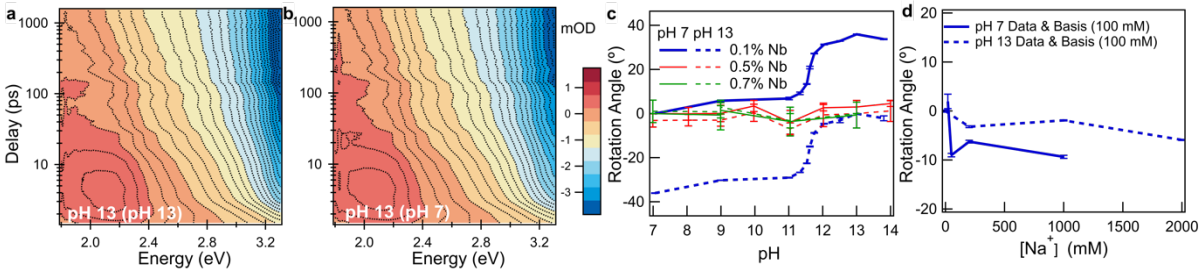

Figure 3.9: Singular value decomposition (SVD) and rotation analysis for the closed circuit data. a) Reconstruction of the pH 13 spectrum from its first two SVD components. b) Reconstruction of the spectrum in a) from the spectral SVD components of the pH 7 transient optical spectra c) Rotation angle analysis for the phosphate buffered pH data set showing a sigmoidal trend across pH in 0.1% Nb STO. The angle is given relative to the pH 7 data in solid lines and relative to the pH 13 data set in dotted lines. Data are shown for all three STO samples (0.1%, 0.5%, and 0.7% Nb). d) Rotation angle analysis for the data set showing little trend with salt concentration for pH 7 (red) and pH 13 (blue) in a Na_2SO_4/NaOH solution. In both pH 7 and pH 13, the reference spectral components are from the corresponding 100 mM [Na^+] spectral map. For c) and d), error bars indicate the standard deviation of the four angles in the rotation matrix R, which measures how orthogonal the transformation is between the reference and final spectral components.

Modulating the Ti-OH* reaction equilibria by pH

The data shown so far in this chapter establishes that a clear and quantifiable trend in pH exists, it does not in itself assign a spectral component to the $Ti-OH^*$ population and its origin from reaction (16). We start with a cartoon of the hydrated STO surface in the dark and under photoexcitation (Fig. 10A). The undoped STO surface is understood to partially dissociate H_2O at neutral conditions[52-54], such that approximately half the titania sites are water absorbed and half hydroxylated. The lightly doped 0.1% Nb STO surface exhibits a similar ratio of hydroxylation to water absorption by ambient pressure X-ray photoelectron spectroscopy in figure 3.4. Since they are separated by $Ti-OH_2$ groups, the isolated $Ti-OH^-$ are well positioned to trap holes quickly (reaction (16)). Further, given the above dichotomy between the emission and absorption, a constrained SVD analysis identifies the rising components of the $Ti-OH^*$ population using the following equation:

$$M^{(n)} = U^{(n)} \cdot S^{(n)} \cdot \left(V^{(n)}\right)^T = U^{(n)} \cdot X^{(n)} \cdot \left(X^{(n)}\right)^{-1} \cdot S^{(n)} \cdot \left(V^{(n)}\right)^T = U^{(t)} \cdot \left(V^{(t)}\right)^T \qquad (19)$$

Here, X is a new matrix that describes the projection of the raw SVD components $U_{1,2}$ onto purely emissive (1) and absorptive (2) spectral components. The procedure to constrain the spectra is outlined in Constrained SVD section of chapter 2. The emissive spectrum (Fig. 3.5d) increases with shorter wavelengths, which may be related to the probe stimulating electrons closer to the surface. The absorptive spectrum has a peak near ~2 eV, as identified in a number of other oxides[20,46,47].

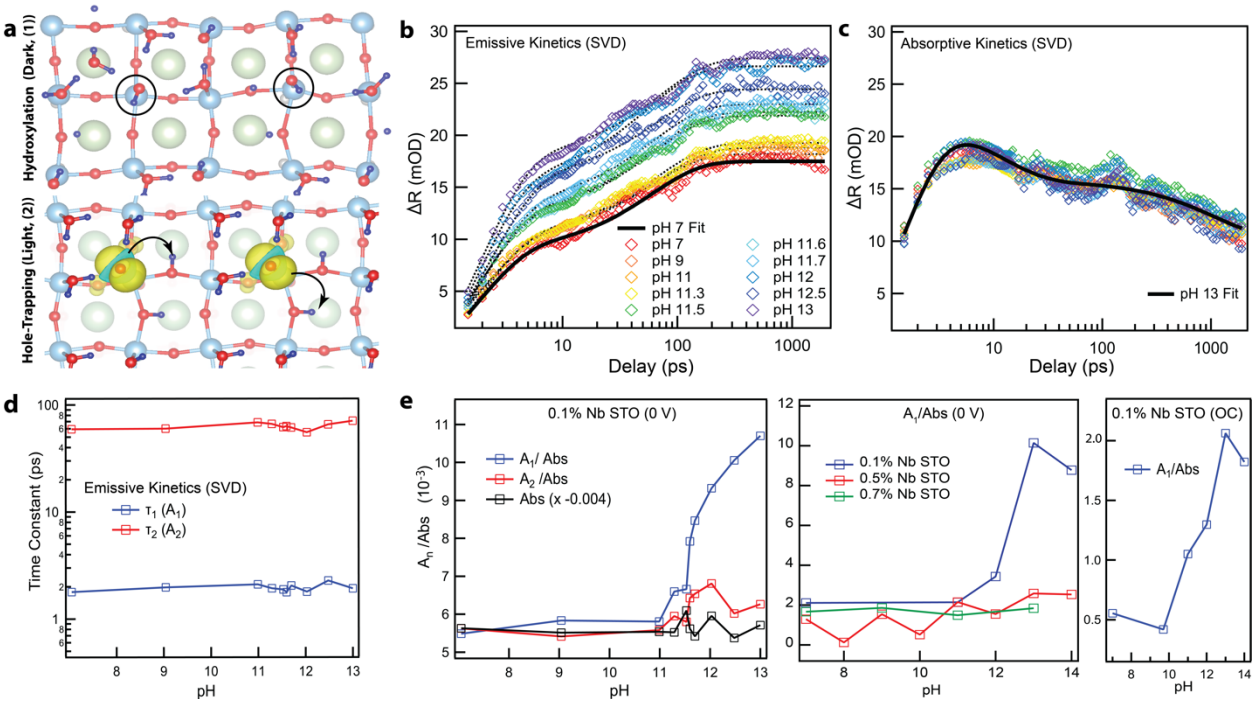

Figure 3.10: Constrained SVD analysis for 0.1% Nb STO phosphate-buffered data at closed circuit unless otherwise specified. a) Cartoon of the 0.1% Nb STO surface in the dark and upon light excitation, reflecting the two separable proton and electron transfer steps. b) Weighted, emissive growth kinetics $(X^{-1}S_{1,2}(V_{1,2})^T)_1$as a function of pH (colored diamonds) fit with two rising exponentials (black solid and dotted lines). c) The same as a), but for the weighted, absorptive decay kinetics $(X^{-1}S_{1,2}(V_{1,2})^T)_2$ d) The time constants of the two rising exponentials for the emissive kinetics as a function of pH e) The populations (A_1, A_2) defined by the two time constants, normalized by the integrated absorption (A_n/Abs), as a function of pH; the integrated absorptive signal (Abs), as a function of pH. Alongside, A_1/Abs is compared for the three n-STO samples, 0.1%, 0.5%, and 0.7% Nb, taken on the same optical setup. A_1/Abs is shown for 0.1% Nb STO under OC conditions with sulfate buffer.

Figure 3.10B shows the constrained kinetics associated with emission, $(X^{-1}S_{1,2}(V_{1,2})^T)_1$, for each pH at 0 V versus SCE. While the kinetics exhibit consistent growth rates across pH, the response amplitude systematically increases. However, the kinetics associated with absorption, $(X^{-1}S_{1,2}(V_{1,2})^T)_2$, exhibit decay kinetics and

show little change with pH (Fig. 3.10C). Fitting the emissive curve with two rising exponentials defines the two timescales ($\tau 1 \approx 2$ ps and $\tau 2 \approx 60$ ps) shown in fig. 3.10D. Since the time-integrated absorption is independent of pH, we can use it to normalize the emission for fluctuations in pump–probe overlap. In fig. 3.10E, we show the normalized emissive response as a function of pH and for different experimental conditions. For 0.1% Nb STO, the amplitude of the fast, 2 ps rise (A_1) has a clear sigmoidal dependence on pH centered at 11.7. For 0.1% Nb STO, the amplitude of the 60 ps rise (A_2) is also fairly pH independent. While in this analysis A_1 and A_2 both report on the $Ti-OH^*$ population, since A_2 occurs later, A_2 represents either a time evolution of the 2 ps $Ti-OH^*$ population or a separate population of $Ti-OH^*$ arising from a different source.

These results establish a sigmoidal pH dependence for the 2 ps component of $Ti-OH^*$ creation from VB holes, which reflects a reaction isotherm and the two reaction steps proposed above. The fast timescale for the A_1 population aids in separating reaction (15) from (16), since any re-equilibration with OH^- in solution should occur at substantially longer timescales[55,56]. It also suggests that the hole transfer occurs without a simultaneous full proton transfer to solution. This is similarly anticipated by ab initio molecular dynamics simulations on titania[20,33].

The absence of a clear H/D kinetic isotope effect (KIE), shown in fig. 3.11 substantiates the lack of free H^+ as a product[57,58]. We tested the kinetic isotope effect in pH 7 and pH 13 conditions using deuterated water and sodium deuteroxide. The kinetic traces taken at 400 nm (Fig. 3.11A) corresponding to various reaction conditions show little difference when directly compared to each other, signaling that a deeper analysis is required. Applying constrained SVD analysis to the data to access the time constants associated with the emissive, ~2 ps A_1 population for both pH 7 and pH 13, with for two trials each, are given in Table 1. The ratio of time

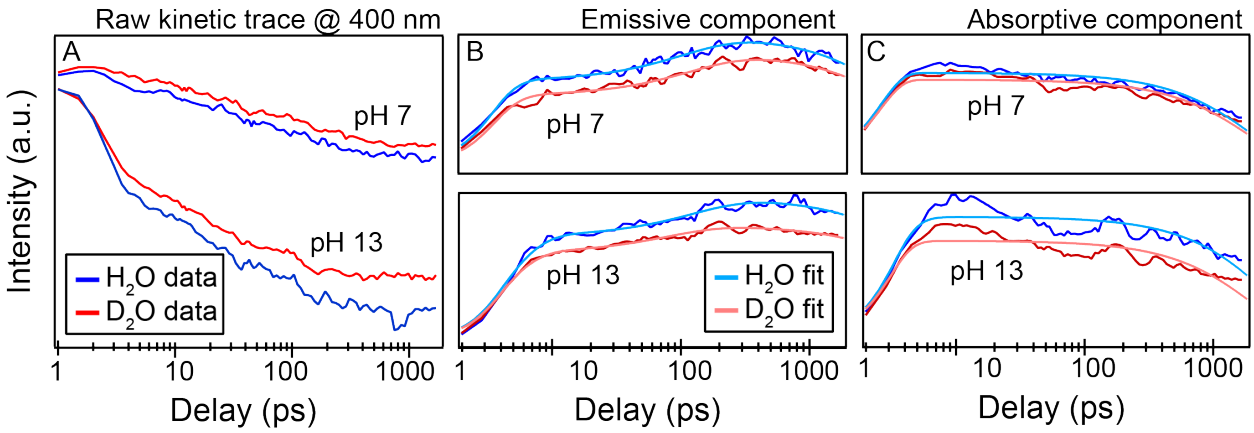

Table 1: KIE constants

KIE 1:		K_1	K_{1H}/K_{1D}
PH 7	D_2O	1.49 ± 0.12	1.40 ± 0.13
PH 7	H_2O	2.09 ± 0.11	
PH 13	D_2O	2.39 ± 0.13	0.96 ± 0.07
PH 13	H_2O	2.31 ± 0.13	
KIE 2:		**T_1 (ps)**	**K_{1H}/K_{1D}**
PH 7	D_2O	2.68 ± 0.20	0.73 ± 0.08
PH 7	H_2O	1.97 ± 0.16	
PH 13	D_2O	2.56 ± 0.12	1.09 ± 0.08
PH 13	H_2O	2.81 ± 0.16	

Figure 3.11: H_2O/D_2O Kinetic Isotope effect. (A) The raw kinetic traces. (B) and (C) Constrained kinetic emissive and absorptive components, respectively. Table 1 shows the time constants of the ~ 2 ps A_1 emissive component and the resulting KIE ratio. Two different trials are shown (KIE 1 and KIE 2).

constants of hydrogenated vs deuterated data sets under similar conditions is in the range of 0.73 to 1.4 and the lack of any observable trend leads us to believe that there is no apparent KIE and thus there are no free protons as products.

Effect of different counter-ion environment on Ti-OH* reaction equilibria vs pH

While the pH dependence shown in fig. 3.1 and fig. 3.10 is taken with a phosphate-buffered solution that allows for finer steps in pH, a sigmoidal pH dependence also occurs for A_1 with a sulfate solution (Fig. 3.12). Importantly, the same methodology extracts a sigmoidal pH dependence from the open-circuit data (Fig. 3.13 and Fig. 3.2) for which no surface degradation exists, and photoexcitation flattens the Schottky barrier; this independently isolates the effect as coming from the interfacial hydroxylation.

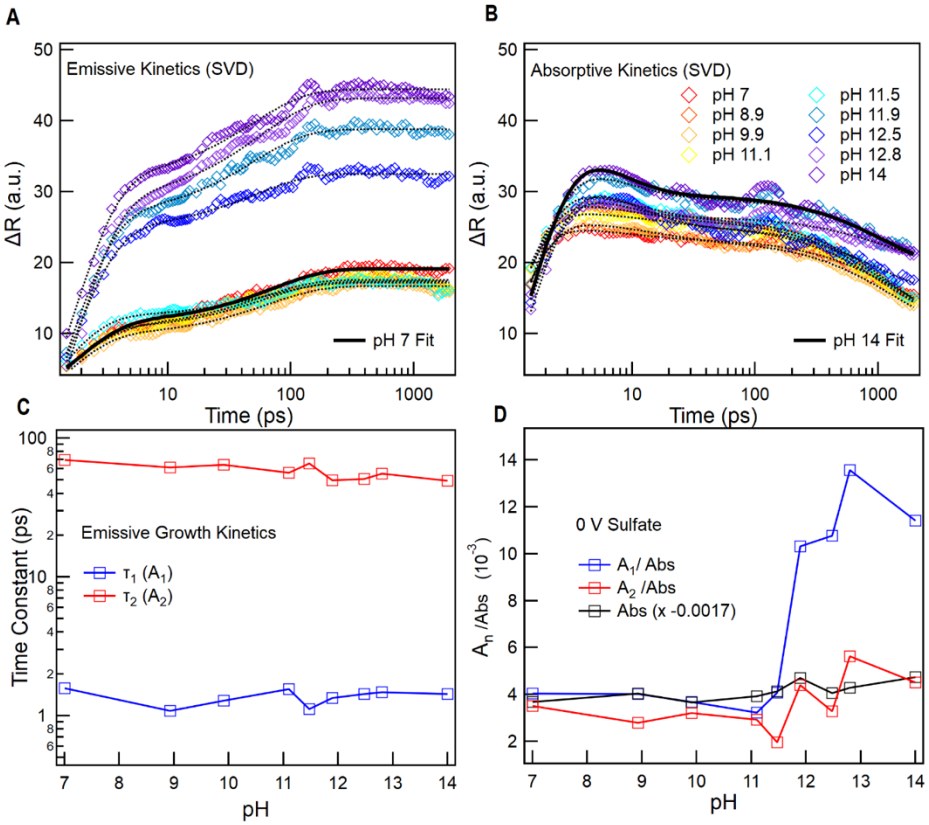

Figure 3.12: Constrained SVD analysis of STO TR in unbuffered electrolyte with Na_2SO_4 as the counter ion (closed-circuit at 0 V). (A) and (B) show the constrained kinetic emissive and absorptive components, respectively. (C) Time constants from the biexponential fit of the constrained kinetics as a function of pH. (D) Amplitudes associated with the emissive time constants normalized by the integrated absorption, as a function of pH.

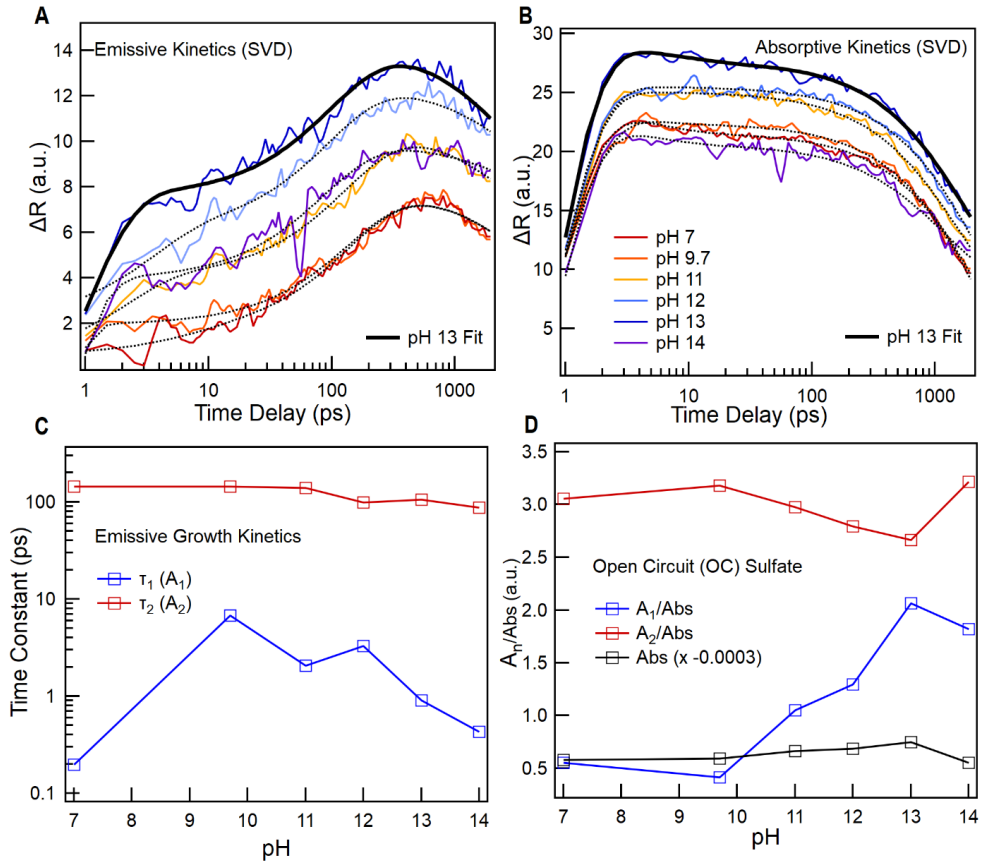

Figure 3.13: Constrained SVD analysis of STO TR in open-circuit conditions. (A) and (B) show the constrained kinetic emissive and absorptive components, respectively. (C) Time constants from the biexponential fit of the constrained kinetics as a function of pH, and (D) Amplitudes associated with the emissive time constants normalized with integrated absorption, as a function of pH.

Modulating Ti-OH* reaction equilibria by pH on a different electrochemical surface

The two separable reactions are also supported by investigating a similar sample, but one for which the surface is expected to be hydroxylated already under neutral conditions. The 0.7% Nb STO indeed exhibits a much higher hydroxylation than 0.1% Nb STO by ambient pressure X-ray photoelectron spectroscopy (Fig. 3.4); the more-electron-dense, in-plane, lattice oxygen sites could promote H_2O dissociation[59].

Ambient Pressure X-ray Photoelectron Spectroscopy (AP-XPS) was collected at Beamline 9.3.2 for 0.1% Nb STO and 0.7% Nb STO for a range of relative humidity achieved using down and up temperature sweeps for several pressures (100mTorr, 500 mTorr, and 700 mTorr) of water vapor. The experimental details are in ref. 1 for an un-doped STO sample.[1] The manuscript also contains a detailed analysis of the AP-XPS data alongside AIMD calculations to determine the first hydration layer, which on un-doped STO is described best by a 50/50 dissociation of H_2O on each Ti atom such that neighboring Ti atoms have H-bonding between a H_2O absorbed group and a hydroxyl group. The dissociated H^+ is accepted by a neighboring, in-plane lattice oxygen atom.

Temp (°C) at 700 mTorr	%RH	0.1% Nb - 0.7% Nb OH/Ox	0.1% Nb - 0.7% Nb H_2O/Ox	OH/Ox 0.7% Nb/0.1% Nb
500	~ 0	0 - 0	0 - 0	N/A
300	~ 1 E-3	0.103 - 0.297	2.57E-4 - 3.87E-2	2.9
150	~ 2 E-3	0.135 - 0.348	2.43E-3 - 8.73E-2	2.6
100	~ 1 E-1	0.158 - 0.503	2.40E-3 - 0.205	3.2
60	~ 0.5	0.354 - 0.595	0.191 - 0.413	1.7
40	~ 1	0.465 - 0.852	0.393 - 0.642	1.8

Table 2: AP-XPS Data for 0.1% and 0.7% Nb doped STO compared for select relative humidity (RH%). OH/Ox and H_2O/Ox are ratios of the integrated peak areas of hydroxyl and water adsorbed groups, respectively, with respect to the area of the lattice oxygen peak. The temperature and %RH are reported as an average of the two data sets, both taken at 700 mTorr and similar temperatures. The last column is the ratio of the OH/Ox peak in 0.7% Nb STO to that of 0.1% Nb STO.

The ambient data were taken from two 700 mTorr decreasing temperature runs, as there was little carbon contamination due to either carbonates or aliphatic carbon (insets of Figure 3.4A). While at the lowest RH (~0%), the 0.1% Nb STO and 0.7% Nb STO AP-XPS are nearly identical, as the RH increases, the 0.7% Nb STO shows significantly more spectral intensity at the higher binding energy side of the main peak. The peak fitting analysis of Figure 3.4B, which follows Table I of ref. 1 [BE energies (widths) of the OH and H_2O are 531.6 eV (1.5 eV) and 534.1 eV (1.5 eV)][1], finds that the main difference in the data is due to an increase in hydroxyl groups for 0.7% Nb STO throughout the RH range. This is not un-anticipated: higher

degree of doping could facilitate hydroxylation by providing a lattice O site that can more readily accept the H^+ from water.

Table I shows the integrated peak areas. The 0.1% Nb STO exhibits a similar lineshape to the un-doped STO, in that near 1 RH there is a near equal contribution of H_2O and OH groups. On the other hand, the 0.7% Nb STO exhibits a OH:Ox peak ratio of 0.5-0.6 already by 10^{-1} RH, and approaches 1 at 1 RH. By this measure, the hydroxylation of 0.7% Nb STO is roughly 2-3 times higher than 0.1% Nb STO (last column in Table 1). This is consistent with a picture whereby the 0.1% Nb STO has a similar hydroxylation as undoped STO, for which ½ the sites (including Ti and O surface atoms) are hydroxylated, ¼ contain water groups (preferentially absorbed on Ti sites), and ¼ are empty lattice oxygen. A fully hydroxylated 0.7% Nb STO should contain OH groups on all sites, so a factor of ~ 2 higher than the 0.1% Nb STO. By this same measure (H_2O:Ox), there is also significantly more water adsorbed groups at lower RH on 0.7% Nb STO. However, it is not clear whether these are interstitial water formed in the layer above or water adsorbed on the STO Ti atoms. Indeed, the hydroxylation saturates at higher RH on diverse oxides[1,2,6,11] (between 0.1-1RH) and the second layer should be comprised of H_2O. Where the first hydration layer ends and the next one begins requires further assessment of doped STO, including sub- and multi-layer models of the AP-XPS data and ideally, AIMD calculations through multiple layers. We leave this for future work.

The contour plots of figure 3.14 visually show that while there is a pH dependence for 0.1% Nb STO, there is no clearly observable pH dependence for the 0.5% or 0.7% Nb STO. Additionally, there is also less overall amount of emission as noted by the significantly different mOD scales in fig. 14 (B and C). These data were all taken on the same experimental setup to facilitate the comparison. Only representative plots are shown, but a fuller pH range was taken (see analysis below).

We note that the optical setup has changed from the one in which the bulk of the 0.1% Nb STO data was taken, including an extension to a longer time range (4 ns) and the

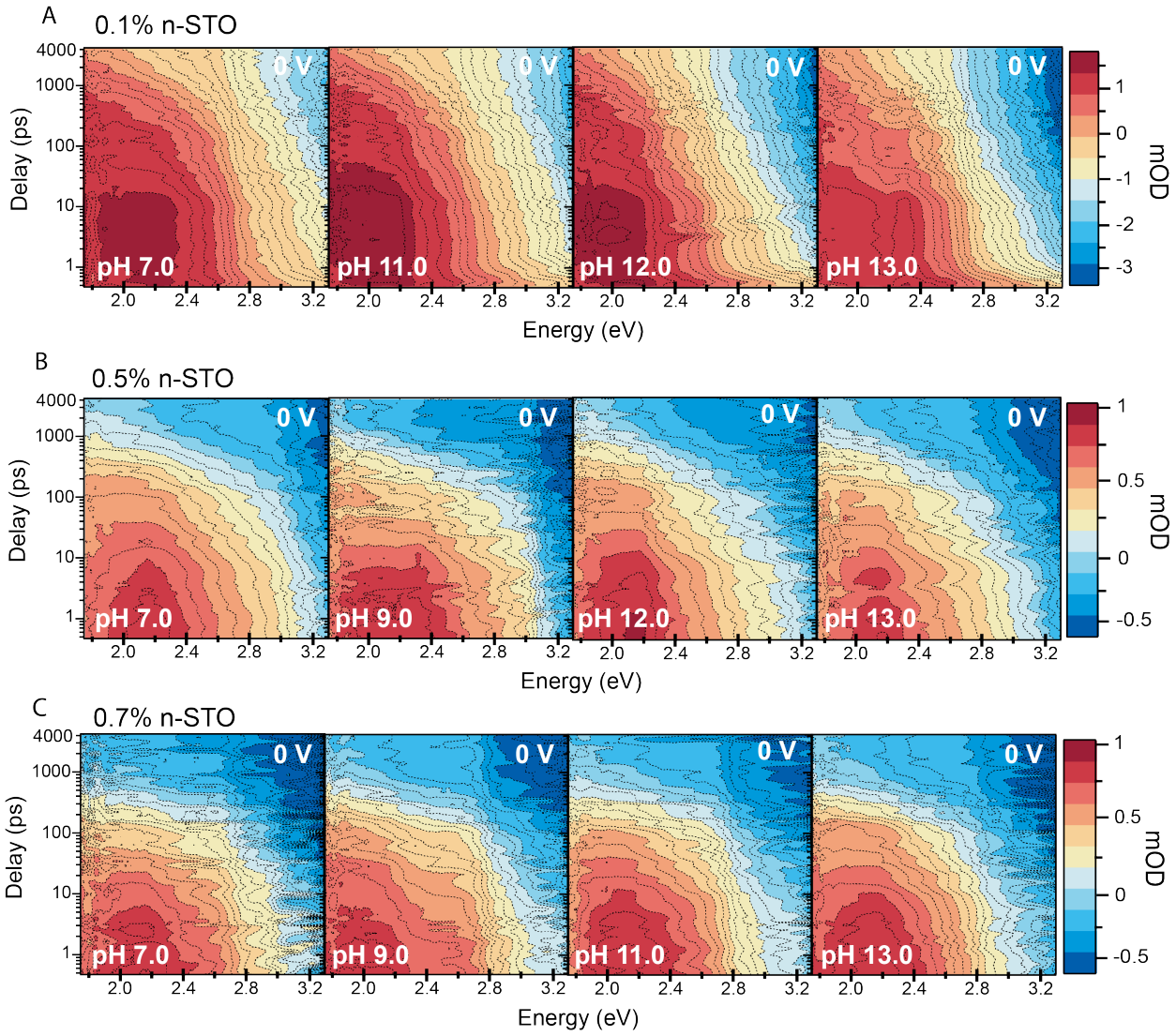

Figure 3.14: pH dependence of different n-doping densities shown for 0.1% Nb-STO in (A), 0.5% Nb-STO in (B), and 0.7% Nb-STO in (C). The data are taken in closed-circuit in phosphate buffer.

introduction of parabolic mirrors that has led to a change in focus, which artificially suppresses the emission in the range of > 3 eV. Nonetheless, the pH dependence in the 0.1% Nb STO is clear.

Since the optical spectra for both 0.5% and 0.7% Nb STO also do not exhibit a resolvable pH dependence, the results reflect a dark equilibrium that cannot be

pushed by pH in basic conditions. In contrast to the more isolated, defect Ti-OH− sites in lightly doped STO, a fully hydroxylated surface in highly doped STO could reflect two-dimensional network for hole trapping. However, the analysis of 0.5% and 0.7% Nb STO shows little pH dependence, reflecting the rotation analysis (Fig. 3.9C).

Figure 3.15 shows the singular value decomposition of the data represented in figure 3.14, which confirms that the two significant components in the 0.1% Nb STO

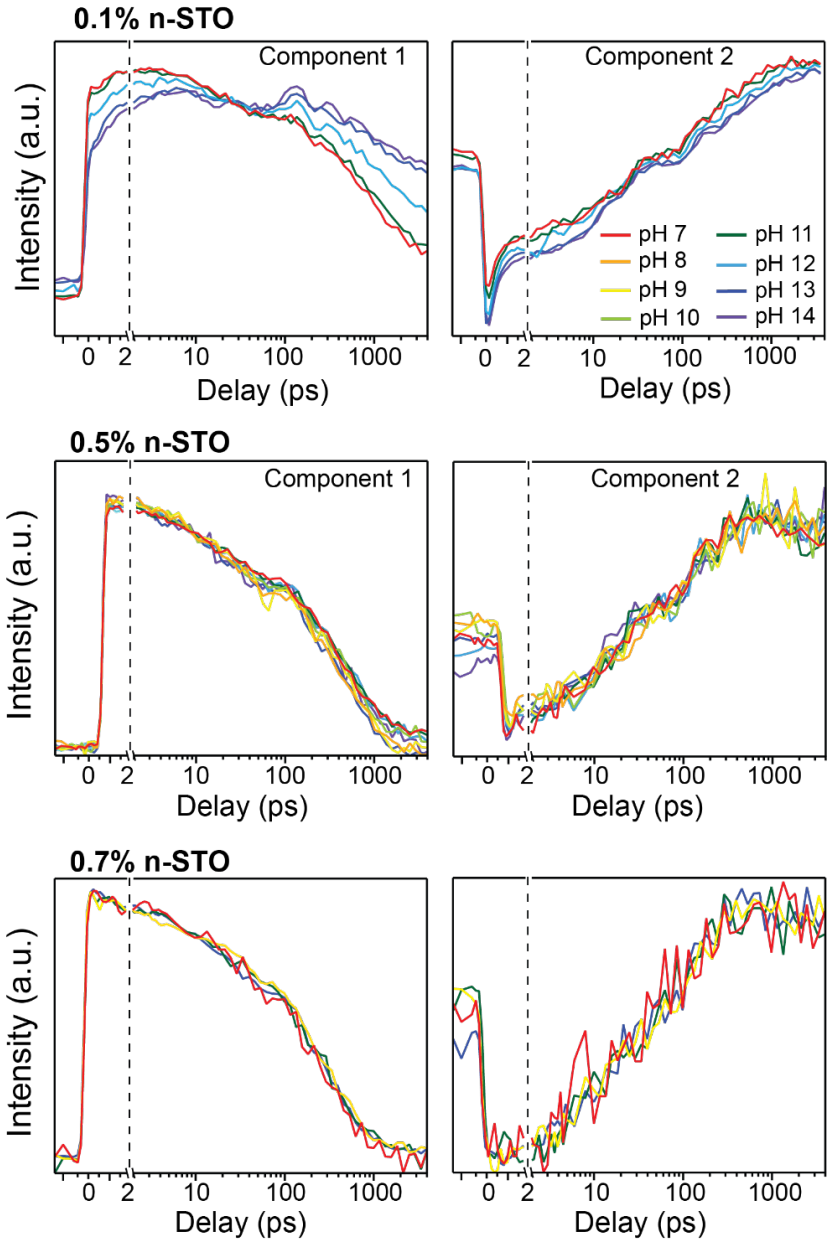

Figure 3.15: Unconstrained SVD of TR data in closed-circuit for the three different doping densities (0.1% top, 0.5% middle, and 0.7% bottom, Nb-STO). The associated kinetic traces of the significant (first two) components are shown.

show a clear pH dependence, while they don't in 0.5% Nb STO and 0.7% Nb STO. The SVD analysis is compared via the kinetic traces, which contain the information on the time-dependent populations. Since this is an unconstrained SVD analysis, the spectrum assigned to these populations will differ based on the range of the data taken (in time and energy).

Figure 3.9C and figure 3.10E shows that the rotation and constrained SVD analysis reproduces a nearly sigmoidal pH-dependence in the newly acquired data on 0.1% Nb STO, while the A1 ~ 2 ps component in the 0.5% Nb STO and 0.7% Nb STO show little observable pH dependence. This confirms the observations based on the raw data (Fig. 3.14) and the unconstrained SVD analysis (Fig. 3.15). We note that the sigmoidal dependence in the rotation analysis is not as clear, likely due to the artificial suppression of the data in beyond 400 nm on this optical setup.

The lack of an observable pH dependence in the TR on samples with higher doping densities reflects a change in the hydroxylation of the highly doped STO surfaces at neutral conditions seen independently by AP-XPS (Figure 3.4 with supporting Table II). The factor of ~2 higher hydroxylation suggests that the explicit equilibrium with the electrolyte (reaction (15)) cannot be pushed in the accessible pH range. While the AP-XPS data on 0.5% Nb STO is unavailable at the time of writing this dissertation, the similarity in the optical data implies that this surface already exhibits high hydroxylation. There is some dependence in the constrained SVD analysis, but this is within the noise; perhaps, a broader probe range towards the deeper UV could reveal some pH dependence. These results both confirm the isotherm model presented and circumscribe it, since the explicit equilibrium in the dark must not be limited by the available sites for $Ti-OH^-$. However, such a highly hydroxylated surface is not anticipated for many lightly doped 3d transition metal oxides on the weak-binding side of the volcano plot. Indeed, 0.5% and 0.7% Nb lead

to an n-doping density in the range of $10^{20}/cm^3$, which is higher than typical (10^{18}-$10^{19}/cm^3$).

A fully hydroxylated surface changes the way one would think about hole-trapping, in that the hole could delocalize among the sites on the now 2D network of hydroxyl groups. This could lead to a lower $\Delta G_{OH^*}(U_{VB})$ for reaction (16) associated with more delocalized hole-polaron orbitals. The lower $\Delta G_{OH^*}(U_{VB})$ implies less trapping, while the delocalization of the hole-polaron orbital implies a weaker optical transition dipole for emission. Both effects imply less overall emission in the TR as observed in fig. 3.14. Therefore, we have a dichotomy between a fully hydroxylated surface (0.7% Nb STO) in which both little pH dependence and less emission is anticipated and a surface with isolated hydroxyls among water adsorbed and bare oxygen sites (undoped, 0.1 % Nb STO), where the equilibrium can be pushed by pH and localized hole traps lead to more emission. In a range of n-doping in between 0.1% Nb and 0.5% Nb, one might expect a pH dependence but with a less emissive signal overall. These considerations do have significant implications on the nature of the first electron transfer intermediates ($M-OH^*$) that lead to O_2 on different oxides, and we leave this for future work.

A Langmuir isotherm with an effective equilibrium constant

The free energies of the relevant steps are depicted within the full photo driven OER reaction in fig. 3.16a. Reaction (15) is described by the chemical potential of $[Ti-OH^-]$ relative to $Ti-OH_2$ along the same free energy surface in the dark (solid black lines). However, reaction (16) involves a crossing of two distinct surfaces, where the light pulse (yellow arrow) first creates the hole on the oxidized surface at the reaction coordinate defined by the reduced VB but then quickly transfers to the surface for which the trapped hole, $Ti-OH^*$, is a minimum.

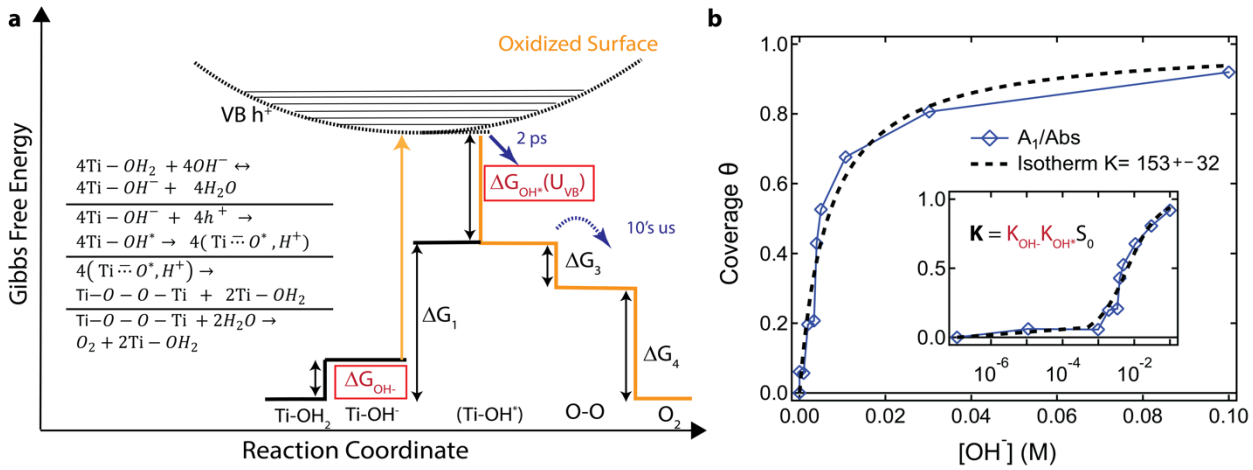

Figure 3.16: (a) Free energy diagram of Ti-OH$^-$ adsorption and Ti-OH* creation in the context of the full reaction scheme. Photoexcitation (yellow arrow) separates the diagram into the equilibrated and driven surfaces. The black dotted line represents the excited hole in the VB, while the yellow solid line represents the pathway to O_2 for a photo-excited hole. The ΔG for each reaction step per site in OER is shown in the standard state, with the ones relevant to the experiment highlighted in red. The time constant (2 ps) for Ti-OH* creation from the VB hole highlighted in this work is shown by the blue arrow; the dotted blue arrow (10's μs) denotes the downhill reaction kinetics for O-O bond formation, as suggested by previous work[21]. The full, multi-site reaction scheme suggested by this diagram is stated to the left. (b) The A_1/Abs component (blue triangles) of 0.1% Nb STO in Figure 3e, where the pH 7 contribution has been subtracted and the pH 14 contribution is normalized to 1. The data points have been fit to the Langmuir isotherm described by eq. 6 & 7 in the text, with coverage $\theta = \frac{[Ti-OH^*]}{[h_0^+]}$ and $K_{eff} = 153 \pm 32$. The inset shows the agreement on a logarithmic scale with the characteristic sigmoidal behavior of an isotherm.

We now turn to the description of the sigmoidal pH dependence using a Langmuir-type reaction isotherm[60], albeit for a meta-stable intermediate population. In a Langmuir isotherm, the sigmoidal rise of the product, an adsorbed surface species, with respect to a tunable reactant concentration reflects the equilibrium constant of the reaction. In Langmuir reaction isotherms, four essential assumptions are being made: First, there are a finite number of total surface sites for an adsorbate; second, all sites on the surface are either occupied by an adsorbate or unoccupied; third, no sites are preferential; and fourth, for each concentration of adsorbate (in volume or in surface), an equilibrium is reached. The saturation in the sigmoid reflects a limiting equation that restricts occupied and unoccupied sites to exchange with each other up to a maximum coverage. It is predicated on a simple adsorption reaction, $S + A \leftrightarrow S - A$, where S is an empty surface site and $S - A$ is an occupied surface site. The tunable reactant is the adsorbent, A, and the limiting equation is

$S_0 = [S] + [S-A]$; S_0 is the total surface site density. The equilibrium constants for reaction (15) and (16) are:

$$K_{OH^-} = \frac{[Ti - OH^-]}{[Ti - OH_2][OH^-]} \qquad (20)$$

$$K_{OH^*} = \frac{[Ti - OH^*]}{[Ti - OH^-][h^+]} \qquad (21)$$

For the simple adsorption isotherm of reaction (15), $Ti - OH^-$ exchanges with $Ti - OH_2$ (treated as the unoccupied sites since it is the reactant) to reach an equilibrium, the tunable reactant is OH^-, through modulating pH of the solution, and the limiting equation is $S_0 = Ti - OH^- + [Ti - OH_2]$; S_0 is the total surface site density. The same Langmuir isotherm would also describe $Ti - OH_2 + H_2O\ (l) \leftrightarrow Ti - OH^- + H_3O^+$. We can be sure that the dark equilibrium (reaction 15) is being modulated throughout the entire range of explored pH based on the linear trend, as shown in fig. 2.5, of open circuit photo-voltage (OCPV) measurements vs pH and open circuit voltage (V_{OC}) measurements vs pH. We note this reaction as well as reaction (15) define the site-acidity or pKa of the site denoted by $Ti - OH_2$. Within the realm of optical spectroscopy there is no straightforward way of experimentally identifying a given surface adsorbed site, with multiple energetically similar local configurations, and measuring its pKa. This means that we must assume the pKa of the surface adsorbed site. Substituting the unoccupied sites for the occupied ones into K_{OH^-} using eq. (21) gives a surface coverage θ of $Ti - OH^-$ in terms of K_{OH^-}:

$$\theta_{OH^-} = \frac{[Ti - OH^-]}{S_0} = \frac{K_{OH^-}[OH^-]}{1 + K_{OH^-}[OH^-]} \qquad (22)$$

However, reaction (16) involves an exchange between delocalized and trapped holes and is tuned by the surface hydroxylation, $Ti - OH^-$. The limiting equation compatible with a Langmuir isotherm is $[h_0^+] = [h^+] + Ti - OH^*$; $[h_0^+]$ represents the total hole density excited by a single laser pulse, which is kept constant at 2% of the

surface site density. In this model, $Ti-OH^-$ independently modulates the isotherm for $Ti-OH^*$ coverage, since $Ti-OH^-$ does not re-equilibrate with OH^- on the picosecond timescale. Therefore, the isotherm of reaction (16) can be written in terms of $[OH^-]$ by using $[Ti-OH^-]$ established in the dark, leading to the following net isotherm for the coverage θ through the following steps:

Substituting the unoccupied site density, $[h^+]$ into eq. (21) for K_{OH^*} gives:

$$K_{OH^*} = \frac{[Ti-OH^*]}{[Ti-OH^-][(h_0^+] + Ti-OH^*)} \qquad (23)$$

Rearranging and dividing the equation by the total hole density, $[h_0^+]$, gives surface coverage, θ_{OH^*}, representing the fraction of total holes trapped as $Ti-OH^*$:

$$\theta_{OH^*} = \frac{[Ti-OH^*]}{[h_0^+]} = \frac{K_{OH^*}[Ti-OH^-]}{1+K_{OH^*}[Ti-OH^-]} \quad (24)$$

While this $[Ti-OH^*]$ coverage is tuned by the $[Ti-OH^-]$ adsorbate, the reactant we directly modulate experimentally is aqueous $[OH^-]$. Therefore, to obtain the final isotherm, we use the $[Ti-OH^-]$ coverage of equation (22) to re-write equation (24) as:

$$\theta_{OH^*} = \frac{K_{OH^-}K_{OH^*}S_0[OH^-]}{1+K_{OH^-}[OH^-](1+K_{OH^*}S_0)}$$

While this coverage could be fit in and of itself, $K_{OH^*}S_0 \gg 1$ given $S_0 \sim 2 \times 10^{15}$ cm-2 and $K_{OH^*} >> 1$ for an exoergic reaction (verified below), a simpler Langmuir isotherm is recovered with one equilibrium constant K_{eff}:

$$\theta_{OH^*} = \frac{K_{eff}[OH^-]}{1+K_{eff}[OH^-]}, \text{where } K_{eff} = K_{OH^-}K_{OH^*}S_0 \quad (25)$$

In the coverage (θ_{OH^*}) shown in Figure 3.16B, the pH 7 contribution has been subtracted to define the zero point of the OH^- titration, while the pH 14 contribution is normalized to 1. The sigmoidal dependence of the extracted coverage is well described by an isotherm with a fitting constant of $K_{eff} = 153$ reflecting the pH = 11.7 inflection point. It is important to note that this K_{eff} is in the context of a continually downhill catalytic cycle for which a meta-stable population is being isolated, rather

than a reaction that reaches completion. Additionally, we must assume the pKa for dark equilibrium given by reaction 15. We can reason that the pKa of the dark equilibrium has to be higher than pH 11.7. If the pKa is lower than pH 11.7 then there would be simply too many surface adsorbed sites suitable for hole trapping, and

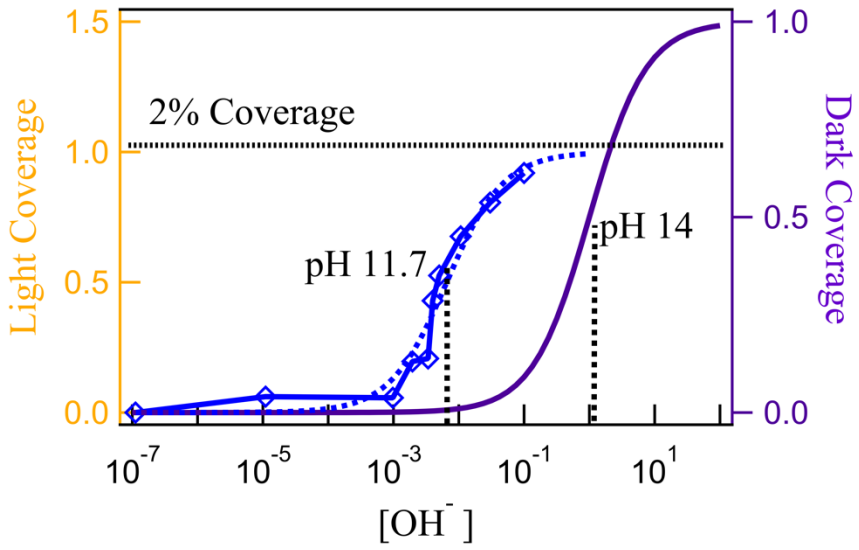

Figure 3.17: Reaction isotherms of the dark equilibrium proton transfer and photo driven hole transfer relative to each other

since we are limited by the hole site density $[h_0^+]$ for the photo driven reaction, all the holes would be trapped, and we wouldn't observe a sigmoidal rise at pH 11.7. Based on this we assume the pKa of the dark equilibrium to be 14 and proceed with the calculations. Figure 3.17 shows the isotherms of the dark equilibrium and the photo driven electron transfer relative to each other.

If all the holes initially created by the laser pulse proceed through reaction (16), $[h_0^+]$ is given by the quantum efficiency for charge separation (>75%) and the laser fluence. Counting the total sites available for occupation by the total hole density is natural in a reaction driven by photon excitation. Since the laser pulse represents only 2% of the site density, it also motivates why the isotherm θ_{OH^*} approaches saturation within the pH range and that a good sigmoid fit is obtained. However, for the purposes here, we could have utilized a different site

number since the effective equilibrium constant is extracted primarily from the sigmoid position vs. pH rather than the saturation coverage, the maximum of θ_{OH^*}.

Next, how the effective equilibrium constant connects to the relevant ΔG, ΔG_{OH^-} for K_{OH^-}, and ΔG_{OH^*} (U_{VB}) for K_{OH^*}, is described. Each of these constants is exponentially dependent on ΔG, in the form of: $K = e^{-\frac{\Delta G}{kT}}$. Each K is unitless when one utilizes the appropriate construction of activities for each reactant and product (dividing by 1 M^{-1} for $[OH^-]$, by 1 cm^{-2} for $[h^+]$, $[Ti-OH_2]$, $[Ti-OH^-]$). Relating K_{OH^-} to ΔG_{OH^-} is then fairly straightforward and reflects the usual definition of pKa. Relating K_{OH^*} to ΔG_{OH^*} (U_{VB}) is more complex since in theoretical calculations, each VB hole is tied to a $Ti-OH^-$ surface site and doesn't appear as a separate concentration, which reflects the predominance of single site mechanisms in theory and an already unitless K_{OH^*} by construction. To make the connection to a surface hole density controlled by the laser pulse, one needs to divide K_{OH^*} by $[h_0^+]$, such that:

$$K_{eff} = K_{OH^-} K_{OH^*} S_0 / [h_0^+] \qquad (26)$$

The surface hole density represents the degeneracy of the VB states that is not considered in a single site model. It increases the number of states in the partition function for holes that goes into K_{OH^*}; since this is on the reactant side of the hole-trapping reaction, the total possible VB hole density involved in the reaction, $[h_0^+]$, decreases the equilibrium constant. Using a pKa = 14 and the ratio of hole density to surface site density of 2%, we can calculate the free energy of hole formation with respect to valence band, ΔG_{OH^*} (U_{VB}), as -0.05 eV.

In the above, the equilibrium constants for the two reactions (K_{OH^-}, K_{OH^*}) are defined along very different reaction trajectories (Fig. 3.16a). Reaction (15) is described by the chemical potential of $[Ti-OH^-]$ relative to $[Ti-OH_2]$ in an aqueous solution along the same, adiabatic potential energy surface (PES, black & dashed lines); ΔG_{OH^-} is the free energy difference. On the other hand, reaction (16) involves

a crossing of two distinct PES's, where the light pulse (yellow arrow) first creates the hole on the oxidized surface at the reaction coordinate defined by the reduced VB PES but then quickly transfers to the PES for which the trapped hole, $[Ti-OH^*]$, has a minimum (yellow line). For reaction (16), ΔG_{OH^*} (U_{VB}) is in effect (minus) the reorganizational energy of creating a trapped hole at a $[Ti-OH^-]$ surface site with respect to the delocalized one[20]. The combination of the adiabatic surface defining ΔG_{OH^-} and the light-driven one defining ΔG_{O^*} (U_{VB}) leads to the doubling of the O* population with pH at picosecond timescales. Basic conditions should then select for a subsequent downhill pathway to O_2 evolution by O^*-O^* bi-radical recombination.

While this is described for a photo-driven reaction, the same $\Delta G_{O^*/OH^*}$ would be expected to describe weakly bound O* intermediates for the purely voltage driven reaction. In the efforts made to understand the trends in energetics for the voltage driven oxygen evolution reaction[10], the energies ΔG_{O^*} and ΔG_{OH^*} have the same meaning whether the energy derives from photoexcitation or an electrode potential. This means that it should be possible to apply the voltage-driven analysis[3] to qualify the catalytic properties of the photo-driven titania surface. The calculations find that the energy efficiency of titania is limited by a too weak binding of the O* and OH* and thus requires a high potential to oxidize water[19]. This is consistent with the results and the analysis of the reaction mechanism seen in fig. 3.16A, where the hole potential (U_{VB}) is needed to form the O* intermediates and they combine via thermal chemical reaction steps to form the oxygen molecule. It is evidenced by both the ability to extract an isotherm with pH for the O* population when $\Delta G_{O^*/OH^*}$ (U_{VB}) is exoergic, and the subsequent downhill decay pathway observed previously[37]. Furthermore, differences between $\Delta G_{O^*/OH^*}$ and ΔG_{OH^-} occur in K_{eff} as they would in a theoretical descriptor on the x-axis of a volcano plot.

In this context, we estimate the anticipated value of the K_{eff} above from theoretical calculations. While the experiments remain in the fairly dilute limit of 2% of O surface sites, we control the VB hole population separately from the $[Ti-OH^{-}]$ population through the laser pulse. Therefore, the degeneracy of holes should be accounted for in defining K_{OH^*}. How a geometrically diverse and interconverting O* population describes the overall O* population is not yet clear, and finally, not all holes need to arrive as O* through hydroxylated sites modulated by pH in basic conditions.

This work discovers a methodology for obtaining quasi-equilibrium constants of meta-stable surface intermediates of a catalytic reaction using Langmuir isotherms and time-resolved optical spectra of the intermediate population. We constructed an effective equilibrium constant of ΔG_{OH^-} and $\Delta G_{O^*/OH^*}$ that defines the reactive O* population for water oxidation to O_2. The results shown here make recent time resolved spectroscopic investigations of the water oxidation reaction germane by uniquely establishing a necessary connection to the free energy differences that are the theoretical descriptors. In this regard, the work finds experimental evidence to support where titania occurs on the x-axis of water oxidation volcano plots, which underpins titania as an electrocatalyst whose energy efficiency is limited by creating rather than removing bound O* intermediates (the weak-binding side). Namely, the applied potential (U_{VB}) provides the reorganizational energy ($\Delta G_{O^*/OH^*}$ (U_{VB}))—evidenced by the ability to extract an isotherm with pH—such that the reaction is then spontaneous. Finally, since the work discovers that combining photoexcitation with surface acidity effectively doubles the initial O* population and it lasts for nanosecond timescales, one could envision selecting for different downhill pathways of O_2 formation from O* by pH or re-directing the pH-modulated highly reactive population to form other products.

Transient optical spectra of the electrochemical interface extending to microsecond timescales.

The optical spectra from time-resolved experiments shown so far only extend to 4 ns at the longest. However, once the O* intermediate population has grown, it is expected to be metastable until the microsecond timescales. The intermediates however can still go through changes and conversions during this period of metastability. Previous work, using a narrowband probe centered at 400 nm, has observed dependencies of decay kinetics associated with O* intermediates on pH and ionic strength of the solution[37]. We aim to expand our understanding of O* intermediates beyond their formation and observe their eventual decay using a broadband WLC probe using time resolved TR pump probe spectroscopy on timescales that extend up to 500 microseconds. The longer timescale data when concatenated with the ultrafast timescale data taken in corresponding reaction

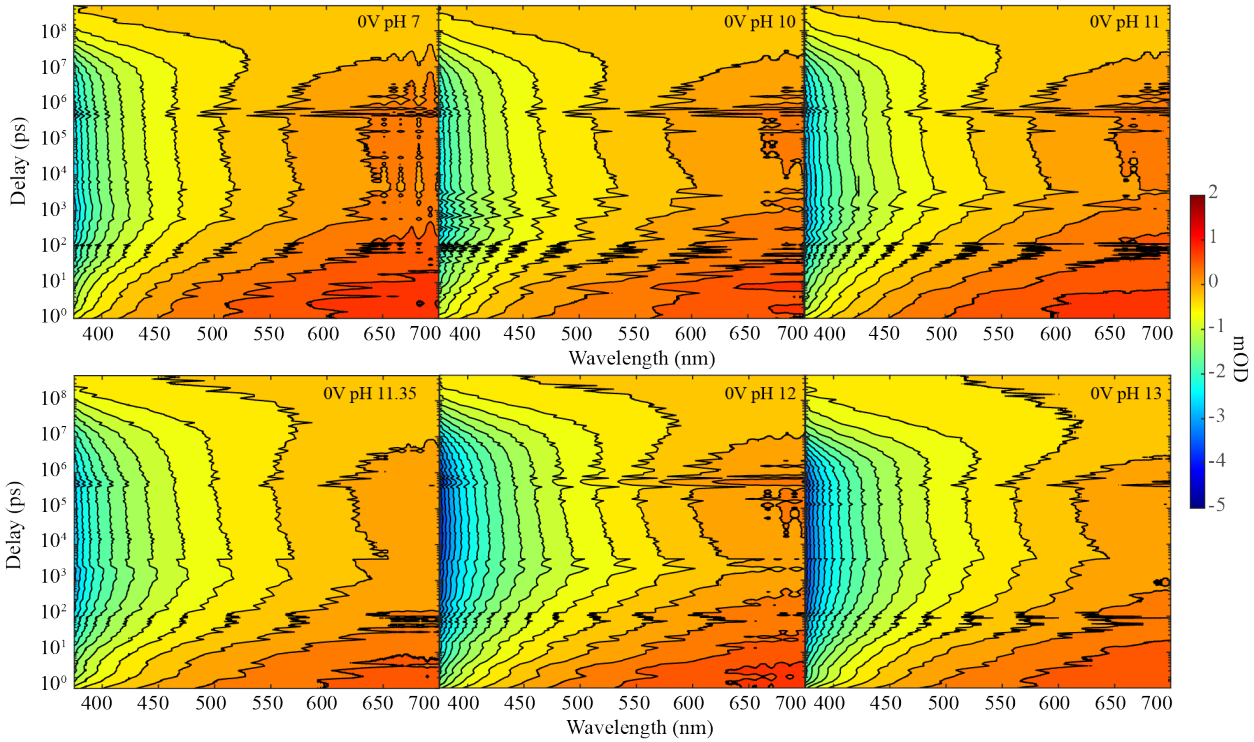

Figure 3.18: Concatenated optical maps of the absorption (red) and emission (blue) in the visible regime for select pH values, in phosphate buffer, in CC conditions.

conditions affords a comprehensive look at the OER from the perspective of optical spectroscopy. By varying pH and ionic strength of the solutions and correlating the kinetics of the ultrafast growth and longer timescale decay we hope to gain insight into the changes that the reactive intermediates might undergo during the period of metastability and eventually develop a full kinetic model for OER.

Figure 3.18 shows the concatenated pH dependent data for CC configuration, in a phosphate buffer similar to data in fig. 3.1. We see the same emissive signal previously assigned to O* intermediates. The absorptive signal is however less present on the longer timescale as the absorptive signal decays very fast (< 2 ns), as seen in the ultrafast data previously. We note that the emissive component stays stable once grown in and starts decaying on the microsecond timescales. The emissive signal increases in magnitude with pH, as seen previously. The data also suggests that the decay of the emissive signal is also pH dependent.

The concatenated contour maps shown in fig. 3.18 are acquired by performing 2 time resolved pump probe experiments. The experiment is with the ultrafast pump (pulse duration of ~400 fs) and gives us a maximum time delay of ~4 ns. The second experiment is conducted in the same conditions but using a separate pump source with a longer pump duration (~1 ns) but with a minimum time delay step size of 500 ps and the time delay range is from -1 ns to 500 μs. The 2 experiments have different temporal resolutions largely because of the difference in pulse duration of the pump sources. Since there are errors associated in the fluence of the two pump sources, kinetic traces in the common time delay range are compared across the two experiments and a scaling factor is applied to the entire longer timescale data set. Part of the longer timescale data set, until the maximum time delay of the ultrafast data set, is replaced by the ultrafast data set giving the concatenated data set. The detailed procedure of concatenation is present in the Appendix.

We were able to apply the spectrally constrained SVD methodology in a similar fashion to the data set in fig. 3.1. However, the concatenated pH dependent data set

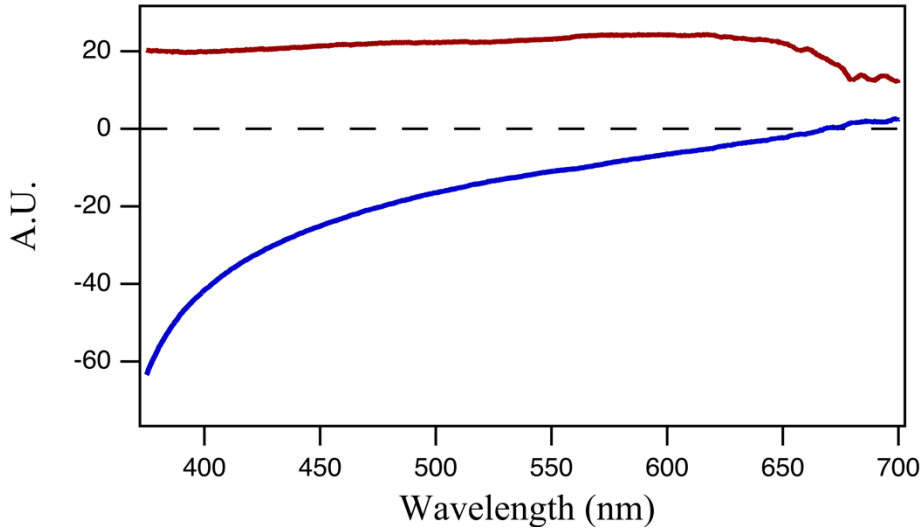

Figure 3.19: Emissive and absorptive spectral basis to constrain the SVD analysis of the concatenated pH dependent data set.

requires the derivation of a new spectral basis of completely absorptive and completely emissive vectors, as shown in fig. 3.19, but with a slightly altered shape compared to the basis vectors shown in fig. 3.5D. The updated spectral basis was made with the same considerations explained previously and uses the same procedure explained in "Spectrally constrained SVD" section of chapter 2. The constrained weighted emissive kinetics obtained were fit with the fit function, equation 14, and are shown in fig. 3.20. The growth part of the fit reaffirms the findings shown above, the decay part of the fit shows that there is bi-exponential decay with time constants in the range of ~8 μs and 60 μs.

$$\textbf{Emission:}\left(\mathbf{V}^{(t)}\right)^{T} = A_1^n\left(1 - e^{-\frac{t}{\tau_1^n}}\right) + A_2^n\left(1 - e^{-\frac{t}{\tau_2^n}}\right) + A_3^n e^{-\frac{t}{\tau_3^n}} + A_4^n e^{-\frac{t}{\tau_4^n}} + k\,; \qquad (27)$$

Where, $A_1^n, A_2^n, A_3^n, A_4^n > 0$

Currently analysis of the constrained weighted emissive kinetics is underway. We have seen that the decay of the intermediates is also bi-exponential, this is not entirely unexpected since the growth is also occurs bi-exponentially. Given that we

are interested in how the associated amplitudes of the growth and the same for the decay correlate with one another. The comprehensive perspective afforded by the concatenation and spectrally constrained SVD could inform us about the possible changes that the intermediate populations might undergo during the significant period of metastability and can possibly assist in the development of a full kinetic model for the oxygen evolution reaction.

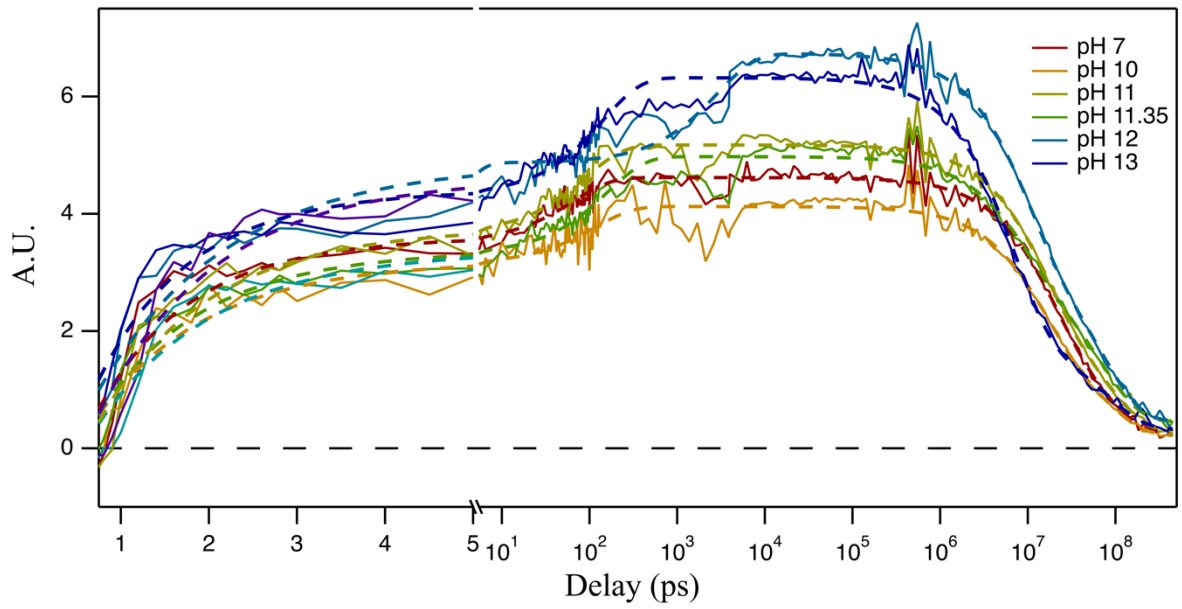

Figure 3.20: Constrained SVD analysis showing the constrained weighted emissive kinetics of the concatenated pH dependent data set.

CHAPTER IV

COHERENT ACOUSTIC INTERFEROMETRY DURING THE PHOTODRIVEN OXYGEN EVOLUTION REACTION ASSOCIATES STRAIN FIELDS WITH THE REACTIVE OXYGEN INTERMEDIATE (Ti-OH*)

Original Publication

This work has been previously published as Singh S, Lyle H, D'Amario L, Magnano E, Vinogradov I, Cuk T. Coherent Acoustic Interferometry during the Photodriven Oxygen Evolution Reaction Associates Strain Fields with the Reactive Oxygen Intermediate (Ti-OH*). J Am Chem Soc. 2021;143(39):15984-15997.

Introduction

Metastable intermediates guide the oxygen evolution reaction (OER) from water and are characterized by a series of electron and proton transfers from a metal-oxide surface[1,2,6]. Often, the first electron and proton transfer from a water adsorbed site is utilized to classify materials' catalytic activity for OER[3,10]. For example, a too strong or weak binding of oxygen to the metal site upon this electron and proton transfer correlates with lower catalytic activity[3], with strong binding implying that O−O bond formation rate limits the reaction and weak binding implying that creating the first intermediate does. While this reactive oxygen intermediate (M−OH*) is often compared energetically between materials[6] by DFT calculations with limited surface relaxation allowed[61], its structural form has only recently been elucidated in a series of in situ and time-resolved experiments using optical[21,25,36,48,49] and vibrational[5,22,31,32] spectroscopy. Significant distortions of the metal−oxygen bond in M−OH* are evidenced by, upon charge-trapping, a double bond on Fe_2O_3 (Fe=O)[32] and Co_3O_4 (Co=O)[31] and a lengthened Ti−O bond on STO[22]. This is not unanticipated by calculations of charge-trapping on surfaces of bulk semiconductors:[20,42,47] when charge traps in periodic lattices, lattice deformations form around the carrier to

create a "polaron" that then transports charge with the accompanying distortions. Hole-polarons are especially ubiquitous in 3d transition metal oxides[46] due to the susceptibility of the 3d M−O 2p octahedral bonding environment to local deformations such as the Jahn−Teller effect. These local deformations can define "active sites" for catalysis at surfaces. On the other hand, surfaces of transition metal oxides are associated with strain fields at the vacuum and liquid interfaces[62,63]. Strain engineering has been utilized to modify the ground state properties of these catalysts, especially within the perovskite families. In-plane compressive and tensile strains modify the adsorption energy of oxygen, the d-bandwidth, and oxygen diffusion,[62,64] with some associations to OER activity; bulk strain also modifies these properties[64]. Further, interfacial strain is invoked in describing catalysts' surface restructuring under potential or light driven conditions. In electrochemistry, Pourbaix diagrams define a surfaces' stability against pH and potential,[65-68] leading to new structural phases very close to the noted stable region of OER on the catalyst and metal leaching into the electrolyte. In recent solar-to-fuel devices, photodriven degradation often exacerbates the problem of finding an active and stable catalyst[69].

Such considerations of interfacial strain fields have largely been based on the catalyst composition in the ground state and its stability against a steady-state potential. However, given that M−OH* itself induces lattice distortions, measured populations are metastable, and the closeness of unstable oxide phases to OER[70], determining the interfacial strain invoked by the M−OH* coverage itself would be important to understanding materials design paradigms for both higher activity and enhanced stability. Here, we employ a mature optical technique, ultrafast coherent acoustic interferometry[71-77], to detect the interfacial strain engendered by Ti−OH* coverage on $SrTiO_3$ (0.1% Nb) during OER. As summarized in figure 4.1A, the optical technique works by first generating a laser triggered interfacial strain (usually

associated with heat or an electron−phonon deformation potential) which results in a propagating acoustic strain pulse into the bulk. The optical probe pulse scatters off this propagating strain pulse with the phase matching conditions of stimulated Brillouin scattering (SBS). The scattered and surface reflected probe beams interfere to generate coherent acoustic waves (CAWs) in the data, defined by the oscillation frequency, amplitude, and phase response as a function of optical wavelength (Figure 1B). We newly apply this technique to OER, utilizing methods established previously to photodriven OER at the $SrTiO_3$/aqueous interface[78] by an ultrafast light pulse. The coherent acoustic interferometry allows for completing the structural characterization of Ti−OH* on lightly doped $SrTiO_3$ (0.1% Nb), which arises from hole-trapping to the surface, as cartooned in Figure 4.1C. Previously, this intermediate had been characterized for the charge trapped through midgap electronic states probed by emission in the UV−visible regime[21] and for the symmetry of the lattice distortions by the appearance of new normal modes[22] (assigned to the terminal "oxyl" Ti−O*−) in the mid-infrared regime. Both the optical and mid-IR responses identified a 1.3 ps time scale for hole-trapping and Ti−OH* formation. The GHz-THz regime of acoustic waves now allows one to assign an interfacial strain to the Ti−OH* coverage achieved with a 0.04 mJ/cm2 excitation associated with ~2% of the surface sites. We apply a spectral analysis, further developed here, for detecting a combination of the spatial extent, magnitude, and generation time of the interfacial strain through especially the phase of the CAW. For STO, we identify the strain generation time (1.31 ± 0.02 ps) to occur simultaneously with Ti−OH* formation, and a tensile strain along the crystal direction of 0.06% (upper limit 0.6%). Below, this tensile strain, in which the c axis expands with respect to the in-plane axes, is associated with lattice deformation mechanisms of how polarons create a continuum strain. Altogether, the methods developed herein are quite general and could be

applied to differentiate photodriven transition metal oxide catalysts by the interfacial strain coincident with M–OH*, informing materials design paradigms for OER.

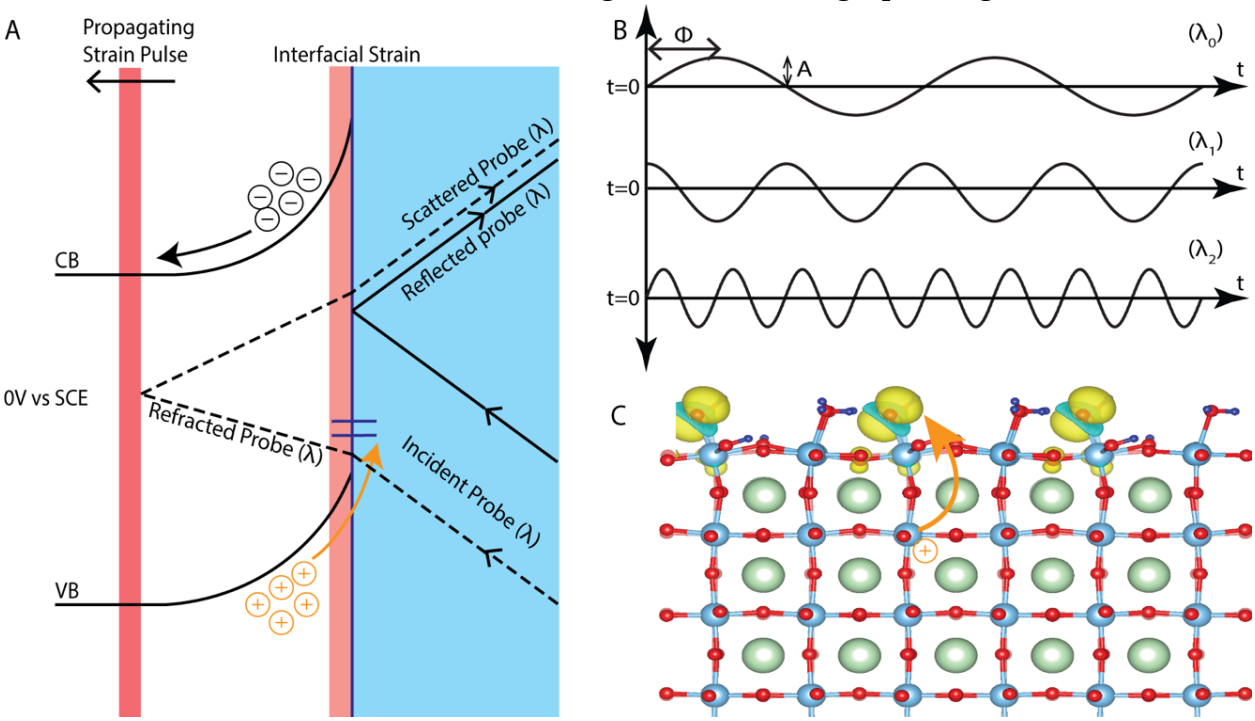

Figure 4.1. Overview of polaron-induced strain and detection of its propagating acoustic strain pulse. (A) Band gap excitation generates carriers, which separate due to the space-charge layer. Holes trap at the surface (panel C) and cause an interfacial strain. Ultrafast generation of the strain launches a propagating strain pulse into the bulk, which we detect as an interference pattern between the surface reflected probe and acoustically scattered probe. We refer to this interference pattern as coherent acoustic waves (CAWs). (B) As the pulse propagates into the bulk and the path length difference between the reflected and scattered probe increases, the CAWs oscillate in time with different frequencies for each optical wavelength (λ). These oscillations are characterized by their amplitude and phase. (C) Small hole-polaron or equivalently, Ti–OH* formation at the STO/water interface by hole-trapping.

Results

We performed picosecond white light transient reflectance (TR) spectroscopy on 0.1% Nb:$SrTiO_3$ (STO) under OC and CC conditions. For CC conditions at 0 V vs SCE, bandgap excitation with a ~400 fs 266 nm pump generated a photocurrent with >70% quantum efficiency (Figure S2B). Both OC and CC TR spectra contained prominent ~50–100 GHz oscillations that we attribute to CAWs. These oscillations are shown in Figure 4.2A. They are an additive contribution to the optical transitions (Figure 4.2A, phonon removed) which we have studied in a previous publication[30]. In the next three sections, we will extract the frequency, amplitude, and phase of these

oscillations and use them to link the CAWs in CC to interfacial strain generated by hole-trapping to create Ti–OH*. The OC condition will be used as a foil, in which the CAWs derive instead from high photocarrier populations. Furthermore, in the phase section, we develop a mathematical model of the CAWs as a function of optical wavelength and fit it to our experimental CAW phase to extract a ~1.3 ps strain formation time in CC and directly link an interfacial and uniaxial tensile strain to polaron formation. This quantitative model will also allow us to estimate the strain's magnitude and a lower bound to the strain's spatial extent, using both the CAW phase and amplitude.

CAWs Frequency

We extracted the wavelength dependent oscillation frequency, amplitude, and phase by fitting the TR kinetic traces for each wavelength to a sum of two growth exponentials, a decay exponential, and oscillatory components that models CAWs in STO and water (Figure 4.2B):

$$\Delta OD = G_{fast} + G_{slow} + D_1 + CAW_{STO} + CAW_{H2O}, \tag{28a}$$

$$G_i = -A_{G,i}\left(1 - \exp\left(-t/\tau_{G,i}\right)\right) \tag{28b}$$

$$D_i = A_{D,i}\exp\left(-t/\tau_{D,i}\right) \tag{28c}$$

$$CAW_i = A_{CAW,i}\exp\left(-t/\tau_{CAW,i}\right)\cos(\Omega_i t + \phi_i) \tag{28d}$$

The two growth exponentials in eq. 28 represent the growth of an emissive signal associated with hole trapping and the decay exponential is associated with the decay of the valance band hole population (described below)[21,22,69,78,79]. For hole trapping, we found that the average fast growth timescale was 1.2 ± 0.3 ps (Figure S6). The average slow growth timescale, which remains unassigned, was 31 ± 9 ps (Figure S6). The two CAW terms are associated with acoustic pulse propagation in STO and in the aqueous electrolyte (Figure S7). The ~5-10 GHz signal contribution

from the electrolyte is described in section S5. The wavelength dependent fit results for STO CAW frequency, amplitude, and phase are summarized in Figure 4.2C-E, respectively.

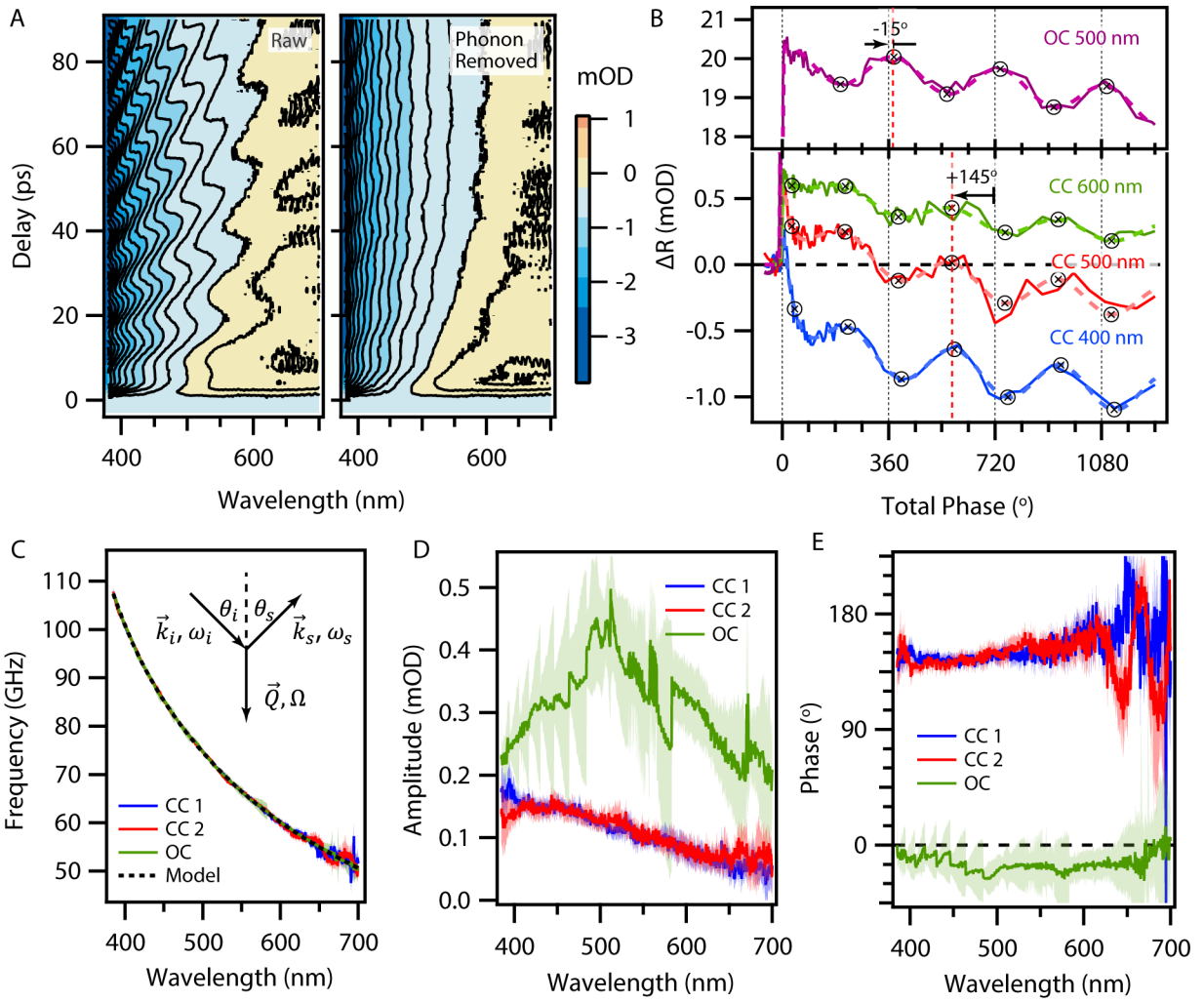

Figure 4.2. A) Example TR data with (left) and without (right) the CAW contribution. B) Equation 1 fit traces for select wavelengths for OC (top) and CC 2 (bottom) conditions. The x-axis is given in terms total phase, ϕ= ⟦Ω(λ)⟧ _STO t, to emphasize the phase shifts in the oscillations. The vertical red lines indicate the average phase shift, ϕ_STO. The crossed circles highlight the local minima and maxima of CAWs, CAW_STO. C) CAW frequency, ⟦Ω(λ)⟧ _STO/2π, as a function of probe wavelength as extracted by the fit via eq. 1. The inset shows the wavevectors for the SBS phase matching conditions. k⃗, ω, and θ represent the optical wavevector, frequency, and angle while the subscripts i and s represent incident and Stokes, respectively. Q⃗ and Ω are the longitudinal acoustic phonon wavevector and frequency. D) The CAW amplitude, A_(CAW, STO), as a function of wavelength for OC and two CC data sets as extracted by the fit via eq. 1. E) The CAW phase, ϕ_(STO), as a function of wavelength for OC and two CC data sets as extracted by the fit via eq. 1. For all panels, OC conditions were acquired at pH 13 with a pump fluence of 2.0 mJ/cm2 and CC conditions were acquired at pH 13 with a pump fluence of 0.04 mJ/cm2. The shaded regions of C, D, and E represent the standard error bounds from the least squares fit. For all panels, the raw TR data used to generate the CAW data in this figure is shown in Figure S3.

We found that the oscillation frequency as a function of probe wavelength matches the stimulated Brillouin scattering (SBS) phase matching condition almost exactly, as shown in Figure 4.2C, with a small error related to spectrometer calibration (Figure S8). The SBS phase matching condition is given by[70,76],

$$\frac{\Omega}{2\pi} = \frac{2vn}{\lambda}\cos\theta_i, \quad (29)$$

where λ is the probe vacuum wavelength, n(λ) is the real part of the index of refraction in 0.1% Nb:STO (Figure S9), v is the acoustic velocity in STO (calculated in Table 3),40 and θ_i (λ) is the incidence angle of the probe in STO as defined in the inset of Figure 4.2C. In addition, the CAWs in water also closely follows this relation (Figure S7), with the corresponding refractive index, acoustic velocity, and incidence angle. These close agreements indicate that the oscillatory signals are CAWs as detected by picosecond interferometry (as opposed to a resonantly enhanced mechanism[80,81], which does not follow the SBS phase matching conditions). For STO, the physical picture that follows is cartooned in Figure 4.1: the interference of the surface reflected probe and transmitted probe scattering from an acoustic strain pulse that propagates into the bulk of the sample[70,72]. This acoustic strain pulse is a direct result of ultrafast strain generation just below the STO surface, which describes uniaxial expansion (tensile strain) or contraction (compressive strain) of the STO lattice in a direction normal to the surface.

CAWs Amplitude

To gain more insight into the source of the interfacial strain, we correlated the CAW amplitude against the amplitudes of the fast emissive component and absorptive component while varying electrolyte pH for CC conditions and pump fluence for OC and CC conditions, as summarized in Figure 4.3. These amplitudes were extracted by performing a spectrally constrained singular value decomposition (SVD) analysis, which yields a single pair of kinetic traces for the absorptive and

emissive component (Figure S10). We fit the resulting kinetic traces to the exponential parts (G_{fast}, G_{slow}, and D_1) of eq. 28a to extract a condition-dependent absorptive amplitude which arises within the excitation pulse width (<400 fs) and a condition-dependent emissive amplitude which formed with a ~2 ps time constant (Figure S11). The advantage of this method is that it allows us to extract condition-dependent kinetic parameters rapidly and robustly from large data sets without the added complexity of fitting multiple probe wavelengths. We emphasize that the ~2 ps emissive component and <400 fs absorptive component is analogous to the amplitudes derived from the emissive rise and absorptive decay exponentials described in eq. 1. More detail is provided in the SI (section S9) and in previous publications[30].

Before proceeding, we will introduce the relevant differences between OC and CC conditions in our STO system, which are summarized in Figure S12. Briefly, under OC conditions with our range of pump fluence, interfacial dynamics are dominated by photocarrier recombination because the built-in potential at the STO/water interface flattens[25]. Similarly, the OC TR spectra are dominated by a decaying absorptive component that forms within the pump pulse duration, which we therefore associate with the photocarrier populations. In contrast, under CC conditions the built-in potential is maintained, causing the photocarriers to separate and to generate a photocurrent (Figure S2) [25]. In this process, the valance band holes are driven to the surface and trap as surface terminal and bridged oxyls, with the associated hole-polaron mid-gap states (Figure S12).[8] We have previously assigned the ~2 ps emissive component to the transition between the conduction band and the hole-trapped states to this Ti-OH* population[21].

Figure 4.3A and figure 4.3B show the most prominent features for varying pH in CC, where there is a stark difference in the CAWs amplitude spectra between neutral and basic pH. In Figure 4.3A, we show that the shape of the spectra within

this data sets is largely the same, indicating that the average CAW amplitude within a single data set (from 400 to 600 nm) can be reliably used to compare against the emissive and absorptive amplitudes. In Figure 4.3B, we show that the average CAW amplitude (red squares) tracks the sigmoidal shape of the ~2 ps emissive amplitude (blue circles) almost exactly. The sigmoidal dependence of the 2 ps population on pH was recently modelled by us using an adsorption reaction isotherm for the meta-stable Ti – OH* population[30]. Briefly, pH increases the surface hydroxylation which then shifts the equilibrium of the hole-trapping reaction on hydroxylated sites (reaction 16) towards the product, Ti – OH*. While simply stated, the model itself requires an extensive development. We simply quote the result here to correlate the CAW amplitude with increasing Ti – OH* surface coverage.

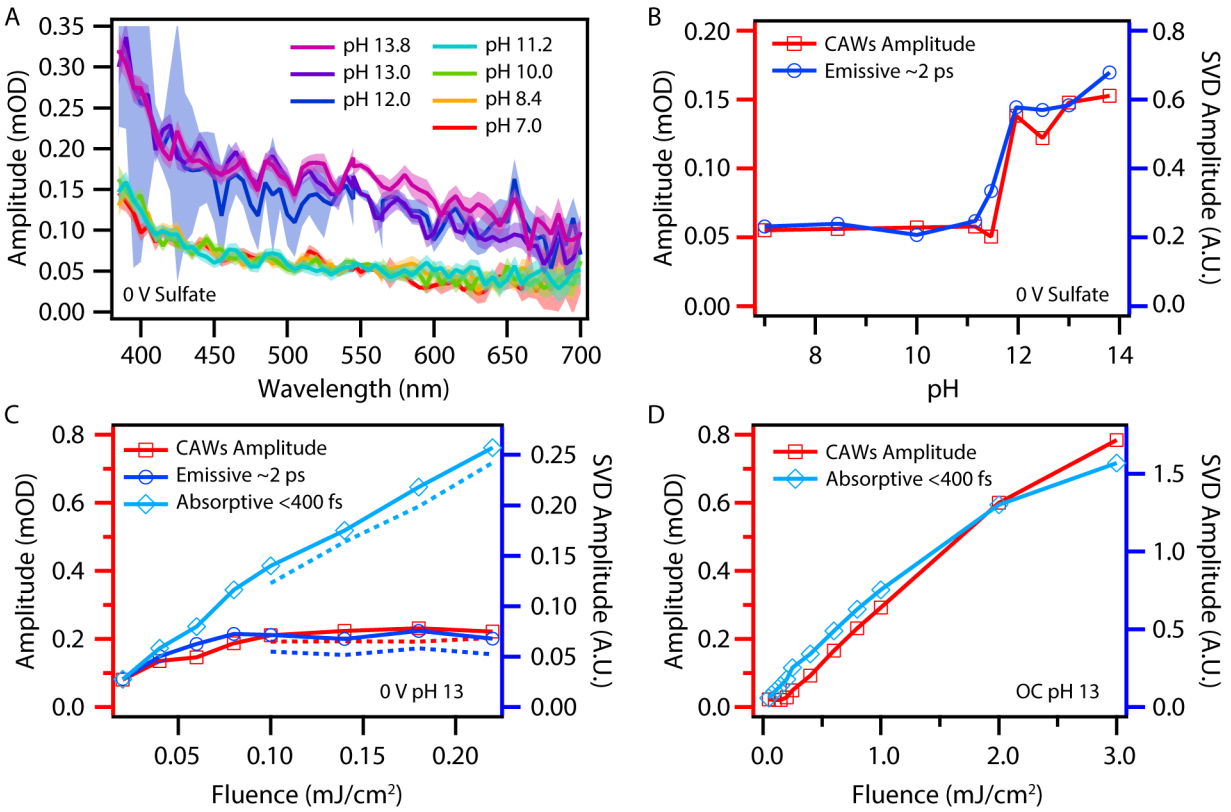

Figure 4.3: Correlating CC CAW amplitude to the ~2 ps emissive amplitude (polaron formation) and OC CAWs to the <400 fs absorptive amplitude (carrier population). A) The CAW amplitude spectrum, as extracted by eq. 28, for CC conditions for various pHs. B) The average CAW amplitude (red squares, left axis) for the data set in A correlated with the ~2 ps emissive amplitude (blue circles, right axis). C) Fluence dependance for CC in pH 13. Here, the CAW amplitude (red squares, left axis) correlates with the ~2 ps emissive amplitude (dark blue circles,

right axis), but not with the <400 fs absorptive amplitude (light blue diamonds, right axis). To show that the effects of surface degradation do not influence the correlation, the solid lines were acquired with a scan speed of 7 μm/s while the dashed lines were acquired at 28 μm/s (see section S5. for more detail). D) Fluence dependance for OC in pH 13 showing that the OC CAW amplitude (red squares, left axis) correlates with the <400 fs absorptive amplitude (light blue diamonds, right axis). For all panels, the ~2 ps emissive amplitude and <400 fs absorptive amplitude were extracted by fitting kinetic components from constrained SVD analysis (see section S10).

Further, when varying pump fluence, the correlation between the CAW amplitude and the emissive amplitude assigned to Ti – OH* is present only under CC conditions and not under OC conditions. As shown in Figure 4.3C, the CC CAW amplitude (red squares) and emissive amplitude (dark blue circles) both exhibit a saturation behavior as the pump fluence is increased, while the absorptive amplitude (light blue diamonds) grows linearly with fluence. In contrast, the OC CAW amplitude (Figure 4.3D, red squares) closely follows the nearly linear increase of the absorptive amplitude (light blue diamonds) and does not exhibit any saturation behavior for the wide range of fluences measured. Further, when normalized for fluence, the CAW signal is approximately 10 times stronger in CC as compared to OC within the CC linear regime. This can be seen by comparing the CC 0.2 mOD CAW amplitude at a fluence of 0.08 mJ/cm^2 in Figure 3C with the OC 0.2 mOD CAW amplitude in Figure 4.3D, which occurs at a fluence of 0.8 mJ/cm^2. That the CAW amplitude correlates with the pH dependence and saturation behavior of the ~2 ps emissive amplitude strongly attributes the CC generation to hole-polaron or Ti – OH* formation. On the other hand, the linear correlation of the CAW amplitude with fluence that patterns the absorptive amplitude, along with its less efficient excitation, attributes the strain formation in OC to high photo-carrier populations.

CAWs Phase Model

We now turn to the model of the CAW amplitude and phase spectra in terms of the sign, magnitude, spatial extent, and formation time of the interfacial strain that generates the propagating strain pulse. We then fit the model to our experimental CC CAW amplitude and phase spectra, which allows us to obtain a

uniaxial tensile strain that leads to c > a, extract a ~1.3 ps interfacial strain formation time, and estimate an interfacial strain magnitude with a lower bound spatial extent. This model will extend the phenomenological model initially developed by Thomsen, et al[71]. in the acoustic interferometry regime[82] by including a strain formation time and broadband response. In addition, we will primarily focus on the CAW phase spectrum because we found that the CAW amplitude spectrum was susceptible to systematic error related to our white light continuum mode quality. Note that a similar formation time vs. phase analysis has also been performed by Babilotte, et al[83].

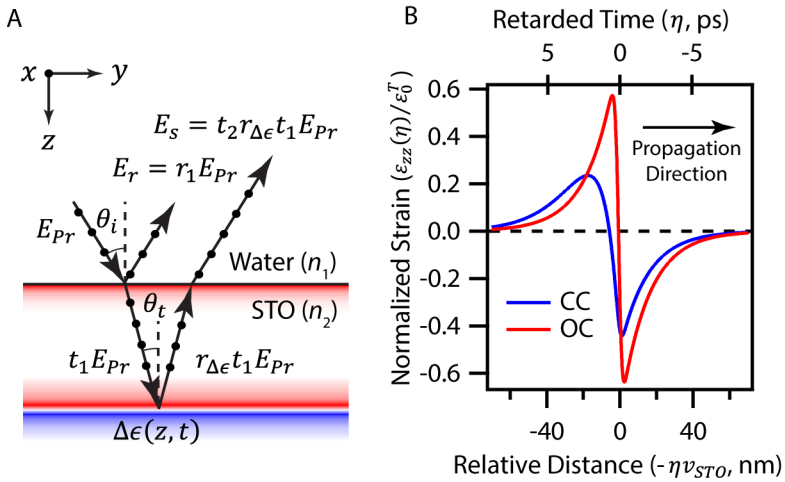

Figure 4.4: A) The reflectance, E/M part of the CAWs model: a diagram defining the coordinate system and symbols used to model the CAW interference signal and probe scattering from a change in permittivity, $\Delta\epsilon(z,t)$, caused by the acoustic strain pulse, ε_{zz}. B) The acoustic strain part of the model: the acoustic strain pulse, $\varepsilon_{zz}(\eta)$ in eq. 31, normalized to the transformation strain amplitude, ε_0^T, that generates it. For comparison, both CC and OC conditions were chosen to have a spatial extent of 15 nm and CC had a formation time of 1.2 ps, while OC had a formation time of 0.1 ps.

Below, we summarize the key features of the model, which are plotted in Figure 4.4. The theory of picosecond acoustic interferometry is typically partitioned into the detection and generation mechanism. In analogy, we have also partitioned Figure 4.4 into the reflectance, E/M part (A) and acoustic strain part (B), where figure 4.4A shows the generation of the CAW interference pattern in terms of the probe's electric

field and figure 4.4B shows the propagating acoustic pulse that scatters the probe. More detail is provided in the SI, along with the key assumptions used in the model.

For the reflectance, E/M part of the model, the signal that we detect is the interference between the surface reflected probe, E_r, and acoustic scattered probe, E_s, as summarized in figure 4.4A. This interference, $|E_r+E_s|^2$, leads to the CAW oscillations seen in our data and those sketched in figure 4.1B as the acoustic pulse propagates away from the surface. For small signals, the interference signal in the absorption convention[8] (an increase in reflectivity corresponds to a negative ΔOD value) is:

$$\Delta OD \approx \frac{2|r_1(\lambda)t_1(\lambda)t_2(\lambda)r_{\Delta\epsilon}(\lambda,t)|}{\ln(10)\,|r_1(\lambda)|^2}\cdot\cos\big(\phi_{total}(\lambda,t)\big) \tag{30a}$$

$$\phi_{\text{total}}(\lambda,t) = 180° - \phi_{r1}(\lambda) + \phi_{t1}(\lambda) + \phi_{t2}(\lambda) + \phi_{r\Delta\epsilon}(\lambda,t) \tag{30b}$$

Note that, in analogy to eq. 28, we have partitioned each complex coefficient in terms of its magnitude and phase and added the negative sign for the absorption convention into the phase as a factor of 180°. Here, $r_1(\lambda)$, $t_1(\lambda)$, and $t_2(\lambda)$ are the complex Fresnel coefficients for probe reflection at the surface, transmission into STO, and transmission out of STO, respectively. These coefficients are calculated from the complex index of refraction $\tilde{n}(\lambda) = n(\lambda) + i\kappa(\lambda)$ for water[84,85] and 0.1% Nb:STO (Figure S9)[25].

The remaining term, $r_{\Delta\epsilon}(\lambda,t)$, is the probe reflection coefficient from the propagating acoustic strain pulse. In the limit that the acoustic pulse has completely left the surface, the reflection coefficient can be written in terms of the acoustic frequency domain spectrum, $\tilde{\varepsilon}_{zz}\big(\Omega(\lambda)\big)$. Here, $\tilde{\varepsilon}_{zz}\big(\Omega(\lambda)\big)$ is the Fourier transform of the time-domain acoustic strain pulse, $\varepsilon_{zz}(\eta)$ with $\eta = t - z/v_{STO}$ (shown in Figure 4.4B), in the absence of any acoustic damping mechanism. With these approximations, and

for s-polarized light (E-field in x) propagating in the yz-plane with an incidence angle of θ_t, the 1st order scattering coefficient is:[86]

$$r_{\Delta\epsilon}(\lambda,t) = \frac{i\pi v_{STO}}{\lambda\tilde{n}(\lambda)\cos(\theta_t)}\frac{\Delta\epsilon_{xx}(\lambda)}{\Delta\varepsilon_{zz}}\tilde{\varepsilon}_{zz}\big(\Omega(\lambda)\big)e^{i\Omega(\lambda)t}, \qquad 31$$

where, assuming an isotropic crystal and uniaxial strain, $\Delta\epsilon_{xx}(\lambda)/\Delta\tilde{\varepsilon}_{zz}(\lambda) = \epsilon_{xx}(\lambda)p_{xxzz}(\lambda)\epsilon_{xx}(\lambda)$ is elasto-optic contribution and $p_{xxzz}(\lambda)$ is the relevant elasto-optic tensor element.

The second half of the theory is the strain generation mechanism, which models the interfacial strain and its resulting acoustic pulse, $\varepsilon_{zz}(\eta)$ (Figure 4.4B). We follow the setup of the problem given by Bushnell and McCloskey[87]. Briefly, the model is composed of two linear-elastic half-spaces which represent the water and STO interface. The main input parameter for this model is the isotropic transformation strain, or eigenstrain[88], ε_{zz}^{T} in eq. 32 below. The transformation strain describes the spatial and temporal dependance of how the lattice transforms (expands or contracts) under conditions of stress-free volume expansion, in analogy to thermal expansion or chemical expansivity[89]. Because our pump diameter (>200 μm), which determines the spatial extent of the strain in the xy-plane, is much larger than the spatial extent of the strain in the z-direction (discussed below) and acoustic pulse propagation distance (<8 μm) that we analyze, we expect all strain components except the zz-component to be negligible. Note that this does not mean that the strain generating process (transformation strain) cannot produce strain along the xx- and yy-components, it instead means that our experimental configuration (flat surface, large uniform excitation area, small strain depth) limits the generated strain to the zz-component. Therefore, we assume translational symmetry in the in-plane coordinates (x and y) and approximate our strain as uniaxial, which reduces the problem to one dimension along z.

We model the transformation strain as:

$$\varepsilon_{zz}^{T}(z,t) = \varepsilon_0^T S(z/\xi)(G(t/t_0) * P(t/\sigma)/\sigma), \quad 32a$$

$$S(x) = \theta(x)e^{-x}, \quad 32b$$

$$G(x) = \int_{-\infty}^{x} g(y)dy = \theta(x)(1-e^{-x}), \quad 32c$$

$$P(x) = (2\pi)^{-1/2} e^{-\frac{x^2}{2}}, \quad 32d$$

where * represents convolution over t, ε_0^T is the strain magnitude, ξ is the spatial extent, t_0 is the strain formation time, σ is the pump intensity duration, and $\theta(x)$ is the Heaviside step function. Equation 32b represents the spatial dependance of the transformation strain along the z-axis, which we assumed to be an exponential decay. Equation 32c represents the transformation strain's temporal dependence, which we set to be a 1st order exponential growth process. Note that this equation is explicitly written as an integral because the solution for the strain, eq. 33, will eventually be written in terms of the growth rate, $g(y)$. Finally, we include finite pump-pulse effects by convolving eq. 32c with the pump-pulse intensity profile in eq. 32d. We took the FWHM pulse duration to be 0.4 ps.

Table 3: Constants, at room temperature, used for the CAW model.

Quantity	Value
Lattice Constant (STO)[40]	0.3904 nm
Density[α, 51]	$\rho_{STO} = 5.12$ g/cm^3 $\rho_{H2O} = 0.998$ g/cm^3
Acoustic Velocity[β, 52]	$v_{STO} = 7.86$ nm/ps $v_{H2O} = 1.49$ nm/ps
Bulk Modulus[40]	$B_{\mathrm{STO}} = 170.57$ GPa
Shear Modulus[40]	$G_{\mathrm{STO}} = 108.46$ GPa
Poisson's Ratio (STO)[40]	$\upsilon = 0.277$
Thermal Expansion Coeff. (STO)[53]	$\alpha_V = 3.23\times10^{-5}$ K^{-1}
Volumetric Heat Capacity (STO)[53]	$C_p = 2.730$ J/(cm^{3}K)
Elasto-Optic Coefficient (STO)[54]	$p_{1122} = 0.095$ at 633 nm
Acoustic Reflection Coefficient[γ]	$R = 0.928$

[α] Calculated from the lattice constant and molar mass of STO.

ß Compressive acoustic velocity calculated from the elastic moduli and density of STO.

ɣ Calculated[87] from the densities and acoustic velocities of STO and water.

Given the transformation strain in eq. 32, the acoustic frequency domain solution for the propagating strain pulse is given by:

$$\tilde{\varepsilon}_{zz}\big(\Omega(\lambda)\big) = -\frac{3B_{\mathrm{STO}}\varepsilon_0^T\xi}{2v_{STO}^3\rho_{STO}}\tilde{T}\left(\frac{\xi\Omega(\lambda)}{v_{STO}}\right)\tilde{g}\big(t_0\Omega(\lambda)\big)\tilde{P}\big(\sigma\Omega(\lambda)\big), \qquad 33$$

where the constants are summarized in Table and where the functional forms of the Fourier transforms, $\tilde{T}(\omega)$, $\tilde{g}(\omega)$, and $\tilde{P}(\omega)$, are given in eq. S34 and the phases of $\tilde{T}(\xi\Omega(\lambda)/v_{STO})$ for various values of ξ and $\tilde{g}\big(t_0\Omega(\lambda)\big)$ for various values of t_0 are plotted in S14. $\tilde{T}(\xi\Omega(\lambda)/v_{STO})$ is defined by the Fourier transform of $T(\eta\, v_{STO}/\xi) = h(\eta)S(|\eta|\, v_{STO}/\xi)$, where $\eta = t - z/v_{STO}$ and where we have dropped the pre-factors associated with Fourier scaling for clarity. Here, $h(\eta)$ is a step function such that $h(\eta < 0) = 1$ and $h(\eta > 0) = -R$ and where R is the STO/water acoustic amplitude reflection coefficient. $S(|\eta|\, v_{STO}/\xi)$ derives from the exponentially decaying spatial dependence of the interfacial strain (eq. 32b) and its reflection from the interface as it gets generated, while $h(\eta)$ accounts for the sign flip of the strain during reflection and its partial transmission into water. Together, $T(\eta\, v_{STO}/\xi)$ spatiotemporally describes the acoustic pulse propagating into the bulk that results from an instantaneously generated interfacial strain ($t_0 = 0$). We therefore call $T(\eta\, v_{STO}/\xi)$ and its Fourier transform, $\tilde{T}(\xi\Omega(\lambda)/v_{STO})$, the spatial part of the strain. However, Figure 4.4B graphs the full $\varepsilon_{zz}(\eta)$, which represents the acoustic propagating pulse in figure 4.1A for a given strain growth rate and spatial extent. Since the strain is instantaneously generated in the OC condition (as described below), $T(\eta\, v_{STO}/\xi)$ directly leads to the OC pulse shape shown in figure 4.4B for a given spatial extent, ξ, of the interfacial strain. The second term in eq. 33, $\tilde{g}\big(t_0\Omega(\lambda)\big)$, is the Fourier

transform of $g(\eta/t_0)$, the transformation strain's growth rate, which we will call the temporal function. For the exponential growth in eq. 32c, $g(\eta/t_0)$ is a one-sided exponential decay. In the spatiotemporal domain, eq. S33, a finite growth rate smears the spatial function, $T(\eta\, v_{STO}/\xi)$, (as a convolution) to give a pulse that resembles the CC pulse shape in figure 4.4B. Finally, the third term is the normalized pump intensity profile and is a symmetric function that does not contribute a net phase to the total CAW phase (eq. 30b).

Using the acoustic frequency domain solution for the propagating strain pulse, $\tilde{\varepsilon}_{zz}\big(\Omega(\lambda)\big)$, eq. 33, figure 4.5A shows how the model's average (400-700 nm) total phase ($\phi_{\text{total}}(\lambda, t)$, eq. 30b) varies as a function of formation time for different spatial extents. In this figure, there are two important implications on the scope of conclusions which we can draw from fitting the model to our phase data. The first and more important implication is that the total CAW phase is sensitive to small spatial extents and fast formation times but is insensitive to large spatial extents and slow formation times. This conclusion arises because the phases of the spatial and temporal functions that determine $\phi_{r\Delta\epsilon}(\lambda, t)$ in eq. 30b have asymptotic relationships with spatial extent (ξ) and formation time (t_0). This is most clearly shown in figure 4.5A: as the spatial extent approaches and exceeds 5 nm, the curves converge to the 15 nm curve, thereby decreasing the model's phase sensitivity to large spatial extents. Similarly, the slope magnitude of any individual curve decreases with larger formation time, indicating that the model becomes insensitive to formation times greater than ~15 ps. Therefore, when parameterized for STO, our model can reliably extract spatial extents of less than ~5 nm and formation times of less than ~15 ps.

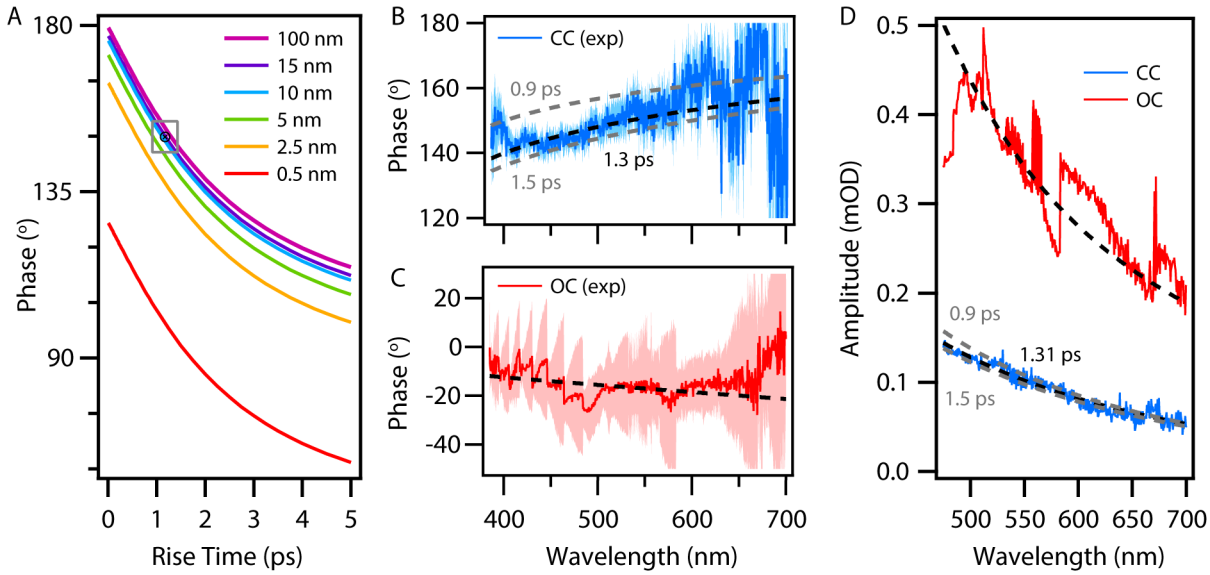

Figure 4.5: A) The dependance of the average phase (averaged from 375 to 700 nm) on the strain's formation time and spatial extent. The slope of each curve indicates the CAW model's sensitivity to the strain's growth rate. The box shows the average phase of the 1.31 ps fit in panel B and the standard deviation of its residuals, 150 ± 4°, and the formation time constrained to be within the emissive growth rate, $\langle \tau_{G,fast} \rangle_\lambda = 1.2 \pm 0.3$ ps as fit by eq. 28 (Figure S6). B) The CAW model's best fit (black dashed line, 1.31 ± 0.03 ps, 100 ± 195 nm) for the CC CAW phase spectrum. To give a sense of our model's error bounds, we also show formation times of 0.9 ps and 1.5 ps, both at 100 nm, in panel B as grey dashed lines. These bounds correspond to the upper left and lower right corner of the box in panel A. C) The CAW model's best fit (black dashed line) to the OC CAW phase spectrum. D) OC (red) and CC (blue) best fit curves for the CAW amplitude spectrum with spatial extent and formation time constrained to the best fits in B and C. In analogy to panel B, for CC we show the effect of formation time on the CAW amplitude spectrum while keeping the strain amplitude at 0.02% and spatial extent at 100 nm. For all panels, the CC data is an average of the figure 4.2**Error! Reference source not found.** results for CC 1 and CC 2. In addition, the x -axis range shows the model fit range of the data and shaded regions show the standard error weights used to fit the phase.

The second implication is that the spatial and temporal phase contributions are additive toward the total phase. This can be seen in figure 4.5A, where the phase vs. formation time curves have the same shape but differ by a vertical offset, which is the phase contribution from the spatial extent. The implication is that for a single probe wavelength, one would not be able to simultaneously extract both a spatial extent and formation time because a single total phase value cannot uniquely determine a pair of additive phases. Fortunately, we have used a broadband version of picosecond acoustic interferometry[77] and acquired a full octave of acoustic bandwidth, where a tilt is clearly present in the CC phase spectrum in figure 4.5B. Because opposite tilts are present in the individual spatial and temporal phase

contributions (Figure S5A), the tilt provides the additional information required to uniquely determine the spatial extent and formation time without constraining one or the other.

With these implications in mind, we performed a weighted least-squares fit of eq. 30b on the CC and OC CAW phase data shown in Figure 4.4B and Figure 4.4C, respectively, with the spatial extent (ξ) and formation time (t_0) as the only free parameters. Both panels show the best fit curves with black dashed lines. For CC, the best fit corresponded to a tensile strain with a formation time of 1.31 ± 0.03 ps and a spatial extent that converged at the 100 ± 195 nm upper bound. For OC, we were unable to get a reliable fit because of the spatial and temporal phases' additive property combined with the larger spread in the OC data. The best fit corresponded to a compressive strain with a formation time that converged at the 0 ps lower bound and a spatial extent of 6 nm with standard error of 1.5×10^4 nm. From this, we can only conclude that the OC strain forms within the pump pulse duration. Note that the uncertainties we report are linearized standard errors and are unlikely to be accurate estimates of the true standard error, especially for the spatial extents because of its asymptotic relationship with phase. Nevertheless, the order of magnitudes of the standard errors strongly suggest that the extracted CC strain formation time is robust. More importantly, our model independently extracts the strain formation time, and this formation time is in quantitative agreement with the fast emissive growth rate as fit by eq. 28 (Figure S6).

Although we could not provide a quantitative estimate for the strain's spatial extent, we can estimate a lower bound by assuming that the strain formation time is the same as the fast emissive rise time as extracted by eq. 28. In Figure 4.5A, we used the exponential fits to the CC fast emissive rise time (Figure S6) to constrain the CC phase to a grey box (1.2 ± 0.3 ps, 150 ± 4°), where the CC average phase was calculated

from the average phase of the 1.31 ps fit and the bounds represent the standard deviation of the residuals. The corners of this box estimate the uncertainty in the spatial extent when using an independent measure of the interfacial strain's formation time from the fast emissive fit in eq. 28. To connect this box to the CAW phase spectrum, we plot in Figure 4.4B the model phase curves for a 0.9 ps formation time with 100 nm spatial extent and a 1.5 ps formation time with 100 nm spatial extent, which represent the upper left and lower right corners on the box, respectively. This gives a visual understanding of the fit quality of the 1.31 ps best fit phase curve, which is the target in the center of the box. In addition, we provide several other best fit curves with various constrained spatial extents in figure S15B. When we constrained the formation time to 1.2 ps in the model, we found the best fit spatial extent to be 12 nm. The lower left corner of the box represents a lower bound estimate for the spatial extent, which we found to be 3.4 nm when we constrained the formation time to 0.9 ps. Visually, this lower bound represents a reasonable lower bound error based on the tilt shown by the black dashed curve in figure S15B. In addition, in figure S15A, we have generated curves to show how the best fit spatial extent varies asymptotically with different constrained formation times ranging from 0.9 to 1.33 ps, which demonstrates why we cannot assign an upper bound to the spatial extent through this model.

To find the strain magnitudes, we turn to the CAW amplitude spectra shown in Figure 4.5D. Because the relationship between the strain magnitude and CAW amplitude depends on both the formation time and spatial extent, we constrained the spatial extents and formation times with the values described above and had the strain magnitude as a free parameter. For pH 13, CC at 0.04 mJ/cm^2, the best fit strain magnitude was 0.06% for 1.2 ps and 12 nm. We estimate an upper bound for this strain to be 0.6% for 0.9 ps and 3.4 nm and an asymptotic lower bound of 0.02%

for 1.31 ps and 100 nm. The dependance of strain magnitude on spatial extent is summarized in figure S15A. Note that the CAW amplitude spectra is fit to eq. 30a and includes a model for elasto-optic dispersion, $\Delta\epsilon_{xx}(\lambda)/\Delta\varepsilon_{zz}$, which is defined in eqs. S17 and S18[90]. Figure S15C shows that the shape of the amplitude spectrum is insensitive to the spatial extent and formation time and is largely determined by this elasto-optic dispersion (Figure S13).

For pH 13 OC at 2.0 mJ/cm^2, we used the pump intensity penetration depth of 15.5 nm (Figure S9B) and formation time of 0 ps to find a strain magnitude of 0.14%. To compare the strain magnitude between OC and CC, we must normalize for the fluence. For OC this yields a strain of 0.07% per mJ/cm^2 and for CC a strain of 1.5% per mJ/cm^2 for the 12 nm estimate. As a comparison, thermal expansion would create a tensile strain magnitude of 0.08% per mJ/cm^2 with a 15.5 nm pump penetration depth (see section S15)[91]. Note that the magnitude agreement between OC strain and thermal strain is coincidental because thermal strain is tensile while our results indicate that OC strain is compressive. This sign difference suggests that the OC strain generation mechanism is related to, but not limited to, carrier deformation coupling[73,74] and is caused by large changes in carrier densities. Finally, this comparison indicates that the CC strain magnitude is unusually strong, with a fluence normalized strain that is ~20 times stronger than routine pump-induced processes, such as thermal expansion.

Discussion

As summarized in Figure 4.6A, in CC we have tensile strain that forms with a 1.31 ps time constant and an estimated a lower bound spatial extent of the strain to be 3.4 nm. The tensile strain magnitude has a range between 0.02% to 0.6%, with a best fit magnitude of 0.06%. We assign this strain to hole-polaron trapping at the surface because of the strong correlations present for the formation time and

amplitude. For OC, the strain was compressive, formed within the pump pulse duration, and correlated with the carrier population; we therefore assign it to carrier deformation coupling[73,74]. The remainder of the discussion will concentrate on the CC strain. We first place the strain found in the CC conditions in the context of strain engineering, based on its upper bound and that it is tensile. We next consider the generation mechanisms by which hole-polarons could induce a similar interfacial strain. Finally, we discuss the possible origins of the 1.31 ps formation time.

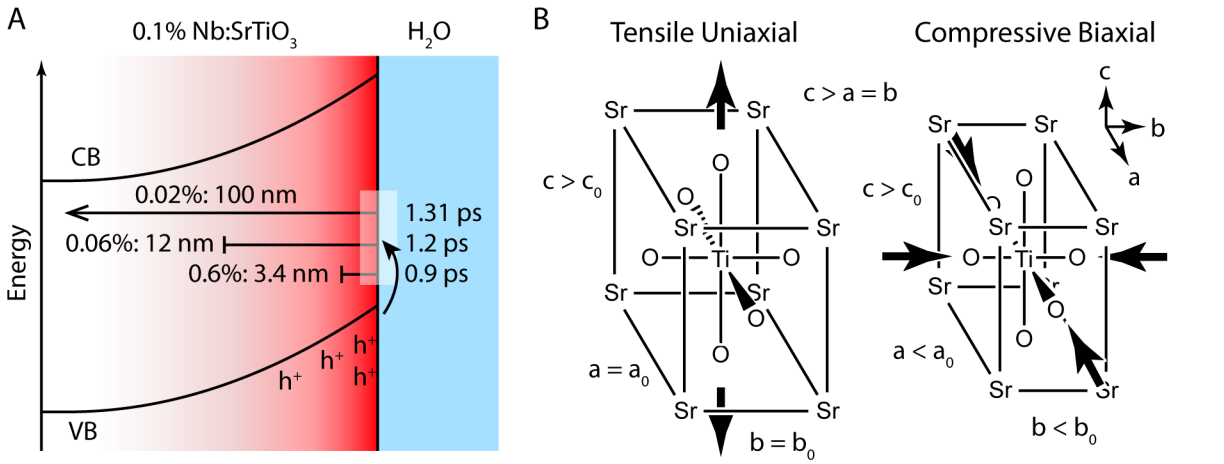

Figure 4.6: A) Graphical summary of the CC strain magnitudes, spatial extents, and formation times, as fit and estimated by the CAWs model. The red gradient represents the decay of the interfacial strain. The transparent white box indicates the mid-gap states. As a comparison, the pump intensity penetration depth is 15.5 nm and the depletion width is ~25 nm.[9] B) A comparison of how the TiO_6 octahedra are distorted under tensile uniaxial and out-of-plane strain (left, our work) and compressive biaxial and in-plane strain (right, strain engineering via lattice mismatch).[56] The arrows indicate the direction of expansion and contraction. Although the volume of the unit cell changes, in both cases the strained crystal *c*-axis is larger than the *a*- and *b*-axis.

The 0.6% upper bound tensile strain is similar in magnitude to strains generated in the field of strain engineering by lattice mismatch in epitaxial thin films[62]. For epitaxial thin films, the strain is typically biaxial and in-plane, whereas in this work the strain is uniaxial and out-of-plane. The two types of strain can be compared by the unit cell's tetragonality[92], which measures the ratio of the unit cell's *c*- (out-of-plane) to *a*- and *b*-axis (in-plane). This is possible because strain introduces Jahn-Teller like distortions to the TiO_6 octahedra, which leads to e_g orbital splitting

into $d_{x^2-y^2}$ and d_{z^2} orbitals, whose energy ordering depends on the magnitude of tetragonality, and modifies Ti 3d orbital filling[92]. As shown in figure 4.6B, our tensile out-of-plane strain correlates with compressive in-plane strain ($c > a$).

While in strain engineering the lattice mismatch to the substrate is encoded in the growth, strain generation mechanisms of surface hole-polarons exist that could give rise to a continuum, tensile strain of a similar magnitude. In the classic Fröhlich (large polaron)[93] and Holstein (small polaron)[94] descriptions, charge trapping is facilitated by optical phonons[95], which do not change the unit cell size and therefore does not directly induce strain. For polarons to induce strain, there must be coupling to acoustic phonons, either through electron-acoustic phonon coupling[96-98] or through optical-acoustic phonon coupling[75]. Two mechanisms exist for the electron-phonon case in particular: through the deformation potential to form an acoustic polaron[96], and through the piezoelectric effect to form a piezoelectric polaron[97]. One possibility for coupling through the deformation potential can be seen through a molecular orbital picture: hole trapping in the valance band, which is mostly of O2p character, reduces the Ti-O bond order and therefore increases the bond length to cause tensile strain. For the piezoelectric coupling, piezoelectricity is normally symmetry forbidden in room temperature STO because it is centrosymmetric, but the recent discovery of a surface piezoelectric effect induced by interfacial electric fields (i.e. electrostriction)[98] and surface relaxation[99] indicates that such an effect is present, possibly to a large extent, at the STO/water interface. It is also worth noting that such a surface piezoelectric effect has been associated with perovskite octahedra rotation[100], which could reduce the effects of strain on OER activity[63].

Other than deformations directly associated with the hole polaron[101], changes in free carrier concentrations can also contribute to interfacial strain. Under CC conditions, valance band holes are the dominant free carrier near the surface because

of the maintained Schottky barrier and resulting electron drift away from the surface (Figure S12)[25]. Under these conditions, the most likely mechanisms for free carrier strain generation are either through carrier deformation coupling[73,74] or through an inverse-piezoelectric effect[83] caused by valance band hole accumulation near the surface and the aforementioned surface piezoelectric effect[99]. We speculate that, if valance band holes do significantly contribute to the strain, it would be dominated by the inverse-piezoelectric effect because carrier deformation coupling is likely weak, as shown by the comparatively weak OC strain. While the above mechanisms are possible, we emphasize that the strong correlation of strain with the hole-polaron population suggests that polaronic distortion is the primary driver.

We now turn to the effects of our interfacial strain on OER catalysis and surface degradation. For OER/ORR catalysis, perovskite strain engineering typically uses a descriptor approach to correlate strain with oxygen adsorbate binding energies[62,64,102,103]. This, combined with the universal scaling relations, can correlate strain with OER activity[3,104]. One such descriptor uses e_g orbital filling to predict the surface metal-oxygen bond strength[62,92,102,105,106]. The rationale behind this descriptor is that the e_g orbital is spatially overlapped with oxygen adsorbate p orbitals[102,105]. When mixed, the partially filled e_g orbital donates its electrons to the resulting metal-oxygen anti-binding sigma-type orbital, which weakens the M-O bond with greater e_g filling[92,102,105,106]. Introducing strain splits the e_g orbital further into the $d_{x^2-y^2}$ and d_{z^2} orbitals, of which the d_{z^2} orbital is overlapped with the adsorbate p-orbital[92,102,105,106]. Our tensile out-of-plane strain, which we argue is equivalent to compressive in-plane strain, lowers the d_{z^2} energy, thereby increasing d_{z^2} filling and weakening the surface M-O bond.

The effects of a weaker M−O bond on OER activity will depend on the potential-limiting step (defined here by the free energy differences between intermediates) in

the catalytic cycle. Assuming a single site OER mechanism, the universal scaling relations subdivide catalysts into "weak-binding" vs "strong-binding", where the designation depends on the potential-limiting step: weak-binding catalysts are limited by the first or second electron transfer step, whereas strong binding catalysts are limited by the third or fourth electron transfer step[3,19]. STO falls under the weak-binding designation, where the first electron transfer step is potential-limiting[19,30,104]. Our system specifically has a fully hydrated or hydroxylated surface depending on pH. Therefore, we define this step as the transfer of an electron from the surface hydroxyl group into the valence band O 2p states: $\Delta G1$, $Ti{-}OH_2 \rightarrow Ti{-}OH^* + H^+ + e^-$, which we normally think of as a hole transfer from the valence band to the surface hydroxyl groups[30].

While the e_g descriptor above is useful for a large selection of perovskite catalysts, STO and other ABO_3 perovskites with d0 electronic configurations in the B-atom are exceptions to the e_g descriptor described above in the sense that the e_g descriptor predicts that these catalysts will be strong-binding, while DFT calculations indicate that these catalysts are weak-binding[104,107]. On a high level, this can be explained by the fact that the Ti–O bond in titania surfaces does not have any antibonding electrons. Therefore, prior to introducing a strain, removing a bonding electron from the Ti–O bond will reduce the bond order and weaken it (positive ΔG_1). Since Ti^{4+} and O^{2-} are in their noble gas electronic configurations, removing the electron for the first electron transfer step is expected to be energetically costly[107]. Analogously, if antibonding electrons occupy the surface M–O bond, removing an antibonding electron should increase the bond order and strengthen it (negative ΔG_1). A lengthened Ti–O bond by compressive in-plane strain of a d0 electronic configuration could introduce such antibonding electrons. However, DFT calculations for STO show that the oxygen dissociative adsorption energy increases for

compressive in-plane strains of up to 2.5%, thereby identifying a weaker oxygen dissociation on a lengthened Ti–O bond[64]. This calculation suggests that our tensile out-of-plane strain would reduce the catalytic activity of $SrTiO_3$, an already weak-binding catalyst.

There are two important caveats for this prediction. For the first caveat, oxygen binding strength may not directly correlate with electroadsorption energies (e.g., ΔG_1). Experimental results on $SrIrO_3$ suggests that, while compressive in-plane strain does weaken oxygen binding strength, its effect on catalytic activity may be diminished because the oxygen binding energy does not directly translate to the oxygen electroadsorption energy and OER activity, contrary to what is suggested by gas-phase DFT studies[63]. The authors show that this is likely caused by the exclusion of surface water interactions in gas-phase DFT studies[63]. Nevertheless, the universal scaling relations, which correlate the electroadsorption energies of the different intermediates, have been shown experimentally to still hold[108,109]. Finally, for the second caveat, the amount of strain depends on the number of holes trapped on the surface. Therefore, the lowering of catalytic activity is likely only relevant under highly driven conditions, such as the ultrafast band gap photoexcitation used in this study.

This descriptor approach has also been used to correlate strain with perovskite ABO_3 A- and B-atom vacancy formation energies, which have implications for surface degradation and amorphization[67,70]. These trends are important because strain may facilitate the surface degradation present in our experiment (Figure S5). Note that surface degradation is also thought of as a kinetically hindered phase transition to a different region on a Pourbaix diagram induced by hole accumulation near the surface[65,69].

Finally, the most striking result from this work is the quantitative agreement between the 1.3 ps CC strain and fast emissive growth rate. Previous work has established that the emissive component is a spectroscopic signature of holepolaron formation at the surface (as a terminal or bridged oxyl species) and, at 0.04 mJ/cm2, occurs with a 1.3 ps time constant[21]. This time constant is also characteristic of the formation of an infrared active subsurface vibration, which is caused by lattice distortions associated with the terminal oxyl[22]. The CAW identification of the 1.3 ps time constant extends the characterization of hole-polaron formation to the GHz, acoustic domain. Namely, the formation of the holepolaron's electronic states are tracked by visible emission, its vibrational states by mid-infrared normal modes, and the continuum, interfacial strain of a surface population by GHz phonons. The fact that the 1.3 ps time constant is common to probes across the electromagnetic spectrum definitively assigns it to a hole-trapping free energy with an elevated, but common temperature of the quantum states. Further, it suggests to which low energy surrounding modes that free energy dissipates. That hole-polaron formation occurs with an interfacial strain field directly implicates the propagating acoustic pulse in the energy dissipation[81,110]. On the other hand, upon subtraction of the lattice phonons in the data, one is left with a GHz mode resulting from Brillouin scattering in the electrolyte (Figure S7), implicating the rotational− vibrational modes of water. Further, the 1.3 ps time constant itself has been assigned to the dissipation of an excited O−H stretch mode of water at interfaces[21,111-114]. While the activation free energy could involve all these modes, and the 1.3 ps could be rate limited by any of one of them, the results show that the hole-trapping event to create OER intermediates in photoelectrochemistry implicates energy dissipation to both sides of the solid−liquid interface.

Conclusion

In this work, we found that ultrafast UV excitation of 0.1% Nb:$SrTiO_3$ generates an interfacial strain at the $SrTiO_3$-water interface that leads to the observed CAWs in our broadband TR spectra. Under CC (OER) conditions, a uniaxial tensile strain is generated which we have assigned to the formation of the first OER intermediate, a hole-polaron trapped at surface oxygen sites. In OC conditions, the strain generation is compressive, 20 times weaker when normalized by pump fluence, and is likely caused by carrier-deformation coupling. For CC, we were able to quantitatively account for the CAWs phase and amplitude spectrum, which allowed us to extract a 1.3 ps formation time for the CC strain and estimate a lower bound spatial extent for the strain to be 3.4 nm with an upper bound strain magnitude to be 0.6%. These results highlight some of the transient effects present under OER conditions that may perturb the OER mechanism and could be involved in the observed surface degradation. Finally, this work provides a more complete spectroscopic characterization of the first OER intermediate in $SrTiO_3$ that now spans from the GHz through to the UV-VIS. The distinctive 1.3 ps formation time coincident with dissipation to low energy modes motivates future work on the dynamics behind hole-trapping, a critical step in any photo-driven electrochemical process.

CHAPTER V

ASSESSING AND QUANTIFYING THERMODYNAMICALLY CONCOMITANT AND KINETICALLY HINDERED DEGRADATION DURING OXYGEN EVOLUTION FROM WATER ON n-$SrTiO_3$

Original Publication

This work has been submitted to be published as Lyle H, Singh, S., et al. Assessing and quantifying thermodynamically concomitant and kinetically hindered degradation during oxygen evolution reaction from water on n-$SrTiO_3$.

Introduction

Water splitting has the potential to produce a clean, renewable, and storable energy source in H_2 and water oxidation is utilized in conjunction with CO_2 reduction for liquid fuels. Yet, the stability of many catalysts that do the oxygen evolution reaction (OER) from water is problematic for the continual and sustainable production of such fuels.

The stability can vary significantly across materials and reaction conditions. While the transition metal (TM) oxides are generally more stable than main group compounds, their stability changes down and across the periodic table and is pH dependent. Further, small amounts of surface degradation—which at the most encompassing level is "any destruction of a material under chemical or electrochemical action of the surrounding environment", altering it from the initial one[115,116]—are relevant for long term fuel production. At electrochemical interfaces, the degradation can be purely chemical, or charge induced. For OER, the surface degradation is often discussed as having two parts[70]: dissolution of the material into the electrolyte and re-construction of a resulting amorphous metal oxide surface from metal cations.

The degradation itself is observed by imaging (atomic force microscopy, electron microscopy), spectroscopy (x-ray photoelectron spectroscopy, x-ray absorption spectroscopy, and optical spectroscopy), and elemental analysis (inductively coupled plasma analysis, energy dispersive diffraction) post catalysis. Some examples of degradation under anodic conditions of OER by either voltage or light excitation include: a) $BiVO_4$ for which Bi and V dissolve into solution[117-118], accompanied by 50-200 nm of the material, yielding an amorphous Bi-O layer[117], b) $Ba_{0.5}Sr_{0.5}Co_{0.8}Fe_{0.2}O_{3-\delta}$ (BSCF) for which the thickness of amorphous regions become > 20 nm after > 100 cycles[119,120], c) Sr leaching from $SrIrO_3$ and other iridates (Sr_2IrO_4, Sr_4IrO_6)[121,122], that leads to Sr^{2+} to diffuse and O^{2-} to reorganize into a disordered Sr_xIrO_3 with higher Ir-O content[121], and d) dissolution of rutile TiO_2 resulting also in the formation of an amorphous layer of titanium hydroxide[123]. The more active materials are less stable and further, often degradation through dissolution and reconstruction creates a more stable, disordered surface while decreasing activity[124].

The similarity of the degradation accompanying OER across all these TM oxides has suggested that common mechanisms are involved. Proposed degradation mechanisms often refer to a Pourbaix diagram[115,125], which calculates the stability of a material with respect to applied potential and pH. Yet, the OER catalysts are found to dissolve and reconstruct in nominally stable regions of the diagram, which has been attributed to reaction kinetics associated with nearby instabilities[69]. The reaction kinetics of especially oxidizing photo-holes has been implicated, with successful surface passivation attributed to judiciously shuttling holes to OER over degradation.[126-130]

On the other hand, a more general thermodynamic argument has been made for TM oxide dissolution. The Pourbaix diagrams are not constructed during OER or

presume a constant partial pressure of O_2. If one utilizes chemical potentials during the reactions, the lattice oxygen, O_2^-, is already thermodynamically unstable at the Nernstian potential of OER by a dominant dissolution reaction.[70] This dissolution reaction is referred to as LOER (lattice oxygen evolution reaction). For a perovskite with A, B noble metal sites, LOER occurs by:

$$ABO_3 \rightarrow BO_2 + A_{aq}^{2+} + \frac{1}{2} O_2 + 2e^- \quad (34)$$

$$BO_2 \rightarrow B_{aq}^{2n+} + \frac{n}{2} O_2 + 2ne^- \quad (35)$$

The generality of these interpretations suggests that quantifying the degradation of OER catalysts would provide key data by which to assess whether the degradation is, in fact, thermodynamically allowed during OER and to what extent it kinetically competes with OER. This work develops a methodology to treat the degradation as a product that can be compared to OER. We utilize a single crystalline and nominally stable TM oxide (0.1% Nb-doped $SrTiO_3$ (100)) selective for OER, highly efficient photoexcitation of an electrochemical current, and a well-defined spot size by a laser beam. Such spatial definition allows a degradation volume to be associated with the charge passed through the photo-excited spot. We also utilize different scan methods, from continuous scan speeds to a static scan, which modulates the way the surface is exposed to a pulsed laser excitation that leads to highly varied degradation volumes. Pulsed photoexcitation also allows for probing the excited state surface and temporally defines the charge reaching the surface.

The surface is probed using a combination of ground and excited state optical reflectance, scanning and transmission electron microscopy, energy dispersive spectroscopy, and x-ray spectroscopy. The following essential findings are made: 1) Upper limits of the charge-induced dissolution are 6% of the total charge passed for pH 13 and 23% for pH 7 (treating both the dissolution and OER as 4-electron processes), 2) An amorphous and porous metal oxide material is left behind,

comprised of local SrO and TiO_2 motifs and a larger percentage of Ti and O compared to stoichiometric $SrTiO_3$, and 3) The pH dependence of the dissolution is anti-correlated with the meta-stable population of trapped holes formed within < 2 ps. The remarkable consistency of the % dissolution in pH 13 electrolyte over a large range of linearly increasing degradation volume and changing electrode composition demonstrates a dominant dissolution reaction to be thermodynamically concomitant with OER. The argument relies on the same upper limit to the % dissolution at a given reaction condition and over-potential as opposed to the particular region accessed within the Pourbaix diagram. Separately, the value of the % dissolution reports on how competitive LOER is with OER for this particular TM oxide and the details of its photo-excitation. Finally, the composition of the remaining amorphous oxide and the pH dependence suggest the relevance of certain, chemical cation re-deposition mechanisms. The results motivate future work utilizing these methods on varied crystal structures of titanium dioxides, in a larger range of electrolytes, and for diverse TM oxides.

Photoelectrochemistry of Nb-STO, Scanning Methods, & Surface Probes

The oxygen evolution reaction from water is driven by band-gap excitation of 0.1% Nb-doped $SrTiO_3$ 100 (n-STO) in an electrochemical cell where the n-STO is held at a constant potential of 0 V vs. Ag/AgCl for which the dark current is negligible. The n-STO bandgap is excited with pulsed 266 nm light (150 fs, 500 Hz) that creates photocurrent. The pump beam has an area of 4.7 $x10^{-4}$ cm^2 (Figure S1) and results in a quantum efficiency of light-to-charge separation of greater than 70 % (Figure S2). The fluence is held constant at 0.04 mJ/cm^2 such that 2% of the surface sites are excited by every pump pulse. The resulting steady state current of 2.5 mA/cm^2 for Faradaic OER corresponds to ~1 O_2/site-sec of the illuminated area; in this calculation, all the surface sites are presumed to contribute to the oxygen evolution.

Predominantly, the data is taken at pH 13 in 0.1 M NaOH electrolyte. The one comparison made is to pH 7 in 0.1 M $NaSO_4$ electrolyte. The photo-holes in the VB of n-STO sit at 2.8 V vs. RHE, which results in an over-potential of 1.6 V for OER.

The particular n-STO electrode was chosen for three reasons. First, the current resulting from ultraviolet photo-excitation on reduced single crystals in 3-electrode configurations with a Pt counter electrode, 0 V vs. SCE, and high quantum efficiency of charge separation (~100% with hv> 330 nm) has been shown to be Faradaic for OER using mass spectrometry and gas chromatography in NaOH electrolyte (Honda, JACS Japan and Ginley JACS). The electron:H_2:O_2 count is as expected, 4:2:1, although some measurements below 0.1 M NaOH report less O_2 measured (~0.7) (Ginley). We confirmed approximately Faradaic OER (± 20%) for our sample using a continuous Xenon lamp and O_2 sensor for 0.1M NaOH in previous work. The same was done with the ultrafast laser albeit with significantly less Coulombic charge accumulated. Therefore, while we cannot rule outside reactions from the electrolyte, they are minimized at higher NaOH concentrations and limited to H_2O_2 formation and free $OH^{\bullet}$; in TiO_2, the free $OH^{\bullet}$ production is measured by coumarin scavenging to be below 1% of the UV photoexcitation (TiO_2 free OH, UV and visible). On the other hand, pH 7 solutions contain 0.1 M $NaSO_4$. While the free radical $SO_4^{\bullet-}$ has been detected, persulfate ($S_2O_8^{2-}$) was present.

Second, in Nb-doped STO, the metals are all noble metals in Ti(IV), Sr(II), and Nb(V) oxidation states. The noble Ti and Sr metals lend a facile comparison to dissolution reactions in which the charge-transfer predominantly involves O atoms (reactions (34) & (35)). Nb in Nb(V) means that the Nb substitutes for Ti and one electron per Nb is donated to the crystal. Further, it has been shown that electrons localized on Ti sites (e.g., Ti(III)) are not detectable in the crystal prior to catalysis and those measurements are repeated here. Third, the 100 crystal face is chosen

because it was utilized extensively in previous characterizations of STO surface termination, photo-electrochemistry of OER, and most recently, transient optical reflectance during OER.

For the photo-excitation, a sequence of ultrafast 266 nm pump pulses arrive at the sample (Figure 5.1). For each data point, there is both a time to acquire from many repetitive pump pulses on the sample (acquisition time) and a time difference between pump and the optical probe (delay time). The acquisition time is the primary metric of the degradation and utilized throughout the manuscript. The degradation was also modulated by the scan method (i.e. x-y-z stage motion) during pump exposure. There are two methods: "static scan" and "continuous scan". In static scan, acquisition times are acquired over multiple spots on the sample that are separated by a fixed distance. Each spot is exposed to the 266 nm pump for a fixed amount of time (e.g. 100 seconds/spot or 50000 pump pulses within 100 s). In continuous scan, the stage moves the sample at a fixed rate (e.g. 7um/s or 28 um/s) while all times are acquired sequentially. For each method, the resulting degradation pattern is represented by a cartoon in figure 5.1A and the photocurrents are shown in figure 5.1B. The sequence of pump and optical probe shots for both methods is shown in figure 5.1C. Continuous scanning creates rows on the sample, while static scanning creates individual spots of degradation. The important distinction between these two methods is that by continuously scanning across the sample, each pump shot arrives on a "clean" sample surface and so sequential time points are treated equally. On the other hand, in the static scan method, the first shot arrives on a clean surface, but each sequential shot arrives on an increasingly degraded one. Figure 5.1D summarizes the naming scheme for the different sample conditions. The letters denote the scan method and speed used, where sequential letters represent increasing acquisition time from a given surface area. The numbers 7 and 13 identify

the solution pH. Representative photocurrents versus acquisition time for all these conditions are reported in supplementary Figure S2.

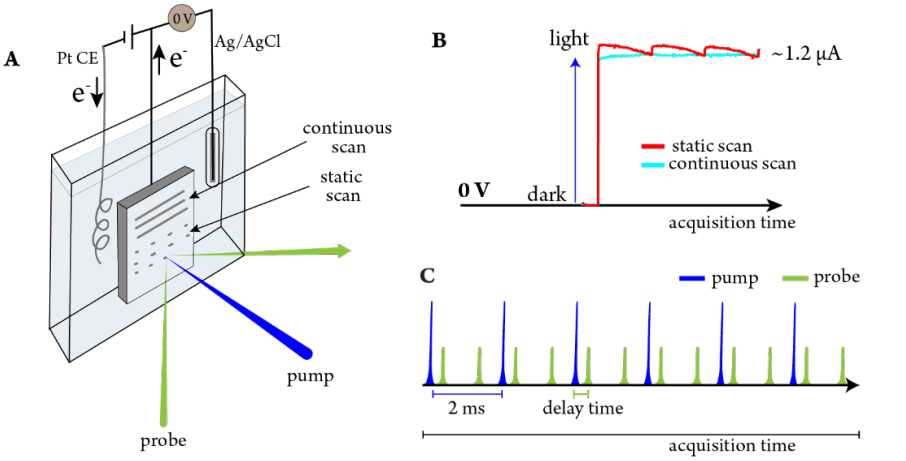

D Sample names

Sample	Electrolyte pH	Scan method
A13	13	28 μm/s
B13	13	7 μm/s
C13	13	100 s/spot
D13	13	60 min/spot
B7	7	7 μm/s

Figure 5.1: Sample geometries and naming scheme. (A) Cartoon of 0.1% Nb-$SrTiO_3$ in the electrolytic cell, in closed-circuit. The pump (266 nm, 0.04 mJ/cm²) is normal to the sample surface, while the broadband white light probe is at 45° angle of incidence. (B) Shows the increase in current from dark conditions (no pump exposure, ~ 0 μA) to "light-on" conditions (0.04 mJ/cm², ~1.2 μA). (C) Cartoon showing sequential on and off shots of the pump and probe pulses. Delay is the time between pump and probe pulses in the on-shot, and acquisition time is the total time passed over all shots taken. (D) Naming scheme for samples with different scan methods and electrolyte

The surface probes organize the rest of the manuscript. We start with the optical reflectance which is collected both in the ground (pump off) and excited state (pump on). The optical reflectance defines the scan methods and identifies the linearity of the degradation with acquisition time when the optical probe is sensitive enough to measure it. Next, scanning electron (SEM) and scanning transmission electron (STEM) microscopies directly observe the degraded volume to quantify the degradation with respect to the measured photocurrents. In the next section, energy dispersive X-ray spectroscopy in STEM (EDS) and X-ray Photoemission (XPS) and Absorption (XAS) Spectroscopy quantify the noble metal dissolution and give an approximate composition for the remaining oxide. Finally, transient optical reflectance compares the changes in the degradation between pH 7 and pH 13 with the initial concentration of trapped holes. The full list of probes are provided along with supplementary Figure S1.

Optical Reflectance

Figure 5.2 reports on the sample degradation by the ground and excited state optical reflectance while the photocurrent evolves in a pH 13 electrolyte. Continuous scanning results in a constant photocurrent, while the static scan method results in a decreasing photo-current during each period (Figure 5.2A). While the photocurrent is higher initially for the static scan, this is due to sample-to-sample variations of the exact quantum efficiency of the prepared electrode. Figure 5.2B shows that the ground state optical reflectance remains constant for the continuous scan while it decreases for the static scan. Given that the static scan involves a decreasing photo-current, the decrease in reflectance can be attributed to a roughened surface that scatters the optical probe, which we return to below.

The excited state reflectance also changes while the photocurrent evolves and as a function of scan method. Upon photoexcitation, surface-trapped holes create electronic states in the middle of the band gap, assigned to Ti – OH* surface species, as determined previously for n-STO[30,131,132]. These excited states lead to emissive transitions in the UV region (< 500 nm) which we probe here at 400 nm. An increasingly negative transient reflectance (ΔR) identifies a larger Ti – OH* population. Since a longer acquisition time on the same spot (i.e., static scan) causes decreasing ground state reflectivity, the resulting transient reflection is also more emissive due to degradation. However, by continuously scanning at faster speeds we decrease the acquisition time from a given surface area and converge to an unchanging ΔR. This is shown by measuring ΔR for scan speeds from 7 μm/s (green trace) to 14 μm/s (purple trace) and finally to 28 um/s (blue trace) for which the ΔR converges (Figure 5.2C). While the ΔR is plotted as a function of delay time, appropriate for the excited state reflectance, each increase in scan speed represents acquisition times that are indeed a factor of two shorter for a given exposed surface

area. This is detailed in the supplementary discussion accompanying Fig. S3. In static scanning, each time the pump moves to a clean surface, ΔR quickly jumps to the same value as ΔR for the 28 μm/s continuous scan, then gradually decreases as the

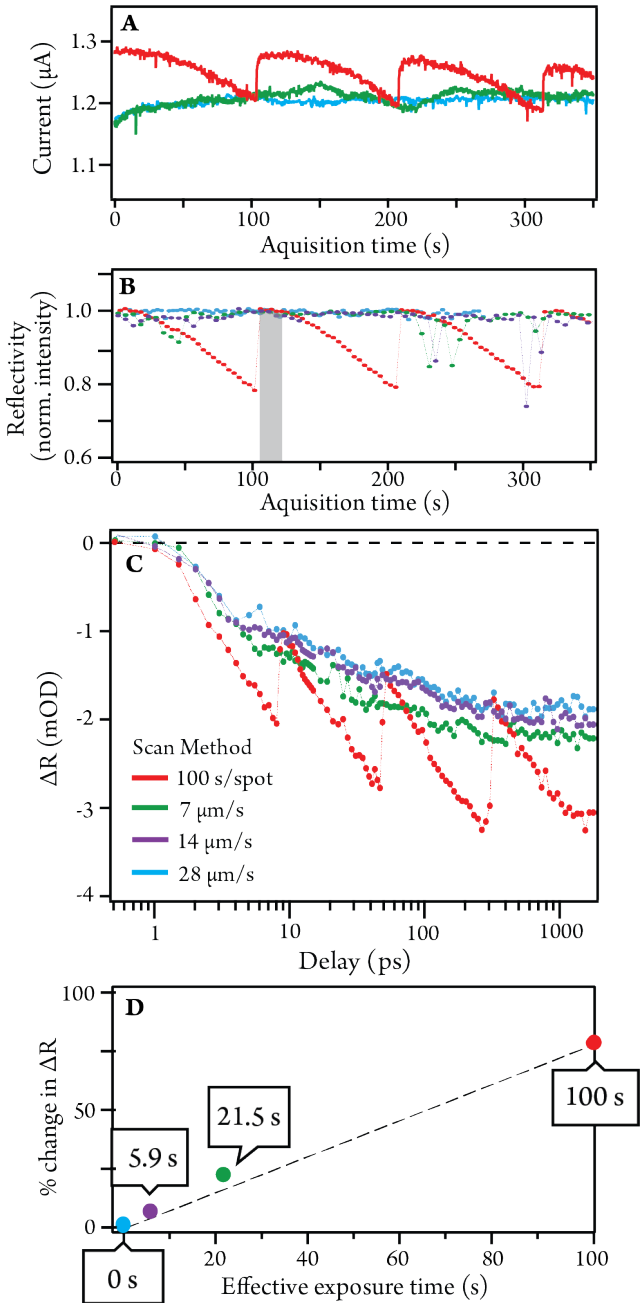

Figure 5.2: Ground and excited state optical reflectance of n-STO in pH 13 at 0 V vs. Ag/AgCl with exposure to 266 nm pump for different scan methods as denoted in red for the static scan and green, purple, blue for continuous scans. (A) Current passing through the electrode vs acquisition time. (B) Intensity of the broadband optical probe reflected from the sample vs acquisition time. (C) Kinetic trace of change in reflectivity from the sample at 400 nm. (D) Percent change in ΔR, with respect to the 28 um/s signal, vs calculated effective pump exposure time (see text and Supplementary Fig. S3).

acquisition time from the same sample spot increases, only to quickly jump back to the converged signal each time the pump is moved to a clean surface. We therefore identify the ΔR from the 28 μm/s scan as that of the nominally clean surface, with negligible contribution from the degradation.

We now turn to the sensitivity of the optical experiments and the origin of the convergence in ΔR with decreasing acquisition time. Optical reflectivity is only so sensitive to surface changes, since it can probe the sample bulk. This is clearly seen in the ground state optical reflectance (Figure 5.2B) for which the optical reflectance change of the 100 s/spot scan with respect to the continuous scans increases linearly, but only past an acquisition time of ~ 20 seconds (gray bar). Excited state data from a transient ΔR would be more sensitive to changes at the surface due to the differential recorded for each data point, but a non-linearity is nonetheless evident in the convergence of the continuous scans. In the following, we determine a lower bound acquisition time for which changes due to the degradation are seen in the optical reflectance and a region in which they occur linearly with acquisition time. To do so, we define an effective exposure time, which is the amount the sample had to be exposed to the beam to achieve a certain ΔR. We utilize an *approximate* linearity of the ΔR with acquisition time (Figure S3) for the 100 s/spot scan to determine the time needed to achieve the relative difference of the ΔR (or % ΔR) in the 7 um/s and 14 um/s scans with respect to 28 um/s, which is defined to have an effective exposure time of 0 s. The effective exposure times are 5.9 s and 21.5 s respectively for the two continuous scans (Figure 5.2D). Given the assumption in linearity for the 100 s/spot scan, the % change in ΔR is also linear with this exposure time. However, the % changes in ΔR do not occur linearly with acquisition time: the 14 um/s should be twice as fast as 7 um/s, but has an effective exposure time ~ 3.6 times shorter. This suggests that for faster scans than 7 um/s associated with a ~20 s effective exposure (Figure

5.2D), we are already in a non-linear regime. Altogether, the non-linearity in the optical reflectance below 20 s (Figure 5.1B), the association of this non-linearity also in ΔR for continuous scans with exposure times < 20 s (Figure 5.1D), and the approximate linearity of the ΔR in the 100 s/spot scan (Figure 5.1C, Figure S3), identify that we are insensitive to the degradation below ~ 20 s acquisition time and subsequently, a linear sensitivity is observed. That the 28 um/s scan does optically represent a nominally clean surface of zero effective exposure time can be seen also by optical microscopy (Figure S4), which shows that darkened areas for the 7 um/s scans are not observed for the 28 um/s scan.

Finally, we propose a mechanism by which increasing emission or negative ΔR occurs due to a degraded surface (Fig. 5.2C). Namely, the degraded surface causes the probe to scatter, such that we collect less light through the lenses, the spectrometer, and onto the detector (Fig. 5.2B). ΔR is calculated as –log (I_{ON}/I_{OFF}) where I_{ON}, I_{OFF} are the intensities of the probe beam with the pump on and off, respectively. For an intrinsic pump-probe ΔR from a nominally clean sample which is emissive ($I_{ON}/I_{OFF} > 0$), where I_{ON} is a sum of I_{OFF} and the intrinsic emission due to the pump on the nominally clean sample (+ΔI), a decrease in counts for the I_{OFF} probe would cause an increase in emission to be observed with increasing acquisition time. Further, for a linear degradation of the probe count of the ground state reflectance, a linear increase in the "extrinsic" emission should be observed.

Scanning and Transmission Electron Microscopy

To connect the changes in reflectivity to degradation, scanning electron microscopy (SEM) and scanning transmission electron microscopy (STEM) images were taken of the degradation within the photo-excited area (Figure 5.3). A cartoon of the cross-section for the STEM is shown to the left, with Pt deposited on top of a degraded area and then cut out using a focused ion beam. Since the sample cut out

is smaller than the degraded area, Atomic Force Microscopy (AFM) was performed from the pristine to the degraded region to show that the surface is level (Figure S5).

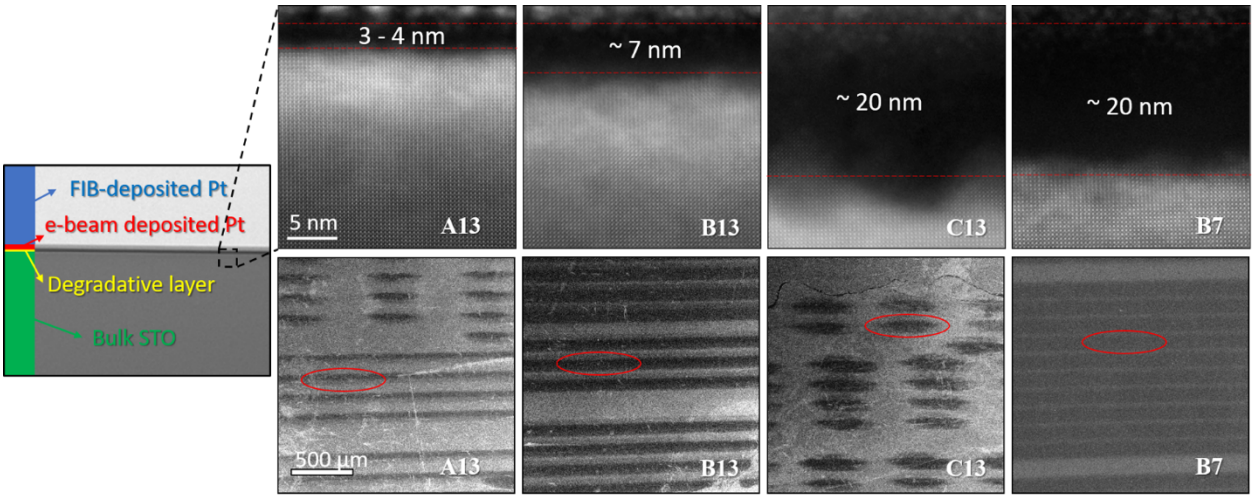

Figure 5.3: (top) TEM images of the cross sections of samples after 266 nm pump exposure at 0 V vs. Ag/AgCl (pH 7 and 13), comparing step scan and continuous scan at two different scan speeds. The bright band at the top of the TEM images (above upper dotted red line) is the protective platinum layer deposited during sample preparation. The black band in the center shows degradation depth contrasted against the bulk (crystal structure below lower dotted red line). To the left of the images, a cross-sectional cartoon of the degradative layer within the full sample cross-section. (bottom) SEM images for the same conditions showing surface area of the degradation. The red oval marks on the SEM images show the place from where cross-sectional TEM specimens are prepared. Dark, oval spots on the sample surface result from static scanning, whereas continuous scanning produces evenly spaced lines.

The SEM images clearly show the undamaged, crystalline sample separately from the photo-excited area, such that need only consider photo-induced degradation. The degraded area for the static scan is measured directly from the photo-excited spot in the SEM images (Figure 5.3 bottom). The depth of degradation is determined from cross-sectional STEM images by measuring the thickness of the darkest layer between the Pt layer and sample bulk (Figure 5.3 top). The STEM and SEM images are shown at different scales, and for the full set of sample conditions, in Supplementary Figure S6.

Samples A13, B13, and C13 compare the degradation for a static scan and two different continuous scan speeds in a pH 13 electrolyte. The 28 um/s continuous scan represents the ideal case, for which each sequential pump and probe pulse incident on the surface are equivalent according to ground state R and excited state

ΔR. However, while we are insensitive to it in the optical experiments, STEM shows that a thin degradative layer of 3-4 nm exists (Figure 5.3 top, Table 4). Increasing surface exposure to the pump causes additional degradation. In pH 13, continuous scanning at 7 um/s and static scanning at 100 s/spot result in degradation depths of 7 nm and 20 nm respectively. Considering the degradation depth in the ideal 28 um/s case as a subtracted "background", this is a 4.7x increase between the 7 um/s scan and 100 s/spot scan. The effective exposure times (21.5 s and 100 s respectively, Figure 5.1D) give equivalently a 4.7x increase in time spent on the sample. So, the degradation is linear with acquisition time, at least within the region of linearity defined by ΔR; we return to this below.

Sample	A13	B13	B7	C13	D13
TEM depth (nm)	3-4	7	20	20	106
SEM area (mm^2)	0.024	0.035	0.059	0.022	0.106
Charge passed ($x10^{-5}$ C)	2.1	8.6	8.3	12	260
# of O-atoms from sample/2 ($x10^{13}$)	0.213	0.604	2.94	1.10	28.1
O_2 from current ($x10^{13}$)	3.28	13.4	13.0	18.8	406
Ratio of O_2 from degradative layer to O_2 from total current (% dissolution)	6.5 ± 3.0	4.5 ± 1.5	23 ± 4	5.9 ± 2.7	6.9 ± 0.7

Table 4: Calculated contribution to surface dissolution reaction.

All samples are measured at 0 V vs. Ag/AgCl with 266 nm pump excitation. Row 1 lists labels the samples by the different scan methods and electrolyte conditions as described in Figure 1. Row 2 is the measured thickness of degradation from STEM; Row 3 is the measured surface area of degradation from SEM. Row 4 is the total charge passed through the sample circuit, calculated by integrating the electrochemical current over a given acquisition time. Row 5 is ½ of the oxygen atoms present in the degradation volume, based on the oxygen-site density of n-STO. Row 6 is the number of O_2 molecules evolved from the electrochemical current using 4 e^-/O_2. Finally, Row 7 is the ratio of O_2 from the degradation volume to that from the electrochemical current with Faradaic OER.

Next, we utilize the depth and areal data from the STEM and SEM images to determine the degraded volume (Table 4). A ratio of O_2 that could have arisen from this degraded volume to O_2 from Faradaic OER then quantifies an upper limit to the dissolution reaction. For example, for C13, the measured depth (7 nm) and area (0.022 mm^2) gives degraded volume of 0.44 x 10^{-6} mm^2. The total number of oxygen atoms

present in that volume is based on the oxygen-site density in STO ($5x10^{22}$ cm^{-3}), which for C13 is $2.2x10^{13}$ oxygen atoms or 10^{13} O_2 molecules. The Faradaic O_2 that could have evolved from the total current is obtained by integrating the current over the acquisition time, 100 s, which for C13 gives $12x10^{-5}$ C of charge passed and 18 x 10^{13} O_2 molecules (4 e^- per O_2).

That the area of degradation (0.022 mm^2) is smaller than the FWHM spot area of the beam (0.047 mm^2) supports using the SEM and STEM data to calculate the degradation volume. It shows that we don't have significant diffusion outside of the excitation area. Further, the areal difference likely arises from a uniform excitation area for catalysis in the center of the beam without much influence of the unexcited edges. The same is true for the rest of the conditions; pH 7 does have a larger degradation area, but only by ~ 0.01 mm^2.

Table 4 shows the dissolution percentage calculated with error bars for the different sample conditions. The error bar is ± 1 nm on the TEM thickness since the AFM thickness profile is flat to well within 1 nm (Figure S5). Table S1-S3 goes through this procedure in greater detail, along with explanations for error propagation. For A13, B13, and C13 the dissolution percentages are 6.5 ± 3.0%, 4.5 ± 1.5 %, and 5.9 ± 2.7% respectively. For the continuous scans, the horizontal diameter of the photo-excited spot is set to the beam size. However, since continuous lines of degradation appear in the SEM images, this diameter is arbitrary.

The above calculations assume that the degradation is linear with acquisition time. There are several ways this is shown by the data: a) the continuity of the degradation lines with a linear scan velocity, b) linearity in the optical reflectance past the ~ 20 s acquisition time, c) Past ~ 20 s, the degradation observed by imaging increases linearly with the exposure time determined by ΔR (the 4.7x factor described above) and d) By imaging, degradation occurs even for the fastest 28 um/s scan.

Finally, that the calculation leads to the same % dissolution for the same reaction condition (pH 13), but highly varied exposures, also implies this linearity.

We now turn to sample D13, which is the hour-long static scan. Here, the photocurrent decays over long periods of time, which is traditionally utilized as one of the first indicators of degradation during OER. The largest decay occurs in the first half hour and then levels off, like other metal oxides[69,123] (Figure S2). Somewhat surprisingly, but in line with the analysis thus far, even for an hour on a spot, the contribution of the dissolution to the charge passed is 6.9 ± 0.7%, which is again within error the same as for the rest of the scan methods at the same reaction condition (pH 13). Thus, the dissolution is a constant percentage of the total charge passed through the area, independently of whether the charge is passed through a single spot or across the entirety of the surface and further, for how long.

Transient Reflectance and pH dependence

We now address the pH 7 conditions for which a clear change in the dissolution percentage from pH 13 is observed. For the same scan method, identical calculations give 23 ± 4% at pH 7 (B7) as compared to 4.5 ± 1.5 % (B13) at pH 13 (Table 4, Table S1-S3). In the following, this pH-dependence and broadband, picosecond transient reflectance spectroscopy are utilized to identify correlations between) the degradation and our converged, emissive kinetics, and b) the pH-dependence of the dissolution percentage and that of the meta-stable population of trapped charge (*e.g.,* Ti – OH*). The first objective builds upon previous work to further assign the emissive signal to the total population of Ti – OH* rather than degradation for fast enough scans, but now by directly imaging the degradation. The second objective informs on potential degradation mechanisms and their timescales, motivating future work on more detailed pH dependencies.

Figure 5.4A and 5.4B show the transient reflectance of the surface at pH 7 (A) and pH 13 (B) using a broad band optical probe (1.8-3.3 eV) through a nanosecond. As shown in detail previously, the absorptive (red) transition is not pH dependent in this time range, while the emissive (red) transition is highly pH dependent[30]. Further, the pH dependence arises from the emissive population created < 2ps[30,133]; there is another rise in the emissive population around ~60 ps but this is not pH dependent. The particular hole trapped population is associated with Ti – OH* or an proton and electron transfer from a surface absorbed site. The assignment derives from a precise time-constant (1.3 ps) for its formation corroborated by vibrational (THz, mid-IR) spectroscopy[22,131] and the increasing emission with pH. Finally, the pH dependence shown here at the two end points can be tracked continuously with pH, resulting in a Langmuir reaction isotherm[30].

Nonetheless, we now test this assignment directly from the point of view of the surface degradation, which also results in an emissive optical signal. In Figure 5.4C, kinetic traces at 400 nm at pH 7 and pH 13 are extracted such that they can be compared with the data in Figure 5.2 and Table 4. The broadband optical data were taken with the 7 um/s scan rate to minimize degradation but also allow for efficient sample use. While the ΔR for pH 13 is a factor of 2-3 larger than for pH 7, the same data taking results in 5x's less degradation in pH 13 (4.4%) than pH 7 (23%) (Table 4). Therefore, for fast enough continuous scans, the pH-dependent, emissive ΔR is anti-correlated with the pH-dependent surface degradation. The anti-correlation of the emission with the degradation is depicted in the bar graph of Figure 5.4D, for which the STEM measured depth is plotted next to the integrated emissive signal of the kinetic traces. Thus, by utilizing short enough acquisition times, we minimize the emissive signal due to degradation and converge to the kinetics of the Ti – OH* population.

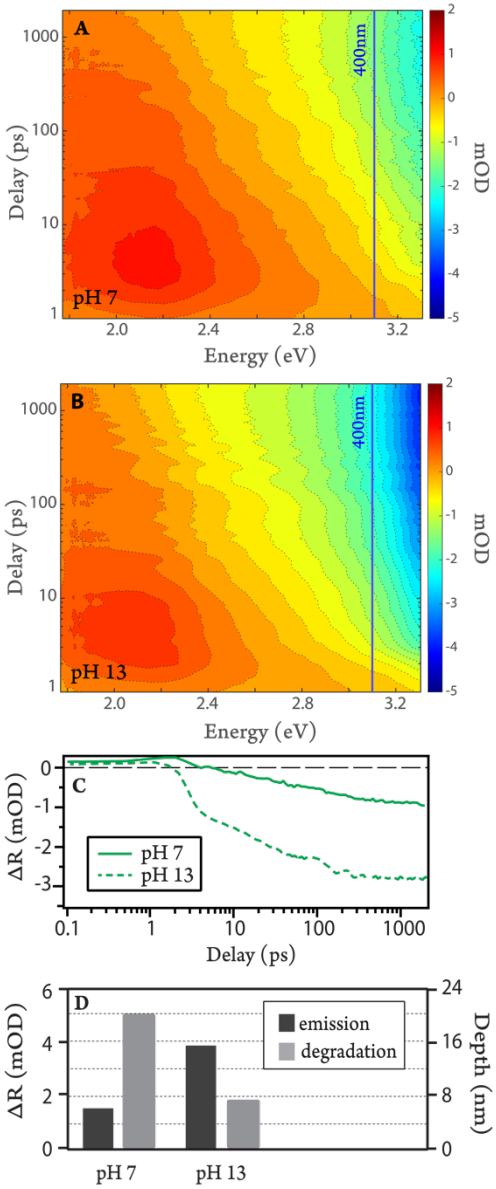

Figure 5.4: Excited state reflectance for n-STO at 0 V vs. Ag/AgCl. (A) and (B) show transient reflectance (ΔR) maps for pH 7 (top) and pH 13 (bottom) electrolytes. The y-axis is the pump-probe delay time. The red part of the spectra is a positive ΔR, representing absorption, while the blue part of the spectra is negative ΔR and represents emission. Vertical green lines indicate kinetic traces at 3.1 eV (400 nm) that are shown in (C), which emphasizes the difference in the magnitude of emission between n-STO in basic (pH13) and in neutral (pH 7) electrolyte. (D) Compares total emission with degradation for each electrolyte condition. On the left axis, total emission is calculated by integrating the emissive ΔR kinetic trace over the entire delay time, then dividing by the integrated delay time. On the right axis, degradation is represented by the depth as measured by STEM.

Given this assessment, the imaging and transient reflectance data together imply that there is also an anti-correlation between the total trapped hole, Ti – OH* population and the extent of surface degradation. Often, the amount of charge created at the surface per unit time—either through shorter laser pulses with higher peak

power or higher fluence for a given laser pulse—is associated with more degradation. For the pH dependent data, the same photoexcitation fluence (0.04 mJ/cm^2) was maintained and it resulted in essentially the same total charge passed through the spot (Table 4, B13 and B7). Given that the total charge passed was constant, anti-correlation between the Ti – OH* population and the surface degradation implies that a larger population of trapped charge created at early times (< 2 ps) is not concomitant with more degradation. There are two possible explanations. One is that the % dissolution is too small to be observed separately from the total trapped charge. The other is that the degradation occurs at much longer time scales. The transient spectroscopy does give a view of the meta-stability of the Ti – OH* population, which reports on how long the pH-dependence of this population is anti-correlated with the % surface dissolution. The trapped hole, Ti – OH* population is stable through a nanosecond as shown here (Fig. 5.4A, 5.4B) and through a microsecond as shown previously[134]. One consistent view of the data is that a small % of charge branches off for degradation past a microsecond, while the reaction steps of OER occur prior.

Elemental Composition of Amorphous Layer

Thus far, the surface degradation has been treated as occurring entirely due to dissolution of the metal oxide electrode into the electrolyte from the degradation volume. While this does give a quantifiable % dissolution, an amorphous layer separate from the bulk is observed (STEM images of Figure S6). The amorphous layer could arise from reconstruction of the metal oxide that hasn't yet dissolved or from cation re-deposition reactions from the electrolyte. In this section, we detail the elemental composition of this amorphous layer using energy dispersive (EDS) and photoelectron (XPS) and absorption (XAS) x-ray spectroscopy of the electrode.

Figure 5.5 represents the results of elemental analysis by EDS in STEM, for which the full data set is shown in Figure S7. First, Figure 5.5A presents a high

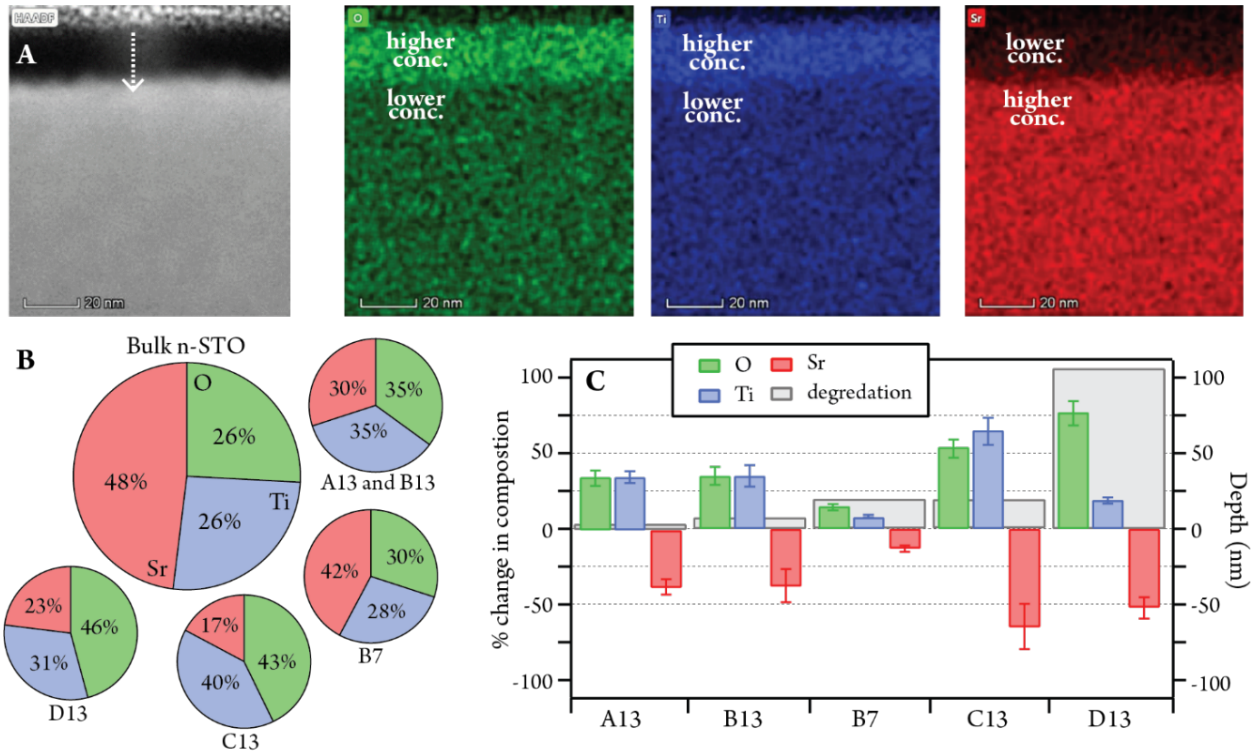

Figure 5.5: Chemical composition of degraded volume compared to bulk n-STO, measured by STEM-EDS. (A) HAADF images of sample C13: static scanning at 100 s/spot in pH 13 electrolyte. In the far-left image, the white dotted arrow indicates the measured depth of degradation. The green image in the middle-left shows an increase in oxygen concentration between the same degraded volume (light green band) vs the sample bulk. A similar increase in titanium concentration from the bulk is shown in the blue image. In the far-right red image, the darker red band at the top indicates a decrease in strontium concentration in the degraded volume compared to the bulk. (B) Quantification of the change in composition. Pie charts show the relative weight percent of each element in bulk n-STO as well as in the degraded volume for each sample condition. (C) Shows how much the concentration of each element within the degraded volume is increasing or decreasing compared to the bulk of the sample. On the left axis, percent change in composition is calculated by taking the difference in weight percent between the degradation volume and the bulk. Green and blue bars show an increase in oxygen and titanium, respectively, while the red bars show a decrease in strontium. This is also compared to the overall amount of degradation (gray bars), represented by the measured thickness from the HAADF images on the right axis.

angular dark field (HAADF) image. The degradative layers appear darker than the n-STO substrate in the HAADF images. Because the HAADF signal is roughly proportional to $Z^{1.8}$, where Z is the atomic number, the low intensity in degradative layers suggests that the density of these layers is significantly lower than the STO substrate. EDS analysis confirms that the lower density of degradative layers is due to loss of materials, mainly leaching of Sr. By comparing the Sr L-edge and Ti K-edge line profiles of the EDS images on the pristine surface to the degraded area, we can determine the total dissolution of Sr and Ti from the degradation volume. As detailed

in Fig. S8 and Fig. S9, approximately 50% of Sr and 20-30% of Ti dissolves into solution from the degraded area for a range of conditions at pH 13: the 28 um/s scan (A13), 7 um/s scan (B13), and 1 hour spot (D13). These are represented in a bar chart in Figure 5.5B.

Figure 5.5C shows the EDS intensity of O, Ti, and Sr as a relative percentage of that element compared to its stoichiometry in the bulk. Overall, an increase of O, Ti and a decrease of Sr relative to the bulk stoichiometry of $SrTiO_3$ is observed. These relative percentages vary across the sample conditions. Figure 5.5C visualizes the changes from the bulk composition (zero line) in a bar graph that generally shows smaller changes the faster the acquisition (scan methods A13, B13 compared to 100 s and 1 hr static scans C13, D13) and the lower the pH (B7 compared to B13).

The amorphous layer was also analyzed using XPS and XAS. Spectra were taken scanning from the pristine surface to the degraded area for the C13 sample using Sr 3d XPS to denote the degraded area, as detailed in Fig. S10. Ti L-edge XAS measured in the pristine area (Fig. 5.6A, bottom spectrum) shows the characteristic lineshape for a perovskite $SrTiO_3$ with the intensity of the e_g peak similar to the t_{2g} peak and no bifurcation of the e_g peak, which are both instead observed in TiO_2 rutile and anatase[135]. The Ti e_g peak shifts to lower photon energy in the spectrum collected from the degraded area. The XAS data is taken in total electron yield (TEY) mode. Previous papers on transition metals and rare earth elements report values less than 5 nm for the surface sensitivity of TEY, as described by Ruosi *et. al.* (ref. [136]) and references therein, definitely smaller than the size of the degraded region[137]. The XPS Ti 2p spectrum also exhibits a core level shift, as reported in Fig. 5.6B; the similar shift probed by XPS, which is surface sensitive to within ~ 1 nm, also identifies the XAS Ti L-edge to probe the degraded layer. Both peak shifts can be ascribed to a change in the chemical environment surrounding of Ti atoms. A similar shift of the

Ti 2p XPS was previously seen in annealed TiO_2 samples and assigned to a locally distorted O_h symmetry with a higher oxidation state of the Ti.[27] A corresponding one in the e_g peaks of Ti L-edge XAS on $SrTiO_3$ has likewise been associated with octahedral distortions related to defects[138]. Therefore the Ti XAS and XPS data together identify local TiO_2 that maintains the octahedral cage of the perovskite, albeit a distorted one.

We now turn to the core-level data from oxygen and strontium. The XAS O K-edge of the pristine sample is dominated by the following features, as labeled by the metal orbitals in Fig. 5.6C and with increasing photon energy. The first two peaks

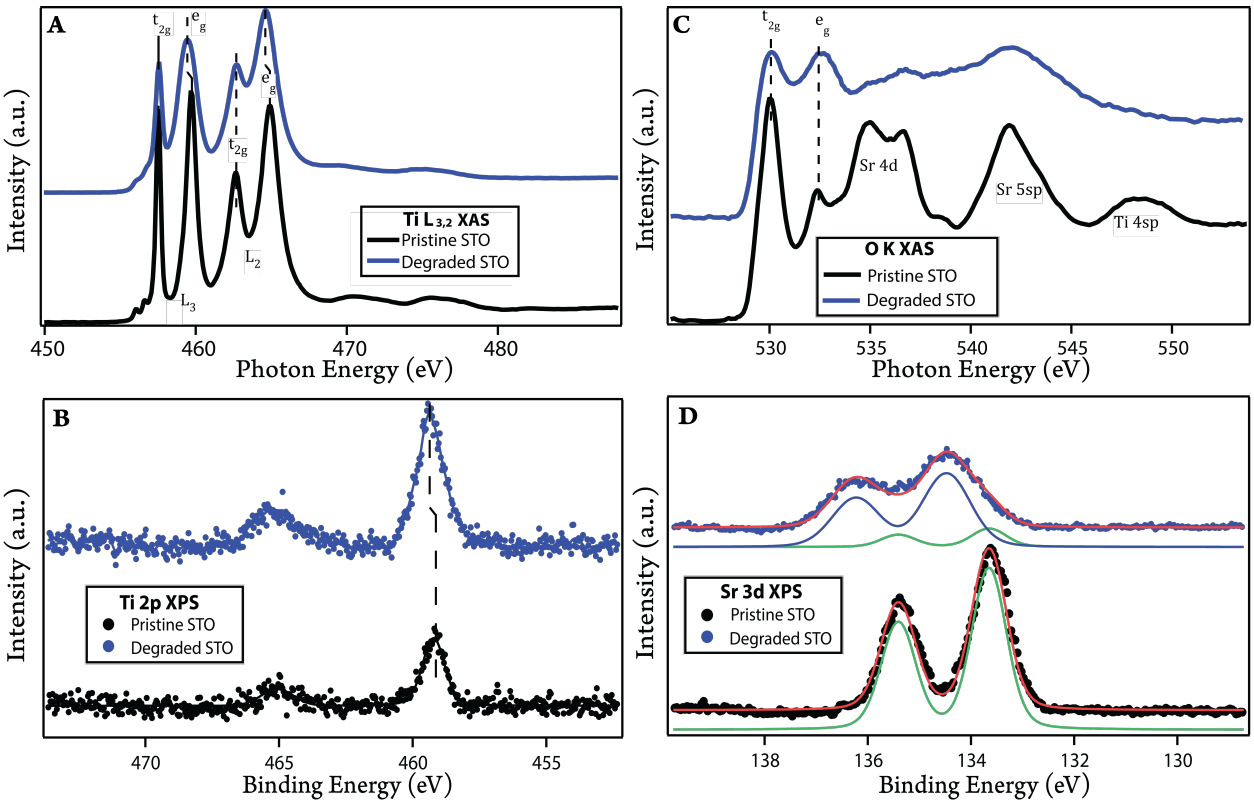

Figure 5.6: XAS and XPS spectra measured on pristine STO (black curves) and degraded STO after laser exposure (blue curves). (A) Ti $L_{3,2}$ XAS spectra: after exposure the e_g peaks shift to lower photon energy which can be explained by a distortion of the O_h symmetry locally. (B) XPS Ti 2p core level spectra: after exposure an increase of the Ti 2p signal is observed together with a shift to higher binding energy in agreement with a different chemical environment of Ti atoms and a larger relative content of Ti:Sr. (C) O K XAS spectra: the spectrum measured after exposure shows a decrease of the intensity of the unoccupied O2p orbitals hybridized with Sr 4d and Sr 5sp in agreement with the observed decrease of Sr at the surface. It also shows a similar relative intensity of the Ti t_{2g} and e_g peaks, which is explained by overlapping peaks related to local SrO_x as described in the text. (D) XPS Sr 3d core levels: after exposure the intensity of Sr 3d signal at the surface decreases and the peak shape changes. The best curve fit, following a previous procedure (see text), is obtained by adding a new component shifted by ~0.9 eV from the Sr 3d pristine STO core-levels that can be explained by the formation of SrO_x.

correspond to transitions from O1s to Ti3d (t_{2g})-O2p and Ti3d (e_g)-O2p hybridized orbitals, respectively. The next bifurcated peak and the final two peaks correspond to transitions from O1s to Sr 4d-O2p, to Sr 5sp-O2p, and to Ti 4sp-O2p hybridized orbitals, respectively[139]. The XAS O K-edge of the degraded layer is markedly different from pristine $SrTiO_3$,[140] with the Ti t_{2g} and e_g peaks of a similar magnitude and a much reduced contribution from Sr 4d and Sr 5sp (Fig. 5.6C). Since about 50% of the Sr dissolves, while only 20-30% of the Ti and further, in the perovskite, O is 2:1 for Ti and 1:1 for Sr, we should see a reduced contribution of Sr in the O K-edge XAS. However, that the Ti t_{2g} and e_g peaks are of similar magnitude cannot be explained by Sr dissolution alone. Previous XAS data shows that the main peak of the O K-edge of SrO_x is located at the same photon energy as the O1s to Ti3d (e_g)-O2p transition of TiO_2[21]. On the other hand, the O1s to Sr 4d-O2p and O1s to Sr 5sp-O2p transitions of SrO_x would remain reduced compared to $SrTiO_3$, since they are not overlapping with any Ti related features. Therefore, the O K-edge of the degraded layer is consistent with a composite of separate TiO_2 and SrO_x local structures, albeit with a higher TiO_2 content. Lastly, XPS line profiles in Fig. 6D show that the majority contribution to the Sr 3d spectra in the degraded layer are Sr 3d peaks at 0.9 eV higher binding energy than for pristine $SrTiO_3$. Assigned previously and especially for Sr defects within $SrTiO_3$,[22,37] this shift conclusively identifies the formation of local SrO separate from TiO_2.

The XPS Ti 2p core-level data was also analyzed for the presence of Ti(III). On the pristine surface, no Ti(III) is observed even in resonant XPS. Further, XPS and resonant XPS together show that there is minimal contribution of Ti(III) within the degraded area (< 3 %) (Fig. S11). So, while oxygen dissolves and could leave some vacancies behind, Ti(III) remains a minority species.

Discussion

The electron imaging (STEM, SEM) and optical reflectance (ground and excited state) show that a portion of the $SrTiO_3$ oxide electrode dissolves into the electrolyte, which consumes an upper limit of 6% of the total charge passed at pH 13 and 23% at pH 7. The dissolution reaction is explicitly charge-induced, rather than chemical, since the electron imaging clearly separates the laser-beam induced damage from the bare electrode/electrolyte contact. It also occurs concomitantly with photo-electrochemical OER from water, since the dissolution comprises a minority of the photo-current and other side reactions are minimized for n-STO in NaOH electrolyte. The degradation occurs linearly with acquisition time, or time exposed to the pump beam. A similar percent dissolution occurs whether the photocurrent arises from new areas of the electrode continually exposed, the same excitation spot, and whether for seconds or hours. The elemental analysis (EDS, XPS, ICP) shows explicitly that Sr and Ti dissolves into the electrolyte and the remaining electrode material has an amorphous structure enriched in Ti and O, with some dependence on pH. In the following, we explain these results using first an LOER dissolution reaction, and second A-site and B-site cation re-deposition reactions which are consistent with the amorphous electrode material. The discussion concentrates on the pH 13 condition but addresses potential mechanisms for the pH dependence.

These reactions have been proposed by several studies of surface degradation of metal oxides during OER. We follow here the reactions and arguments developed within ref. 70, that provides a general context for dissolution and reconstruction of metal-oxide electrodes during OER[70]. Further, the specific delineation of reactions there applies to metal oxides without a change in the oxidation state of the metal, appropriate for “noble” transition metals Ti(IV) and Sr(II) within $SrTiO_3$.

A lattice oxygen evolution reaction (LOER) which dissolves the electrode can arise from the instability of the oxygen anion in the metal oxide lattice. To summarize the argument, the chemical potentials within LOER are not independent of OER, which derives an over-potential for LOER that is larger than or equal to OER. While many oxides are found to be stable at OER potentials by Pourbaix diagrams, these diagrams presume that O_2 is not evolving or more explicitly, the oxygen partial pressure is always in equilibrium, and this is not the case during OER. For a perovskite with A, B metal sites, LOER occurs by reaction (34) and (35) in the introduction.

For $SrTiO_3$, the A-site is the dissolution of the 2+ cation, Sr^{2+}, and the B-site is the dissolution of the 4+ cation, Ti^{4+}. Thus, the reaction (34) and (35) mean that for every oxygen in the $SrTiO_3$ lattice, ½ O_2 and 2 e^- are released in LOER, with one ½ O_2 arising from the Sr-dissolution and one O_2 arising from the Ti-dissolution. Equivalently, 4 e^- are consumed for each O_2 released, which was utilized to calculate the percent dissolution in Table 4. Since the total degradation volume was utilized for the calculation, and electrode material does remain, this percentage represents an upper limit.

Overall, the reactions are appropriate since material from the electrode is dissolved, and electrons occupy the oxygen orbital valence band within the electronic structure of $SrTiO_3$. However, further, more detailed assessments from the data can be made. Common chemical potentials within LOER and OER are the underlying thermodynamic argument for dissolution during OER. If so, then the amount of dissolution compared to the photocurrent should depend on the type of metal oxide and the over-potential at a particular reaction condition but should be independent of details such as the history of the electrode exposure and for how long the reactions occur. Indeed, the experiment maintains a constant current density (2.5 mA/cm^2)

across all samples by the same fluence (0.04 mJ/cm^2), quantum efficiency (>70%), and applied potential (0 V vs. Ag/AgCl) at a given reaction condition, which demonstrates a consistent over-potential for photo-holes, whether at the nominal VB edge (2.8 V vs. RHE) or a shifted one. Then, at a given pH, we obtain the same percent dissolution, regardless of whether a continuous or static scan method was employed and for highly varied acquisition times. Conversely, had kinetic processes from the electrolyte or electrode been decisive for the amount dissolved, different % dissolutions would have been obtained as the electrode evolves into an amorphous structure. This is especially anticipated for the hour spot for which the current degrades substantially (by ~50%) and a thick 100 nm amorphous layer forms, and yet, the percentage of the total current that goes towards dissolution remains, within error, the same. In other words, for a large range of linearly increasing degradation volumes, we obtain a remarkably consistent % dissolution. This means that, for a given over-potential for OER at a particular reaction condition, the competition between OER and LOER is the same regardless of the history of the electrode. As such, we can really think of the chemical potential of the reactants within both as defining two concurrent reactions and further, one dominant dissolution reaction that competes with OER.

The LOER that dominates the dissolution reaction should be considered as separate from reconstructed phases in Pourbaix diagrams. For $SrTiO_3$ in particular, there are several stable phases as a function of potential and pH. At the potential of the VB that drives the OER reaction with photo-holes (1.6 V over-potential for OER) and for pH > 7, the stable phase predicted is a reconstructed one with 3 monolayers of TiO_2 and inclusive of O* intermediates[125]. While this phase may be achieved by a concurrent reaction, the same % dissolution despite the history of the electrode means that one dominant dissolution reaction (*e.g.* LOER) defines the degradation layer

volume. We note that rutile TiO_2 is similarly nominally stable in Pourbaix diagrams over a large range potential-pH range, but also exhibits degradation[117].

A way to further test these conclusions is to apply the same methodology to other facets of n-STO and to the diversity of crystal structures within titanium dioxides, which would modulate the ease with which O_2 is extracted by LOER from a similar electronic structure. It would also be important to apply the methodology to other TM oxides, which would modulate the hybridization of oxygen with the metal site. Interestingly, a degradation volume reaching up to 20-100 nm is also found after electrochemical cycling on the OER electrode BaSrCoFeO (BSCF82), and a similar procedure was utilized to estimate the contribution to charge passed[120].

We next turn to the cation re-deposition reactions which can cause the appearance of an amorphous metal oxide within the degradation volume. The AFM line profiles show that while the electrode has dissolved into the electrolyte, another porous material has filled the volume up to essentially the same level as the initial surface. The elemental analysis by EDS shows that while we definitively lose Sr (~50%) and Ti (~20-30%) to the electrolyte, the relative ratios of the elements in the remaining amorphous metal oxide are lower for Sr, and higher for Ti and O compared to stoichiometric $SrTiO_3$.

We consider two simplified cation re-deposition reactions. One is the cation re-deposition reaction for the Ti, or B-site of the perovskite:

$$TiO_2 \rightarrow Ti^{4+}_{LOER} \rightarrow TiO_2$$

Since this cycle does not involve any electrons other than that evolving the O_2 to create Ti^{4+}, the re-deposition would be entirely chemical and could be described, in basic conditions, by:

$$Ti^{4+}_{LOER} + 4OH^- \rightarrow TiO_2 + 2H_2O$$

The Ti cation re-deposition reaction is supported by the XAS and XPS data in the following way: a TiO_2 local structure separate from $SrTiO_3$ is seen by the distorted O_h environment of the Ti L-edge XAS and Ti 2p XPS and as a component of a composite O K-edge XAS. Furthermore, the resonant XPS and XPS together show that while Ti^{3+} is present, it is a minority species (< 3%) and therefore electron transfers are not prominent in the re-deposition.

A possible cation re-deposition mechanism for the A-site of the perovskite is:

$$Sr^{2+}_{LOER} + 2OH^- \rightarrow SrO + H_2O$$

This cation re-deposition reaction is supported by XPS data of the Sr 3d core-levels that distinctly show the formation of local SrO. The composite O K-edge XAS of local TiO_2 and SrO supports both cation re-deposition reactions.

The extent to which both re-deposition reactions take place at pH 13 can be assessed from the EDS results. With a total of 20-30% of Ti dissolving into solution (at pH 13), 70-80% of the Ti cations are either re-deposited or did not leave. With a total of 50% of Sr dissolving into solution, 50% of the Sr cations are either re-deposited or did not leave. Given that there is an amorphous metal oxide, the re-deposition reactions are expected at least to compete with the LOER dissolution reaction. Given that more Sr is dissolved than Ti, we anticipate the B-cation re-deposition reaction to be more effective, as has been suggested previously (CoO_x and BaSrFeCoO)[119,120]. The preferential re-deposition of the B-cation is also consistent with a higher O content in the amorphous metal oxide, since more O re-deposits with Ti than Sr.

On the other hand, at pH 7, the relative elemental percentages from EDS show that the remaining material is closer to the stoichiometry of bulk $SrTiO_3$. Given the basic conditions required for both cation re-deposition reactions and a preference for B-cation re-deposition, repopulating TiO_2 within the degradative volume would be more efficient at pH 13 than pH 7. We also observe a larger degradative volume at

lower pH, which would suggest that the cation re-deposition reactions compete with LOER to limit the dissolution at higher pH. However, an understanding of these mechanisms would require a more detailed pH dependence and the exploration of acidic pH, both of which motivate future applications of this methodology.

Though they naturally explain a local octahedral TiO_2 separate from SrO, these re-deposition reactions are certainly simplified. Indeed, surface reconstructions predicted by Pourbaix diagrams could also lead to higher Ti and O content at higher pH[125]. It is also possible that excess O-O bonds are formed in a variety of configurations with Ti and Sr cations, though the dominant octahedral environment is preserved. Another possible reaction includes the formation of oxyhydroxides,[117] with additional O and H within SrO and TiO_2. Further, the exact composition does seem to depend on the scan method and acquisition time from a given area, with less change from the bulk stoichiometry for lower acquisition times. The re-deposition reactions will occur concomitantly with LOER, which changes the reactant Ti^{4+} concentration near the electrode dynamically and likely in ways that do depend on diffusive processes and electrode morphology.

Finally, we address future work that could take advantage of the quantification of the dissolution observed here. While the competition between LOER and OER is the same for the different sample conditions at a given pH, OER is favored. The question is whether we can understand the favorable kinetics at a given over-potential and then control them to reduce the degradation further. Multi-scale and multi-physics models of main group semiconductors have been employed to define photostability as a percentage of the current going to OER over degradation, which is the same as our metric here[128]; the models are carried out as a function of surface potential and charge transfer rate. The same analyses could also be applied to TM oxides. Here, the surface potential is circumscribed by the excitation condition

of 0.04 mJ/cm^2 at 0 V vs. Ag/AgCl. Also defined are the relevant rates—the charge transfer to the surface (2% of sites excited each pulse) and the total turnover rate (~ 1 O_2/site-sec). Passivation methods for degradative photo-holes, proposed within the analysis but also more generally, rely on another material accepting the holes that would otherwise go to degradation and in certain cases, shuttling them to OER instead[69,126,127,129,130,141]. Here, the time-resolved spectroscopy shows that the total trapped charge going to either OER or LOER is anti-correlated with the percent dissolution through pH, which in and of itself suggests that there are multifaceted pathways for controlling the degradative holes. Another proposition based particularly on the use of an ultrafast repetitive laser is to modulate the timing of the laser pulses to alter when and how much charge reaches the surface.

Conclusion

By utilizing spatially and temporally defined photoexcitation of a single-crystal surface, n-$SrTiO_3$, the work quantifies a dominant electrode dissolution reaction (represented by LOER) to be thermodynamically concomitant with OER, but kinetically hindered. The competition between LOER and OER is set by the over-potential of the electrode and independent of the history of the electrode exposure to OER, as demonstrated by a remarkably consistent % dissolution despite linearly increasing degradation volume and a changing electrode composition. Cation re-deposition mechanisms, chemical in nature, are suggested by the pH-dependence of the electrode dissolution and the elemental analysis of the remaining amorphous metal oxide. The quantification of the electrode dissolution reaction by an upper bound that is anti-correlated with the total surface trapped charge suggests avenues to further suppress the degradation.

CHAPTER VI

DIFFERENTIATING INTERMEDIATES USING VIBRATIONAL SPECTROSCOPY AND FUTURE WORK

The next steps in studying photo-electro catalytic OER would be to differentiate the O* intermediates structurally and observe their evolution through the catalytic cycle. This can be achieved through vibrational spectroscopy because it is sensitive to the unique structural geometry of the chemical species in question. Theoretical exploration of the STO/aqueous and TiO_2/aqueous interfaces predicts multiple energetically similar intermediates with different local geometries, some of them are predicted to be IR active while others can be Raman active. There has been some exploration using a vibrational probe using an infrared technique called attenuated total reflection infrared spectroscopy (ATR-IR) that identified a particular intermediate through its sub-surface vibration. The local geometries of intermediates can differ which affects the visibility of a given intermediate. They can be IR-active, if there is a dipole moment change in the bond that is being probed, or possibly Raman active if there is no dipole moment change. To probe the O* intermediates that are not IR active, various Raman spectroscopy techniques can be employed. The technique most suitable for studying O* intermediates of OER is Femto-second Stimulated Raman Spectroscopy or FSRS.

Raman spectroscopy is a powerful analytical technique that is widely used to study the vibrational modes of molecular species. Briefly, it works by measuring the inelastic scattering of light, which causes a shift in the frequency of the scattered photons due to interactions with the molecules in the sample. By analyzing the resulting Raman spectrum, researchers can identify the chemical composition of a sample, as well as gain insight into its molecular structure and dynamics. One of the

main limitations of traditional Raman spectroscopy is that it suffers from low sensitivity, which can make it difficult to detect weak Raman signals originating from samples with a small absorption cross-section, which can happen at an interface. Additionally, Raman spectroscopy is inherently limited in its time resolution, which means that it cannot be used to probe and track fast molecular dynamics on picosecond timescales.

Femtosecond Stimulated Raman Spectroscopy (FSRS)

In recent years, advances in laser technology have led to the development of a new variant of Raman spectroscopy known as femtosecond stimulated Raman spectroscopy (FSRS). FSRS overcomes the limitations of traditional Raman spectroscopy. This technique builds on the principles of traditional Raman spectroscopy but utilizes ultrafast laser pulses with durations on the order of femtoseconds to probe molecular vibrations with extremely fine time resolution. Furthermore, FSRS is inherently more sensitive than traditional Raman spectroscopy, as it can generate larger Raman signals from small or dilute samples. This allows the study of dynamics of chemical reactions and other fast processes at the molecular level such as the reactive intermediates of OER, shedding light on the mechanisms behind these processes in a way that was previously impossible.

FSRS was developed to overcome these limitations of traditional Raman spectroscopy. By utilizing ultrafast laser pulses with durations on the order of femtoseconds, FSRS can probe molecular vibrations with unprecedented time resolution, allowing researchers to study fast processes on timescales as short as tens of femtoseconds[142]. Furthermore, FSRS is inherently more sensitive than traditional Raman spectroscopy, as it incorporates the use of stimulated transitions as opposed to spontaneous transitions in traditional Raman spectroscopy. Another advantage of FSRS is its ability to selectively probe specific vibrational modes of molecules. For

our purposes, exploring the intermediates of OER created in the excited state of the system, FSRS allows us to resonate on the broadband optical transitions of the O* intermediates and differentiate them using their unique vibrational signatures. This allows us to selectively study the dynamics of specific molecular vibrations associated with the reactive intermediates of OER, which can provide insights into the OER mechanisms and its intermediate populations. A schematic of how FSRS will be applied to study the reactive intermediates of OER is shown in figure 6.1.

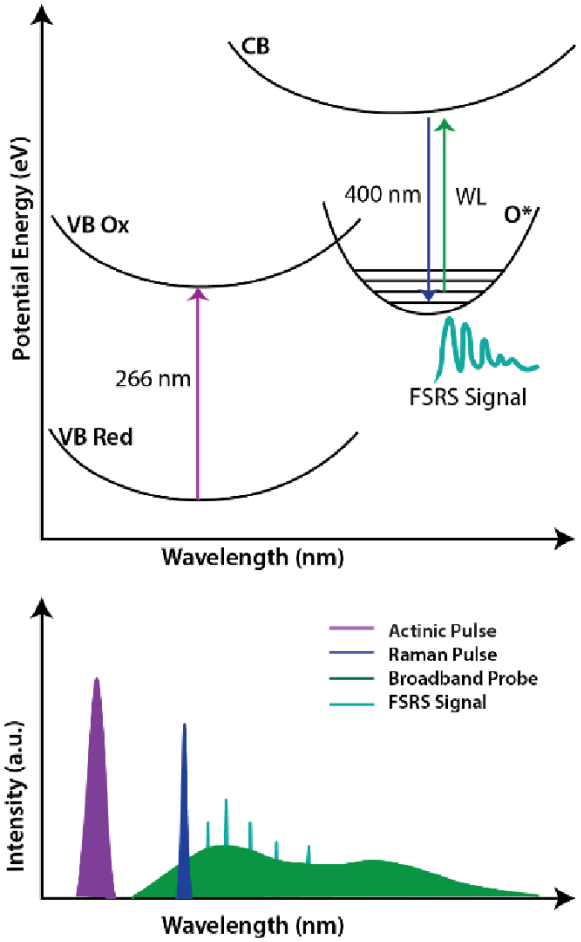

Figure 6.1: Top) PE surface of FSRS set up, with actinic (266 nm) beam exciting the catalytic surface while the Raman & WL beams stimulate a coherence between vibrational energy levels (Bottom) Spectral content of the three beams and the FSRS signal.

To perform FSRS experiments and study the excited state intermediates of OER the optical spectroscopy setup needs to be updated. A third beam, known as the

Raman Pump, needs to be added. Additionally, the WLC probe needs to be modified as well. The optical setup was also updated to be able to support both transmissive and reflective geometries to allow for more versatility in the setup as well as allowing the use of liquid samples which can be used to troubleshoot the setup.

Raman Pump (400 nm): Second Harmonic Generation (SHG)

The Raman pump suitable for our experiments is a narrowband (± 0.2 nm) pulse centered at 400 nm with a pulse duration of 1 ns. Ideally, for FSRS the temporal energy profile of the Raman pump would be very asymmetrical. All these requirements for the Raman pump are fulfilled by having the 800 nm fundamental go through a second harmonic generation (SHG) stage, similar to the first part of the THG generation process detailed in chapter 2, to output 400 nm light, and then an Etalon (Fabry-Perot interferometer).

The Etalon is basically an optical cavity made of two highly reflective mirrors that are parallel to each other and separated by a small distance. When light is incident on the etalon, it is partially reflected by each of the mirrors. The reflected waves then interfere with each other, producing a pattern of constructive and destructive interference. The resulting interference pattern depends on the wavelength of the incident light and the distance between the mirrors. The output of an etalon is usually tuned to a certain wavelength of light and is determined by the spacing between the highly reflective mirrors. As a result, the etalon "selects" a certain wavelength from the input and outputs light of the selected wavelength with a very narrow spread. Effectively it turns the 400 ± 4 nm SHG output into 400 ± 0.2 nm light. An additional effect of this "selection" that the etalon performs is that since it rejects a lot of the other wavelengths, there is a decrease in total power along with the temporal intensity profile becoming highly asymmetric. Another consideration, specific to our system to some extent, is that the path length of the Raman pump line

needs to be the same as the path length for the probe which makes sure that any time delay introduced on the 266nm beam line affects the Raman pump and the WLC probe in the same way.

WLC Probe: Correction of Group Delay Dispersion (GDD)

The refractive index of any material is wavelength dependent, i.e., different wavelengths of light thus experience a slightly different refractive index when travelling through any material. The broadband WLC (375 nm - 700 nm) probe accumulates a significant amount of "positive" group delay dispersion (GDD) because of transmissive optics and the column of aqueous solution that it must travel through to get to the sample. This effectively makes the time zero delay point, with respect to the pump (266 nm), for different parts of the WLC spectrum different. GDD of the WLC probe in TR experiments doesn't affect the generation of signal so it is commonly addressed during post processing of the data. However, in FSRS the GDD of the WLC probe does affect generation of signal and ideally, we would like no GDD within the WLC probe. This is achieved by sending the WLC probe through a "chirped mirror pair" which introduces "negative" GDD to counteract the "positive" GDD that the WLC probe will inevitably accumulate. This results in minimizing the GDD within the WLC probe when it reaches the sample. A noticeable tradeoff for using a chirped mirror pair is a reduction in the bandwidth of the WLC probe which for our FSRS setup, encompasses a wavelength range of 375 nm to 450 nm. This wavelength range is plenty since we are probing vibrations. With respect to the Raman pump, centered at 400 nm, the WLC probe with its reduced bandwidth encompasses a range of -1500 to ~3000 cm^{-1} allowing a large stokes window as well as a significant anti-stokes window. The FSRS optical setup is shown schematically in figure (6.2).

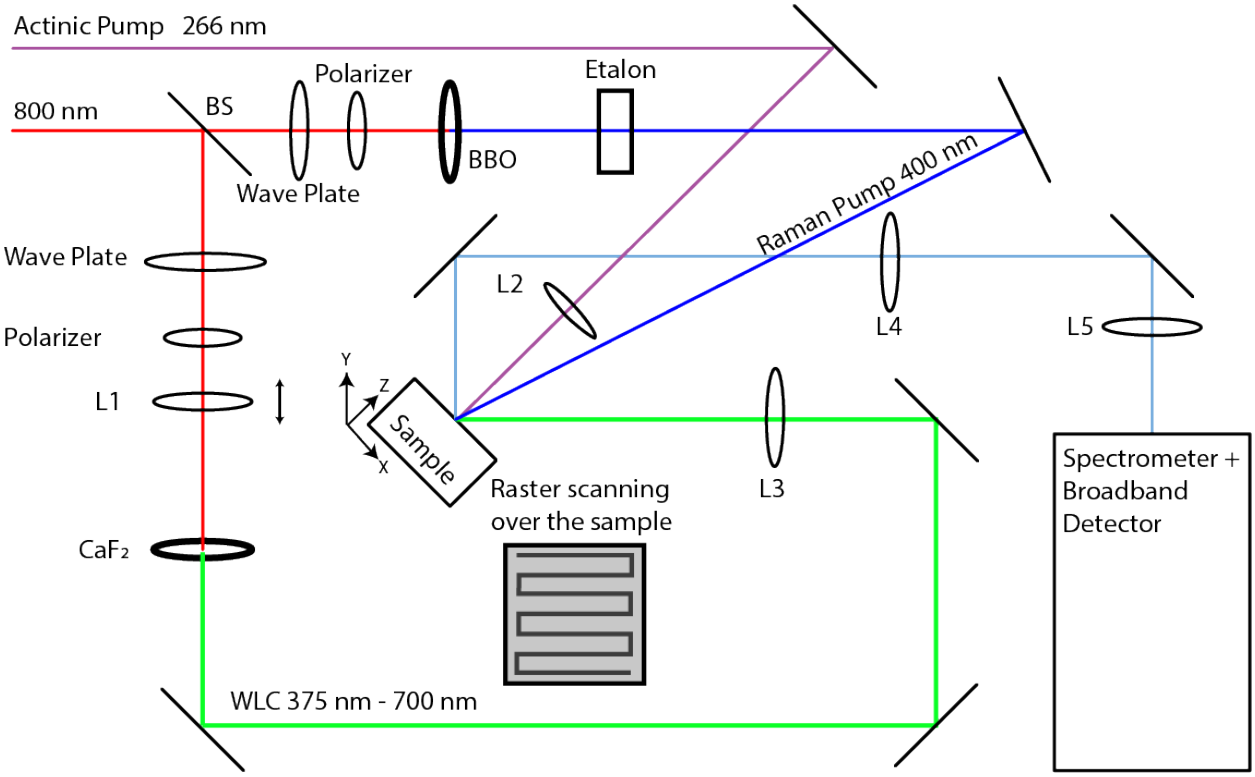

Figure 6.2: Ground state Raman spectra of methanol acquired using FSRS.

FSRS on Single Crystal STO during OER

FSRS can be executed using just the Raman pump and the WLC probe, doing so gives us the ground state Raman spectra. We confirmed that our optical setup can execute FSRS by acquiring the ground spectra of methanol, a standard chemical with a well characterized Raman spectra and is shown in figure 6.3.

We then performed FSRS experiments on the single crystal STO/aqueous interface in both ground state and the excited state but were unfortunately unable to see any appreciable signal in the excited state from the interface in reflection geometry. A possible reason for this is a small absorption cross-section of the species at the interface for stimulated Raman spectroscopy. We were able to get a ground state Raman spectrum of the STO bulk using the transmission geometry without being exposed to the aqueous solution, as shown in figure 6.4. A detailed analysis of this spectra isn't available at the time of writing this thesis.

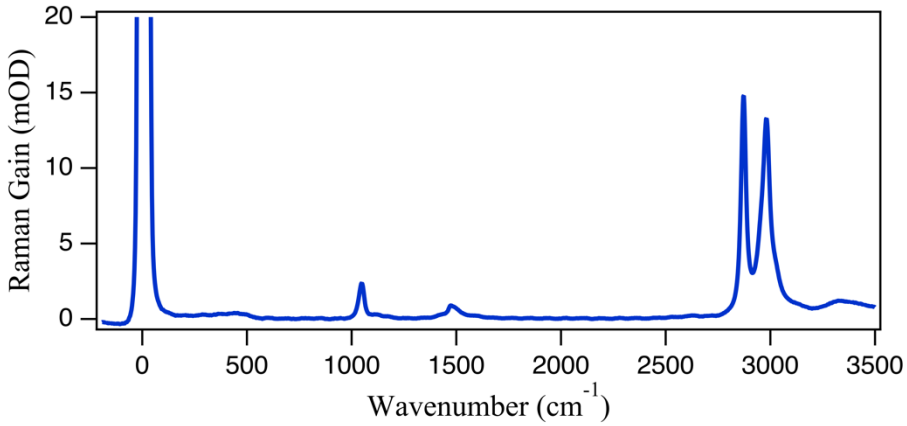

Figure 6.3: Ground state Raman spectra of methanol acquired using FSRS.

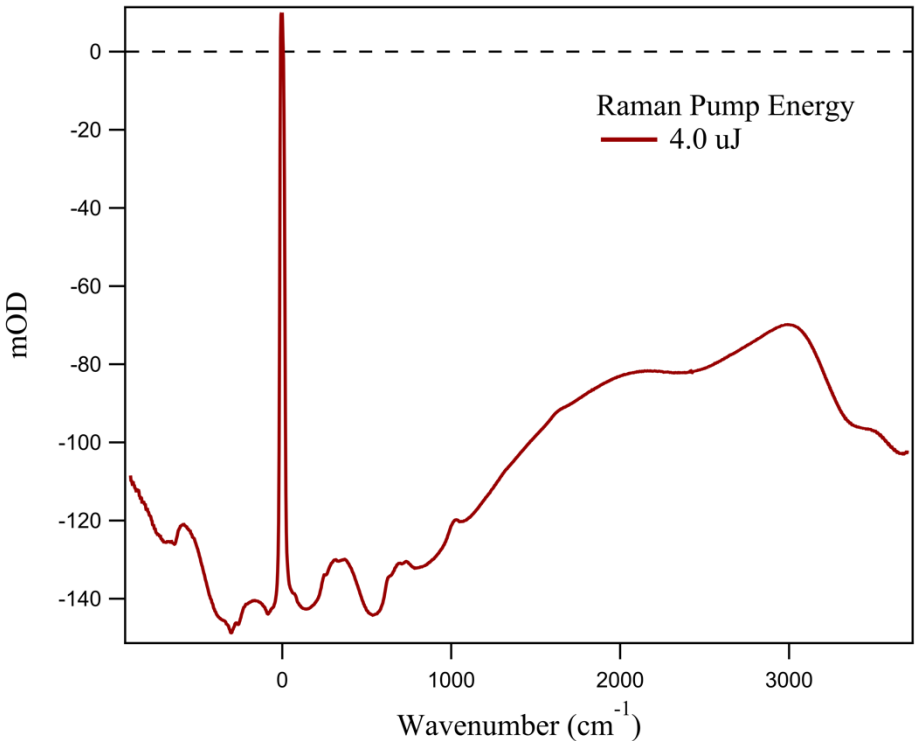

Figure 6.4: Ground state Raman spectra of bulk STO acquired using FSRS.

Future Work

The work presented in this thesis has made significant contributions to better our understanding of the oxygen evolution reaction on a semiconductor/aqueous interface through the application of time resolved pump probe spectroscopy along with the development of experimental methodologies, analysis methods, and phenomenological modelling. However, there are several open questions that have yet to be addressed along with avenues for future research that could further expand upon these findings.

Firstly, one could explore other catalytic semiconductors in an aqueous environment, such as TiO_2 and RuO_2, and determine if these materials also exhibit the Langmuir reaction isotherm for reactive intermediates formed in the excited state of the system as seen in STO. If they do, then one could compare the reaction isotherms across an axis of catalytic materials to generalize the understanding of OER and the associated models that describe the formation of reactive intermediates.

Secondly, the analysis performed in chapter 3 shows that the excited state absorption signal along with the second exponentially growing population (with a time constant of ~60 ps) are both independent on almost all reaction conditions except for the fluence. Experiments could be designed and performed to explore the indifference of these two features of the system to make a better assignment for them and understand them.

Thirdly, since the single crystal STO/aqueous interface isn't sensitive to vibrational probing using FSRS, one could use alternative forms of STO, e.g., STO nanoparticles, that can have a higher cross-section of absorption and can possibly show a higher signal when probed using FSRS. This would greatly help in exploring the identities of the reactive intermediates which will retroactively help improve the phenomenological models developed in this work.

BIBLIOGRAPHY

1. Hammer, B.; Norskov, J. K., Theoretical surface science and catalysis--calculations and concepts. Advances in Catalysis **2004**, 45, 71-129.
2. Markovic, N. M., Electrocatalysis: Interfacing electrochemistry. Nature materials **2013**, 12 (2),101-2.
3. Rossmeisl, J.; Qu, Z. W.; Zhu, H.; Kroes, G. J.; Nørskov, J. K., Electrolysis of water on oxide surfaces. Journal of Electroanalytical Chemistry **2007**, 607 (1-2), 83-89.
4. Kern, J.; Chatterjee, R.; Young, I. D.; Fuller, F. D.; Lassalle, L.; Ibrahim, M.; Gul, S.; Fransson, T.; Brewster, A. S.; Alonso-Mori, R.; Hussein, R.; Zhang, M.; Douthit, L.; de Lichtenberg, C.; Cheah, M. H.; Shevela, D.; Wersig, J.; Seuffert, I.; Sokaras, D.; Pastor, E.; Weninger, C.; Kroll, T.; Sierra, R. G.; Aller, P.; Butryn, A.; Orville, A. M.; Liang, M.; Batyuk, A.; Koglin, J. E.; Carbajo, S.; Boutet, S.; Moriarty, N. W.; Holton, J. M.; Dobbek, H.; Adams, P. D.; Bergmann, U.; Sauter, N. K.; Zouni, A.; Messinger, J.; Yano, J.; Yachandra, V. K., Structures of the intermediates of Kok's photosynthetic water oxidation clock. Nature **2018,** 563 (7731), 421-425.
5. Zhang, M.; Frei, H., Towards a Molecular Level Understanding of the Multi-Electron Catalysis of Water Oxidation on Metal Oxide Surfaces. Catalysis Letters **2014**, 145 (1), 420-435.
6. Seh, Z. W.; Kibsgaard, J.; Dickens, C. F.; Chorkendorff, I.; Norskov, J. K.; Jaramillo, T. F., Combining theory and experiment in electrocatalysis: Insights into materials design. Science **2017**, 355 (6321).
7. A. Marshall, M. Tsypkin, B. Børresen, G. Hagen, R. Tunold, Preparation and characterization of nanocrystalline IrxSn1−xO2 electrocatalytic powders. Mater. Chem. Phys. 94 (**2005**) 226–232.
8. (a) S. Trasatti, Electrocatalysis in the anodic evolution of oxygen and chlorine. Electrochim. Acta. 29 (**1983**) 1503–1512; (b) S. Trasatti, Physical electrochemistry of ceramic oxides. Electrochim. Acta. 36 (**1991**) 225–241.
9. A. Marshall, M. Tsypkin, B. Børresen, G. Hagen, R. Tunold, Nanocrystalline $Ir_xSn_{(1-x)}O_2$ Electrocatalysts for Oxygen Evolution in Water Electrolysis with Polymer Electrolyte – Effect of Heat Treatment. J. New Mater. Electrochem. Syst. 7 (**2004**) 197–204.
10. Busch, M.; Halck, N. B.; Kramm, U. I.; Siahrostami, S.; Krtil, P.; Rossmeisl, J., Beyond the top of the volcano? – A unified approach to electrocatalytic oxygen reduction and oxygen evolution. Nano Energy **2016**, 29, 126-135.
11. Weckhuysen, B. M., Chemical Imaging of Spatial Heterogeneities in Catalytic Solids at Different Length and Time Scales. Angew. Chem.-Int. Edit. **2009**, 48 (27), 4910-4943.
12. Buurmans, I. L. C.; Weckhuysen, B. M., Heterogeneities of individual catalyst particles in space and time as monitored by spectroscopy. Nat. Chem. **2012**, 4 (11), 873-886.

13. Norskov, J. K.; Bligaard, T.; Hvolbaek, B.; Abild-Pedersen, F.; Chorkendorff, I.; Christensen, C. H., The nature of the active site in heterogeneous metal catalysis. Chem. Soc. Rev. **2008**, 37 (10), 2163-2171.
14. Hammarstrom, L.; Hammes-Schiffer, S., Artificial Photosynthesis and Solar Fuels. *Accounts of Chemical Research* **2009,** *42* (12), 1859-1860.
15. Truhlar, D. G.; Garrett, B. C.; Klippenstein, S. J., Current Status of Transition-State Theory. *J. Phys. Chem.* **1996,** *100*, 12771-12800.
16. Dellago, C.; Bolhuis, P. G.; Csajka, F. S.; Chandler, D., Transition path sampling and the calculation of rate constants. *The Journal of Chemical Physics* **1998,** *108* (5), 1964-1977.
17. Stewart, G. W., On the Early History of the Singular Value Decomposition. *SIAM Review* **1993,** *35* (4), 551-566.
18. Fano, U., *Physical Review* **1961,** *124*, 1866.
19. Man, I. C.; Su, H.-Y.; Calle-Vallejo, F.; Hansen, H. A.; Martínez, J. I.; Inoglu, N. G.; Kitchin, J.; Jaramillo, T. F.; Nørskov, J. K.; Rossmeisl, J., Universality in Oxygen Evolution Electrocatalysis on Oxide Surfaces. ChemCatChem **2011**, 3 (7), 1159-1165.
20. Cheng, J.; VandeVondele, J.; Sprik, M., Identifying Trapped Electronic Holes at the Aqueous TiO2 Interface. J. Phys. Chem. C **2014**, 118 (10), 5437-5444.
21. Chen, X.; Choing, S. N.; Aschaffenburg, D. J.; Pemmaraju, C. D.; Prendergast, D.; Cuk, T., The formation time of Ti-O• and Ti-O•-Ti radicals at the n-SrTiO3/aqueous interface during photocatalytic water oxidation. Journal of the American Chemical Society **2017**, 139, 1830-1841.
22. Herlihy, D. M.; Waegele, M. M.; Chen, X.; Pemmaraju, C. D.; Prendergast, D.; Cuk, T., Detecting the oxyl radical of photocatalytic water oxidation at an n-SrTiO3/aqueous interface through its subsurface vibration. Nat Chem **2016**, 8 (6), 549-55.
23. Yamaguchi, Y.; Hida R.; Suzuki T.; Kannari F., Supercontinuum generation by self-phase modulation and induced phase modulation at fused silica thin plate array. 2017 Conference on Lasers and Electro-Optics Pacific Rim (CLEO-PR), Singapore, **2017**.
24. De Gryse, R.; Gomes P. W.; Cardon F.; Vennik J.; On the interpretation of Mott Schottky plots determined at semiconductor/electrolyte systems. J. Electrochem. Soc. **1975,** 122, 711.
25. Waegele, M. M.; Chen, X.; Herlihy, D. M.; Cuk, T. How Surface Potential Determines the Kinetics of the First Hole Transfer of Photocatalytic Water Oxidation. J. Am. Chem. Soc. **2014**, 136, 10632.
26. Sharma, S. K.; Pavithra, D.; Sivakumar, G.; Srinivasamurthy, N.; Agrawal, B. L., Determination of solar cell diffusion capacitance and its dependence on temperature and 1 MeV electron fluence level. *Solar Energy Materials and Solar Cells* **1992,** *26* (3), 169-179.
27. Xu, Y.; Schoonen, M. A. A., The absolute energy positions of conduction and valence bands of selected semiconducting minerals. *American Mineralogist* **2000,** *85* (3-4), 543-556.

28. Sundararaman, R.; Letchworth-Weaver, K.; Schwarz, K. A., Improving accuracy of electrochemical capacitance and solvation energetics in first-principles calculations. *The Journal of Chemical Physics* **2018,** *148* (14), 144105.
29. Li, J.-Q.; Meng, L.; Sprik, M.; Cheng, J., Thermodynamic Investigation of Proton/Electron Interplay on the Pourbaix Diagram at the TiO2/Electrolyte Interface. *The Journal of Physical Chemistry C* **2020,** *124* (35), 19003-19014.
30. Vinogradov, I., Singh, S., Lyle, H. et al. Free energy difference to create the M-OH*intermediate of the oxygen evolution reaction by time-resolved optical spectroscopy. Nat. Mater. **2021**, 88–94 (2022)
31. Zhang, M., de Respinis, M. & Frei, H. Time-resolved observations of water oxidation intermediates on a cobalt oxide nanoparticle catalyst. *Nature Chem* 6, 362–367 (**2014**).
32. Zandi, O., Hamann, T. Determination of photoelectrochemical water oxidation intermediates on haematite electrode surfaces using operando infrared spectroscopy. *Nature Chem* **8**, 778–783 (**2016**).
33. Chen J, Li YF, Sit P, Selloni A. Chemical dynamics of the first proton-coupled electron transfer of water oxidation on TiO2 anatase. Journal of the American Chemical Society. **2013** Dec;135(50):18774-18777.
34. Kraack JP, Hamm P. Surface-Sensitive and Surface-Specific Ultrafast Two-Dimensional Vibrational Spectroscopy. Chem Rev. **2017** Aug 23;117(16):10623-10664.
35. Kraack, Jan & Käch, Andres & Hamm, Peter. (**2016**). Surface-Enhancement in Ultrafast 2D ATR IR Spectroscopy at the Metal-Liquid Interface. The Journal of Physical Chemistry C. 120. 3350-3359.
36. Klahr, B., Gimenez, S., Fabregat-Santiago, F., Bisquert, J. & Hamann, T. W. Photoelectrochemical and impedance spectroscopic investigation of water oxidation with "Co-Pi"-coated hematite electrodes. J. Am. Chem. Soc. 134, 16693–16700 (**2012**).
37. Chen, X.; Aschaffenburg, D. J.; Cuk, T., Selecting between two transition states by which water oxidation intermediates decay on an oxide surface. Nature Catalysis **2019**, 2 (9), 820-827.
38. Libuda J., Meusel, I., Hartmann, J. & Freund, H. J. A molecular beam/surface spectroscopy apparatus for the study of reactions on complex model catalysts. *Rev. Sci. Instrum*. 71, 4395–4408 (**2000**).
39. Parsons, R., The rate of electrolytic hydrogen evolution and the heat of adsorption of hydrogen. *Transactions of the Faraday Society* **1958,** *54* (0), 1053-1063.
40. Zhang, Y. et al. A review on thermalization mechanisms and prospect absorber materials for the hot carrier solar cells. Sol. Energy Mater. Sol. Cells 225, 111073 (**2021**).
41. Bhattacharya, C. et al. Sustainable nanoplasmon-enhanced photoredox reactions: synthesis, characterization, and applications. Adv. Energy Mater. 10, 2002402 (**2020**).
42. Janotti, A., Varley, J. B., Choi, M. & Van de Walle, C. G. Vacancies and small polarons in SrTiO3. Phys. Rev. B 90, 085202 (**2014**).

43. Chen, H. & Umezawa, N. Hole localization, migration, and the formation of peroxide anion in perovskite SrTiO3. Phys. Rev. B 90, 035202 (**2014**).
44. Rubano, A., Paparo, D., Granozio, F. M., Uccio, U. & Marrucci, L. Blue luminescence of SrTiO3 under intense optical excitation. J. Appl. Phys. 106, 103515 (**2009**).
45. Mochizuki, S., Fujishiro, F. & Minami, S. Photoluminescence and reversible photo-induced spectral change of SrTiO3. J. Phys. Condens. Matter 17, 923–948 (**2005**).
46. Schirmer, O. F. O− bound small polarons in oxide materials. J. Phys. Condens. Matter 18, R667–R704 (**2006**).
47. Deskins, N. A. & Dupuis, M. Intrinsic hole migration rates in TiO2 from density functional theory. J. Phys. Chem. C 113, 346–358 (**2009**).
48. Formal, F. L.; Pastor, E.; Tilley, D.; Mesa, C. A.; Pendlebury, S. R.; Gratzel, M.; Durrant, J. R., Rate Law Analysis of Water Oxidation on a Hematite Surface. J. Am. Chem. Soc. **2015**, 137, 6629-6637.
49. Kafizas, A.; Ma, Y.; Pastor, E.; Pendlebury, S. R.; Mesa, C.; Francàs, L.; Le Formal, F.; Noor, N.; Ling, M.; Sotelo-Vazquez, C.; Carmalt, C. J.; Parkin, I. P.; Durrant, J. R., Water Oxidation Kinetics of Accumulated Holes on the Surface of a TiO2 Photoanode: A Rate Law Analysis. ACS Catalysis **2017**, 7 (7), 4896-4903.
50. Mandal, A., Ramasesha, K., Marco, L. D. & Tokmakoff, A. Collective vibrations of water-solvated hydroxide ions investigated with broadband 2DIR spectroscopy. J. Chem. Phys. 140, 204508 (**2014**).
51. Baiz, C. R., Peng, C. S., Reppert, M. E., Jones, K. C. & Tokmakoff, A. Coherent two-dimensional infrared spectroscopy: quantitative analysis of protein secondary structure in solution. Analyst 137, 1793–1799 (**2012**).
52. Guhl, H.; Miller, W.; Reuter, K., Water adsorption and dissociation on $SrTiO_3$(001) revisited: A density functional theory study. Physical Review B **2010**, 81 (15).
53. Hinojosa, B. B.; Van Cleve, T.; Asthagiri, A., A first-principles study of H_2O adsorption and dissociation on the SrTiO3(100) surface. Mol. Simul. **2010**, 36 (7-8), 604-617.
54. Holmstrom, E., Spijker, P., and Foster, A.S., The interface of $SrTiO_3$ and H_2O from density functional theory molecular dynamics. Proc. R. Soc. A. 472, **2016** 0293.
55. Roberts, S. T., Ramasesha, K., Petersen, P. B., Mandal, A. & Tokmakoff, A. Proton transfer in concentrated aqueous hydroxide visualized using ultrafast infrared spectroscopy. J. Phys. Chem. A 115, 3957–3972 (**2011**).
56. Marx, D., Chandra, A. & Tuckerman, M. E. Aqueous basic solutions: hydroxide solvation, structural diffusion, and comparison to the hydrated proton. Chem. Rev. 110, 2174–2216 (**2010**).
57. Perakis, F., Widmer, S. & Hamm, P. Two-dimensional infrared spectroscopy of isotope-diluted ice Ih. J. Chem. Phys. 134, 204505 (**2011**).
58. De Marco, L. et al. Differences in the vibrational dynamics of H2O and D2O: observation of symmetric and antisymmetric stretching vibrations in heavy water. J. Phys. Chem. Lett. 7, 1769–1774 (**2016**).

59. Selcuk, S. & Selloni, A. Facet-dependent trapping and dynamics of excess electrons at anatase TiO2 surfaces and aqueous interfaces. Nat. Mater. 15, 1107–1112 (**2016**).
60. Swenson, H.; Stadie, N. P., Langmuir's Theory of Adsorption: A Centennial Review. Langmuir **2019**, 35 (16), 5409-5426.
61. Vojvodic, A.; Nørskov, J. K. Optimizing Perovskites for the Water-Splitting Reaction. Science **2011**, 334, 1355.
62. Hwang, J.; Feng, Z.; Charles, N.; Wang, X. R.; Lee, D.; Stoerzinger, K. A.; Muy, S.; Rao, R. R.; Lee, D.; Jacobs, R.; Morgan, D.; Shao-Horn, Y. Tuning perovskite oxides by strain: Electronic structure, properties, and functions in (electro)catalysis and ferroelectricity. Mater. Today **2019**, 31, 100.
63. Kuo, D.-Y.; Eom, C. J.; Kawasaki, J. K.; Petretto, G.; Nelson, J. N.; Hautier, G.; Crumlin, E. J.; Shen, K. M.; Schlom, D. G.; Suntivich, J. Influence of Strain on the Surface−Oxygen Interaction and the Oxygen Evolution Reaction of SrIrO3. J. Phys. Chem. C **2018**, 122, 4359.
64. Akhade, S. A.; Kitchin, J. R. Effects of strain, d-band filling, and oxidation state on the surface electronic structure and reactivity of 3d perovskite surfaces. J. Chem. Phys. **2012**, 137, No. 084703.
65. Zhang, R. H.; Dubouis, N.; Ben Osman, M.; Yin, W.; Sougrati, M. T.; Corte, D. A. D.; Giaume, D.; Grimaud, A. A Dissolution/ Precipitation Equilibrium on the Surface of Iridium-Based Perovskites Controls Their Activity as Oxygen Evolution Reaction Catalysts in Acidic Media. Angew. Chem., Int. Ed. **2019**, 58, 4571.
66. Kim, B. J.; Cheng, X.; Abbott, D. F.; Fabbri, E.; Bozza, F.; Graule, T.; Castelli, I. E.; Wiles, L.; Danilovic, N.; Ayers, K. E.; Marzari, N.; Schmidt, T. J. Highly Active Nanoperovskite Catalysts for Oxygen Evolution Reaction: Insights into Activity and Stability of Ba0.5Sr0.5Co0.8Fe0.2O2+delta and PrBaCo2O5+delta. Adv. Funct. Mater. **2018**, 28, 1804355.
67. Han, B. H.; Risch, M.; Lee, Y. L.; Ling, C.; Jia, H. F.; Shao- Horn, Y. Activity and stability trends of perovskite oxides for oxygen evolution catalysis at neutral pH. Phys. Chem. Chem. Phys. **2015**, 17, 22576.
68. Kim, B. J.; Abbott, D. F.; Cheng, X.; Fabbri, E.; Nachtegaal, M.; Bozza, F.; Castelli, I. E.; Lebedev, D.; Schaublin, R.; Coperet, C.; Graule, T.; Marzari, N.; Schmidt, T. J. Unraveling Thermodynamics, Stability, and Oxygen Evolution Activity of Strontium Ruthenium Perovskite Oxide. ACS Catal. **2017**, 7, 3245.
69. Toma, F. M.; Cooper, J. K.; Kunzelmann, V.; McDowell, M. T.; Yu, J.; Larson, D. M.; Borys, N. J.; Abelyan, C.; Beeman, J. W.; Yu, K. M.; Yang, J. H.; Chen, L.; Shaner, M. R.; Spurgeon, J.; Houle, F. A.; Persson, K. A.; Sharp, I. D. Mechanistic insights into chemical and photochemical transformations of bismuth vanadate photoanodes. Nat. Commun. **2016**, DOI: 10.1038/ncomms12012.
70. Binninger, T.; Mohamed, R.; Waltar, K.; Fabbri, E.; Levecque, P.; Kotz, R.; Schmidt, T. J. Thermodynamic explanation of the universal correlation between oxygen evolution activity and corrosion of oxide catalysts. Sci. Rep. **2015**, 5, 12167.

71. Thomsen, C.; Grahn, H. T.; Maris, H. J.; Tauc, J. Surface generation and detection of phonons by picosecond light pulses. Phys. Rev. B: Condens. Matter Mater. Phys. **1986**, 34, 4129.
72. Gusev, V. E.; Ruello, P. Advances in applications of timedomain Brillouin scattering for nanoscale imaging. Appl. Phys. Rev. **2018**, 5, No. 031101.
73. Pollock, K. L.; Doan, H. Q.; Rustagi, A.; Stanton, C. J.; Cuk, T. Detecting the Photoexcited Carrier Distribution Across GaAs/ Transition Metal Oxide Interfaces by Coherent Longitudinal Acoustic Phonons. J. Phys. Chem. Lett. **2017**, 8, 922.
74. Mante, P.-A.; Stoumpos, C. C.; Kanatzidis, M. G.; Yartsev, A. Electron−acoustic phonon coupling in single crystal CH3NH3PbI3 perovskites revealed by coherent acoustic phonons. Nat. Commun. **2017**, 8, 14398.
75. Willatzen, M.; Wang, Z. L. Unified treatment of coupled optical and acoustic phonons in piezoelectric cubic materials. Phys. Rev. B: Condens. Matter Mater. Phys. **2015**, 92, 224101.
76. Chen, I. J.; Mante, P.-A.; Chang, C.-K.; Yang, S.-C.; Chen, H.- Y.; Huang, Y.-R.; Chen, L.-C.; Chen, K.-H.; Gusev, V.; Sun, C.-K. Graphene-to-Substrate Energy Transfer through Out-of-Plane Longitudinal Acoustic Phonons. Nano Lett. **2014**, 14, 1317.
77. Brivio, S.; Polli, D.; Crespi, A.; Osellame, R.; Cerullo, G.; Bertacco, R. Observation of anomalous acoustic phonon dispersion in SrTiO3 by broadband stimulated Brillouin scattering. Appl. Phys. Lett. **2011**, 98, 211907.
78. Aschaffenburg, D. J.; Chen, X.; Cuk, T. Faradaic oxygen evolution from SrTiO3 under nano- and femto-second pulsed light excitation. Chem. Commun. **2017**, 53, 7254.
79. Feng, Y.; Vinogradov, I.; Ge, N.-H. Optimized noise reduction scheme for heterodyne spectroscopy using array detectors. Opt. Express 2019, 27, 20323.
80. Lu, Y.; Jia, D.; Gao, F.; Chen, Z.; Hu, T. First-principles study on the elastic properties of Sr−Ti−O ceramics. Solid State Commun. **2014**, 182, 43.
81. Morrissey, F. X.; Dexheimer, S. L. Coherent acoustic phonon generation in exciton self-trapping. Phys. Rev. B: Condens. Matter Mater. Phys. **2010**, 81, No. 094302.
82. Thomsen, C.; Grahn, H. T.; Maris, H. J.; Tauc, J. Picosecond interferometric technique for study of phonons in the brillouin frequency range. Opt. Commun. **1986**, 60, 55.
83. Babilotte, P.; Ruello, P.; Pezeril, T.; Vaudel, G.; Mounier, D.; Breteau, J.-M.; Gusev, V. Transition from piezoelectric to deformation potential mechanism of hypersound photogeneration in n-doped GaAs semiconductors. J. Appl. Phys. **2011**, 109, No. 064909.
84. Daimon, M.; Masumura, A. Measurement of the refractive index of distilled water from the near-infrared region to the ultraviolet region. Appl. Opt. **2007**, 46, 3811.
85. Polyanskiy, M. N. Refractive index database. https:// refractiveindex.info/?shelf=main&book=H2O&page=Daimon-21.5C (accessed 2021-03-12).
86. Matsuda, O.; Wright, O. B. Laser picosecond acoustics in a two-layer structure with oblique probe light incidence. Ultrasonics **2004**, 42, 653.

87. Bushnell, J. C.; McCloskey, D. J. Thermoelastic Stress Production in Solids. J. Appl. Phys. **1968**, 39, 5541.
88. Voorhees, P. W.; Johnson, W. C. The Thermodynamics of Elastically Stressed Crystals. In Solid State Physics; Ehrenreich, H., Spaepen, F., Eds.; Academic Press, **2004**; Vol. 59, pp 1.
89. Adler, S. Chemical Expansivity of Electrochemical Ceramics. J. Am. Ceram. Soc. **2001**, 84, 2117.
90. Wemple, S. H.; DiDomenico, M. Theory of the Elasto-Optic Effect in Nonmetallic Crystals. Phys. Rev. B 1970, 1, 193.
91. de Ligny, D.; Richet, P. High-temperature heat capacity and thermal expansion of SrTiO3 and SrZrO3 perovskites. Phys. Rev. B: Condens. Matter Mater. Phys. **1996**, 53, 3013.
92. Pesquera, D.; Herranz, G.; Barla, A.; Pellegrin, E.; Bondino, F.; Magnano, E.; Sánchez, F.; Fontcuberta, J. Surface symmetry-breaking and strain effects on orbital occupancy in transition metal perovskite epitaxial films. Nat. Commun. **2012**, 3, 1189.
93. Fröhlich, H. Electrons in lattice fields. Adv. Phys. **1954**, 3, 325.
94. Holstein, T. Studies of polaron motion: Part II. The "small" polaron. Ann. Phys. **1959**, 8, 343.
95. Austin, I. G.; Mott, N. F. Polarons in crystalline and noncrystalline materials. Adv. Phys. **1969**, 18, 41.
96. Higashimura, T. Second-order energy shifts of the three types of bound polarons: the Frohlich, deformation potential and piezoelectric polarons. J. Phys. C: Solid State Phys. **1987**, 20, 723.
97. Peeters, F. M.; Devreese, J. T. Acoustical polaron in three dimensions: The ground-state energy and the self-trapping transition. Phys. Rev. B: Condens. Matter Mater. Phys. **1985**, 32, 3515.
98. Engineer, M.; Whitfield, G. Strong-Coupled Piezoelectric Polaron. Phys. Rev. **1969**, 179, 869.
99. Yang, M.-M.; Luo, Z.-D.; Mi, Z.; Zhao, J.; E, S. P.; Alexe, M. Piezoelectric and pyroelectric effects induced by interface polar symmetry. Nature **2020**, 584, 377.
100. Meirzadeh, E.; Christensen, D. V.; Makagon, E.; Cohen, H.; Rosenhek-Goldian, I.; Morales, E. H.; Bhowmik, A.; Lastra, J. M. G.; Rappe, A. M.; Ehre, D.; Lahav, M.; Pryds, N.; Lubomirsky, I. Surface Pyroelectricity in Cubic SrTiO3. Adv. Mater. **2019**, 31, 1904733.
101. Wu, B.; Ning, W.; Xu, Q.; Manjappa, M.; Feng, M.; Ye, S.; Fu, J.; Lie, S.; Yin, T.; Wang, F.; Goh, T. W.; Harikesh, P. C.; Tay, Y. K. E.; Shen, Z. X.; Huang, F.; Singh, R.; Zhou, G.; Gao, F.; Sum, T. C. Strong self-trapping by deformation potential limits photovoltaic performance in bismuth double perovskite. Sci. Adv. **2021**, 7, eabd3160.
102. Suntivich, J.; May, K. J.; Gasteiger, H. A.; Goodenough, J. B.; Shao-Horn, Y. A Perovskite Oxide Optimized for Oxygen Evolution Catalysis from Molecular Orbital Principles. Science **2011**, 334, 1383.

103. Grimaud, A.; May, K. J.; Carlton, C. E.; Lee, Y.-L.; Risch, M.; Hong, W. T.; Zhou, J.; Shao-Horn, Y. Double perovskites as a family of highly active catalysts for oxygen evolution in alkaline solution. Nat. Commun. **2013**, 4, 2439.
104. Montoya, J. H.; Doyle, A. D.; Nørskov, J. K.; Vojvodic, A. Trends in adsorption of electrocatalytic water splitting intermediates on cubic ABO3 oxides. Phys. Chem. Chem. Phys. **2018**, 20, 3813.
105. Suntivich, J.; Gasteiger, H. A.; Yabuuchi, N.; Nakanishi, H.; Goodenough, J. B.; Shao-Horn, Y. Design principles for oxygenreduction activity on perovskite oxide catalysts for fuel cells and metal–air batteries. Nat. Chem. **2011**, 3, 546.
106. Petrie, J. R.; Cooper, V. R.; Freeland, J. W.; Meyer, T. L.; Zhang, Z.; Lutterman, D. A.; Lee, H. N. Enhanced Bifunctional Oxygen Catalysis in Strained LaNiO3 Perovskites. J. Am. Chem. Soc. **2016**, 138, 2488.
107. Calle-Vallejo, F.; Inoglu, N. G.; Su, H.-Y.; Martínez, J. I.; Man, I. C.; Koper, M. T. M.; Kitchin, J. R.; Rossmeisl, J. Number of outer electrons as descriptor for adsorption processes on transition metals and their oxides. Chemical Science **2013**, 4, 1245.
108. Kuo, D.-Y.; Paik, H.; Kloppenburg, J.; Faeth, B.; Shen, K. M.; Schlom, D. G.; Hautier, G.; Suntivich, J. Measurements of Oxygen Electroadsorption Energies and Oxygen Evolution Reaction on RuO2(110): A Discussion of the Sabatier Principle and Its Role in Electrocatalysis. J. Am. Chem. Soc. **2018**, 140, 17597.
109. Kuo, D.-Y.; Kawasaki, J. K.; Nelson, J. N.; Kloppenburg, J.; Hautier, G.; Shen, K. M.; Schlom, D. G.; Suntivich, J. Influence of Surface Adsorption on the Oxygen Evolution Reaction on IrO2(110). J. Am. Chem. Soc. **2017**, 139, 3473.
110. Brown, D. W.; Lindenberg, K.; West, B. J. On the dynamics of polaron formation in a deformable medium. J. Chem. Phys. **1986**, 84, 1574.
111. Asbury, J. B.; Steinel, T.; Kwak, K.; Corcelli, S. A.; Lawrence, C. P.; Skinner, J. L.; Fayer, M. D. Dynamics of water probed with vibrational echo correlation spectroscopy. J. Chem. Phys. **2004**, 121, 12431.
112. Asbury, J. B.; Steinel, T.; Stromberg, C.; Corcelli, S. A.; Lawrence, C. P.; Skinner, J. L.; Fayer, M. D. Water Dynamics: Vibrational Echo Correlation Spectroscopy and Comparison to Molecular Dynamics Simulations. J. Phys. Chem. A **2004**, 108, 1107.
113. Loparo, J. J.; Roberts, S. T.; Tokmakoff, A. Multidimensional infrared spectroscopy of water. I. Vibrational dynamics in twodimensional IR line shapes. J. Chem. Phys. **2006**, 125, 194521.
114. Sanders, S. E.; Vanselous, H.; Petersen, P. B. Water at surfaces with tunable surface chemistries. J. Phys.: Condens. Matter **2018**, 30, 113001.
115. Pourbaix, M., In *Lectures on Electrochemical Corrosion*, Plenum Press: New York-London, 1973.
116. Hu, S.; Lewis, N. S.; Ager, J. W.; Yang, J.; McKone, J. R.; Strandwitz, N. C., Thin-Film Materials for the Protection of Semiconducting Photoelectrodes in Solar-Fuel Generators. *The Journal of Physical Chemistry C* **2015,** *119* (43), 24201-24228.

117. Eichhorn, J.; Liu, G. J.; Toma, F. M., Degradation of Semiconductor Electrodes in Photoelectrochemical Devices: Principles and Case Studies. In *Integrated Solar Fuel Generators*, Sharp, I. D.; Atwater, H. A.; Lewerenz, H. J., Eds. **2019**; Vol. 22, pp 281-303.
118. Venugopal, A.; Kas, R.; Hau, K.; Smith, W. A., Operando Infrared Spectroscopy Reveals the Dynamic Nature of Semiconductor-Electrolyte Interface in Multinary Metal Oxide Photoelectrodes. *Journal of the American Chemical Society* **2021,** *143* (44), 18581-18591
119. May, K. J.; Carlton, C. E.; Stoerzinger, K. A.; Risch, M.; Suntivich, J.; Lee, Y. L.; Grimaud, A.; Shao-Horn, Y., Influence of Oxygen Evolution during Water Oxidation on the Surface of Perovskite Oxide Catalysts. *Journal of Physical Chemistry Letters* **2012,** *3* (22), 3264-3270.
120. Risch, M.; Grimaud, A.; May, K. J.; Stoerzinger, K. A.; Chen, T. J.; Mansour, A. N.; Shao-Horn, Y., Structural Changes of Cobalt-Based Perovskites upon Water Oxidation Investigated by EXAFS. *The Journal of Physical Chemistry C* **2013,** *117* (17), 8628-8635.
121. Wan, G.; Freeland, J. W.; Kloppenburg, J.; Petretto, G.; Nelson, J. N.; Kuo, D. Y.; Sun, C. J.; Wen, J. G.; Diulus, J. T.; Herman, G. S.; Dong, Y. Q.; Kou, R. H.; Sun, J. Y.; Chen, S.; Shen, K. M.; Schlom, D. G.; Rignanese, G. M.; Hautier, G.; Fong, D. D.; Feng, Z. X.; Zhou, H.; Suntivich, J., Amorphization mechanism of SrIrO3 electrocatalyst: How oxygen redox initiates ionic diffusion and structural reorganization. *Science Advances* **2021,** *7* (2).
122. Strickler, A. L.; Higgins, D.; Jaramillo, T. F., Crystalline Strontium Iridate Particle Catalysts for Enhanced Oxygen Evolution in Acid. *Acs Applied Energy Materials* **2019,** *2* (8), 5490-5498.
123. Yang, Y.; Ling, Y.; Wang, G.; Liu, T.; Wang, F.; Zhai, T.; Tong, Y.; Li, Y., Photohole Induced Corrosion of Titanium Dioxide: Mechanism and Solutions. *Nano Letters* **2015,** *15* (10), 7051-7057.
124. Danilovic, N.; Subbaraman, R.; Chang, K. C.; Chang, S. H.; Kang, Y. J.; Snyder, J.; Paulikas, A. P.; Strmcnik, D.; Kim, Y. T.; Myers, D.; Stamenkovic, V. R.; Markovic, N. M., Activity-Stability Trends for the Oxygen Evolution Reaction on Monometallic Oxides in Acidic Environments. *The journal of physical chemistry letters* **2014,** *5* (14), 2474-8.
125. Xiong, Y.; Dabo, I., Influence of surface restructuring on the activity of SrTiO3 photoelectrodes for photocatalytic hydrogen reduction. **2019,** *3*.
126. Abdi, F. F.; Han, L.; Smets, A. H. M.; Zeman, M.; Dam, B.; van de Krol, R., Efficient solar water splitting by enhanced charge separation in a bismuth vanadate-silicon tandem photoelectrode. *Nature Communications* **2013,** *4* (1), 2195.
127. Seabold, J. A.; Choi, K.-S., Efficient and Stable Photo-Oxidation of Water by a Bismuth Vanadate Photoanode Coupled with an Iron Oxyhydroxide Oxygen Evolution Catalyst. *Journal of the American Chemical Society* **2012,** *134* (4), 2186-2192.

128. Nandjou, F.; Haussener, S., Modeling the Photostability of Solar Water-Splitting Devices and Stabilization Strategies. *ACS Applied Materials & Interfaces* **2022,** *14* (38), 43095-43108.
129. Laskowski, F. A. L.; Nellist, M. R.; Qiu, J.; Boettcher, S. W., Metal Oxide/(oxy)hydroxide Overlayers as Hole Collectors and Oxygen-Evolution Catalysts on Water-Splitting Photoanodes. *Journal of the American Chemical Society* **2019,** *141* (4), 1394-1405.
130. Nellist, M. R.; Qiu, J.; Laskowski, F. A. L.; Toma, F. M.; Boettcher, S. W., Potential-Sensing Electrochemical AFM Shows CoPi as a Hole Collector and Oxygen Evolution Catalyst on BiVO4 Water-Splitting Photoanodes. *ACS Energy Letters* **2018,** *3* (9), 2286-2291.
131. Singh S, Lyle H, D'Amario L, Magnano E, Vinogradov I, Cuk T. Coherent Acoustic Interferometry during the Photodriven Oxygen Evolution Reaction Associates Strain Fields with the Reactive Oxygen Intermediate (Ti-OH*). J Am Chem Soc. **2021**;143(39):15984-15997.
132. Lyle, H.; Singh, S.; Paolino, M.; Vinogradov, I.; Cuk, T., The electron-transfer intermediates of the oxygen evolution reaction (OER) as polarons by in situ spectroscopy. *Physical Chemistry Chemical Physics* **2021,** *23* (44), 24984-25002.
133. Krüger, P., Multichannel multiple scattering calculation of ${L}_{2,3}$-edge spectra of ${\text{TiO}}_{2}$ and ${\text{SrTiO}}_{3}$: Importance of multiplet coupling and band structure. *Physical Review B* **2010,** *81* (12), 125121.
134. Matouk, Z., Islam, M., Gutierrez, M., Pireaux, J.-J., Achour, A., X-ray Photoelectron Spectroscopy (XPS) Analysis of Ultrafine Au Nanoparticles Supported over Reactively Sputtered TiO2 Films. . *Nanomaterials* **2022,** *12*.
135. Lobacheva, O.; Chavarha, M.; Yiu, Y. M.; Sham, T. K.; Goncharova, L. V., The local structure and ferromagnetism in Fe-implanted SrTiO3 single crystals. *Journal of Applied Physics* **2014,** *116* (1), 013901.
136. Ruosi, A.; Raisch, C.; Verna, A.; Werner, R.; Davidson, B. A.; Fujii, J.; Kleiner, R.; Koelle, D., Electron sampling depth and saturation effects in perovskite films investigated by soft x-ray absorption spectroscopy. *Physical Review B* **2014,** *90* (12), 125120.
137. Bhogra, A.; Masarrat, A.; Meena, R.; Hasina, D.; Bala, M.; Dong, C.-L.; Chen, C.-L.; Som, T.; Kumar, A.; Kandasami, A., Tuning the Electrical and Thermoelectric Properties of N Ion Implanted SrTiO3 Thin Films and Their Conduction Mechanisms. *Scientific Reports* **2019,** *9* (1), 14486.
138. Nakai, S.-i.; Mitsuishi, T.; Sugawara, H.; Maezawa, H.; Matsukawa, T.; Mitani, S.; Yamasaki, K.; Fujikawa, T., Oxygen K x-ray-absorption near-edge structure of alkaline-earth-metal and 3d-transition-metal oxides. *Physical Review B* **1987,** *36* (17), 9241-9246.
139. Bachelet, R.; Sánchez, F.; Palomares, F. J.; Ocal, C.; Fontcuberta, J., Atomically flat SrO-terminated SrTiO3(001) substrate. *Applied Physics Letters* **2009,** *95* (14), 141915.
140. Yoo, H. K.; Schwarz, D.; Ulstrup, S.; Kim, W.; Jozwiak, C.; Bostwick, A.; Noh, T. W.; Rotenberg, E.; Chang, Y. J., Direct visualization and control of SrOx

segregation on semiconducting Nb doped SrTiO3 (100) surface. *Journal of the Korean Physical Society* **2022,** *80* (11), 1042-1047.
141. Ma, Y.; Le Formal, F.; Kafizas, A.; Pendlebury, S.; Durrant, J., Efficient Suppression of Back Electron/Hole Recombination in Cobalt Phosphate Surface-Modified Undoped Bismuth Vanadate Photoanodes. *Journal of Materials Chemistry A* **2015,** *3*.
142. Kukura P, McCamant DW, Mathies RA. Femtosecond stimulated Raman spectroscopy. Annu Rev Phys Chem. 2007;58:461-88.

APPENDIX

Optical Spectroscopy Setup

Here I showcase the optical spectroscopy setup in detail that is used for all the experiments presented in this thesis. The optical setup essentially has three beam lines that meet up the sample. The three beams are, the actinic pump (266 nm) as shown in figure A1, the WLC probe as shown in figure A2, and the Raman pump which is shown in figure A3.

Actinic Pump Beam Line (266 nm)

Here I showcase the CAD drawing of the actinic pump beam line, fig. A1, which routes the beam into a beam-splitter (BS) and sends the pump arm through an electronically controlled delay stage. The beam then enters the THG box which converts the 800 nm light (red) into 266 nm light (magenta), the process is explained in detail in chapter 2. The beam is sent through the pump cleanup stage, explained below, to improve the quality of the beam mode and is then routed to the sample and is focused using a 100 mm convex lens.

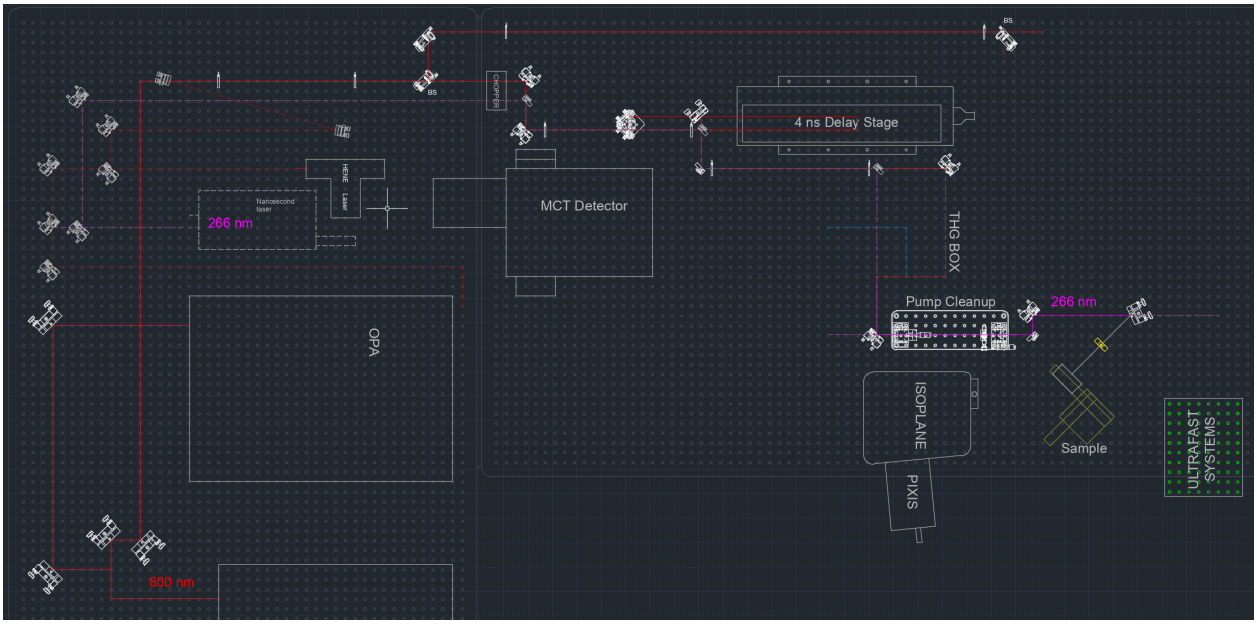

Figure A1: The actinic pump (266 nm) beam line schematic on the optical table

White light continuum (WLC) Beam Line (375 - 700 nm)

Here I showcase the CAD drawing of the WLC beam line, fig. A2. The other half of the split fundamental is split using a beam splitter and routed into the white light generation stage. In the white light generation stage the fundamental goes through the following optics, waveplate and polarizer to ensure S polarization and act as a variable attenuator, iris to modulate the f-number of the beam, focusing lens which focuses the fundamental into the moving CaF_2 crystal. The CaF_2 broadens the fundamental into the WLC (green) which is then routed to the sample. Along the way is a chirped mirror setup which helps with minimizing the GDD of the WLC probe, see chapter 6 for explanation. Additionally, the WLC is also split using a beam-splitter (BS) and one arm of the WLC is sent to the referencing camera through the referencing line.

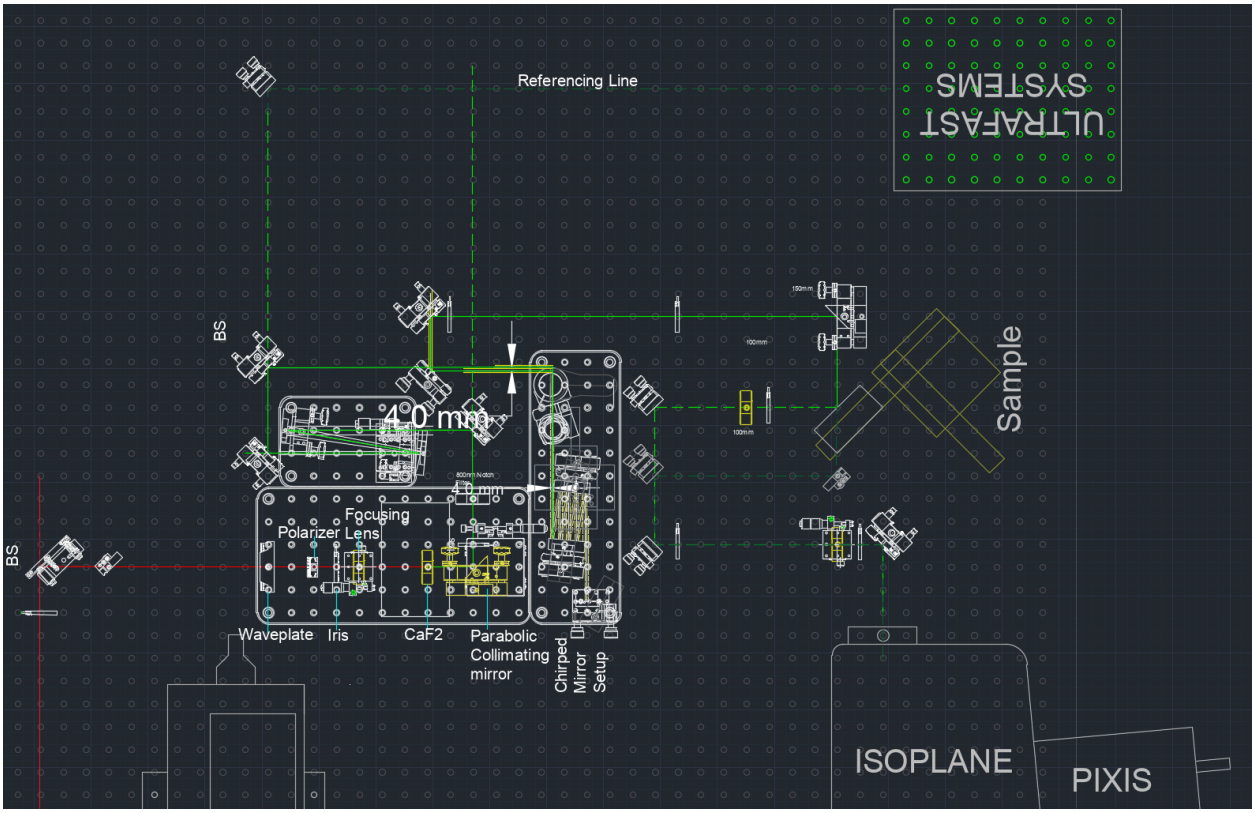

Figure A2: WLC probe beam line schematic on the optical table. Also shows the referencing beam line.

Raman Pump Beam Line (400 nm)

Here I showcase the CAD drawing of the Raman pump beam line, fig. A3. The arm of the beam after the second split of the fundamental is used to generate the Raman Pump. The fundamental is sent through a manual delay line, to make sure that the Raman pump path length is the same as the WLC probe path length, followed by a self-doubling stage, explained in chapter 6, to output 400 nm (blue) light. The

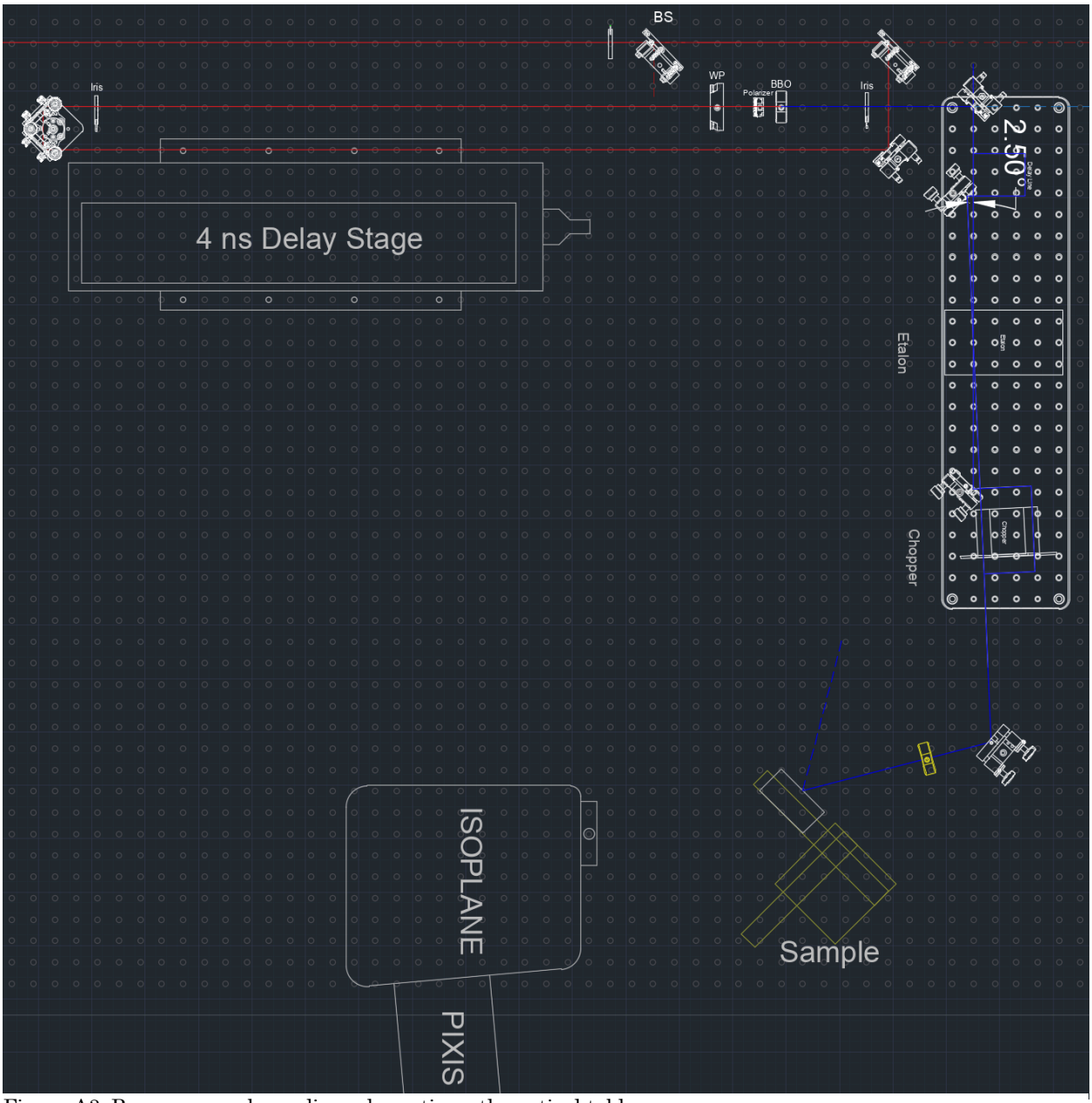

Figure A3: Raman pump beam line schematic on the optical table.

400 nm light is then routed through an Etalon, see chapter 6 for explanation, and another chopper to finally be focused on the sample using a focusing lens.

Actinic Pump Beam Cleanup Stage

The actinic pump is sent through the beam cleanup stage to improve the spatial mode quality of the actinic pump. A detailed diagram of this stage is shown in figure A4. This stage is basically a telescope (using convex mirrors) but has a small pinhole (<150 μm) at the focus of the first focusing lens. This stage can be used to improve the mode quality of any beam. The actinic pump in its collimated state (unfocused) can develop hotspots or other undesirable spatial features for various reasons and this can have adverse effects when the beam is focused on the sample. The hotspots become diffused when the beam is focused, this focused spot is usually not symmetrical, the pinhole only allows the part of the beam that matches its symmetric and circular cross-section. The cleaned-up spot is then collimated.

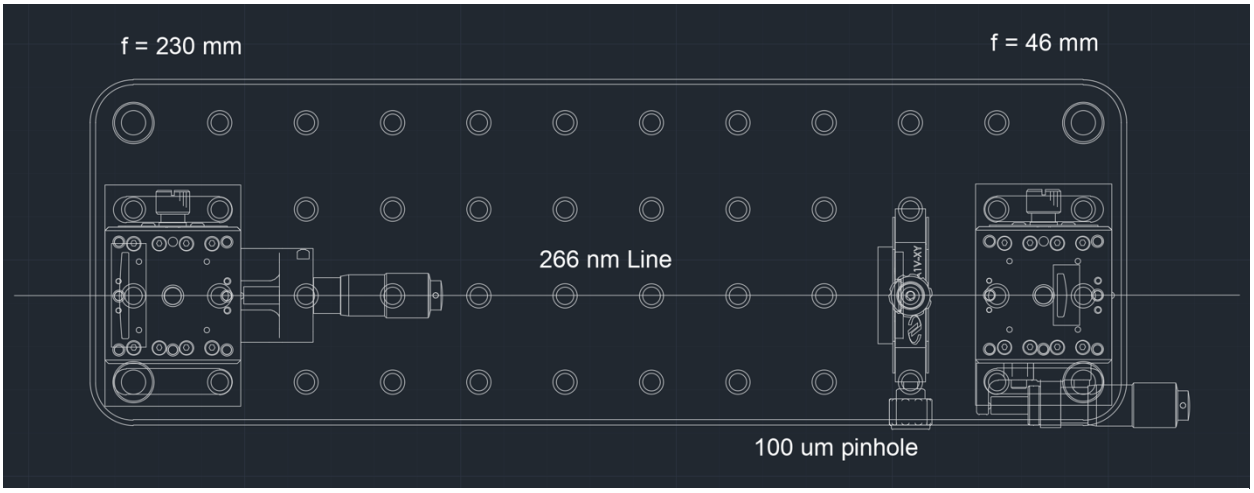

Figure A4: CAD diagram showing the actinic pump cleanup board.

The optical setup uses many different optics which are mounted, here is a list of some of the special optics and mounts for referencing future purchases. Almost all optics have been purchased from Thorlabs (www.thorlabs.com) or Newport (www.newport.com). They are listed in no particular order:

- 2” parabolic mirror (silver) – TH MPD254508-90-P01
- Ultima 170 TPI mount (Overlap mirrors) – NP U100-A2K-170N
- Ultima 100 TPI mount (Overlap mirror) – NP U200-A2K
- Newfocus delay mirror mount (manual retroreflector stages)
- Square mirror mount – TL KM100SL
- Square mirrors -TL BBSQ1-E02
- Polaris mirror mount – K25S4
- Newport compact mirror mount – V100-AX
- Newport corner mount – 9809NF
- Thorlabs compact kinematic mirror mount – KMS
- Kinematic prism mount – TL KM100PM
- Roof Mirror (UV-AI) – TL HRS1015-F01
- Polaris mount 1” (Chirped mirror setup) – TL POLARIS-K1-2AH
- Grating adapter – TL KGM20
- Chirped mirror pair – LT 148920

Determining Working Range for Single Crystal Samples

This section outlines the procedure for finding the working range of the sample. Once the WLC probe is aligned to the sample and the spectrometer, the labview programs for the stage movement and lightfield must be opened. The following steps get the working range of the sample:

- The WLC probe needs to be roughly centered on the sample.
- Using the actuators for the x direction, scan across to note the point where the WLC intensity is extinguished, repeat in the other direction. Subtract 0.5 mm from either extreme points, this gives the rough x range. (e.g., 7.5 – 16.5, turns into 8 - 16)
- Repeat the previous step but in the y direction to gather the rough y range.

- Use the center points of the rough x and y ranges to find the center point of the sample.
- Use the actuators to move to one of the corners that can be calculated using the rough x and y range. Adjust the x and y range if there is no WLC intensity seen in lightfield.
- Scan across to the other corners and adjust the x and y range incase no WLC intensity seen in lightfield.
- Compile the 4 corners to get the working range and calculate final center of the sample's working range.

MATLAB Code for Data Processing and Analysis

This section provides the MATLAB code for some critical analyses that were discussed in earlier chapters. For all the following analyses the CukLabScripts MATLAB package needs to be installed to enable the object-oriented workflow. The first section is for loading the data which can look different dependent on the user's workflow as well as the data set.

Rotation Analysis

```
% %% Load phosphate metadata
% conn = dbConn();
%
% % 0.1% phosphate data in Nat. Mat. paper
% dataList = conn.fetch(strjoin(...
%     ["SELECT ID, FileName, FilePath, ShortName",...
%      "FROM TRPhononRemoved",...
%      "WHERE ID IN (63, 24) OR ID BETWEEN 66 AND 74",...
%      "ORDER BY ID;"],' '));
%
% conn.close();
%
% %% Load phosphate data into object
% % Extract pH values and sort in ascending order
% c = regexp(dataList.ShortName,'(?<=pH )\d+\.?\d*','match');
% [pH, idx] = sort(cellfun(@(c) str2double(c), vertcat(c{:})));
% dataList = dataList(idx,:);
%
% % Load data
```

```
% myTR = wlTR(fullfile(repoPath(), dataList.FilePath,
dataList.FileName),'loadType','cListFile','shortName',dataList.ShortName);
load('ConcatObjFull.mat'); % Load all concatenated data
myTR = Concatobj(1:end-1); % Remove pH 14 as it is bad
pH = [7 10 11 11.35 11.82 12 13]; % pH list, normally would be generated by the regexp
resorting

%% Clean data and calculate SVD in SVD object
[s,l,t] = getNumeric(myTR.trim('wavelengths',[375,700]));  %return "cleaned" data from
myTR object array
trSVD = svdObj(s);   % perform the SVD analysis with default 2 components

%% Plot results (raw)
% Unflipped (raw) SVD preview
figure; previewr(trSVD,2,'xVals',l,'yVals',t,'xLabel','nm','yLabel','ps');

% Preview raw singular values by returning the diagonal of obj.Sr by calling obj.Srd
figure; plot(1:trSVD.nS,trSVD.Srd,'o');
xlabel('Component #'); xlim([1, 5]);
ylabel('Singular Value');

%% Flip basis components
% Note: in general the raw SVD results will be data set specific. Adding or
% removing a spectrum can change other spectra svd flips. I recommend
% trying to come up with a rule to establish which spectra need to be
% flipped or swapped. Keep in mind this rule may be different for different
% types of data sets.
trSVD = trSVD.resetC(); %resets flips and permutes
trSVD = trSVD.permuteC(1:trSVD.nSets,[2,1]); %swaps absorptive with emissive so that
absorptive is 1st and emissive is 2nd
trSVD = trSVD.flipC(1,squeeze(trSVD.Ur(end,1,:)<0),true);   % flip 1st component based
on raw kinetic traces--must end as a number greater than zero (emissive growth)
trSVD = trSVD.flipC(2,squeeze(trSVD.Ur(end,2,:)<0),true); % flip 2st component based
on raw kinetic traces--must end as a number less than zero (absorptive decay)

% Plot 'display' results after flipping and swapping
figure; preview(trSVD,'xVals',l,'yVals',t,'xLabel','nm','yLabel','ps');

%% Rotation Analysis
% Do the rotation analysis
[th, R] = trSVD.rotAnalysis();

% Plot the constrained spectra and kinetics to the 7th data (pH 13)
figure;
previewc(trSVD.constrain(trSVD.U(:,:,7)),'xVals',l,'yVals',t,'xLabel','nm','yLabel','p
s',...
         'legend',cellfun(@(c) strcat({'pH '}, num2str(c)), num2cell(pH)));

% Plot the rotation angle w.r.t. pH 7 and ph 13
figure;
    plot(pH, 180/pi*th(:,[1,7]));
xlabel('pH');
ylabel('angle (deg)');
legend('pH 7','pH 13');

%% Check Spectra
figure; hold on;
for ii = 7%1:length(myTR)
    plot(l,trSVD.U(:,2,ii));
end
```

Basis Generation for Constrained SVD Analysis

```
%% Initialize data
load("ConcatObjFull.mat"); % Load concatenated data
myTR = Concatobj(1:end-1); % Exclude pH 14 data cuz it nasty
pH = [7 10 11 11.35 11.82 12 13];

%% Clean data and calculate SVD in SVD object
[s,l,t] = getNumeric(myTR.trim('wavelengths',[375,700]));  %return "cleaned" data from
myTR object array
trSVD = svdObj(s);   % perform the SVD analysis with default 2 components

%% Plot results (raw)
% Unflipped (raw) SVD preview
figure; previewr(trSVD,2,'xVals',l,'yVals',t,'xLabel','nm','yLabel','ps');

% Preview raw singular values by returning the diagonal of obj.Sr by calling obj.Srd
figure; plot(1:trSVD.nS,trSVD.Srd,'o');
xlabel('Component #'); xlim([1, 5]);
ylabel('Singular Value');

%% Flip basis components
% Note: in general the raw SVD results will be data set specific. Adding or
% removing a spectrum can change other spectra svd flips. I recommend
% trying to come up with a rule to establish which spectra need to be
% flipped or swapped. Keep in mind this rule may be different for different
% types of data sets.
trSVD = trSVD.resetC(); %resets flips and permutes
trSVD = trSVD.permuteC(1:trSVD.nSets,[2,1]); %swaps absorptive with emissive so that
absorptive is 1st and emissive is 2nd
trSVD = trSVD.flipC(1,squeeze(trSVD.Ur(end,1,:)<0),true);   % flip 1st component based
on raw kinetic traces--must end as a number greater than zero (emissive growth)
trSVD = trSVD.flipC(2,squeeze(trSVD.Ur(end,2,:)<0),true); % flip 2nd component based
on raw kinetic traces--must end as a number less than zero (absorptive decay)

% Plot 'display' results after flipping and swapping
figure; preview(trSVD,'xVals',l,'yVals',t,'xLabel','nm','yLabel','ps');
% 1st column is absorptive, 2nd is emissive.

%% Get concatenated Raw SVD components into easy to work with variables
% 1st column is absorptive, 2nd is emissive, confirm with previous section
SpectComps = trSVD.U;

% Set up variable for storing basis. Spectral Components need to be ordered as
Absorptive Emissive
SpectCompsTrue = zeros(size(SpectComps));
%% Take linear combinations of the raw SVD components, normalize, plot, and compare
new absorptive basis

% Define the parameteric range for each condition in iiList
% X = cell(size(SpectComps));
% a1 = [-0.2:0.05:0.1]; b1 = [-1.25:0.05:-0.95];
a1 = -1.2; b1 = 0.175; % pH 7, store in absbasispH7 manually
% a1 = -0.9; b1 = 0; % pH 10, store in absbasispH10 manually
% a1 = -0.9; b1 = 0.0; % pH 11, store in absbasispH11 manually
% a1 = -0.6; b1 = -0.2; % pH 11.35, store in absbasispH11.35 manually
% a1 = -0.45; b1 = -0.35; % pH 11.82, store in absbasispH11.82 manually
% a1 = -0.45; b1 = -0.3; % pH 12, store in absbasispH12 manually
% a1 = -0.5; b1 = -0.3; % pH 13, store in absbasispH13 manually
```

```
for ii = 1%:size(SpectComps,3)

    figure; hold on;

    for jj = 1:length(a1)

                X = [1 a1(jj);b1(jj) 1];
                X(:,1) = X(:,1)/norm(X(:,1));
                X(:,2) = X(:,2)/norm(X(:,2));

                SpectCompsTrue(:,:,ii) = SpectComps(:,:,ii)*X;

                plot(l,SpectCompsTrue(:,:,ii),l,SpectComps(:,:,ii),'--');

    end

    title(['pH ' num2str(pH(ii))]);
    legend('AutoUpdate','off','Location','southeast');
    yline(0,'--k');
    box on;

end

%% Average and Save the new absorptive basis and plot to check
% Average the absorptive basis
const_abs = squeeze(SpectCompsTrue(:,1,:));
const_abs = mean(const_abs,2);
const_abs = const_abs/norm(const_abs);
% Average the emmissive basis
const_em = squeeze(SpectCompsTrue(:,2,:));
const_em = mean(const_em,2);
const_em = const_em/norm(const_em);

nm = l;

figure; plot(l,const_abs,'-r',l,const_em,'-b');

title('Spectral Basis');
legend('Absorptive basis','Emissive basis','Location','southeast','Autoupdate','off');
yline(0,'--k');
box on;


% save([ParentFolder DataFolder_PR 'Basis Spectra and Constrained SVD
Components/Concat Basis 2022/pH dep concatenated SVD basis new
final.mat'],"nm","const_abs","const_em");
save('Basis Spectra and Constrained SVD Components/Concat Basis 2022/phosphate pH dep
concat SVD basis offset.mat',"nm","const_abs","const_em");
```

Spectrally Constrained SVD Analysis

```
%% Load metadata of required data sets for constrained SVD

% For Windows OS use the following code to establish connection to database
% conn = database('Raman.accdb','','');

% For MAC OC use the follwing code to establish connection to database,
% update db_path according where the Raman database is stored locally on
```

```
% the system
db_path = fullfile(filesep,'Users','suryansh','Work','CUB','TC research
group','Data','New Data','Raman.accdb');
url = ['jdbc:ucanaccess://' db_path];
conn = database('','','','net.ucanaccess.jdbc.UcanaccessDriver',url);

% Query 0.1% phosphate data in Nat. Mat. paper
dataList = conn.fetch(strjoin(...
    ["SELECT ID, FileName, FilePath, ShortName",...
     "FROM TRPhononRemoved",...
     "WHERE ID IN (63, 24) OR ID BETWEEN 66 AND 74",...
     "ORDER BY ID;"],' '));

conn.close();

%% Load phosphate data into object
% Extract pH values and sort in ascending order
c = regexp(dataList.ShortName,'(?<=pH )\d+\.?\d*','match');
[pH, idx] = sort(cellfun(@(c) str2double(c), vertcat(c{:})));
dataList = dataList(idx,:);

% Load data into TR objects for Windows
% myTR = wlTR(fullfile(repoPath(), dataList.FilePath,
dataList.FileName),'loadType','cListFile','shortName',dataList.ShortName);


% Load data into TR objects on MAC OS systems, make sure to be Volumes directory
data_path = fullfile(repoPath(), dataList.FilePath, dataList.FileName); % Path needs
to be modified
data_path = strrep(data_path,'\','/');
data_path = strrep(data_path,'G:','GoogleDrive'); % This step may look different
depending on how google drive was setup
myTR = wlTR(data_path,'loadType','cListFile','shortName',dataList.ShortName);

%% Constrained SVD
% Absorptive components are stored in SUconstKeep{ii}(:,1), Emissive components in
SUconstKeep{ii}(:,2)

% t_log plots time axis on log scale (t_log = true) or linear scale (t_log = false)
t_log = true;
saving = false;
offset = false;
IntAbs = true;

% Load data
[s,l,t] = getNumeric(myTR.trim('wavelengths',[375,700]));  %return "cleaned" data from
myTR object array
nameList = cell(1,length(myTR));

% Variables to store constrained components + weights for IGOR export
SUconstKeep = cell(1,length(myTR));
VconstKeep = cell(1,length(myTR));
WeightsNorm = zeros(length(myTR),2);

figSAbs = figure; figSEm = figure;
figKAbs = figure; figKEm = figure;

if offset
    figKAbsoff = figure;
end
```

```
% load SVD basis from GoogleDrive, update this as needed
% For MAC OS
% basis_path = fullfile(strrep(repoPath(),'G:','GoogleDrive'),'CukResearchGroup','TR-
VIS','SVD Basis','Nov 11 2019','0V_Aritra_SVD_Basis.mat');
% For Windows OS
% basis_path = fullfile(repoPath(),'CukResearchGroup','TR-VIS','SVD Basis','Nov 11
2019','0V_Aritra_SVD_Basis.mat');

% load(basis_path); % Loads SVD Basis


%Loop through selected entries in conditionList using iiList
for ii = 1:length(myTR)

    data = (s(:,:,ii)')/1000; %

    %interpolates basis along new wavelength axis and normalized
    const_abs_interp = interp1(nm,const_abs,l,'linear','extrap');
    const_em_interp = interp1(nm,const_em,l,'linear','extrap');
    constV = zeros(length(l),2);
    constV(:,1) = const_abs_interp/norm(const_abs_interp);
    constV(:,2) = const_em_interp/norm(const_em_interp);

    %calculates SVD of data and does the constraint
    [U,S,V] = svd(data);
    X = V(:,1:2)'*constV;
    V_const = V(:,1:2)*X;
    SU_const = (X\S(1:2,1:2)*U(:,1:2)')';
    SUconstKeep{ii}=SU_const;
    VconstKeep{ii}=V_const;

    WeightsNorm(ii,1) = S(1,1)/(S(1,1)+S(2,2));
    WeightsNorm(ii,2) = S(2,2)/(S(1,1)+S(2,2));

    figure(figKAbs); hold on;
%     plot(t,SU_const(:,1)/trapz(SU_const(:,1)));
    plot(t,SU_const(:,1));

    if IntAbs
            figure(figKEm); hold on;
            temp = trapz(SU_const(:,1));
            plot(t,SU_const(:,2)/temp);
    else
            figure(figKEm); hold on;
            plot(t,SU_const(:,2));
    end

    if offset
        figure(figKAbsoff); hold on;
        plot(t,(SU_const(:,1)-SU_const(end,1)));
    end

    figure(figSAbs); hold on;
    plot(l,V_const(:,1));

    figure(figSEm); hold on;
    plot(l,V_const(:,2));

    nameList{ii} = strrep(myTR(ii).shortName,'_',' ');
end
```

```
figure(figKAbs);
    yline(0,'k--','LineWidth',1);
    if t_log
        xlim([1 max(t)]);
        set(gca,'XScale', 'log');
    else
        xlim([min(t) max(t)]);
    end
    legend(nameList);
    xlabel('Time Delay (ps)');
    ylabel('A.U.');
    title('Constrained Absorptive Kinetics');
    box on;

% Update the function with the directory where you'd want to save the figures
if saving
    saveas(gcf,['Concat constrained Abs Kinetics' '.png']);
    saveas(gcf,['Concat constrained Abs Kinetics' '.fig']);
end

if offset
    figure(figKAbsoff);
    yline(0,'k--','LineWidth',1);
    if t_log
        xlim([1 max(t)]);
        set(gca,'XScale', 'log');
    else
        xlim([min(t) max(t)]);
    end
    legend(nameList);
    xlabel('Time Delay (ps)');
    ylabel('A.U.');
    title('Constrained Absorptive Kinetics offset');
    box on;
end
figure(figSAbs);
    plot(l,const_abs_interp/norm(const_abs_interp),'k--','LineWidth',1);
    yline(0,'k--','LineWidth',1);
    legend(nameList,'Location','southeast');
    xlabel('Wavelength(nm)');
    ylabel('A.U.');
    title('Constrained Absorptive Spectra');
    box on;

% Update the function with the directory where you'd want to save the figures
if saving
    saveas(gcf,['Concat constrained Abs spectra' '.png']);
    saveas(gcf,['Concat constrained Abs spectra' '.fig']);
end

figure(figKEm);
    yline(0,'k--','LineWidth',1);
    if t_log
        xlim([1 max(t)]);
        set(gca,'XScale', 'log');
    else
        xlim([min(t) max(t)]);
    end
    legend(nameList,'Location','south');
    xlabel('Time Delay (ps)');
    ylabel('A.U.');
```

```
    title('Constrained Emissive Kinetics');
    box on;

    if IntAbs
        figure(figKEm);
        yline(0,'k--','LineWidth',1);
        if t_log
        xlim([1 max(t)]);
        set(gca,'XScale', 'log');
        else
        xlim([min(t) max(t)]);
        end
        legend(nameList,'Location','south');
        xlabel('Time Delay (ps)');
        ylabel('A.U./(Intergrated Absoprtion)');
        title('Constrained Emissive Kinetics');
        box on;
    end

% Update the function with the directory where you'd want to save the figures
if saving
    saveas(gcf,['Concat constrained Ems Kinetics' '.png']);
    saveas(gcf,['Concat constrained Ems Kinetics' '.fig']);
end

figure(figSEm);
    plot(l,const_em_interp/norm(const_em_interp),'k--','LineWidth',1);
    yline(0,'k--','LineWidth',1);
    legend(nameList,'Location','southeast');
    xlabel('Wavelength(nm)');
    ylabel('A.U.');
    title('Constrained Emissive Spectra');
    box on;

% Update the function with the directory where you'd want to save the figures
if saving
    saveas(gcf,['Concat constrained Ems Spectra' '.png']);
    saveas(gcf,['Concat constrained Ems Spectra' '.fig']);
end

%% Constrained SVD components export into IGOR compatible format for fitting with
statistics, make sure you're in the rgiht directory before exporting

plotdata = true; % Check early timescale of data to make the rise of the data looks
reasonable
export = true;

% % Defines Gaussian pulse to convolve the constrained SVD components
% dt = 0.05; tConv = -1:dt:1;
% pulse = @(w,t) 1/(w*sqrt(2*pi))*exp(-t.^2/(2*w^2)); %pulse envolope to convolute
data with
% fwhm = 0.406; %width in ps
%
% t_convlim = max(tConv); % time delay in ps units until which the data is convolved
with the pulse
% t_convlim_ind = zeros(size(t_convlim));
%
% SUconstConv = cell(size(SUconstKeep));

if plotdata
    Const_EM_K = figure; Const_AB_K = figure;
```

```
end

if export
    fileName = 'Phosphate_pH_dep_constSVDKinetics';
    save(fileName,'t');
end

for ii = 1:length(myTR)

%     [~,t_convlim_ind] = min(abs(t-t_convlim));
%
%     temp =
nonuniformConv(SUconstKeep{ii}(1:t_convlim_ind,1),t(1:t_convlim_ind),pulse(fwhm/2.355,
tConv),dt); % Convolves absorptive component with the pulse
%     SUconstConv{ii}(:,1) = 100*heaviside(t-
0.2).*[temp;SUconstKeep{ii}(t_convlim_ind+1:end,1)];
%
%     temp =
nonuniformConv(SUconstKeep{ii}(1:t_convlim_ind,2),t(1:t_convlim_ind),pulse(fwhm/2.355,
tConv),dt); % Convolves emissive component component
%     SUconstConv{ii}(:,2) = 100*heaviside(t-
0.2).*[temp;SUconstKeep{ii}(t_convlim_ind+1:end,2)];

    if plotdata
    figure(Const_EM_K); hold on;
    plot(t,SUconstKeep{ii}(:,2));

    figure(Const_AB_K); hold on;
    plot(t,SUconstKeep{ii}(:,1));
    end

    if export

        tempd = [strrep(nameList{ii},' ','_') '_Abs'];
        tempd = strrep(tempd,'.','p');
        tempd = strrep(tempd,'#','');
        tempd = strrep(tempd,'%','_');
        tempd = strrep(tempd,'Na','IS');
        tempd = strrep(tempd,'+','');
        tempd = strrep(tempd,'0-500us','ns');
        tempd = strrep(tempd,'0-500_us','ns');

        eval([tempd ' = SUconstKeep{ii}(:,1);']);
        save(fileName,tempd,'-append');

        tempd = [strrep(nameList{ii},' ','_') '_Em'];
        tempd = strrep(tempd,'.','p');
        tempd = strrep(tempd,'#','');
        tempd = strrep(tempd,'%','_');
        tempd = strrep(tempd,'Na','IS');
        tempd = strrep(tempd,'+','');
        tempd = strrep(tempd,'0-500us','ns');
        tempd = strrep(tempd,'0-500_us','ns');

        eval([tempd ' = SUconstKeep{ii}(:,2);']);
        save(fileName,tempd,'-append');

    end

end
```

```
if plotdata

    figure(Const_EM_K);
            yline(0,'k--','LineWidth',1);
            xlim([-0.2 max(t)]);
%     set(gca,'XScale', 'log');
            legend(nameList,'Location','southeast');
            xlabel('Time Delay (ps)');
            ylabel('A.U.');
            title('Constrained Emissive Kinetics');
            box on;

    figure(Const_AB_K);
            yline(0,'k--','LineWidth',1);
            xlim([-0.2 max(t)]);
%     set(gca,'XScale', 'log');
            legend(nameList,'Location','southeast');
            xlabel('Time Delay (ps)');
            ylabel('A.U.');
            title('Constrained Absorptive Kinetics');
            box on;
end
```

ConcatObj Method for Concatenating ultrafast and longer timescale data sets

```
function ConcatObj = concatData(obj,varargin)
% CONCATDATA merges ultrafast data with longtime data
% output is an object comprising of data concatenated along the
% delay axis. This function mimics the functionality of merge
% method but applies it to the delay axis.
% *Requirements for the data*
% 1. Data must be in *2 rows or columns*, corresponding to
% ultrafast and longtime respectively, same number of datasets in
% each column or row is required, if input object is of 2*2 dimensions
% then make sure the data in one row correspond to only longtime and the other only
ultrafast
%
% 2. All data sets in the object must be pruned, averaged, and
% stitched properly, to make sure that the gPos, rpts, and
% Schemes dimensions are 1, this reduces the dimension of the spectra
% variable to 2D making concatenation easier
%
% 3. Data in 1 column or row must correspond to the data in the other column
%
% ConcatObj = obj.concat(concatMethod); Returns a wlTRC object with the
% scaling factor as properties of the object
%
%
% Implemented concatMethod keywords:
% 'Single' Concatenates the two corresponding datasets using only 1 scaling
% factor computed by comparing spectra at the time delay of
% concatenation
%
% 'Multi' Concatenates the two corresponding datasets using an
% average scaling factor. The method compares spectra at all
% common time delay points and averages all those scaling factors
% and uses it to scale the data sets and then concatenates them.
%
```

```
% 'None' Concatenates the two data sets without any scaling,
% should be used for comparisons if/when Single or Multi modes are
% misbehaving

          % 1. Asserts that the obj array is of 2*n and reshapes if needed
          objSizeOr = size(obj);
          if objSizeOr(1) ~= 2
              obj = obj';
          end

          objSize = size(obj); % Updates object size to be 2*n

          % 2. Make sure that the first row is longtime data and the
          % second row is ultrafast
          if max(obj(1,1).delays) < 5000 % Checks if first row of object is ultrafast
                obj([1 2],:) = obj([2 1],:); % Switches the rows if first row of
object is ultrafast
          end

          % 3. Trim all data sets to appropriate wavelength range & Interpolate pairs
of data sets on the same wavelength axis

          obj = obj.trim('wavelengths',[375 700]);

          for ii = 1:objSize(2)
                l = obj(1,ii).wavelengths.data; % Extract wavelengths axis from
longtime data
                obj(2,ii) = obj(2,ii).interp('wavelengths',l); % Interpolate the
ultrafast data onto the longtime data axis
          end

          % 4. Check if using 'Single' or 'Multi' or 'None' case,
          % isolate the pairs of spectra to be used to find the scaling factors in
          % approprtiate variables, scale the longtime data to the
          % ultrafast data, and trim the longtime data appropriately
          if isempty(varargin)
              varargin{1} = 'None';
          end

          all_sf = cell(1,objSize(2));
          avg_sf = zeros(2,objSize(2));
          l_range = [375 700]; % limits the spectral wavelength range in order to
reduce the contribution of noise in the scaling factor calculation
          l_range_ind = zeros(1,2);

          for ii = 1:objSize(2)

              switch varargin{1}

                  case 'Single'
                      % Uses scaling factor at only the delay point of concatenation
                      t_conc = max(obj(2,ii).delays.data); % Find point of
concatenation
                      [~,t_conc_ind_l] = min(abs(t_conc-obj(1,ii).delays.data)); %
Find index of point of concatenation in the longtime delay axis

                      [~,l_range_ind(1)] = min(abs(l_range(1)-
obj(1,ii).wavelengths.data)); % Find index of wavelength range
                      [~,l_range_ind(2)] = min(abs(l_range(2)-
obj(1,ii).wavelengths.data)); % Find index of wavelength range
```

```
                    long =
obj(1,ii).spectra.data(l_range_ind(1):l_range_ind(2),t_conc_ind_l,:,:,:); % Spectra
from longtime data
                    short =
obj(2,ii).spectra.data(l_range_ind(1):l_range_ind(2),end,:,:,:); % Spectra from
ultrafast data

                    all_sf{1,ii} = (short'*long)/(long'*long); %Scaling factor to
normalize longtime data to ultrafast data

                    avg_sf(1,ii) = all_sf{1,ii};

                    obj(1,ii).spectra.data = avg_sf(1,ii)*obj(1,ii).spectra.data; %
Scaling longtime data

                    obj(1,ii) =
obj(1,ii).trim('delays',[t_conc,max(obj(1,ii).delays.data)]); % Trim the longtime
data, removes all delay points until point of concatenation

%                       obj(1,ii).spectra_std.data =
rmmissing((sqrt(avg_sf))*obj(1,ii).spectra_std.data(:,t_conc_ind_l:end,:,:,:)); % Trim
the spectra_std of the scaled longtime data

                    obj(1,ii).description = [obj(1,ii).description ' Concatenated
using 1 scaling factor at point of concatenation']; % Updates description to indicate
the method of concatenation

                case 'Multi'
                    % Uses scaling factors from all common time delays
                    % greater than zero
                    t_conc = max(obj(2,ii).delays.data); % Find point of
concatenation
                    [~,t_conc_ind_l] = min(abs(t_conc-obj(1,ii).delays.data)); %
Find index of point of concatenation in the longtime delay axis

                    [~,l_range_ind(1)] = min(abs(l_range(1)-
obj(1,ii).wavelengths.data)); % Find index of wavelength range
                    [~,l_range_ind(2)] = min(abs(l_range(2)-
obj(1,ii).wavelengths.data)); % Find index of wavelength range

                    t_l = obj(1,ii).delays.data(1:t_conc_ind_l); % Obtain longtime
delays until the point of concatenation
                    temp = find(t_l<1500);
                    t_l(temp) = []; % Drop the time delay points smaller than 1500
ps, Since the pulse duration of the longtime pump is ~1ns, spectral comparisons below
1.5ns aren't meaningful

                    for kk = 1:length(t_l) % Looping over all common delays>1ps and
finding scaling factors

                        [~,t_l_ind] = min(abs(t_l(kk)-obj(1,ii).delays.data)); %
Find index of point of concatenation in the longtime delay axis
                        [~,t_s_ind] = min(abs(t_l(kk)-obj(2,ii).delays.data)); %
Find index of point of concatenation in the ultrafast delay axis

                        long =
obj(1,ii).spectra.data(l_range_ind(1):l_range_ind(2),t_l_ind,:,:,:); % Spectra from
longtime data
                        short =
obj(2,ii).spectra.data(l_range_ind(1):l_range_ind(2),t_s_ind,:,:,:); % Spectra from
ultrafast data
```

```
                        all_sf{1,ii}(kk,1) = (short'*long)/(long'*long); %Scaling
factor to normlaize longtime data to ultrafast data
                    end

                    avg_sf(1,ii) = mean(all_sf{1,ii});

                    obj(1,ii).spectra.data = avg_sf(1,ii)*obj(1,ii).spectra.data; %
Scaling longtime data

                    obj(1,ii) =
obj(1,ii).trim('delays',[t_conc,max(obj(1,ii).delays.data)]); % Trim the longtime
data, removes all delay points until point of concatenation

%                     obj(1,ii).spectra_std.data =
rmmissing((sqrt(avg_sf))*obj(1,ii).spectra_std.data(:,t_conc_ind_l:end,:,:,:)); % Trim
the spectra_std of the scaled longtime data

                    obj(1,ii).description = [obj(1,ii).description ' Concatenated
using scaling factors from all common time points']; % Updates description to indicate
the method of concatenation

                case 'None'
                    % No scaling factors invloved
                    t_conc = max(obj(2,ii).delays.data); % Find point of
concatenation

                    obj(1,ii) =
obj(1,ii).trim('delays',[t_conc,max(obj(1,ii).delays.data)]); % Trim the longtime
data, removes all delay points until point of concatenation

%                     obj(1,ii).spectra_std.data =
rmmissing(obj(1,ii).spectra_std.data(:,t_conc_ind_l:end,:,:,:)); % Trim the
spectra_std of the scaled longtime data

                    obj(1,ii).description = [obj(1,ii).description ' Concatenated
without any scaling']; % Updates description to indicate the method of concatenation

                case 'Offset'
                    % Combines the Multi method with offsets
                    t_conc = max(obj(2,ii).delays.data); % Find point of
concatenation
                    [~,t_conc_ind_l] = min(abs(t_conc-obj(1,ii).delays.data)); %
Find index of point of concatenation in the longtime delay axis

                    [~,l_range_ind(1)] = min(abs(l_range(1)-
obj(1,ii).wavelengths.data)); % Find index of wavelength range
                    [~,l_range_ind(2)] = min(abs(l_range(2)-
obj(1,ii).wavelengths.data)); % Find index of wavelength range

                    spectra_s_conc =
obj(2,ii).spectra.data(l_range_ind(1):l_range_ind(2),end,:,:,:); % Finds ultrafast
spectra at point of concatenation

                    [~,min_ind] = min(abs(spectra_s_conc)); % Finds index of
wavelength where the spectra crosses zero roughly
                    x = [min_ind-150:min_ind+100]; % Bracket indices around the
min_ind
                    y = spectra_s_conc(min_ind-150:min_ind+100); % Isolate data for
fitting around min_ind
                    p = polyfit(x,y,1); % Fit data with a line
```

```
                    Fit = p(1)*x + p(2); % Put the fit into a variable

                    [~,min_ind] = min(abs(Fit));
                    min_ind = x(min_ind); % Find index of wavelength where the
linear fit of the spectra crosses zero

                    offset = obj(1,ii).spectra.data(min_ind,t_conc_ind_l,:,:,:); %
Finds the offset from the longtime data

                    obj(1,ii).spectra.data = obj(1,ii).spectra.data - offset; %
corrects the offset from the entire longtime dataset

                    t_l = obj(1,ii).delays.data(1:t_conc_ind_l); % Obtain longtime
delays until the point of concatenation
                    temp = find(t_l<1500);
                    t_l(temp) = []; % Drop the time delay points smaller than 1500
ps, Since the pulse duration of the longtime pump is ~1ns, spectral comparisons below
1.5ns aren't meaningful

                    for kk = 1:length(t_l) % Looping over all common delays>1ps and
finding scaling factors

                        [~,t_l_ind] = min(abs(t_l(kk)-obj(1,ii).delays.data)); %
Find index of point of concatenation in the longtime delay axis
                        [~,t_s_ind] = min(abs(t_l(kk)-obj(2,ii).delays.data)); %
Find index of point of concatenation in the ultrafast delay axis

                        long =
obj(1,ii).spectra.data(l_range_ind(1):l_range_ind(2),t_l_ind,:,:,:); % Spectra from
longtime data
                        short =
obj(2,ii).spectra.data(l_range_ind(1):l_range_ind(2),t_s_ind,:,:,:); % Spectra from
ultrafast data

                        all_sf{1,ii}(kk,1) = (short'*long)/(long'*long); %Scaling
factor to normlaize longtime data to ultrafast data
                    end

                    avg_sf(1,ii) = mean(all_sf{1,ii}); avg_sf(2,ii) = offset;

                    obj(1,ii).spectra.data = avg_sf(1,ii)*obj(1,ii).spectra.data; %
Scaling longtime data

                    obj(1,ii) =
obj(1,ii).trim('delays',[t_conc,max(obj(1,ii).delays.data)]); % Trim the longtime
data, removes all delay points until point of concatenation

%                     obj(1,ii).spectra_std.data =
rmmissing((sqrt(avg_sf))*obj(1,ii).spectra_std.data(:,t_conc_ind_l:end,:,:,:)); % Trim
the spectra_std of the scaled longtime data

                    obj(1,ii).description = [obj(1,ii).description ' Concatenated
using scaling factors from all common time points and offset from the point of
concatenation']; % Updates description to indicate the method of concatenation

                otherwise
                    error([varargin{1} ' is not a valid operational scheme, try
Single or Multi or None']);

            end
        end
```

```
          % 4. Merge longtime data to to the ultrafast data, 2 properties
          % need to be merged, the delays and spectra

           ConcatObj(1,objSize(2)) = wlTRC(); % Output object starts off as an object
of a new class to enable having scaling factors as properties

           for ii = 1:objSize(2)

               ConcatObj(1,ii).avg_sf = avg_sf(:,ii); % Write the average scaling
factor into the new object

               ConcatObj(1,ii).all_sf = all_sf{1,ii}; % Write all scaling factors into
the new object

               ConcatObj(1,ii).chirpParams = obj(1,ii).chirpParams; % Copy the
chirpParam field

               long = obj(1,ii).spectra.data; % Extract longtime data
               short = obj(2,ii).spectra.data; % Extract ultrafast data

               % Check if the dimensions of the data are correct
               ConcatObj(1,ii).spectra.data = [short long]; % Append and input the
spectra
%
%                longstd = obj(1,ii).spectra_std.data; % Extract std dev of longtime
data
%                shortstd = obj(2,ii).spectra_std.data; % Extract std dev of ultrafast
data

               ConcatObj(1,ii).spectra_std.data = obj(1,ii).spectra_std.data; % Append
and input the std dev of spectra

               ConcatObj(1,ii).wavelengths = obj(1,ii).wavelengths; % Write the
wavelengths into the new object

               longDelay = obj(1,ii).delays.data; % Extract longtime delay axis
               shortDelay = obj(2,ii).delays.data; % Extract ultrafast delay axis

               ConcatObj(1,ii).delays.data = [shortDelay;longDelay]; % Vertical Concat
the two axes and input into object

               ConcatObj(1,ii).t0 = obj(1,ii).t0; % Copy t0 into object

               ConcatObj(1,ii).gPos = obj(1,ii).gPos; % Copy gPos into object

               ConcatObj(1,ii).name = ['Concatenated ' strrep(obj(1,ii).name,'_','
')]; % Write the name field

               ConcatObj(1,ii).shortName = obj(1,ii).shortName; % Copy the shortName
field

               ConcatObj(1,ii).description = obj(1,ii).description; % Copy the
description into the new object

               ConcatObj(1,ii).schemes = obj(1,ii).schemes; % Copy the schemes into
the new object

               ConcatObj(1,ii).sizes = obj(1,ii).sizes; % Copy sizes into the new
object
```

```
                ConcatObj(1,ii).sizes.nDelays = size(ConcatObj(1,ii).delays.data,1);%
Update delay size in object

            end

          % 5. Transposes the ConcatObj to match the variable dimension of
          % the initial object, i.e. if obj is n*2, concatObj is n*1 as well
          if objSizeOr(1) ~= 2
              ConcatObj = ConcatObj';
          end

          end

    end
```